UiT The Arctic University of Norway

Faculty of Science and Technology
Department of Physics and Technology

Intermittent fluctuations in the boundary of magnetically confined fusion plasmas

Sajidah Ahmed

A dissertation for the degree of Philosophiae Doctor, August 2023

Abstract

Fluctuation-induced transport is a profound concern for the successful operation of commercially-viable fusion reactors. These turbulent phenomena are inherent in the outer midplane, where the enclosed plasma core meets the scrape-off layer (SOL). The SOL is the region of magnetic field lines intersecting with the material surfaces. Here, hot and dense blob-like filaments elongated along the magnetic field lines detach from the main plasma and propagate radially outward with high velocities. These filaments lead to damaging plasma–wall interactions, enhancing erosion of the material surfaces and subsequently leading to the degradation of the plasma confinement.

Filaments appear as high amplitude fluctuations in stationary time series. They are notably diagnosed in ion saturation current measurements from Langmuir probes, or in emitted light intensity measurements from gas puff imaging (GPI). These intermittent fluctuations are known to display skewed and flattened probability density functions. Moreover, their frequency power spectra manifest a characteristic Lorentzian shape. These statistical properties remain consistent across different fusion devices, confinement modes, and plasma parameters. A well-known stochastic model, called the filtered Poisson process (FPP), can accurately reproduce these salient statistical features.

This thesis presents an in-depth study into fluctuations in the region close to the wall, known as the far SOL, from low-confinement mode plasmas. Under various plasma and machine parameters, the Richardson-Lucy deconvolution method is employed for amplitude and waiting-time extraction, revealing how these change with the aforementioned parameters. This departure from the traditional conditional averaging technique, with its high thresholding requirements, leads to improved amplitude and waiting-time statistics. The strengths and weaknesses of this new approach are reported.

A detailed analysis of far SOL fluctuations in Alcator C-Mod was performed, encompassing a broader range of densities that have not been studied before using the FPP. Trends in the FPP model parameters are observed, estimated from Langmuir probes and GPI. The mean amplitudes and fluxes increase with density thereby amplifying plasma–wall interactions. Insights into the behaviour of far SOL fluctuations emerge across six distinct devices: Alcator C-Mod, TCV, DIII-D, KSTAR, MAST, and MAST-U. Across all of these devices, the amplitudes increase linearly with the plasma density. However, the study shows no universal relationship between Greenwald fraction and the FPP model parameters. The disparities in the behaviour of the far SOL fluctuations are highlighted between conventional and spherical tokamaks. The study underlines how plasma and machine parameters effect far SOL fluctuation statistics, offering a nuanced perspective for next-step fusion devices.

Acknowledgements

First and foremost, I would like to express my sincerest thanks and gratitude to my main supervisor, Audun Theodorsen. I am immensely grateful for the discussions, detailed feedback on this thesis and manuscripts, and the opportunities to travel. Your patience and candour has been extremely valuable.

I am grateful to my co-supervisor, James Terry (Jim), at the MIT Plasma Science and Fusion Center (PSFC), with whom I have had the privilege to work and interact. Our discussions, particularly regarding gas puff imaging, have been engaging and enlightening. Thank you for dedicating time in carefully reviewing my manuscripts.

My appreciation extends to my co-supervisor, Odd Erik Garcia, for important discussions on the broader perspective and for offering helpful suggestions.

I am thankful to Adam Kuang at Commonwealth Fusion Systems for providing insights into experiments and for patiently addressing my inquiries despite his demanding schedule. I am also thankful for the uplifting conversations that have provided encouragement.

My thanks goes to UiT The Arctic University of Norway and the Tromsø Forskningsstiftelse for funding this project and facilitating the research stays. My seven-month research stay at MIT PSFC has been remarkably productive. I would like to convey my thanks to the entire PSFC community for their warm hospitality. The vibrant enthusiasm for fusion energy research is something that will stay with me. Similarly, I am appreciative of the one-month research stay at the UK Atomic Energy Authority (UKAEA), during which I benefited from the guidance and discussions with Peter Ryan.

I also extend my thanks to the following collaborators for sharing experimental data and/or engaging in helpful discussions: Scott Allan (UKAEA), Jose Boedo (General Atomics), Raymond Diab (MIT), William Fuller (UKAEA), Theodore Golfinopoulos (MIT), Woonghee Han (MIT), Earl Marmar (MIT), Nicola Offeddu (EPFL) and Christian Theiler (EPFL).

I thank my colleagues at the UiT Complex Systems Modelling Group, especially Gregor Decristoforo, Juan Manuel Losada, and Aurora Driveklepp Helgeland and my office mates, Kai-Uwe Eiselt and Eirik Rolland Enger. On a more personal note, I extend my thanks to my dear friends whom I met in Worcester, Bath, Oxford, Tromsø, and Boston, MA. In particular, I wish to thank my friends Amanda Ho, Adriana Perez de Bartolome, and Tejal Chhaya for reading my thesis. I am grateful to my friend Anna Parkinson for her guidance in enhancing my communication skills, which benefited my thesis.

Lastly, I want to convey my deepest appreciation to my incredible partner, Gregor. I am thankful for your unwavering support, encouragement, calming presence, making me laugh, and for keeping me nutritionally complete.

Contents

1 | Magnetically confined fusion

Nuclear fusion has provided a glimpse into humanity's future of potentially harnessing limitless energy. For more than half a century, scientists have been fascinated by nuclear fusion [1], lured by the promise of a sustainable, carbon-free solution to the world's burgeoning energy needs [2]. In the pursuit of nuclear fusion, one of the greatest challenges is the need to achieve extraordinary temperatures while simultaneously maintaining a cool environment. This requires the fuel to exist as a plasma, an ionised gas characterized by extremely high temperatures [3, 4]. This striking disparity in temperature between the plasma and the material surfaces housing fusion reactions poses a problem, as such strong temperature gradients do not exist anywhere else on Earth. The need to preserve this demarcation between the plasma and the material walls is one of the keys to the stable operation of a fusion power plant.

In the boundary region of fusion devices, where the plasma interacts with the material walls, turbulent phenomena are omnipresent. These are characterized by hot and dense, large-amplitude fluctuations of order-unity. Plasma turbulence presents a formidable challenge, leaving scientists grappling with its complexities. It is at the boundary plasma that the realms of physical turbulence and the practical demands of fusion engineering converge. This presents a dilemma for discharging the plasma exhaust that must be addressed [2, 5, 6].

Chapter 1 serves as a brief introduction, outlining the concept of nuclear fusion and explaining how this process is realized on Earth using fusion reactors. In Chapter 2, a concise overview will be presented, delving into current knowledge of fluctuations occurring at the boundary of fusion plasmas. Theoretical underpinnings of the stochastic model employed to analyse these plasma fluctuations will be discussed in Chapter 3. The research papers that are the primary contributions to this thesis will be summarized in Chapter 4. Lastly, Chapter 5 will draw the thesis to a conclusion, encapsulating the findings and insights gained from this work, while also offering an outlook on future developments.

1.1 Nuclear fusion

Currently, the best fuel for nuclear fusion energy production is the deuterium-tritium (D–T) reaction:

$$D + T \rightarrow \alpha + n + 17.6\,\text{MeV}. \tag{1.1}$$

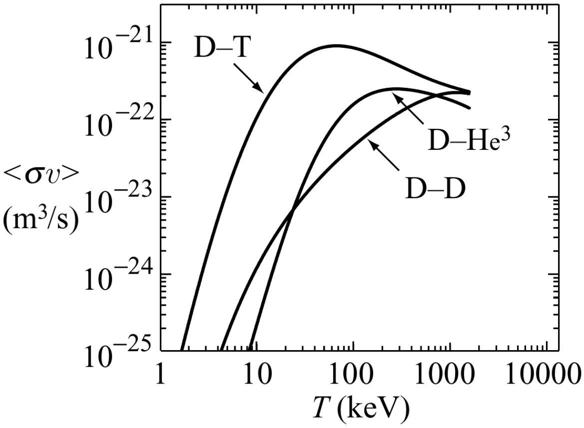

Figure 1.1: The velocity-averaged cross-sections of the fusion reactions as a function of temperature. These are shown for for three nuclear processes of interest: deuterium-tritium (D–T), deuterium-deuterium (D–D) and deuterium-helium (D–He^3). Reproduced from [4].

An α-particle ($^4_2$He) with an energy of 3.5 MeV and a highly energetic neutron (n) provide a combined energy of 17.6 MeV ($1\,\text{eV} \sim 1.6 \times 10^{-19}\,\text{J}$) [5]. This is on the order of millions of times higher than the energy yield of chemical combustion reactions using fossil fuels [7].

There are alternative fusion reactants such deuterium-deuterium (D–D) and deuterium-helium (D–He^3). Fig. 1.1 shows the temperature requirements for these three fuel choices. The nuclear cross-section given by σ is a measure of the probability that a reaction will occur given the kinetic energy of the reactant nuclei. These options presented in Fig. 1.1 have energy requirements that are significantly low [3]. The main benefit of the D–T process can be seen in Fig. 1.1. D–T provides the highest reaction rate at the lowest attainable temperatures [3, 4]. Furthermore, D–T reactions have a considerably larger energy gain compared to the aforementioned reactants [4].

Deuterium is abundant in seawater and can be extracted through distillation or electrolysis, whereas tritium is radioactive and does not occur naturally.

With a half-life of only 12.5 years, tritium can be obtained by bombarding an isotope of lithium (^{6}Li) with a neutron [3]. The known reserves of ^{6}Li are usually available from ore deposits in the Earth's crust.

Despite the relatively low temperature requirement shown above, even now, fusion reactions are difficult to achieve. This is a temperature of the order of 100 million degrees Kelvin, approximately ten times hotter than the core of the Sun [4]. Such high temperatures need to be held long enough to overcome the Coulomb repulsion of like charges, allowing the strong nuclear force to dominate. At these scorching temperatures, the fusion fuel is then transformed into a plasma state where electrons and ions roam freely.

The Sun is a perfect example of fusion in which immense gravitational fields and compression provide the necessary conditions for fusion processes to occur. However, it only produces enough fusion reactions to sustain itself because of its size [8]. On Earth, alternative methods are required to confine the hot plasma and sustain fusion reactions for long periods of time. To contain the plasma, powerful magnetic fields are used to constrain the particle motion. By shaping the magnetic field into a torus shape (resembling a doughnut) particles will mainly follow its path and avoid interacting with the vessel walls. The configuration that has the greatest promise of delivering fusion energy is the tokamak, explained below.

1.2 The tokamak

The tokamak is a doughnut-shaped device with a series of magnetic coils that surround it, as shown in Fig. 1.2. The name originates from a Russian acronym which means "*toroidal chamber with magnetic coils*".

The central transformer in the middle of the tokamak is a large solenoid that induces a plasma current I_P, and produces a poloidal magnetic field B_pol, that goes the short way around the torus. This also provides an ohmic heating source for the plasma. The toroidal magnetic field coils produce the toroidal magnetic field lines B_T, that goes the long way around the device. The superposition of these magnetic fields gives rise to helical magnetic field lines, as shown by the solid black line in Fig. 1.2. This prevents the plasma from drifting radially outward, thereby reducing particle interactions with the plasma-facing components. The density of the confined plasma is commonly described by the line-averaged density $\overline{n}_\mathrm{e}$. It is called as such as it is calculated by integrating density of the plasma along a line of sight, typically through the centre of the plasma, and dividing it by the length of that line [10].

The tokamak shown in Fig. 1.2, is considered to be of the standard type and therefore termed *conventional*. Another type of fusion device, called a

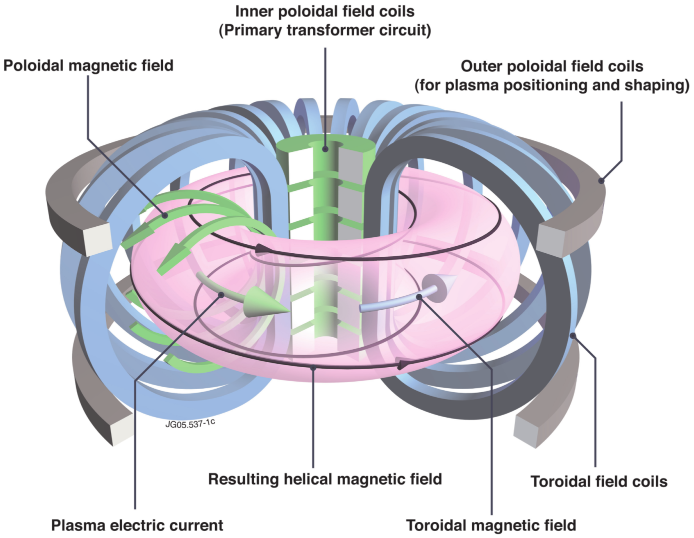

Figure 1.2: Schematic illustration of a tokamak showcasing the magnetic field coils. The solid black line is the resulting helical magnetic field. Image courtesy of EUROfusion [9].

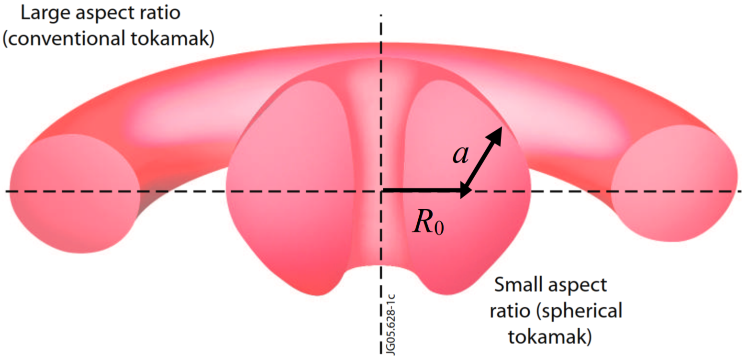

Figure 1.3: Edited illustration of a conventional and spherical tokamak comparison. The added arrows showcase the major radius R_0, and the minor radius a of the device. Image courtesy of EUROfusion [9].

stellarator, is known for its highly optimized magnetic configuration, resulting in twisted magnetic fields to confine the plasma. The lack of a central solenoid, means that stellarators can provide longer plasma discharges [11, 12]. However, this thesis focuses exclusively on tokamaks. The size of the tokamak can be specified by the major radius R_0, which is the distance from the centre of the torus to the centre of the plasma, and the minor radius a, the distance between

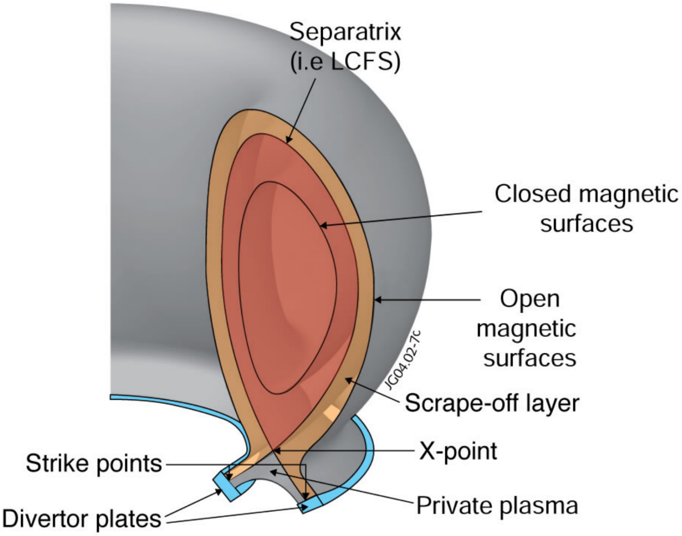

Figure 1.4: Poloidal cross-section of a tokamak. The scrape-off layer encapsulates the region of open magnetic surfaces. Image courtesy of EUROfusion [9].

the centre of the plasma and the vessel walls. Fig. 1.3 provides an illustration where the labels indicate R_0 and a.

Other examples include the spherical tokamak which resembles more of a ‘cored apple’ shape, with a major radius similar to that of the minor radius of the device [13]. From this, a dimensionless parameter called the *aspect ratio* can be defined as R_0/a. Therefore, spherical tokamaks are considered to be small aspect ratio devices, while conventional tokamaks are considered to have large aspect ratios. A comparison of the spherical tokamak with the conventional tokamak can be seen in Fig. 1.3.

An advantage of the spherical tokamak is that the magnetic fields nearer to the centre of the ring are stronger; therefore, the plasma sits closer to the centre. As a result, the energy used to generate magnetic fields in spherical tokamaks is less than that of a conventional tokamak, providing a potential route to compact and cost-efficient fusion power plants [13, 14].

The magnetic field lines of the tokamak lie on a set of nested toroidal magnetic surfaces called flux surfaces. A cross-section of the plasma in the tokamak can be seen in Fig. 1.4. The last-closed flux surface (LCFS) separates closed magnetic field lines from open ones. The separatrix is associated to the X-point where the poloidal magnetic field is null. In addition to the magnetic fields shaping the plasma this also produces the divertor geometry as seen in Fig. 1.4, where open magnetic surfaces intersect with the divertor plates.

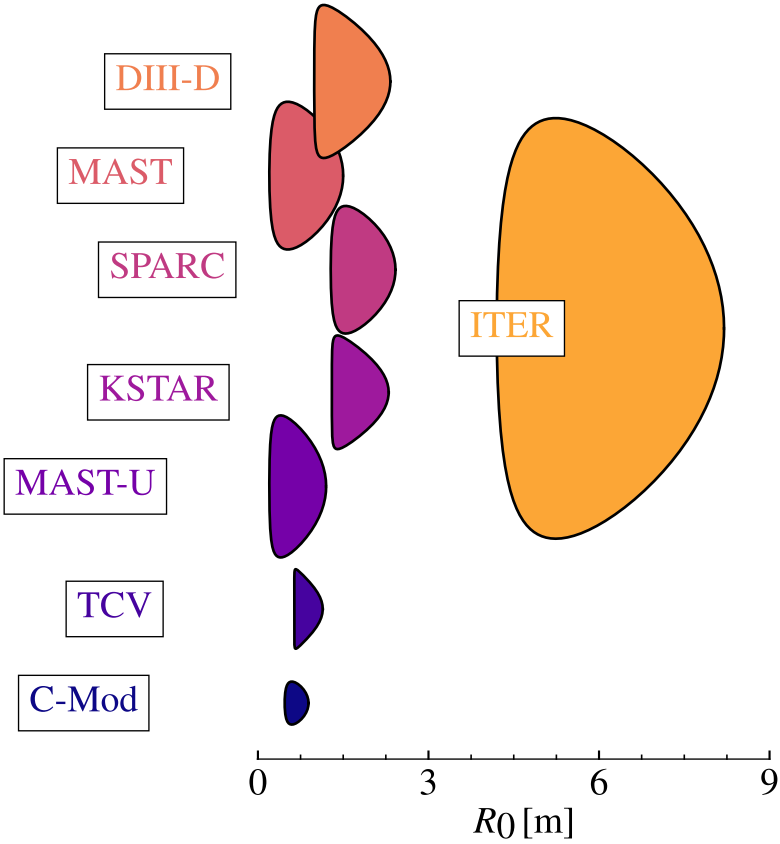

Figure 1.5: Comparison of cross-sections from several fusion devices. The equations used to generate analytical contours are from Ref. [15]. R_0 is the major radius of the machine. Table 1.1 contains the design machine parameters used to generate the contours.

This open-magnetic field line region is the *scrape-off layer*. The combined purpose of the scrape-off layer and the divertor is to address turbulent transport by diverting the plasma exhaust away from the confined plasma column and transporting it down to the divertor plates. The distance between the X-point and the divertor plate is extended, making it possible for the plasma to cool before contact. This also isolates plasma–surface interactions far from the core plasma, improving its performance by reducing the flow of impurities into it. This can otherwise cause radiation losses, therefore cooling down the core.

The shape of the plasma can be manipulated as one of the ways to improve its performance. In particular, the elongation of the plasma κ, can be increased by vertically stretching it such that the plasma is able to carry more I_P hence increasing B_pol. Spherical tokamaks naturally exhibit more elongation compared to its conventional counterparts, another reason for its machine efficiency [14].

Triangularity is another aspect of the shaping and describes how 'D-shaped' the plasma appears. In Fig. 1.5, the cross-sections of various fusion devices are shown in which the machine parameters are used to generate the contours of the LCFS based on analytical equations [15]. The details of these machine parameters can be viewed in Table 1.1. Here, it can be seen that TCV, KSTAR and DIII-D appear more 'D-shaped,' corresponding to highly positive triangularities that are attainable on these machines. The cross-sections of the machines shown in Fig. 1.5 utilize positive values of triangularity δ, and therefore manifest 'D-shaped' plasmas. In negative δ plasmas, the curved part of the 'D-shape' faces towards the central axis of the torus. In Sec. 2.2.2, it will be elucidated how changing the triangularity can be beneficial. The TCV device, otherwise known as *Tokamak à Configuration Variable*, allows for studying plasma shaping. True to its name, a variety of configurations are achievable, as demonstrated by the maximal κ and δ possible with this tokamak.

There are many experimental devices beyond those shown in Fig. 1.1, and the ones listed are of particular interest to the thesis. Note that SPARC and ITER are yet to be built and will be discussed later. Among the devices listed in Table 1.1, MAST and MAST-U are the spherical tokamaks, while the rest are conventional tokamaks. The smallest device studied in this thesis is Alcator C-Mod, notable for its high magnetic fields and compact size, which ceased operations in 2016. Furthermore, it is the only device with molybdenum walls, a material with a particularly high atomic number, while the others have carbon walls. As of now, TCV, MAST-U, KSTAR, and DIII-D are currently in operation in which KSTAR has the largest major radius, studied in this work. Although not studied in this thesis, it is worth mentioning that the largest fusion experiment in operation, with a major radius of $R_0 = 2.96\,\mathrm{m}$ is the *Joint European Torus* (JET), based in Oxfordshire, England.

Looking ahead, the next-step devices include SPARC, which is based in Devens, Massachusetts, and ITER, located in Cadarache, France. Both of these devices are currently under construction. As one can see from Fig. 1.5, SPARC is similar in size to the existing devices whereas ITER is approximately ten times the volume. The SPARC device is based on the compact, high-magnetic field approach, as demonstrated by its predecessor Alcator C-Mod [16]. As shown in Table 1.1, SPARC is planned to reach the highest magnetic field strengths of up to 12.2 T by utilizing new magnetic technology and is

Table 1.1: The design machine parameters of various fusion devices. R_0 is the major radius, a is the minor radius, B_T is the toroidal magnetic field, I_P is the plasma current, κ is the elongation and δ is the triangularity. The design parameters here are the maximal values according the provided references.

	R_0 [m]	a [m]	B_T [T]	I_P [MA]	κ	δ	Reference(s)
C-Mod	0.68	0.21	8.0	2.0	1.8	0.40	[16]
TCV	0.89	0.25	1.54	1.2	2.8	0.90	[17, 18]
MAST-U	0.7	0.5	0.92	2.0	2.5	0.60	[19–21]
KSTAR	1.80	0.50	3.5	2.0	2.0	0.80	[22]
MAST	0.85	0.65	0.52	1.3	2.0	0.50	[19, 20, 23]
DIII-D	1.66	0.67	2.2	2.0	2.01	0.75	[24]
SPARC	1.85	0.57	12.2	8.7	1.97	0.54	[16]
ITER	6.2	2.0	5.3	15.0	1.85	0.48	[25]

predicted to produce $50 - 100\,\mathrm{MW}$ of fusion power. On the other hand, ITER will utilize its large size and is predicted to produce $500\,\mathrm{MW}$ of output power. To understand the potential physics basis and engineering design of ITER, several fusion devices such as JET [26], TCV [27] and DIII-D [28] have paved the way. Despite their distinct differences in size and magnet technology, both ITER and SPARC share a common primary objective in achieving net energy gain.

The several tokamaks shown in Fig. 1.5 are indeed different from each other. From this, a few questions arise: Does turbulence behave the same way in all of these different machines? Are the sputtering effects on the vessel walls the same? Can we find operating regimes that limit these detrimental effects? The transport of plasma across the scrape-off layer is of great concern due to it highly turbulent state consisting of strongly intermittent, large-amplitude bursts. As a result, high particle density and heat fluxes arrive at the main chamber walls. This can enhance plasma–wall interactions, leading to deleterious effects for the first wall of fusion devices [5, 29, 30]. A solid understanding of the scrape-off layer is therefore necessary for an accurate prediction of turbulence and, ultimately, adaptation of its properties to the development of future fusion reactors.

2 | Scrape-off layer fluctuations

Plasma interactions with the first wall of fusion devices lead to sputtering and erosion, the particles of which can be transported back to the plasma core, inevitably degrading the magnetic confinement [31–38]. Evidently, it is desirable and necessary to reduce plasma–wall interactions as much as possible. As discussed previously, the scrape-off layer (SOL) is the open-magnetic field line region, magnetically connected to the material surfaces, where fluctuations of order-unity are ubiquitous. In this chapter, a concise overview of earlier studies on SOL plasma fluctuations is discussed.

2.1 Early formalism of scrape-off layer transport

In the late 90s, the understanding behind the turbulent transport in the SOL was largely inspired by the radial gradients that drive the plasma transport in the core [39]. The mechanism behind this formalism revolves around classical transport where binary collisions cause the guiding centres of the electrons and ions to shift from one orbit to the next. This was encapsulated by the diffusive model following Fick's law

$$\Gamma_\perp = -D_\perp^{\mathrm{eff}} \frac{\partial n_\mathrm{e}}{\partial r}, \tag{2.1}$$

where $\Gamma_\perp$ is the cross-field particle flux, n_e is the electron density, r is the radial coordinate and $D_\perp^{\mathrm{eff}}$ is the diffusivity coefficient estimated from plasma parameters. However, this simple diffusive model fails to take into consideration experimental observations and requires significantly higher diffusion coefficients than classical diffusion [40, 41]. To address the applicability of this model, radial profiles of the SOL must be discussed.

Exponential radial profiles of the electron density and temperature are typically observed in the SOL of many fusion devices [32, 40, 42–49, 49–62]. An example of this is presented in Fig. 2.1 for low and high values of $\overline{n}_\mathrm{e}$, in the TCV device. The SOL profile usually exhibits a two-layer structure: a

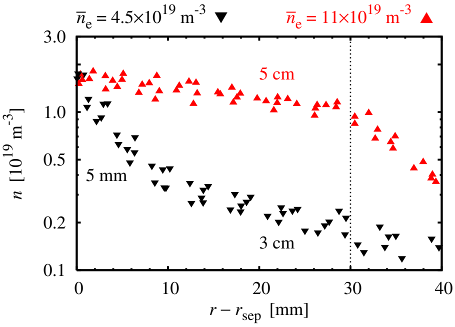

Figure 2.1: Time-averaged particle density profiles from TCV. Dotted line shows the limiter shadow. Image courtesy of O. E. Garcia.

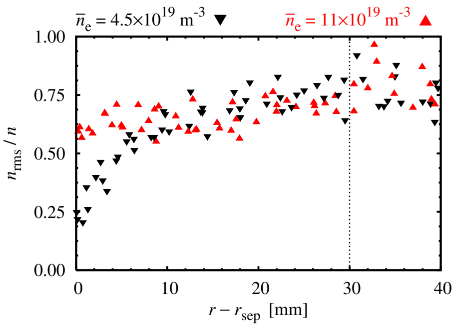

Figure 2.2: Relative fluctuations levels of the particle density profiles from TCV. Dotted line shows the limiter shadow. Image courtesy of O. E. Garcia.

relatively steep region with moderate fluctuation levels, called the near SOL, which extends outward from the magnetic separatrix. Then at a certain break point ($r - r_{\rm sep} \approx 8\,\mathrm{mm}$), the scale length of the profile becomes longer with high relative fluctuation levels, forming a "shoulder" in what is commonly called the far SOL. As the main plasma density increases, *broadening* occurs when the break point between the near and far SOL moves radially inward. During this time, the scale length of the profile increases, a phenomenon commonly referred to as *flattening*. Due to the progressive flattening of the SOL, the particles and heat transported by high-amplitude fluctuations arriving at the main chamber wall increase significantly. This cross-field transport is correlated with $\overline{n}_{\rm e}$, or rather the Greenwald fraction $f_{\rm GW}$, which is simply the ratio between $\overline{n}_{\rm e}$ and the empirical discharge density limit $n_{\rm G}$ [45]. This empirical discharge density limit is defined as $n_{\rm G} = (I_{\rm P}/\pi a^2) \times 10^{20}\,\mathrm{m}^{-2}$, where $I_{\rm P}$ is the axial toroidal plasma current in units of mega-amperes [63]. Observations from the study in Ref. [45] indicated that as fusion devices approach their empirical density limit, the interaction between plasma and the vessel walls becomes stronger, and the likelihood of a disruption increases.

The description of SOL transport given by Eq. (2.1) with some constant diffusivity coefficient, would indicate an increase in the density gradient. This expectation was refuted by a study on the TCV device, in which no linear relationship was found [64]. As well as TCV [64], in other devices such as JET [5] and Alcator C-Mod [40, 43], $D_\perp^{\rm eff}$ varies by several orders of magnitude as a function of radius, further challenging the concept of a simple diffusivity model for the SOL as shown in Fig. 2.3. For the DIII-D experiment, the

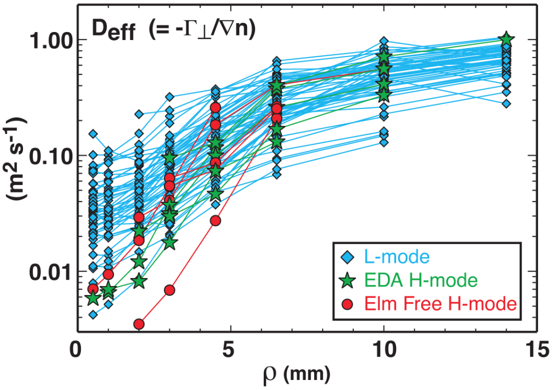

Figure 2.3: Effective diffusivity profiles for various operational modes in the Alcator C-Mod. $D_{\perp}^{\text{eff}}$ must change by several orders of magnitude to match the pure diffusion transport model. The midplane distance relative to the LCFS is given by ρ. Reprinted from [43], with the permission from IAEA.

UEDGE transport simulations did not find any matching diffusion coefficients [65]. Motivated by these findings, corrections to Eq. (2.1) were made to include an effective perpendicular velocity $v_{\perp}^{\text{eff}}$, allowing for a variety of particle density profiles,

$$\Gamma_{\perp} = -D_{\perp}^{\text{eff}} \frac{\partial n_{\text{e}}}{\partial r} + v_{\perp}^{\text{eff}} n_{\text{e}}. \tag{2.2}$$

However, ESEL simulations of edge plasma at constant temperature [66] revealed that there was no functional relationship of the form of Eq. 2.2, indicating that the diffusion-convection model may also not be appropriate for SOL plasmas. Therefore the diffusive approach is invalidated and cannot be considered for predictability towards future fusion reactors. Understanding SOL turbulence and describing the role of fluctuations under various plasma conditions requires a different methodology. To achieve such a formalism, a fresh grasp of the current understanding of SOL fluctuations is needed.

2.2 Intermittent fluctuations

Experimental measurements of SOL plasma fluctuations can provide insight into how to best model cross-field transport. High relative fluctuation levels have been routinely observed since the first measurements of fluctuations in the edge region of fusion devices. The Caltech tokamak was one of the first experiments to record fluctuation levels of approximately 10–90% of the mean

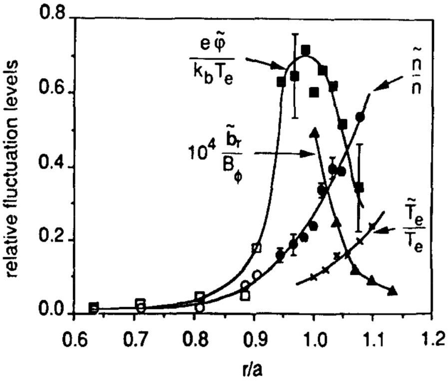

Figure 2.4: Fluctuation levels of various plasma parameters in edge region in the TEXT tokamak were measured by electric probes measuring different plasma parameters. Reproduced from [70] with permission from AIP Publishing.

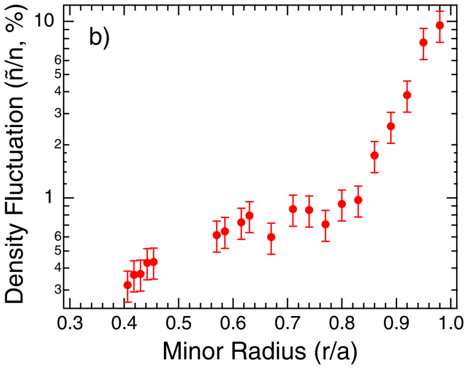

Figure 2.5: Fluctuation levels in the core and boundary of DIII-D were measured by beam emission spectroscopy to determine the fluctuation levels. Reproduced from [72] with permission from JSPF.

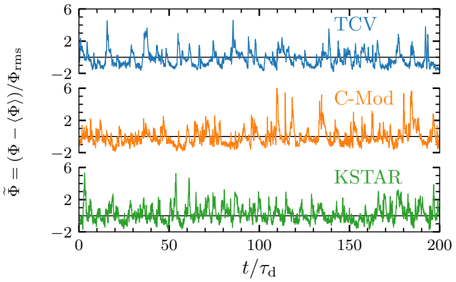

Figure 2.6: Far SOL measurements from Alcator C-Mod, TCV and KSTAR. The time is normalised by the characteristic duration time of the fluctuations. The black line indicates the mean value of the signal. Image courtesy of A. Theodorsen [73].

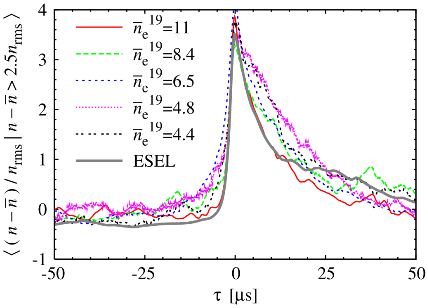

Figure 2.7: Conditionally averaged waveforms at various line-averaged densities from TCV and the comparison to a ESEL simulation. Reprinted from [71], with permission from IAEA.

from ion saturation current measurements in the early 1980's [67–69]. Similar observations were made in other experimental devices, including TEXT [70] and TCV [71]. As shown in Fig. 2.4, relative fluctuations in local plasma parameters reached values greater than 0.5 in the TEXT device.

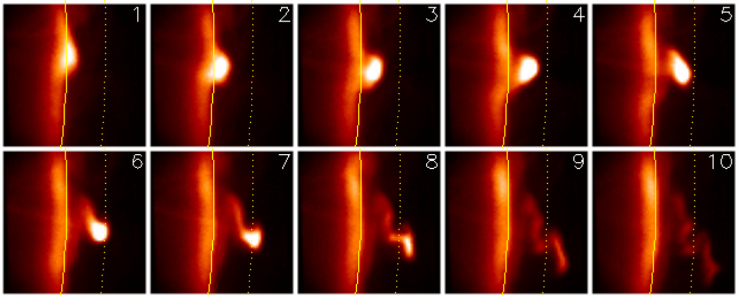

Figure 2.8: Snapshots of a blob-like structure detaching from the main plasma, moving from the LCFS (solid line) out towards the limiter shadow (dotted line) in NSTX. Reproduced from [74]. Originally from [75], reprinted with permission from Elsevier.

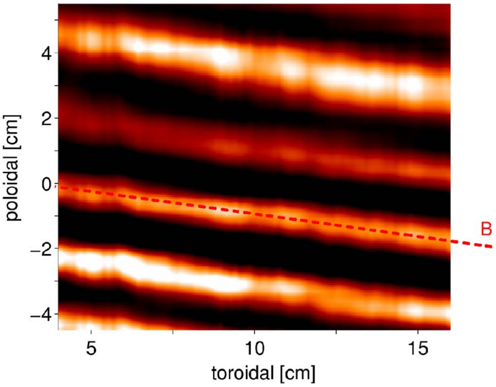

Figure 2.9: Filaments observed by the gas puff imaging in Alcator C-Mod in the toroidal-poloidal plane. The red dashed-line indicates a magnetic field line. Reproduced from [76] with permission from AIP Publishing.

Fig. 2.2 shows that the relative fluctuation levels increase significantly with the radial coordinate from the near SOL to the far SOL at low $\overline{n}_\mathrm{e}$ and stay approximately constant in the far SOL where these are above 0.5. For a wider range of line-averaged densities, the TCV far SOL appears to be independent of $\overline{n}_\mathrm{e}$ [71]. Together with Fig. 2.1, broad profiles in the far SOL can be associated with high relative fluctuation levels.

Further evidence of this can be seen in Fig. 2.5, where large relative fluctuation levels can also be observed close to the wall radius of DIII-D at $r/a > 0.85$ [72]. Below this point, small relative fluctuation levels lower than 1% are noted. Large relative fluctuation levels can be attributed to intermittent plasma fluctuations of high amplitude with a fast rise and a trailing wake. This is apparent in Fig. 2.6 where exceptionally long time-series measurements were obtained from Langmuir probes dwelling in the far SOL of TCV [77], Alcator C-Mod [78], and KSTAR [55]. The fluctuations in the far SOL appear asymmetric in time, as shown by the conditionally averaged waveforms for various $\overline{n}_\mathrm{e}$ from TCV and ESEL simulations in Fig. 2.7.

The origins of these large-amplitude fluctuations were revealed by two-dimensional (2D) imaging of the SOL. Using 2D probe arrays in the Caltech tokamak and then visible imaging with fast cameras in the TFTR tokamak, coherent structures, called blobs or filaments, were detected in the SOL [67–69]. Snapshots of this structure taken with the gas puff imaging diagnostic on the NSTX device, a spherical tokamak, can be seen in Fig. 2.8. The filament is observed in the plane perpendicular to the magnetic field lines and in this context, the appearance is that of a blob. Once again, a steep front and a trailing wake can be seen as the blob propagates radially outwards, consistent with the findings in Fig. 2.7 and previous experimental studies [44, 46, 50, 77, 79–88]. As clearly shown in Fig. 2.9, these blob-like filaments are elongated along the magnetic field lines, where transport along the magnetic field lines is much faster than across it. In relation to this present work, the main diagnostics considered are Langmuir probes and gas puff imaging that measures the far SOL fluctuations. Brief summaries of these diagnostics are discussed as follows.

Langmuir probes Measurements of local plasma density in the SOL are performed regularly using Langmuir probes, to name a few, see Refs. [44, 49, 89–95]. Filaments are usually identified as density and temperature perturbations when analysing time series.

When the probe is inserted into a plasma, a thin layer of negative charge will form around it. This happens because electrons strike the surface at a higher rate than ions due to their small mass [5, 96, 97]. The electron flow is then impeded because of the resulting negative bias on the surface, also attracting ions. These processes balance and thus no net current is drawn by the probe. A few Debye lengths wide, this positively-charged region is known as the sheath. The Debye length is given by $\lambda_\mathrm{D} = \sqrt{\epsilon_0 T_\mathrm{e}/n_\mathrm{e} e^2}$, where ϵ_0 is the vacuum permittivity, and T_e is the electron temperature [96]. The current drawn by a Langmuir probe is thus governed by an applied voltage to the probe surface which modifies the surface electric field, adjusting the ratio of ions to electrons collected. When the probe is strongly negatively biased ($V_\mathrm{probe} < -3T_\mathrm{e}$), all electrons are rejected and only ions are collected [89, 97]. This results in a saturation of the current collected with the value known as the ion saturation current I_sat. This work is mainly interested in I_sat for fluctuation analysis where

$$I_{\mathrm{sat}} \approx A_{\mathrm{p}} e n_{\mathrm{e}} \sqrt{\frac{T_{\mathrm{e}}}{m_{\mathrm{i}}}}. \tag{2.3}$$

Here, A_{p} is the projected area of the probe that measures the fluctuations and m_{i} is the mass of the ion [44]. I_{sat} is a reasonable proxy for n_{e} measurements, since there exists a linear relationship [96]. Therefore, fluctuations in the ion saturation current are governed by fluctuations in density. However, T_{e} fluctuations are also significant and are correlated with n_{e} fluctuations [81, 98], complicating the linearity of this relationship.

The electron saturation current E_{sat}, may also be used as a proxy but is a rarely measured variable of SOL fluctuations. In theory, E_{sat} is proportional to the local plasma density but there are some issues when it comes to comparisons. Electrons drain much quicker due to small mass, and has greater relative standard deviation leading to noisier fluctuation measurements.

The radial component of the velocity of these fluctuations can be calculated. The local poloidal electric field is estimated by the difference in the measured plasma potential between two pins. Assuming a uniform plasma temperature across the two pins, the difference in the plasma potentials would be equivalent to the difference between the measured floating potential V_{f}, by the Langmuir probes. Hence, the radial velocity using the Langmuir probe measurements is given by

$$\mathbf{V}_E = \frac{\triangle V_{\mathrm{f}}}{B_{\mathrm{probe}} \triangle Z}, \tag{2.4}$$

where $\triangle V_{\mathrm{f}}$ is the potential difference between the vertically spaced floating pins, $\triangle Z$ is the distance between those pins and B_{probe} is the magnetic field strength at the probe location [44, 77, 99]. Details about filament motion is discussed in more detail in Sec. 2.2.1. Among others, further details of the Langmuir probe systems that measure fluctuations in the SOL can be inferred for Alcator C-Mod [89] and DIII-D [94] in the provided literature. Typical analysis methods on the Langmuir probe measurements include inferring to the statistical features of the filaments, where this will be discussed in further detail in Sec. 2.2.3. In Papers II and III, filaments propagating past the probe tip are registered as positive bursts in the normalized ion saturation current measurements.

Gas puff imaging Commonly used to diagnose the characteristics of a turbulent plasma is an optical diagnostic known as gas puff imaging (GPI) [100–102]. The GPI can access regions inaccessible to the Langmuir probes, such as studying fluctuations a few millimetres inside the LCFS under various conditions.

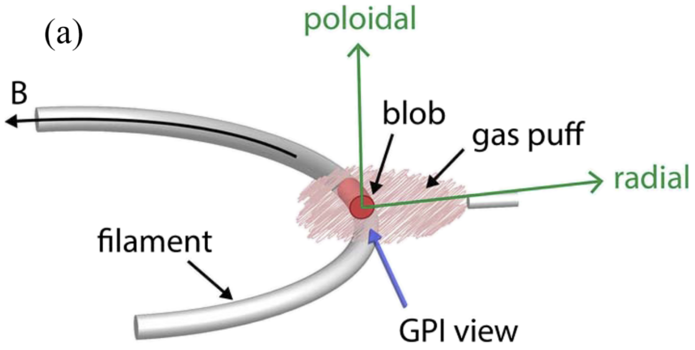

Figure 2.10: Schematic diagram showing a magnetically field-aligned three-dimensional filament bombarded by a gas puff cloud. Reproduced from [103], with permission from AIP Publishing. Originally seen in [112].

A gas nozzle, usually located near the outer-midplane, injects a neutral gas puff cloud of some species, typically deuterium or helium. This enters the SOL and interacts with the plasma turbulence in a well-defined region resulting in line emission from collisionally excited atoms. This local light emission is viewed by an imaging system that couples the light to a 2D detection system such that the lines of sight are approximately parallel to the magnetic field at the location of the gas puff [103]. Fig. 2.10 shows an illustration of the gas cloud interacting with the filament.

Before the light reaches the detectors, which are typically CMOS sensors or avalanche photodiodes, the desired line emission is isolated using the appropriate interference filter. Regions of increased light emission radiation usually indicate the presence of these coherent structures elongated along the magnetic field lines, as presented in Fig. 2.9. Generally, the 2D cross-section of the filament in the plane perpendicular to the magnetic field appears blob-like, as shown in Fig. 2.8. The intensity of the emitted light depends on n_e, T_e, the density of the neutral gas puff, and the radiative decay rate of the transition. Therefore, the emissivity fluctuations respond to and serve as a proxy for local electron density and temperature fluctuations. The response is non-linear and is typically dominated by n_e fluctuations [85, 104]. Correlations between n_e and T_e may affect the GPI measurements [105]. Further details on this can be viewed in Ref. [103]. Typical analytical methods for 2D measurements include reconstruction of phase velocity flow fields using time delay correlation techniques [106–111]. Currently, the work presented in Papers II and III focuses purely on light intensity fluctuations serving as a proxy for the plasma density.

2.2.1 Motion of filamentary structures

The velocities of blob-like filaments are of great interest, since much of the particle density [44, 50, 113] and heat [46, 95, 114] are transported by the filaments across the SOL. The interchange mechanism behind filament motion was first proposed by Krasheninnikov in his seminal paper [115].

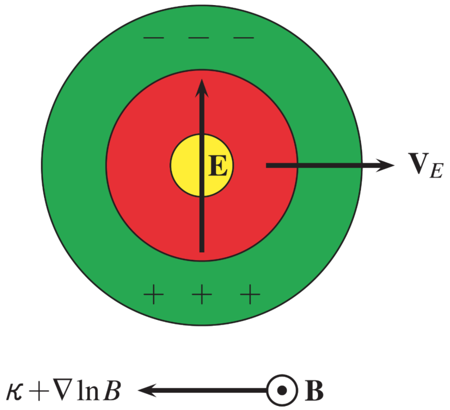

Figure 2.11: The physical mechanism for the blob interchange motion. The magnetic field is pointing out of the page. Reprinted from [116] with permission from JSPF.

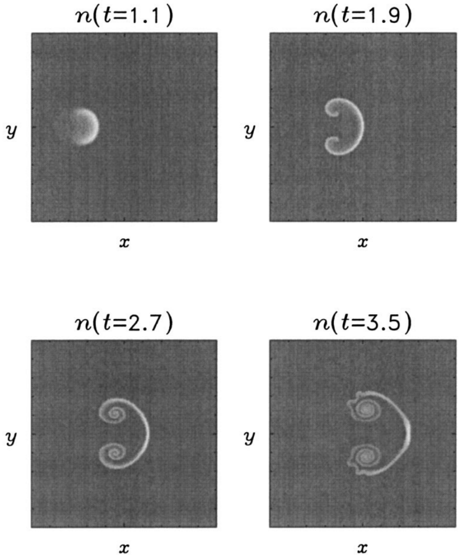

Figure 2.12: Contour plot showing the time evolution of a blob structure. Reprinted from [117], with the permission from AIP Publishing

On the outboard side of the SOL, both the magnetic field curvature vector κ and the gradient ∇B point radially inward, presented in Fig. 2.11 [116]. Here, the magnetic field $\mathbf{B}$, is pointing out of the page. Thus, both magnetic curvature and gradient particle drifts are downward for ions and upward for electrons, owing to charge dependence. For a filament of excess pressure compared to the background plasma, this leads to the separation of charges. Known as charge polarization, an internal poloidal electric field structure (or a potential dipole) is established, which in turn leads to a collective $\mathbf{E} \times \mathbf{B}$ drift, propelling the filament radially outward with velocity

$$\mathbf{V}_E = \frac{\mathbf{E} \times \mathbf{B}}{B^2}. \tag{2.5}$$

On the upper end, these velocities are usually on the order of $\sim 1\,\mathrm{km\,s^{-1}}$,

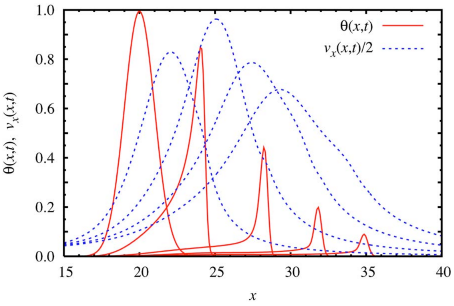

Figure 2.13: The radial variation of the plasma density (solid line) and the radial velocity (dashed line) at the symmetry axis of a seeded blob. Reprinted from [123], with the permission from AIP Publishing.

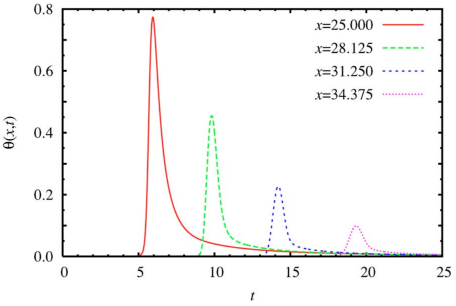

Figure 2.14: The plasma density at the symmetry axis monitored over time for different radial positions x. Reprinted from [123], with the permission from AIP Publishing.

as widely observed in many fusion experiments using Langmuir probes [44, 99, 118] and optical imaging techniques such as GPI and fast visible imaging [102, 106, 108, 119–122].

Sparked by the suggestion of an interchange mechanism describing the blob motion, several simulations were performed. The first of many seeded blob simulations was in 2003 [117]. Fig. 2.12 shows the initialisation of a 2D symmetric Gaussian blob on a constant plasma background. As the blob evolves in space and time, it acquires a mushroom-shaped form. For clarity, the variation of the density in the radial direction according to the velocity is shown in Fig. 2.13, represented by the solid line. As shown, the peak of the radial velocity $v_x(x,t)$, indicated by the dashed line, is followed by the peak of the density described by $\theta(x,t)$. A steepening of the blob front can be observed as a result. Measured at a single point, the corresponding temporal evolution of the seeded blob is presented in Fig. 2.14 for various radial positions. The waveforms demonstrate a fast rise and a slow decay, which is consistent with previous experiments and observations [44, 50, 77, 79–86].

Indeed, several other important aspects of blob dynamics exist, such as velocity scaling laws [124–126], the effects of divertor configuration [58, 59, 127–129], the impact of neutrals [130, 131], and many others, listed in a comprehensive review on SOL filaments [74]. The aspects mentioned above are central to this work.

2.2.2 Plasma and machine parameters

In many fusion experiments and simulations, the study of particle and heat fluxes carried by these blob-like filaments is of significant interest. Numerous investigations have been performed under various plasma parameters and confinement modes in order to understand how these affect the behaviour of turbulent phenomena [75, 79, 88, 108, 132–134]. It is well known that the characteristics of the filaments change with typical plasma parameters such as the line-averaged density [44, 49, 71, 79, 81, 95, 98, 102, 108, 135, 136], the plasma current [50, 60], and the magnetic field [87, 137]. Some of these studies will be discussed as follows to provide a brief overview of these effects on plasma fluctuations in the SOL.

To reiterate, the effect of increasing the line-averaged density ($\overline{n}_\mathrm{e}$), shows broadening and flattening of the particle density profiles seen in Fig. 2.1. Hence, the relative fluctuation levels increase significantly across the entire SOL, as presented in Fig. 2.2, leading to an inherently fluctuating state. Changes to the shape of the radial profile are commonly observed in various tokamaks with increasing $\overline{n}_\mathrm{e}$, as shown by the results from AUG, JET, and COMPASS in Fig. 2.15. The changing parameter in the Greenwald fraction (f_GW), defined previously in Sec. 2.1, was the core plasma density. In these individual machine scans, the plasma conditions were held constant, and the profiles were observed in low-confinement mode (L-mode) plasmas. With increasing f_GW, the density profiles in the SOL change shape from an exponential to a broadened and flattened profile in these tokamaks. Similar observations were made in the MAST device [54]. Consequently, the particle and heat fluxes transported toward the wall substantially increase with f_GW, enhancing

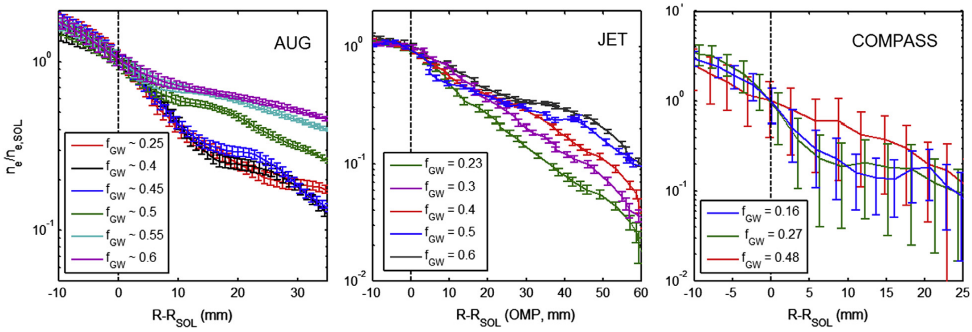

Figure 2.15: Radial profiles of the SOL density for various Greenwald fraction values f_GW. The dotted line is the position of the LCFS. Reprinted from [53], with permission from Elsevier.

plasma–wall interactions [93].

Increasing $\overline{n}_\mathrm{e}$ has implications for the sizes of these filaments. In a TCV study using the Langmuir probe, the conditionally averaged waveform appeared to be robust against increasing $\overline{n}_\mathrm{e}$ as seen in Fig. 2.7 implying that the duration times of the fluctuations do not vary [93]. However, from GPI studies on TCV [102], blob sizes and therefore the duration times, were shown to increase with increasing $\overline{n}_\mathrm{e}$ as seen in Paper III. This disparity in the observation already indicates diagnostic differences between the Langmuir probe and the GPI as will be discussed in Paper II for Alcator C-Mod. In Alcator C-Mod, blob sizes were shown to weakly increase with $\overline{n}_\mathrm{e}$, as confirmed by GPI results [135]. Concerning the radial velocities of the filaments, it has been observed in TCV [102] and Alcator C-Mod [108, 135] that they increase with $\overline{n}_\mathrm{e}$. On the other hand, no changes in the radial velocities were observed with increasing $\overline{n}_\mathrm{e}$, as reported in the DIII-D study [81].

The effects of varying the plasma current (I_P) on SOL profiles and fluctuation levels have been previously reported [49, 50, 81, 121]. Presented in the upper panel of Fig. 2.16, in the TCV device, decreasing I_P under constant plasma conditions led to the broadening and eventual flattening of the particle density profiles, as indicated by the red triangular markers ▲. This shows the same effect at increasing $\overline{n}_\mathrm{e}$, highlighted in Fig. 2.15. Such profiles are not observed at high I_P, represented by the black inverted triangles ▼. Consequently, at low I_P, the particle density flux shown in the lower panel of Fig. 2.16 is notably higher, suggesting that high plasma currents are beneficial for reducing particle density and heat fluxes impinging on the vessel walls. The effects of increasing I_P are noticeable on the fluctuation amplitudes in DIII-D, as shown in Refs. [49, 81]. The signal amplitudes appear suppressed at higher currents, as seen in the lower panel of Fig. 2.17. This further suggests that filaments play an important role in determining radial profiles in the SOL.

Furthermore, associated with a decreasing I_P were increasing filament radial velocities, as observed in MAST using fast visible imaging [121]. This was linked to a significant increase in the density e-folding length, as well as cross-field transport. Simultaneously, the radial size of the filament was found to increase with decreasing I_P in MAST. In Alcator C-Mod, the radial velocities estimated from cross-correlation analysis also increased with decreasing I_P using the GPI [101]. Overall, the effects of decreasing I_P plays a similar role to increasing $\overline{n}_\mathrm{e}$, where the radial SOL profiles change shape and the properties of the intermittent fluctuations are impacted.

Strong magnetic fields, as discussed in Sec. 1.2, stabilize the plasma, preventing drifts and thereby reducing particle interactions with material surfaces. However, despite this stabilization, filaments persist and propagate radially

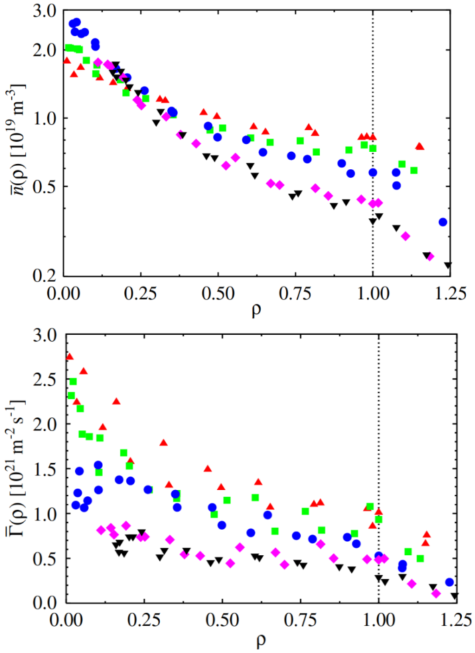

Figure 2.16: Radial particle density profile (upper panel) and the radial flux profile (bottom panel) for various plasma currents in TCV. ▲ is the lowest I_P where as ▼ is the highest I_P. Reproduced from [50]. ©IOP Publishing. Reproduced with permission. All rights reserved.

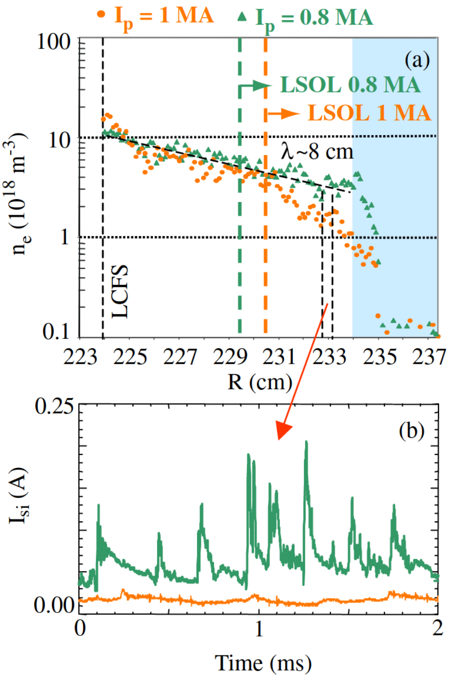

Figure 2.17: Radial profiles of the SOL density (upper panel) and ion saturation current time traces (lower panel) for two different plasma currents, $I_P = 0.8\,\mathrm{MA}$ and $I_P = 1.0\,\mathrm{MA}$ in DIII-D. Reprinted from [81], with the permission from IAEA.

across the magnetic field lines. High magnetic fields lead to a reduction in the radial velocity, as indicated in Eq. 2.5. A few of experimental studies have investigated how filaments behave under varying magnetic fields [87, 137]. Nevertheless, these results are elaborated upon in the following.

Experiments on AUG investigated variations in B_T effects on SOL filaments [87]. Despite the considerable variation in B_T under approximately constant plasma conditions, the radial electron density profiles remained the same. Larger fluctuations were observed at higher B_T compared to lower B_T, where these structures appeared to be short-lived. Under constant I_P, the number of blobs per second decreased with increasing B_T. However, no changes were observed in the radial sizes, radial velocities, or relative amplitudes.

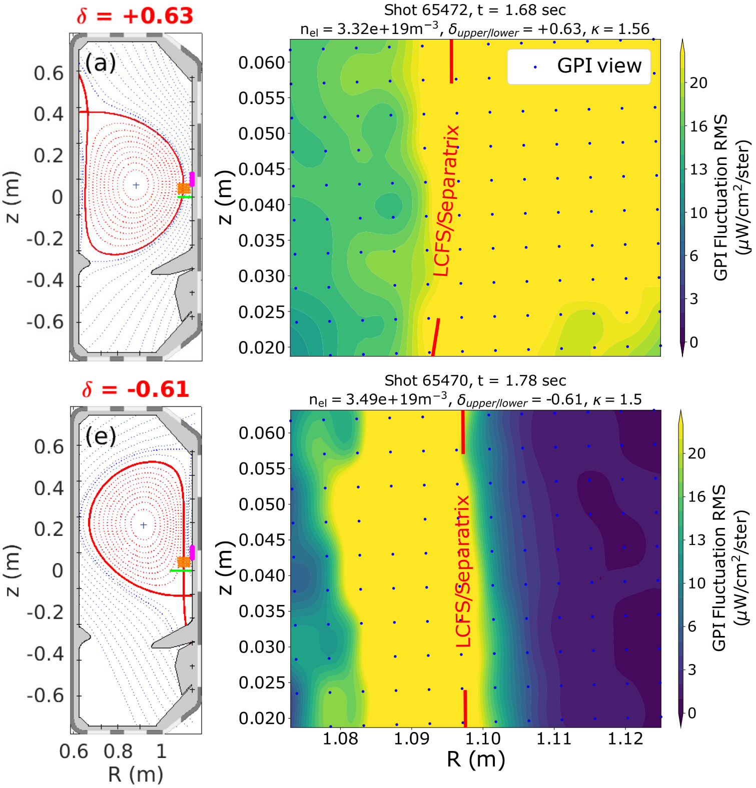

Figure 2.18: Poloidal cross-sections of the TCV tokamak showing the differences between positive δ (upper panel) and negative δ (lower panel). The corresponding fluctuation root-mean square (RMS) of the brightness were measured from the GPI diode views. Reprinted from [138], with the permission from IAEA.

The QUEST device is a spherical tokamak which studied how the ratio of the poloidal and toroidal fields $B_{\mathrm{pol}}/B_{\mathrm{T}}$, impacted the filaments in the SOL [137]. This is known as the magnetic field pitch. As mentioned in Sec. 1.2, the combination of B_{pol} due to a toroidal I_{P}, and B_{T} gives rise to a helical magnetic field. The slope of this helical magnetic field line is therefore called the magnetic field pitch angle, defined by $\theta = \arctan\left(B_{\mathrm{pol}}/B_{\mathrm{T}}\right)$. This experiment on QUEST focused on varying the B_{pol}. It was found that at $B_{\mathrm{pol}}/B_{\mathrm{T}} = 0$, the plasma fluctuations were less obvious. At higher ratios of $B_{\mathrm{pol}}/B_{\mathrm{T}}$, intermittent convective structures were observed. As a result, the intensity of these fluctuation amplitudes grew with $B_{\mathrm{pol}}/B_{\mathrm{T}}$. Despite this observation, radial velocities remained invariant to the magnetic field pitch.

The consequences of plasma shaping on intermittent SOL fluctuations have been elucidated by a few studies [138–140]. Focusing on a recent experiment on TCV, triangularity scans have been performed on L-mode plasmas [138]. Filaments in negative and positive triangularities were compared using the GPI, ranging from $-0.61 \leq \delta < +0.64$. In TCV, a significant reduction in SOL fluctuations was reported, as shown in Fig. 2.18. The fluctuations in the case of $\delta = +0.64$ are higher compared to $\delta = -0.61$ beyond the LCFS. This demonstrated a suppression of first-wall plasma interactions in negative δ plasmas which potentially could be beneficial for future reactors.

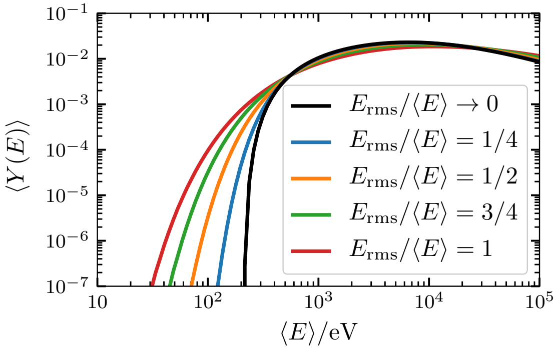

Figure 2.19: Mean yield function as a function of the mean energy for deuterium on a tungsten wall and for various relative fluctuation levels shown in the legend. Image courtesy of A. Theodorsen [73].

Next-step fusion devices are projected to operate at high densities [16, 25]. As the discharge density limit is approached, the far SOL profiles become gradually broader and flatter [45, 53, 93]. This leads to a notable increase in the particle fluxes at the wall radius, as explained previously. Fluctuations in particle energy which are directly connected to T_e lead to sputtering even when the mean energy suggests sputtering does not occur [36].

To elaborate, Fig. 2.19 shows the mean sputtering yield $\langle Y(E) \rangle$, as a function of the mean energy $\langle E \rangle$ of a deuterium ion incident on a tungsten surface [73]. This was plotted for various ranges of relative fluctuation levels. The black curve in Fig. 2.19 shows the case where $E_{\mathrm{rms}}/\langle E \rangle \to 0$. Sputtering is seen to occur for mean energies below 200 eV when $E_{\mathrm{rms}}/\langle E \rangle > 0$ even though these energies are rather low. Thus, it is essential to have an accurate formulation of the anticipating plasma–wall interactions in future fusion reactors.

In summary, intermittent fluctuations in the SOL can exhibit similar behaviour in the density profiles across devices, but show some differences in other aspects such as radial velocities, amplitudes, and blob sizes. Based on this notion, these previous experiments lead to questioning whether the turbulence in the SOL behaves similarly across devices when one parameter is varied. In Paper III, this question is further discussed.

2.2.3 Statistical properties

Universality in the statistical characteristics of SOL fluctuations has been demonstrated frequently across various fusions devices, plasma parameters and confinement modes [50, 78, 80, 88, 93, 137, 141–145]. The term *universality* refers to the similarity in statistics.

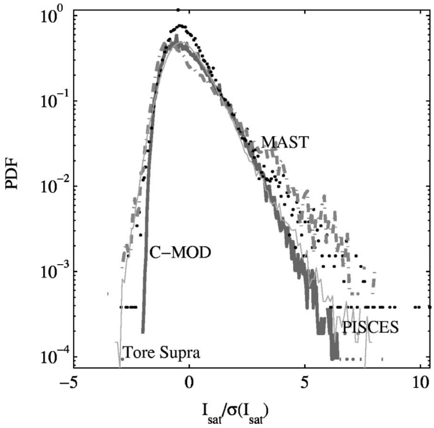

Figure 2.20: Skewed ion saturation current PDFs from the boundary region of various fusion devices. Reproduced from [80], with the permission of AIP Publishing.

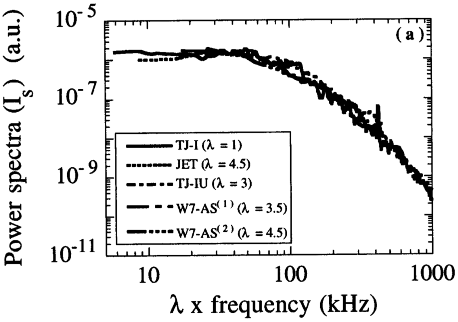

Figure 2.21: PSDs of the ion saturation current from various fusion devices. Figure reprinted with permission from [146]. Copyright (1999) by the American Physical Society.

Among these statistical properties, the probability distribution functions (PDFs) of the measured time series from Langmuir probes [55, 59, 77, 113, 147–150] and GPI [85, 143, 144, 151] show a Gamma distribution. This is a continuous probability distribution that describes right-skewed data and is parameterized by a shape and a scale. Independent of the position in the far SOL, unimodal positively skewed and flattened distributions of fluctuation time series are frequently observed, as shown in Fig. 2.20 for several fusion devices. To explain, the skewness describes the symmetry of the shape of the distribution. For a skewness of zero, the distribution will be symmetric whereas for positive skewness, the long tail of the distribution will point towards the right thus appearing asymmetric. The flatness describes how peaked the distribution appears and how heavy the tails are compared to a normal distribution. A sharp

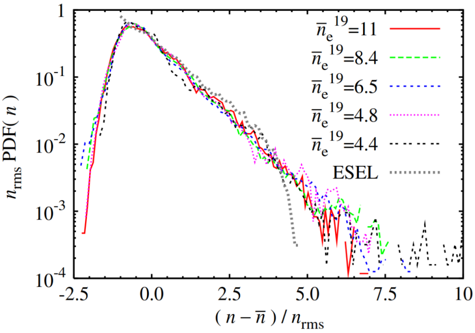

Figure 2.22: PDFs of the particle density measurements at various line-averaged densities from TCV. The dotted line represents the ESEL simulation. Reprinted from [71] with the permission from IAEA.

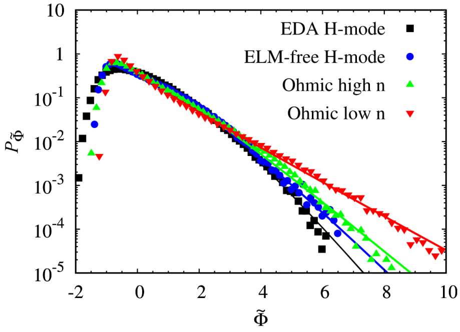

Figure 2.23: PDFs of the GPI light intensity measurements in various confinement modes from Alcator C-Mod. The solid lines show the agreement with the stochastic model. Reprinted with permission from AIP Publishing [88].

distribution or one with very heavy tails has a large flatness value. Therefore, the skewness and the flatness are positive for these measurements, which were found to be approximately 3 and 10, respectively [80]. The parabolic relationship between the skewness and the flatness is observed in many tokamak experiments and is usually related to the PDFs of the SOL time series [147, 152–155]. These positive statistical moments in the SOL are a consequence of the presence of filaments, as demonstrated by an exponential-like tail toward positive values in Fig. 2.20.

Previous studies have indicated an invariance of the PDFs with changing plasma parameters. For increasing line-averaged densities, it was shown in TCV that the PDFs do not change shape as seen in Fig. 2.22. Similar results were also shown for TCV by instead varying the plasma current [50]. However, this is not the case for the far SOL in Alcator C-Mod as presented in Paper II when the line-averaged density was varied. Nonetheless, continuing to agree with the previous results of the Langmuir probe measurements in TCV, the GPI diagnostic installed in TCV shows that the PDFs of the normalized time series are also independent of the line-averaged density, as presented in Paper III. For different radial positions in the SOL, the shape of the PDF has been shown to change, where, in the vicinity of the LCFS, the PDFs resemble a Gaussian [143, 156]. For several confinement modes in Alcator C-Mod, Fig. 2.23, the shape of the PDFs change, where the ohmic low confinement mode case shows the most skewed Gamma distribution [88].

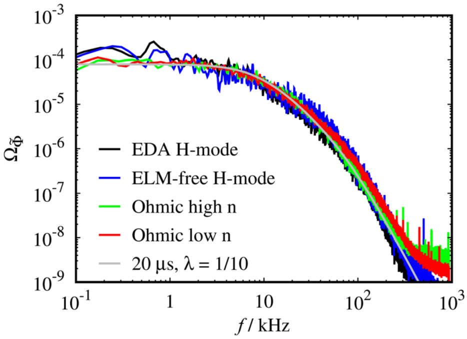

Figure 2.24: PSDs of the GPI light intensity measurements in various confinement modes from Alcator C-Mod. The solid line shows the agreement with the stochastic model. Reprinted with permission from AIP Publishing [88].

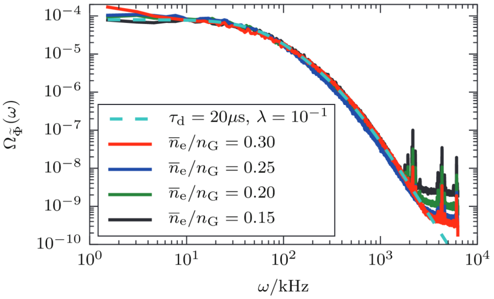

Figure 2.25: PSDs of the GPI light intensity for various line-averaged densities at the outermost diode view. The dashed line is the agreement with the stochastic model. Reprinted from [143] with the permission from IAEA.

The frequency power spectral densities (PSDs) of single-point measurements have a flat region for low frequencies and appear to have a Lorentzian-like decay for high frequencies [47, 142, 146, 156, 157]. This is shown for various fusion devices in Fig. 2.21 where the PSDs collapse to a similar shape given by the appropriate scaling on the frequency axis. In Fig. 2.21, λ scales the frequency axis to highlight this similarity. In the framework of stochastic modelling which will be discussed in Chapter 3, it has been shown that the similarity in the PSDs can be attributed to the underlying pulse shape of the fluctuations. For various confinement regimes as seen in Refs. [88, 144] or increasing the line-averaged densities [143] it has been shown that the PSDs of the far SOL GPI time series measured in Alcator C-Mod do not change. However, diagnostic differences in PSDs exist between the Langmuir probe and the GPI as discussed in detail in Paper II. Furthermore, it was implied by conditional averaging that duration times are independent of line-averaged density in TCV far SOL Langmuir probe measurements [71]. A discrepancy was observed in the TCV GPI results where this is not the case, as shown in Paper III.

In order to extract the amplitudes and waiting times from intermittent time-series measurements, it is common to apply a thresholding method known as the *conditional averaging technique*. This is used to reveal the statistical properties of the large-amplitude fluctuations [77, 88, 93]. Waiting times between these fluctuations can give insight on the rate at which blobs are

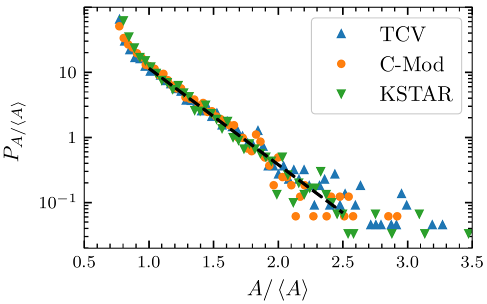

Figure 2.26: PDFs of the normalized amplitude distribution using the conditional averaging technique applied to the time series in Fig. 2.6. Image courtesy of A. Theodorsen [73].

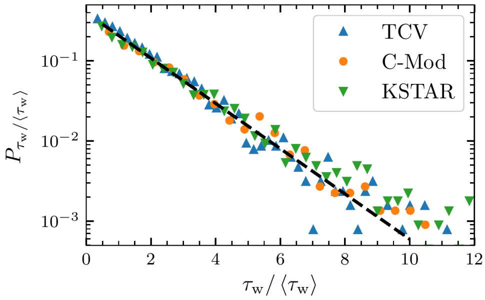

Figure 2.27: PDFs of the normalized waiting time distribution using the conditional averaging technique applied to the time series in Fig. 2.6. Image courtesy of A. Theodorsen [73].

formed. A brief explanation of this method involves a threshold of approximately $2.5\Phi_{\rm rms}$, where $\Phi_{\rm rms}$ is the root mean square of the time series under investigation. Conditional averaging has been applied to Langmuir probe measurements and GPI measurements [44, 50, 77–79, 83, 84, 98, 102, 150, 158–162]. The application of conditional averaging has been mostly to unravel the average waveform of the fluctuations. As shown in Fig. 2.7, the average waveform across line-averaged densities in TCV show a fast rise and a slow decay. ESEL simulations also appear to qualitatively agree with the experimental results in conjunction with the results in Fig. 2.14. However, this is not a widely agreed threshold amongst the community, since in some cases a higher threshold is used when processing experimental time-series measurements from various diagnostics [74]. Nevertheless, once an arbitrary threshold is set, every time the signal crosses this threshold, a conditional window around the signal is recorded, thus considering the peak amplitude of this pulse. The amplitude and waiting time distributions are presented using conditional averaging on Langmuir probe data from TCV, Alcator C-Mod, and KSTAR in Figs. 2.26 and 2.27, respectively. These show that the amplitudes and the waiting times between the consecutive fluctuations after applying such arbitrary thresholds are exponentially distributed, indicating similarity to that also observed in other works [88]. However, there are some issues:

- The conditional amplitudes distribution is decided by the tail of the PDF of the time series, not by the underlying amplitude distribution.
- The level of overlapping fluctuations in the time series may influence the average waveform.

- The conditional waiting times do not accurately reflect the intermittency of the fluctuations.

A detailed study on the conditional averaging technique has been performed where the reader may look to Ref. [163] for further information. Paper I focuses on an alternative way of extracting amplitudes and waiting times, but applied to synthetic time series based on the stochastic model. The applications of this new method can be seen in Papers II and III. However, before discussing the content of these papers, an overview of the stochastic model is necessary.

3 Stochastic modelling

The stochastic model, known as the filtered Poisson process (FPP), serves as a powerful tool for describing the intermittent fluctuations observed in the boundary of magnetically confined fusion plasmas. This model captures the statistical features of these fluctuations by depicting them as a superposition of uncorrelated pulses.

In 1909, the model initially emerged as a means to characterize noise in vacuum tubes [164–166]. Exploring this model, specifically in relation to SOL plasma fluctuations, was initiated in 2012 [167]. Since then, its applicability has been extended to interpret and describe Langmuir probe and GPI measurements in various tokamaks and confinement modes [55, 57, 77, 78, 85, 88, 144, 145]. These studies have provided evidence that the major assumptions and predictions of the stochastic model align remarkably well with the observed statistical properties of SOL fluctuations. The salient features of the statistics that are reproducible by the FPP are:

- The parabolic relationship between the skewness and flatness.
- Strongly skewed and flattened probability distribution with a tail toward large signal values.
- The frequency power spectra are flat for low frequencies, and the high frequencies are Lorentzian like.

Hitherto, SOL fluctuations from various experiments have shown to exhibit:

- Relative fluctuation levels radially increasing from the LCFS towards the far SOL.
- Probability density functions that are close to Gaussian near the LCFS and a strongly skewed Gamma distribution in the far SOL.

3.1 Filtered Poisson Process

The stochastic model describes single-point measurements in the SOL [167] as a superposition of uncorrelated pulses

$$\Phi_K(t) = \sum_{k=1}^{K(T)} A_k \varphi\left(\frac{t - s_k}{\tau_\mathrm{d}}\right). \tag{3.1}$$

The time series Φ to be analysed is either given by light intensity measurements from GPI or I_sat from Langmuir probes. Here, $K(T)$ is a Poisson process which takes place in the time interval $t \in [0, T]$ where T is the duration of the process. A_k refers to the amplitudes of each pulse and s_k is the arrival time. Furthermore, each pulse has an associated duration time τ_d. $K(T)$ follows a Poisson distribution in the given time interval with an intensity $1/\tau_\mathrm{w}$,

$$P_K(K|T) = \frac{1}{K!}\left(\frac{T}{\tau_\mathrm{w}}\right)^K \exp\left(-\frac{T}{\tau_\mathrm{w}}\right) \tag{3.2}$$

where τ_w is the mean time between consecutive pulses. As a result, the pulse arrival times s_k are independent and uniformly distributed in the interval, and the waiting times $w_k = s_k - s_{k-1}$ are independent and exponentially distributed with a mean value τ_w.

For the most relevant pulse shape for the SOL fluctuation analyses [55, 57, 77, 78, 85, 144], we assume that the pulse function is given by an asymmetric two-sided exponential

$$\varphi(\theta) = \begin{cases} \exp(-\theta/(1-\lambda)), & \theta \geq 0, \\ \exp(-\theta/\lambda), & \theta < 0. \end{cases} \tag{3.3}$$

The dimensionless variable is given by θ and λ represents the pulse asymmetry where $\lambda \in (0, 1)$. The case of a one-sided exponential pulse shape is given by $\lambda = 0$, whereas $\lambda = 1/2$ leads to a symmetric two-sided exponential pulse shape. Utilizing integrals of the pulse shape defined as

$$I_n = \int_{-\infty}^{\infty} d\theta \varphi(\theta, \lambda)^n, \tag{3.4}$$

moments of the distributions of the process may be derived. For a two-sided exponential pulse shape as shown in Eq. (3.3), $I_n = 1/n$ is independent of λ. A further simplification of the pulse shape would be to consider a one-sided exponential pulse, where the asymmetry parameter is set to $\lambda = 0$, which are also observed in Papers II and III.

Considering a train of delta pulses $\mathcal{F}_K$, Eq. (3.1) can rewritten as convolution between φ and $\mathcal{F}_K$,

$$\Phi_K\left(t\right) = \int_{-\infty}^{\infty} d\theta\, \varphi\left(\frac{t}{\tau_\mathrm{d}} - \theta, \lambda\right) \mathcal{F}_K(\theta) = \left[\varphi * \mathcal{F}_K\right]\left(\frac{t}{\tau_\mathrm{d}}\right), \tag{3.5}$$

where

$$\mathcal{F}_K\left(t\right) = \sum_{k=1}^{K(T)} A_k \delta\left(\frac{t - s_k}{\tau_\mathrm{d}}\right). \tag{3.6}$$

Thus, this process is expressed as a delta pulse train that consists of amplitudes and arrival times, filtered through the pulse shape with a constant pulse duration time τ_d, giving rise to a *filtered Poisson process*. The formulation above is strictly for a constant τ_d. In Sec. 3.2, this feature of the stochastic model is used to deconvolve amplitudes and arrival times given a known pulse shape.

The fundamental parameter of the stochastic model is the *intermittency parameter* defined by

$$\gamma = \frac{\tau_\mathrm{d}}{\tau_\mathrm{w}}, \tag{3.7}$$

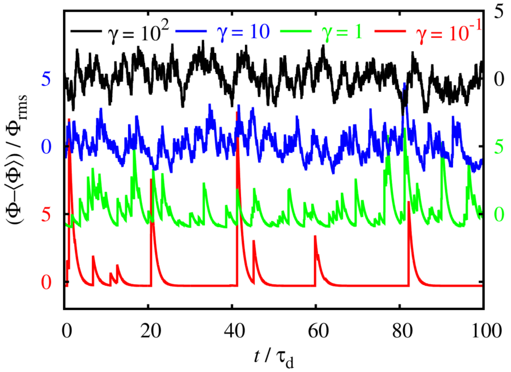

Figure 3.1: Normalized realizations of the stochastic model for various levels of intermittency parameters given by γ. The time axis is normalized by τ_d. Reprinted from [168] with permission from AIP Publishing.

which determines the degree of pulse overlap. Despite the fact that $1/\tau_\mathrm{w}$ indicates the intensity of the process, it does not provide a good sense of how intermittent Φ is in actuality. For different pulse duration times at fixed waiting times, broad pulses will lead to a slowly-varying process at low intensities. A high-intensity process will result in a high intermittency in the case of narrow pulses. Therefore, Eq. (3.7) is a better metric for describing the level of pulse overlap. The consequences of pulse overlap are clearly illustrated in Fig. 3.1 for the normalized process with exponentially distributed pulse amplitudes and waiting times. When γ is small, the pulses appear isolated in the realizations of Φ, resulting in a strongly intermittent process. A small mean value is expected with large relative fluctuations about the mean. When γ is large, there is a significant overlap of pulses, resulting in a weakly intermittent process. We have a large mean value and small relative variation around the mean. For $\gamma \to \infty$, the FPP approaches a normally distributed process. In the far SOL, it is typical to expect $\gamma < 5$ based on the studies shown in Papers II and III.

3.1.1 Moments and distributions

The four lowest order central moments of the FPP according to [167] are

$$\langle\Phi\rangle = \gamma\langle A\rangle I_1, \tag{3.8a}$$

$$\Phi_{\text{rms}}^2 = \gamma\langle A^2\rangle I_2, \tag{3.8b}$$

$$S_\Phi = \frac{1}{\gamma^{1/2}}\frac{\langle A^3\rangle I_3}{\langle A^2\rangle^{3/2} I_2^{3/2}}, \tag{3.8c}$$

$$F_\Phi = 3 + \frac{1}{\gamma}\frac{\langle A^4\rangle I_4}{\langle A^2\rangle^2 I_2^2}, \tag{3.8d}$$

where S_Φ is the skewness, F_Φ is the flatness, and $\langle\cdot\rangle$ denotes the mean value. These moments exhibit the parabolic relationship

$$F_\Phi = 3 + \frac{\langle A^2\rangle\langle A^4\rangle}{\langle A^3\rangle^2}\frac{I_2 I_4}{I_3^2} S_\Phi^2. \tag{3.9}$$

Utilizing Eq. (3.4) for exponential pulses and $\langle A^n\rangle = n!\langle A\rangle^n$ as we have exponentially distributed amplitudes, the central moments simplify to

$$\langle\Phi\rangle = \gamma\langle A\rangle, \tag{3.10a}$$

$$\Phi_{\text{rms}}^2 = \gamma\langle A^2\rangle, \tag{3.10b}$$

$$S_\Phi = \frac{2}{\gamma^{1/2}}, \tag{3.10c}$$

$$F_\Phi = 3 + \frac{6}{\gamma}. \tag{3.10d}$$

Thus, the relative fluctuation level describing the variation around the mean is found to be

$$\frac{\Phi_{\text{rms}}}{\langle\Phi\rangle} = \gamma^{-1/2}. \tag{3.11}$$

The universal parabolic relationship between the higher order moments is given by

$$F_\Phi = 3 + \frac{3}{2} S_\Phi^2. \tag{3.12}$$

Here, for a given pulse shape Eq. (3.12) is independent of λ. Due to the fact that we have exponentially distributed amplitudes, the relation is also independent of $\langle A \rangle$. Therefore, for any value of γ used in the process described by Eq. (3.1), different values of F_Φ and S_Φ will lie on the parabolic relation given by Eq. (3.12). The skewness and flatness increase with decreasing γ, and vanishes in the limit $\gamma \to \infty$.

For the case of exponentially distributed amplitudes, the PDF of the process is given by a Gamma distribution

$$P_\Phi(\Phi) = \frac{1}{\langle A \rangle \Gamma(\gamma)} \left(\frac{\Phi}{\langle A \rangle} \right)^{\gamma - 1} \exp\left(-\frac{\Phi}{\langle A \rangle} \right), \ \Phi > 0, \tag{3.13}$$

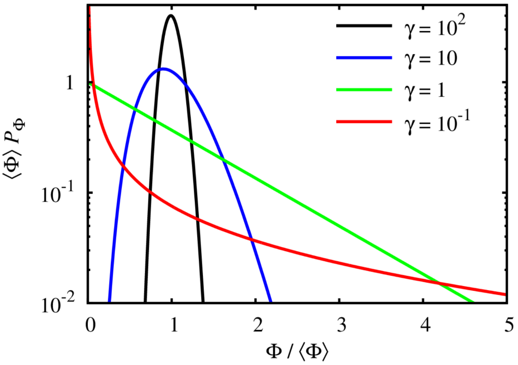

Figure 3.2: PDFs of the process normalized by the mean for various levels of intermittency given by γ. Reprinted from [169] with permission from AIP Publishing.

where the scale parameter is given by $\langle A \rangle$, the shape parameter is given by γ and Γ denotes the Gamma function. The derived expression is not new and has been shown in previous literature [170]. An illustration of the effects of the intermittency parameter on the normalized Gamma distribution is presented in Fig. 3.2. The limits of strong and weak intermittency impact the PDF of the random variable. For $\gamma \to \infty$, the normalized probability density function resembles a normal distribution with a mean of unity [169]. In the case of small γ, a strongly skewed Gamma distribution of the process can be observed. Such distributions observed in SOL plasmas can be therefore explained using γ.

Furthermore, the intermittency parameter is also reflected in the relative fluctuation level presented in Eq. (3.11). Decreasing γ suggests an increase in relative fluctuation levels shown by gradually skewed PDFs radially outward [143], or an increase in the line-averaged density at a single point in the far SOL, as seen in Paper II. Hence, both of these characteristics indicate a decrease in the value of γ. Finally, the result in Eq. (3.13) may be derived as shown in Ref. [169], with I_n as presented in Eq. (3.4). This means that the distribution is the same, *irrespective* of λ. In general, one can conclude that the intermittency of the fluctuations determines the shape of the distribution of the process.

In some cases, measurement data from the SOL may need to be detrended because of a moving plasma column. This also facilitates comparisons between measurements under similar conditions. Under the normalization

$$\widetilde{\Phi} = \frac{\Phi - \langle \Phi \rangle}{\Phi_{\mathrm{rms}}}, \tag{3.14}$$

Eq. (3.13) becomes

$$P_{\widetilde{\Phi}}(\widetilde{\Phi}) = \frac{\gamma^{\gamma/2}}{\Gamma(\gamma)}(\gamma^{1/2} + \widetilde{\Phi})^{\gamma-1} \exp\left(-\gamma - \gamma^{1/2}\widetilde{\Phi}\right). \tag{3.15}$$

Eq. (3.14) may also be extended to normalizing the signal by eliminating the running mean and dividing by the running standard deviation, since Eq. (3.1) is statistically a stationary process [57, 88]. For time series measured in the SOL, a drifting plasma column may contribute to trends seen, and preferably this is removed using running normalization described previously [57, 85].

The PDF of the normalized process, given by Eq. (3.15), depends entirely on γ and is independent of $\langle A \rangle$. The character of the process is determined by γ, whereas $\langle A \rangle$ simply scales the process. Therefore, it is important to estimate γ correctly from the fluctuation analysis. Indeed, it is also desirable to determine $\langle A \rangle$ since it is closely related to the absolute values of the process. However, this may not always give physical insight in some experiments. As previously explained in Sec. 2.2, the GPI light intensity is non-linearly dependent on the n_{e}, T_{e} and the neutral gas cloud from the injected gas puff. Thus, estimating $\langle A \rangle$ from GPI measurements may be considered dubious as they cannot be directly related to any of the local plasma parameters.

3.1.2 Power spectral density

Analysing the frequency components of Φ is useful in characterizing the underlying turbulent phenomena measured in time series. This is one of the standard ways to investigate fluctuations in SOL plasmas. To achieve this, we turn to the frequency domain, where the power spectrum of the signal can

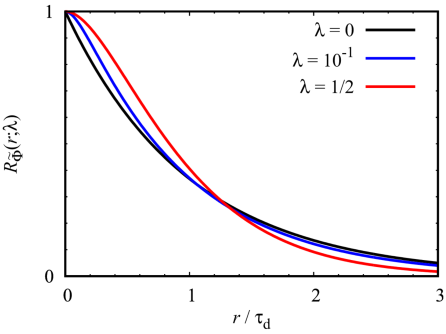

Figure 3.3: ACFs of the normalized process consisting of two-sided exponential pulses with various asymmetry parameters, λ. Reprinted from [168] with permission from AIP Publishing.

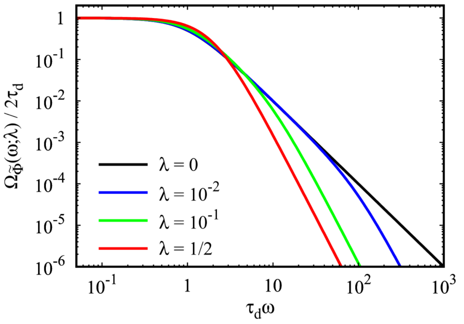

Figure 3.4: The PSDs of the normalized process consisting of two-sided exponential pulses with various asymmetry parameters, λ. Reprinted from [168] with permission from AIP Publishing.

be determined using the convolution form of Φ given by Eq. (3.5). To then find the autocorrelation function (ACF), the inverse Fourier transform can be applied, as described in Ref. [171] for the case $\lambda = 0$. The formalism of Φ provided by Eq. (3.5) is straightforward, describing the process as a convolution between φ and $\mathcal{F}_K$. This suggests that the power spectrum of Φ is the product of the power spectra of φ and $\mathcal{F}_K$. The power spectrum of $\mathcal{F}_K$ is flat under the assumption of uncorrelated delta pulses describing the process. Therefore, the frequency spectrum of Φ is entirely dependent on φ. The ACF is given by the Fourier transform of the PSD of the normalized process according to Eq. (3.14). Thus, the ACF and the PSD are given by

$$R_{\tilde{\Phi}}(r;\lambda) = \frac{1}{1-2\lambda}\left[(1-\lambda)\exp\left(-\frac{|r|}{(1-\lambda)\tau_\mathrm{d}}\right) - \lambda\exp\left(-\frac{|r|}{\lambda\tau_\mathrm{d}}\right)\right] \tag{3.16}$$

and

$$\Omega_{\tilde{\Phi}}(\omega;\lambda) = \frac{2\tau_\mathrm{d}}{[1+(1-\lambda)^2\tau_\mathrm{d}^2\omega^2][1+\lambda^2\tau_\mathrm{d}^2\omega^2]}, \tag{3.17}$$

respectively where a two-sided exponential pulse function is considered. Here, r comes from a change in variables $\theta = |r|/\tau$ [168]. Due to normalization, these expressions do not depend on $\langle\Phi\rangle$ or Φ_rms.

The ACFs and PSDs are presented for various λ in Figs. 3.3 and 3.4 respectively. Contrary to the PDFs, these second-order statistics are independent of γ but vary with λ. For one-sided exponential pulses with $\lambda = 0$ with constant duration, the ACF is a purely symmetric exponential and the PSD acquires a

Lorentzian shape. This is a well-known frequency spectrum that is flat for low frequencies and has a Lorentizian-like decay for high frequencies. For $\lambda \ll 1$ and $1 - \lambda \ll 1$, the PSD adopts a broken power law in an intermediate range of frequencies where the spectrum falls with ω^{-2} before falling with ω^{-4} in the high-frequency limit. As a result, the spectrum appears to be curved, as shown in Fig. 3.4. The expression presented in Eq. (3.17) is therefore an excellent description of the power spectrum of experimental measurements as shown in Fig. 2.21 with $\lambda = 1/10$. Since the spectrum is independent of γ, conditions that lead to different degrees of pulse overlap do not play a role.

3.2 Richardson-Lucy deconvolution

The aforementioned conditional averaging technique has been commonly used on SOL fluctuation time series for determining amplitudes and waiting time distributions [57, 77, 78, 85, 151, 172]. However, recent results from a study on conditional averaging [163], shows there are severe limitations to the method. Therefore, the current work moves away from this method and uses a modified Richardson-Lucy (RL) deconvolution algorithm, or the iterative space reconstruction algorithm (ISRA) [173, 174]. This method was originally developed for deblurring image data in astronomy. Its applications to SOL fluctuation measurements from Alcator C-Mod have been previously reported [144, 145].

The FPP can be written as a convolution between a known pulse shape and a forcing consisting of a train of delta pulses, as shown in Eq. (3.5). It is recognized that noise is inherent in time series, and the FPP and its statistical moments have been considered in the presence of noise [171]. Nevertheless, this common pulse shape for all arrivals in the time series can be used to reproduce the forcing under the maximum-likelihood sense in the presence of normally distributed and uncorrelated noise. The iteration scheme is therefore given by

$$\mathcal{F}_j^{(n+1)} = \mathcal{F}_j^{(n)} \frac{(\Phi * \widehat{\varphi})_j + b}{\left(\mathcal{F}^{(n)} * \varphi * \widehat{\varphi}\right)_j + b}, \tag{3.18}$$

which is known to converge asymptotically. Here, the hat symbol $\widehat{\cdot}$ denotes a flipped vector, $\widehat{\varphi}_j = \widehat{\varphi}_{-j}$. To ensure a non-negative initial guess remains non-negative, the parameter b is chosen such that $(\Phi * \widehat{\varphi})_j + b > 0 \, \forall j$ [175]. Filaments appear as large positive bursts in times-series measurements; therefore, positive-definite sections of the signal are of interest. The standard deviation of the noise, or alternatively, the signal-to-noise ratio, plays no role in the iterations scheme. The choice of the initial guess $\mathcal{F}^{(0)}$ and the value of b may play a role in the rate of convergence, but these does not affect the overall result as long as it is small compared to the signal values.

The estimate of $\mathcal{F}$ may contain spurious pulses that are not significant. An appropriate peak-finding algorithm may be used to extract amplitudes and arrival times. In the present work, a three-point running maxima are employed, where the relevant peak is classified if it is larger than both neighbouring points. From this, probability distributions of the amplitudes and waiting times can be determined, or one may be interested in reconstructing the time series which include the relevant pulses of interest. Paper I presents a detailed study of the modified RL deconvolution under various intermittency parameters, noise levels, distributions of the amplitudes, waiting times and pulse duration times as well as a reconstruction of the pulse shape under a known forcing.

3.3 Average radial profiles

SOL density profiles can be unravelled by extending the stochastic model for the advection of single pulses. This is achieved by covering the radial direction and the time coordinate. The first attempt has been shown for Poisson distributed pulses and constant velocity [169]. Consider a superposition of pulses as explained in Ref. [169],

$$\Phi_K(x,t) = \sum_{k=1}^{K} \phi_k(x,t). \tag{3.19}$$

Here, ϕ_k contains both the amplitude and the pulse shape. The evolution of individual pulses where the pulses do not interact, is given by the modified advection equation,

$$\frac{\partial \phi_k}{\partial t} + v_k \frac{\partial \phi_k}{\partial x} + \frac{\phi_k}{\tau_\parallel} = 0, \tag{3.20}$$

where v_k is the radial velocity of each pulse, $\tau_\parallel$ describes the parallel drainage along the magnetic field lines due to acoustic streaming. Both of these parameters are assumed to be constant in time and radial positions for all blobs. Assuming the same size $l_\perp$ and velocity $v_\perp$ for all pulses, the mean profile according to Ref. [169] takes the exponential form

$$\langle \Phi \rangle(\xi) = \frac{\tau_\mathrm{d}}{\tau_w} \langle A_0 \rangle \exp\left(-\frac{\xi}{v_\perp \tau_\parallel} \right). \tag{3.21}$$

The duration time, $\tau_\mathrm{d} = \tau_\parallel \tau_\perp / (\tau_\parallel + \tau_\perp)$ is the harmonic mean of the perpendicular and parallel transit time. For context, the transit time past the probe is the perpendicular transit time $\tau_\perp$, given by $\tau_\perp = l_\perp / v_\perp$. If $v_\perp$ is low, then $\tau_\perp$ is long, and the probe registers a pulse decay primarily due to parallel drainage.

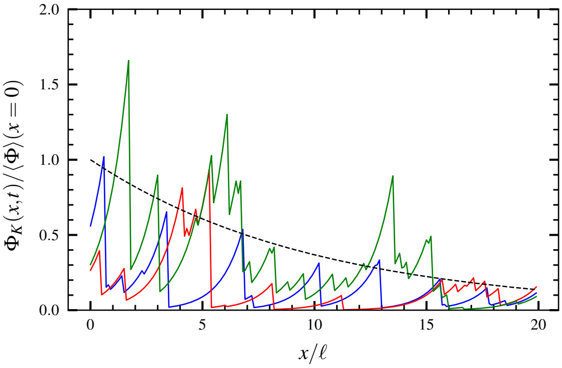

Figure 3.5: Radial profile from a superposition of one-sided exponential pulses with a degenerate distribution of velocities and sizes. The coloured lines represent multiple realizations of the process. The black dashed line is the predicted profile. The radial position is given by x/l instead of ξ and is normalized to the size of the pulse l. Reproduced from [176].

If $\tau_{||}$ is long, then the advection velocity sets the pulse decay time observed by the probe.

Here, $\langle A_0 \rangle$ is the mean of the initial amplitudes at $\xi = 0$. The resulting exponential radial profiles are presented in Fig. 3.5. The black dashed line is the theoretical prediction with exponentially distributed amplitudes for a constant number of one-sided exponential pulses, where the velocities and sizes are fixed.

However, these assumptions made of the model present some limitations. Assuming constant radial velocities and pulse sizes over-simplifies filamentary transport, hence the variation observed in SOL profiles. τ_w and therefore γ are radially constant, and this is not in agreement with the experimental observations [143]. The interactions between individual filaments, blob dispersion, and poloidal motion are not taken into account.

Recently, a theoretical framework based on the stochastic model was proposed to address some of these limitations [176]. A different attempt was pursued in Refs. [56, 177–179] in which the model included spatial and temporal evolution of the pulse widths and velocities. Focusing on Ref. [176], the study instead generalizes the stochastic model by employing a discrete uniform distribution of velocities. This is the simplest case for a velocity distribution where the resulting profiles show that broadening and flattening can be achieved. One-sided exponential pulses with a fixed pulse size were used in this formalism.

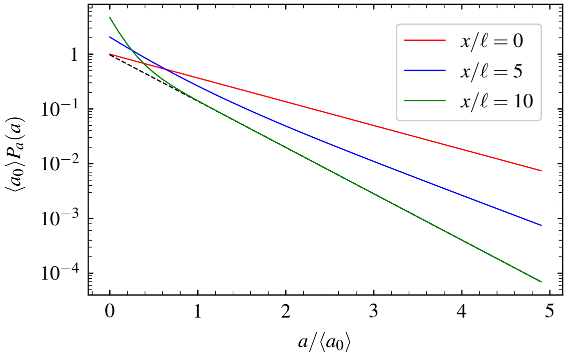

Figure 3.6: PDFs of the amplitude for a discrete uniform distribution of pulse velocities at different radial positions. The dashed line is the amplitude distribution for fast pulses. Reproduced from [176].

The amplitude distribution which results from using a discrete uniform distribution of pulse velocities, is shown for different radial positions in Fig. 3.6. In this case at $x = 0$, the distribution is exponentially distributed, while for large values of x, a bi-exponential behaviour is exhibited with an increased probability for small amplitudes. The black dashed line indicates the case for fast pulses. These analytical findings on the amplitude distribution motivated the use of a bi-exponential description for the amplitude distribution from experimental measurements in Papers II and III. The expression for this is given by

$$P_A(A) = \frac{q}{\langle A_< \rangle} \exp\left(-\frac{A}{\langle A_< \rangle}\right) + \frac{1-q}{\langle A_> \rangle} \exp\left(-\frac{A}{\langle A_> \rangle}\right), \tag{3.22}$$

where $0 < q < 1$ represents the probability that pulse corresponds to a small-amplitude fluctuation. $\langle A_< \rangle$ and $\langle A_> \rangle$ are the mean of small and large-amplitude fluctuations, respectively. The larger-amplitude fluctuations are of significant interest since it is assumed that these are impacted the least by parallel drainage [176]. In a similar fashion to Eq. (3.22), the mean of the long waiting times $\langle w_> \rangle$, may also be estimated where the mean of the small waiting times $\langle w_< \rangle$ are considered to be from noise. This formulation is used rather than a simple tail fit to avoid setting arbitrary thresholds in the fits to the amplitude and waiting time distributions. In relation to this thesis, the major goal is to determine how the properties of the far SOL fluctuations vary under different plasma conditions.

4 Summary of Papers

This thesis analysed the applications of the stochastic modelling framework, known as the filtered Poisson process (FPP), in greater depth. In particular, far SOL fluctuations in L-mode plasmas with varying plasma and machine parameters were studied. For amplitude and waiting-time extraction, the Richardson-Lucy (RL) deconvolution was used to understand how the estimated mean values varied with these parameters of interest.

Paper I presents a detailed study on the strengths and weaknesses of the modified form of the RL deconvolution algorithm. To improve waiting-time statistics, this strategy is preferable over the widely utilized conditional averaging methodology. By reformulating the stochastic model as a convolution of the pulse shape and the impulse process consisting of amplitudes and arrival times, this forcing can be recovered. For simplicity, one-sided exponential pulses are employed in several synthetic realizations using the stochastic model. The RL deconvolution was tested on these realizations of various intermittency parameters and different distributions of amplitudes, waiting times, and duration times. Other considerations such as noise levels, sampling times, and incorrectly estimated duration times were also tested.

The method shows that a time series can be reconstructed for various pulse amplitude and waiting-time distributions. Although the modified form is restricted to recover positive-definite pulses, negative pulse amplitudes may also be recovered by simply flipping the sign of the time series. Under moderate amounts of additive noise and correlated noise, the RL deconvolution performs well. Employing a pulse shape of constant duration time is a strict requirement for the RL deconvolution. Upon further investigation, for the RL deconvolution to work on time series, the ratio between the sampling time and the average waiting time between pulses must be about 1/20 or smaller. Furthermore, one may also estimate the shape given a known forcing, and this was found to be only weakly constrained by the intermittency.

Subsequently, Paper II details a comprehensive study on far SOL fluctuations in time-series measurements from Alcator C-Mod. The analysis was carried out on a line-averaged density scan under constant conditions in L-mode, lower diverted single-null plasmas. The densities were varying from $0.46 \times 10^{20}\,\mathrm{m}^{-3}$ to $2.83 \times 10^{-3}\,\mathrm{m}^{20}$ giving a wider range of Greenwald fractions than previously studied in Refs. [85, 95, 143, 151]. The far SOL measurements were considered from dwell experiments of the so-called "mirror" Langmuir probe (MLP) [89] and light intensity measurements from the gas puff imaging (GPI) diagnostic [110]. These measurements provided several hundreds of milliseconds of time series over a wide density range. Long time-series enables the use of stochastic model to estimate parameters reliably. PDFs and PSDs are presented to showcase the changes in the statistical features of the far SOL measurements.

Firstly, for increasing line-averaged densities, it was found from the ion saturation current measurements that the intermittency parameter monotonically decreases. The GPI fluctuation analysis does not show this but coincides with the MLP results at Greenwald fractions higher than 60% of the density limit. Approximately around this f_{GW}, the time-averaged radial profiles of the SOL are broad and flat. This analysis of the GPI measurements under a wider range of densities was performed in comparison to the results shown in Refs. [85, 143, 151] where this feature was not observed.

Diagnostic differences are further highlighted by analysing the pulse duration times of the MLP and GPI time series. Due to the spatial averaging along the toroidal extent, the GPI registers longer duration times and broader pulse shapes compared to the MLP. Both show constant duration times with increasing Greenwald fraction. These differences were reported previously but were not systematically studied [145].

Motivated by the outcomes of Paper I, the RL deconvolution was used to recover the mean amplitudes and mean waiting times in Paper II. The difference between the RL deconvolution used here and in previous studies [144, 145] is that no parameter was adjusted to extract the expected amount of pulses. The RL deconvolution was only used to recover the mean waiting times from the GPI measurements. Absolute values of the mean amplitudes from the GPI were not provided since the light intensity measurements are strongly impacted by the neutral density, therefore not meaningful. From the MLP measurements, the mean amplitudes and therefore the fluxes near the wall increase linearly with line-averaged density. Although the fluctuations are arriving at the far SOL less frequently as a result of longer mean waiting times, the mean amplitudes become higher as the density limit is approached, therefore significantly amplifying plasma–wall interactions. Despite this being a single-machine scan, the expected wall fluxes for SPARC for an L-mode scenario [16] was found to be $7 \times 10^{18}\,\mathrm{m}^{-2}\mathrm{s}^{-1}$.

A multimachine comparison of far SOL fluctuation statistics has been performed in Paper III. Alcator C-Mod, DIII-D, TCV, KSTAR, MAST, and MAST-U time series from Langmuir probes were analysed. In the study, it is highlighted that the MAST-U data are electron saturation current measurements due to a wrongly-biased probe. The rest of the analysis was performed on the ion saturation current measurements from the other devices. Despite the incorrectly-measured variable, electron saturation current was considered as a proxy for the local density in this case.

There have been previous multimachine studies focusing on profiles [53] and SOL statistics using the GPI [154]. In this study, it is the first time that far SOL measurements have been investigated using the FPP in a systematic way across several fusion devices. Measurements were taken from Langmuir probes from dwell experiments in Alcator C-Mod from Paper II, TCV [77], KSTAR [55] and MAST-U; reciprocating Langmuir probe measurements from MAST and DIII-D, and from the GPI diagnostics in Alcator C-Mod (see Paper II) and TCV [102].

The far SOL fluctuation statistics continue to agree with the stochastic model indicating no new physics due to similar distributions and spectra. Individual model parameter scans of the FPP were performed with f_{GW}. In all tokamaks, the mean amplitudes were shown to increase approximately linearly with f_{GW}. This is a significant increase in the case for Alcator C-Mod.

It is a well-known result that in TCV, the PDFs of the ion saturation current for various densities do not change, hence the intermittency parameters in the far SOL are robust against f_{GW} [71]. This was in agreement with the TCV GPI, DIII-D, MAST and MAST-U Langmuir probe data as shown in Paper III. However, the intermittency parameter changes with f_{GW} in Alcator C-Mod and does so over a wide range of line-averaged densities. Furthermore, the duration times are independent of f_{GW} in conventional tokamaks. However, in spherical tokamaks the duration times τ_{d}, were seen to increase with increasing f_{GW}. The difference in the mean waiting times τ_{w}, across devices indicate that rate of filament formation are also different. In devices such as C-Mod, TCV, MAST and MAST-U, τ_{w} increases with f_{GW} whereas this is not the case in DIII-D, based on the available data. Overall, there is no universal trend with f_{GW} with the model parameters (γ, τ_{d} and τ_{w}) across these devices apart from the mean amplitudes.

The variation of the stochastic model parameters with other plasma and machine parameters was strongly indicated in Paper III. Firstly, the values of the intermittency parameter decreased with increasing plasma current. This is expected since it was found in DIII-D that the plasma current has a significant impact on the signal amplitudes of the fluctuations [81]. Secondly, no trends were observed when these fluctuation statistics were plotted as a function of minor radius. The lack of trends with the minor radii of these devices indicated that the Greenwald fraction may not be the correct choice for parameterizing the stochastic model parameters in the cross-machine comparison, even though the Greenwald fraction showed some trends in the single-machine scans.

The radial velocities calculated from the maximum of the cross-conditional averaging were invariant against the changing engineering parameters across devices. The study in DIII-D also showed no changes in the radial velocity at varying densities [81]. In Alcator C-Mod, Ref. [135] and Paper II showed a slight increase in the radial velocity with increasing plasma density. A recent study has shown that negative triangularity in TCV L-mode plasmas demonstrate the suppression of first-wall turbulence [138]. The triangularity of these L-mode plasmas across devices in this study did not show trends in the stochastic model parameters.

For spherical and conventional tokamaks, the distinction between the two was shown to be clear. In conventional tokamaks, duration times of the fluctuations showed to be independent of the line-averaged density. In spherical tokamaks which known to be smaller in aspect ratio and higher in elongation, the duration times were shown to increase with increasing density and blobs appeared to be larger in amplitude and longer is mean waiting times. When viewing the FPP model parameters as a function of aspect ratio on the available data, the duration times showed a linear trend with increasing aspect ratio in conventional tokamaks. The outcomes of this study that have been highlighted indicate that the plasma–wall interactions may behave differently across these devices.

5 | Conclusion and outlook

Monitoring and predicting the expected wall fluxes is vital for the successful operation of future fusion reactors. Analysing these inherent fluctuations of plasma density in the framework of stochastic modelling allows one to gain statistical insight especially when plasma conditions and machine parameters are varying. The model is capable of reproducing salient features of the many statistical properties of the fluctuations; such as PDFs, frequency power spectra, the parabolic relationship between skewness and flatness and possibly, the time-averaged radial profiles of the SOL.

In this thesis, a detailed study of the far SOL fluctuation statistics is presented over a wide range of densities – up to 85% of the density limit in Alcator C-Mod. The stochastic model continues to hold for such densities close to the empirical discharge density limit. The Richardson-Lucy (RL) deconvolution algorithm is used to recover amplitudes and waiting times, as opposed to the much-used conditional averaging technique. As a consequence of approaching the empirical density limit, far SOL fluctuations occur less frequently but increase in amplitude and wall fluxes, enhancing plasma–wall interactions. Diagnostic differences are highlighted between the mirror-Langmuir probe and the gas puff imaging (GPI) in Alcator C-Mod. These observations require further studies to understand the role of detachment and neutral interaction.

The multimachine comparison of the far SOL statistics in L-mode across several tokamaks is reported. From this systematic analysis, it was found that the stochastic model continues to hold for all the fusion devices considered and in some cases, showing trends with Greenwald fraction for the individual machine scans. TCV, DIII-D, MAST and MAST-U show unchanging intermittency parameters of the far SOL fluctuations with increasing density. This was not the case for Alcator C-Mod where the intermittency parameter is unequivocally a function of density. The varying behaviour of the waiting times across these devices and therefore the rate of the pulses determined by the blob formation further highlight the differences between the machines. Engineering parameters such as aspect ratio, plasma current, toroidal magnetic field, poloidal magnetic field, elongation, triangularity and major and minor radii were investigated. No trends were found between the far SOL statistics and the minor radii across all devices.

Analysing far SOL fluctuations in the cross-machine comparison indicate no new physics due to similar distributions and spectra. In all cases, the amplitudes increase approximately linearly across all devices. Velocities appear invariant to most variables except density. However, the values of the stochastic model parameter are changing with plasma parameters/machines in different ways. There are notable differences between conventional and spherical tokamaks. Duration times do not change with Greenwald fraction for conventional tokamaks. Blobs appear larger in amplitude, longer in duration times and mean waiting times in spherical devices. Behaviours with Greenwald fraction is not consistent across all tokamaks therefore, no universal relationship was found between Greenwald fraction and the stochastic model parameters. This calls for an in-depth study on the variable quantities of the Greenwald fraction, in particular, the line-averaged density and the plasma current.

Future work would entail expanding on the existing L-mode database incorporating more Langmuir probe data from other tokamaks. An underlying question exists as to whether the stochastic model can be used to aid the understanding of the plasma turbulence and eventually become predictive. Although clear trends between model and machine and plasma parameters are present in this study, open questions remain. Previously, a comparative study has been performed using the GPI [154]. Assessing the trends of the stochastic model parameters using the GPI data from other devices could be considered. Investigating far SOL statistics in stellarators in which a Greenwald limit does not exist would also be interesting [180].

The stochastic model used in this thesis does not take into account the effects of divertor closure and main chamber recycling which could possibly explain the differences in the statistics in the multimachine comparison. As highlighted earlier, the waiting times ultimately come from the interplay between blob formation, advection and dissipation. Different waiting times indicate the disparities between the machines. Although the velocities are of similar order of magnitude, the dissipation and hence the different divertor configurations across machines may play a role. Recently, it was shown that neutrals have an impact on the density shoulder amplitude in TCV, thus indicating consequences on the filamentary transport across the boundary plasma [131].

The analysis of SOL statistics and hence the time-averaged profiles under different confinement regimes should also be considered. It has been suggested in previous work that high confinement modes in the absence of edge-localised modes show suppressed filamentary transport indicated by the PDFs of the fluctuation measurements [88]. Investigating these effects in the extended theoretical work done to describe profiles using the stochastic model [176] would be insightful. This would incorporate many diagnostics to reproduce profiles, such as using the GPI to estimate blob sizes and velocities.

The stochastic model has previously been used as a metric for the validation of numerical turbulence simulations to check whether the derived statistics are in agreement with the experimental results [181]. Validating the profiles from these simulations with blob properties estimated via blob tracking or similar methods would bring further confidence. In addition, the effect of neutrals may also be simulated with existing codes in order to investigate how these profiles are impacted. This may offer a perspective on how to incorporate neutrals in the stochastic model.

Bibliography

[1] A. S. Eddington. The internal constitution of the stars. *The Scientific Monthly* **11**, 297–303 (1920).

[2] P. Barabaschi, D. Borba, G. Federici, L. Horton, R. Neu, D. Stork, H. Zohm, et al. Fusion electricity: A roadmap to the realization of fusion energy. EFDA (2012).

[3] J. Wesson and D. Campbell. *Tokamaks*. International series of monographs on physics. Clarendon Press (2004).

[4] J. P. Freidberg. *Plasma physics and fusion energy*. Cambridge University Press (2008).

[5] P. C. Stangeby. *The plasma boundary of magnetic fusion devices*. Plasma physics series. Institute of Physics Pub, Bristol ; Philadelphia (2000).

[6] W. Fundamenski. *Power Exhaust in Fusion Plasmas*. Cambridge University Press (2010).

[7] ITER. Advantages of fusion. `http://www.iter.org/sci/fusion`.

[8] EUROfusion. Should you not try fusion under pressure as that is how it takes place in the sun? `https://euro-fusion.org/faq/fusion-under-pressure/`.

[9] EUROfusion. `https://euro-fusion.org/`.

[10] Y. U. Nam and J. Chung. Analysis of line integrated electron density using plasma position data on Korea Superconducting Tokamak Advanced Research). *Rev. Sci. Instrum.* **81**, 10D510 (2010).

[11] P. Helander, C. D. Beidler, T. M. Bird, M. Drevlak, Y. Feng, R. Hatzky, F. Jenko, R. Kleiber, J. H. E. Proll, Y. Turkin, and P. Xanthopoulos. Stellarator and tokamak plasmas: a comparison. *Plasma Phys. Control. Fusion* **54**, 124009 (2012).

[12] T. K. *et. al.* Overview of first wendelstein 7-x high-performance operation. *Nucl. Fusion* **59**, 112004 (2019).

[13] A. E. Costley. Towards a compact spherical tokamak fusion pilot plant. *Philos. Trans. Royal Soc. A* **377**, 20170439 (2019).

[14] M. Windridge. Smaller and quicker with spherical tokamaks and high-temperature superconductors. *Philos. Trans. Royal Soc. A* **377** , 20170438 (2019).

[15] O. Beeke, M. Barnes, M. Romanelli, M. Nakata, and M. Yoshida. Impact of shaping on microstability in high-performance tokamak plasmas. *Nucl. Fusion* **61**, 066020 (2021).

[16] A. J. Creely, M. J. Greenwald, S. B. Ballinger, D. Brunner, J. Canik, J. Doody, T. Fülöp, D. T. Garnier, R. Granetz, T. K. Gray, C. Holland, N. T. Howard, J. W. Hughes, J. H. Irby, V. A. Izzo, G. J. Kramer, A. Q. Kuang, B. LaBombard, Y. Lin, B. Lipschultz, N. C. Logan, J. D. Lore, E. S. Marmar, K. Montes, R. T. Mumgaard, C. Paz-Soldan, C. Rea, M. L. Reinke, P. Rodriguez-Fernandez, K. Särkimäki, F. Sciortino, S. D. Scott, A. Snicker, P. B. Snyder, B. N. Sorbom, R. Sweeney, R. A. Tinguely, E. A. Tolman, M. Umansky, O. Vallhagen, J. Varje, D. G. Whyte, J. C. Wright, S. J. Wukitch, J. Zhu, and the SPARC Team. Overview of the SPARC tokamak. *J. Plasma Phys.* **86**, 865860502 (2020).

[17] EPFL Swiss Plasma Center. Technical data. `https://www.epfl.ch/research/domains/swiss-plasma-center/research/tcv/research_tcv_tokamak/tcv-technical-data/`.

[18] F. Hofmann, R. Behn, S. Coda, T. P. Goodman, M. Henderson, P. Lavanchy, P. Marmillod, Y. Martin, A. Martynov, J. Mlynar, J.-M. Moret, A. Pochelon, H. Reimerdes, O. Sauter, S. Alberti, C. Angioni, K. Appert, J. Bakos, P. Blanchard, P. Bosshard, R. Chavan, I. Condrea, A. Degeling, B. P. Duval, D. Fasel, J.-Y. Favez, A. Favre, I. Furno, P. Gomez, P. Gorgerat, J.-P. Hogge, P.-F. Isoz, B. Joye, I. Klimanov, J. B. Lister, X. Llobet, J.-C. Magnin, A. Manini, B. Marlétaz, J.-M. Mayor, P. Nikkola, P. J. Paris, A. Perez, Z. A. Pietrzyk, V. Piffl, R. A. Pitts, A. Scarabosio, E. Scavino, A. Sushkov, G. Tonetti, M. Q. Tran, H. Weisen, and A. Zabolotsky. Stability and energy confinement of highly elongated plasmas in TCV. *Plasma Phys. Control. Fusion* **43**, A161 (2001).

[19] A. W. Morris. MAST: Results and Upgrade Activities. *IEEE Trans. Plasma Sci.* **40**, 682–691 (2012).

[20] J. Harrison, R. Akers, S. Allan, J. Allcock, J. Allen, L. Appel, M. Barnes, N. B. Ayed, W. Boeglin, C. Bowman, J. Bradley, P. Browning, P. Bryant, M. Carr, M. Cecconello, C. Challis, S. Chapman, I. Chapman, G. Colyer, S. Conroy, N. Conway, M. Cox, G. Cunningham, R. Dendy, W. Dorland, B. Dudson, L. Easy, S. Elmore, T. Farley, X. Feng, A. Field, A. Fil, G. Fishpool, M. Fitzgerald, K. Flesch, M. Fox, H. Frerichs, S. Gadgil, D. Gahle, L. Garzotti, Y.-C. Ghim, S. Gibson, K. Gibson, S. Hall, C. Ham, N. Heiberg, S. Henderson, E. Highcock, B. Hnat, J. Howard, J. Huang, S. Irvine, A. Jacobsen, O. Jones, I. Katramados, D. Keeling, A. Kirk, I. Klimek, L. Kogan, J. Leland, B. Lipschultz, B. Lloyd, J. Lovell, B. Madsen, O. Marshall, R. Martin, G. McArdle, K. McClements, B. McMillan, A. Meakins, H. Meyer, F. Militello, J. Milnes, S. Mordijck, A. Morris, D. Moulton, D. Muir, K. Mukhi, S. Murphy-Sugrue, O. Myatra, G. Naylor, P. Naylor, S. Newton, T. O'Gorman, J. Omotani, M. O'Mullane, S. Orchard, S. Pamela, L. Pangione, F. Parra, R. Perez, L. Piron, M. Price, M. Reinke, F. Riva, C. Roach, D. Robb, D. Ryan, S. Saarelma, M. Salewski, S. Scannell, A. Schekochihin, O. Schmitz, S. Sharapov, R. Sharples, S. Silburn, S. Smith, A. Sperduti, R. Stephen, N. Thomas-Davies, A. Thornton, M. Turnyanskiy, M. Valovič, F. V. Wyk, R. Vann, N. Walkden, I. Waters, H. Wilson, the MAST-U Team, and the EUROfusion MST1 Team. Overview of new MAST physics in anticipation of first results from MAST Upgrade. *Nucl. Fusion* **59**, 112011 (2019).

[21] MAST Upgrade Capabilities | MAST-U Users. `https://users.mastu.ukaea.uk/capabilities`.

[22] G. Lee, M. Kwon, C. Doh, B. Hong, K. Kim, M. Cho, W. Namkung, C. Chang, Y. Kim, J. Kim, H. Jhang, D. Lee, K. You, J. Han, M. Kyum, J. Choi, J. Hong, W. Kim, B. Kim, J. Choi, S. Seo, H. Na, H. Lee, S. Lee, S. Yoo, B. Lee, Y. Jung, J. Bak, H. Yang, S. Cho, K. Im, N. Hur, I. Yoo, J. Sa, K. Hong, G. Kim, B. Yoo, H. Ri, Y. Oh, Y. Kim, C. Choi, D. Kim, Y. Park, K. Cho, T. Ha, S. Hwang, Y. Kim, S. Baang, S. Lee, H. Chang, W. Choe, S. Jeong, S. Oh, H. Lee, B. Oh, B. Choi, C. Hwang, S. In, S. Jeong, I. Ko, Y. Bae, H. Kang, J. Kim, H. Ahn, D. Kim, C. Choi, J. Lee, Y. Lee, Y. Hwang, S. Hong, K.-H. Chung, D.-I. Choi, and K. Team. Design and construction of the KSTAR tokamak. *Nucl. Fusion* **41**, 1515 (2001).

[23] T. O'Gorman. *Investigation of neoclassical tearing modes on MAST using Thomson scattering.* PhD thesis, University College Cork (2012).

[24] J. L. Luxon. A brief introduction to the DIII-D tokamak. *Fusion Sci. Technol.* **48**, 828-833 (2005).

[25] M. Shimada, D. Campbell, V. Mukhovatov, M. Fujiwara, N. Kirneva, K. Lackner, M. Nagami, V. Pustovitov, N. Uckan, J. Wesley, N. Asakura, A. Costley, A. Donné, E. Doyle, A. Fasoli, C. Gormezano, Y. Gribov, O. Gruber, T. Hender, W. Houlberg, S. Ide, Y. Kamada, A. Leonard, B. Lipschultz, A. Loarte, K. Miyamoto, V. Mukhovatov, T. Osborne, A. Polevoi, and A. Sips. Chapter 1: Overview and summary. *Nucl. Fusion* **47**, S1 (2007).

[26] J. M. et. al. Overview of jet results for optimising iter operation. *Nucl. Fusion* **62**, 042026 (2022).

[27] H. Reimerdes, M. Agostini, E. Alessi, S. Alberti, Y. Andrebe, H. Arnichand, J. Balbin, F. Bagnato, M. Baquero-Ruiz, M. Bernert, W. Bin, P. Blanchard, T. Blanken, J. Boedo, D. Brida, S. Brunner, C. Bogar, O. Bogar, T. Bolzonella, F. Bombarda, F. Bouquey, C. Bowman, D. Brunetti, J. Buermans, H. Bufferand, L. Calacci, Y. Camenen, S. Carli, D. Carnevale, F. Carpanese, F. Causa, J. Cavalier, M. Cavedon, J. Cazabonne, J. Cerovsky, R. Chandra, A. Chandrarajan Jayalekshmi, O. Chellaï, P. Chmielewski, D. Choi, G. Ciraolo, I. Classen, S. Coda, C. Colandrea, A. Dal Molin, P. David, M. De Baar, J. Decker, W. Dekeyser, H. De Oliveira, D. Douai, M. Dreval, M. Dunne, B. Duval, S. Elmore, O. Embreus, F. Eriksson, M. Faitsch, G. Falchetto, M. Farnik, A. Fasoli, N. Fedorczak, F. Felici, O. Février, O. Ficker, A. Fil, M. Fontana, E. Fransson, L. Frassinetti, I. Furno, D. Gahle, D. Galassi, K. Galazka, C. Galperti, S. Garavaglia, M. Garcia-Munoz, B. Geiger, M. Giacomin, G. Giruzzi, M. Gobbin, T. Golfinopoulos, T. Goodman, S. Gorno, G. Granucci, J. Graves, M. Griener, M. Gruca, T. Gyergyek, R. Haelterman, A. Hakola, W. Han, T. Happel, G. Harrer, J. Harrison, S. Henderson, G. Hogeweij, J.-P. Hogge, M. Hoppe, J. Horacek, Z. Huang, A. Iantchenko, P. Innocente, K. Insulander Björk, C. Ionita-Schrittweiser, H. Isliker, A. Jardin, R. Jaspers, R. Karimov, A. Karpushov, Y. Kazakov, M. Komm, M. Kong, J. Kovacic, O. Krutkin, O. Kudlacek, U. Kumar, R. Kwiatkowski, B. Labit, L. Laguardia, J. Lammers, E. Laribi, E. Laszynska, A. Lazaros, O. Linder, B. Linehan, B. Lipschultz, X. Llobet, J. Loizu, T. Lunt, E. Macusova, Y. Marandet, M. Maraschek, G. Marceca, C. Marchetto, S. Marchioni, E. Marmar, Y. Martin, L. Martinelli, F. Matos, R. Maurizio, M.-L. Mayoral, D. Mazon, V. Menkovski, A. Merle, G. Merlo, H. Meyer, K. Mikszuta-Michalik, P. Molina Cabrera, J. Morales, J.-M. Moret,

A. Moro, D. Moulton, H. Muhammed, O. Myatra, D. Mykytchuk, F. Napoli, R. Nem, A. Nielsen, M. Nocente, S. Nowak, N. Offeddu, J. Olsen, F. Orsitto, O. Pan, G. Papp, A. Pau, A. Perek, F. Pesamosca, Y. Peysson, L. Pigatto, C. Piron, M. Poradzinski, L. Porte, T. Pütterich, M. Rabinski, H. Raj, J. Rasmussen, G. Rattá, T. Ravensbergen, D. Ricci, P. Ricci, N. Rispoli, F. Riva, J. Rivero-Rodriguez, M. Salewski, O. Sauter, B. Schmidt, R. Schrittweiser, S. Sharapov, U. Sheikh, B. Sieglin, M. Silva, A. Smolders, A. Snicker, C. Sozzi, M. Spolaore, A. Stagni, L. Stipani, G. Sun, T. Tala, P. Tamain, K. Tanaka, A. Tema Biwole, D. Terranova, J. Terry, D. Testa, C. Theiler, A. Thornton, A. Thrysøe, H. Torreblanca, C. Tsui, D. Vaccaro, M. Vallar, M. Van Berkel, D. Van Eester, R. Van Kampen, S. Van Mulders, K. Verhaegh, T. Verhaeghe, N. Vianello, F. Villone, E. Viezzer, B. Vincent, I. Voitsekhovitch, N. Vu, N. Walkden, T. Wauters, H. Weisen, N. Wendler, M. Wensing, F. Widmer, S. Wiesen, M. Wischmeier, T. Wijkamp, D. Wünderlich, C. Wüthrich, V. Yanovskiy, J. Zebrowski, and T. EUROfusion MST1 Team. Overview of the TCV tokamak experimental programme. *Nucl. Fusion* **62**, 042018 (2022).

[28] M. E. F. et. al. DIII-D research advancing the physics basis for optimizing the tokamak approach to fusion energy. *Nucl. Fusion* **62**, 042024 (2022).

[29] S. Krasheninnikov, A. Smolyakov, and A. Kukushkin. *On the Edge of Magnetic Fusion Devices.* Springer Series in Plasma Science and Technology. Springer International Publishing, Cham (2020).

[30] F. Militello. *Boundary Plasma Physics: An Accessible Guide to Transport, Detachment, and Divertor Design*, volume 123 of *Springer Series on Atomic, Optical, and Plasma Physics.* Springer International Publishing, Cham (2022).

[31] R. A. Pitts, J. P. Coad, D. P. Coster, G. Federici, W. Fundamenski, J. Horacek, K. Krieger, A. Kukushkin, J. Likonen, G. F. Matthews, M. Rubel, J. D. Strachan, and J.-E. contributors. Material erosion and migration in tokamaks. *Plasma Phys. Control. Fusion* **47**, B303–B322 (2005).

[32] D. G. Whyte, B. L. Lipschultz, P. C. Stangeby, J. Boedo, D. L. Rudakov, J. G. Watkins, and W. P. West. The magnitude of plasma flux to the main-wall in the DIII-D tokamak. *Plasma Phys. Control. Fusion* **47**, 1579–1607 (2005).

[33] B. Lipschultz, X. Bonnin, G. Counsell, A. Kallenbach, A. Kukushkin, K. Krieger, A. Leonard, A. Loarte, R. Neu, R. Pitts, T. Rognlien,

J. Roth, C. Skinner, J. Terry, E. Tsitrone, D. Whyte, S. Zweben, N. Asakura, D. Coster, R. Doerner, R. Dux, G. Federici, M. Fenstermacher, W. Fundamenski, P. Ghendrih, A. Herrmann, J. Hu, S. Krasheninnikov, G. Kirnev, A. Kreter, V. Kurnaev, B. LaBombard, S. Lisgo, T. Nakano, N. Ohno, H. Pacher, J. Paley, Y. Pan, G. Pautasso, V. Philipps, V. Rohde, D. Rudakov, P. Stangeby, S. Takamura, T. Tanabe, Y. Yang, and S. Zhu. Plasma–surface interaction, scrape-off layer and divertor physics: implications for ITER. *Nucl. Fusion* **47**, 1189–1205 (2007).

[34] Y. Marandet, A. Mekkaoui, D. Reiter, P. Börner, P. Genesio, F. Catoire, J. Rosato, H. Capes, L. Godbert-Mouret, M. Koubiti, and R. Stamm. Transport of neutral particles in turbulent scrape-off layer plasmas. *Nucl. Fusion* **51**, 083035 (2011).

[35] G. Birkenmeier, P. Manz, D. Carralero, F. Laggner, G. Fuchert, K. Krieger, H. Maier, F. Reimold, K. Schmid, R. Dux, T. Pütterich, M. Willensdorfer, E. Wolfrum, and The ASDEX Upgrade Team. Filament transport, warm ions and erosion in ASDEX Upgrade L-modes. *Nucl. Fusion* **55**, 033018 (2015).

[36] Y. Marandet, N. Nace, M. Valentinuzzi, P. Tamain, H. Bufferand, G. Ciraolo, P. Genesio, and N. Mellet. Assessment of the effects of scrape-off layer fluctuations on first wall sputtering with the TOKAM-2D turbulence code. *Plasma Phys. Control. Fusion* **58**, 114001 (2016).

[37] M. Reinhart, S. Brezinsek, A. Kirschner, J. Coenen, T. Schwarz-Selinger, K. Schmid, A. Hakola, H. Van Der Meiden, R. Dejarnac, E. Tsitrone, R. Doerner, M. Baldwin, D. Nishijima, and W. P. Team. Latest results of Eurofusion plasma-facing components research in the areas of power loading, material erosion and fuel retention. *Nucl. Fusion* **62** , 042013 (2022).

[38] A. Zito, M. Wischmeier, A. Kappatou, A. Kallenbach, F. Sciortino, V. Rohde, K. Schmid, E. Hinson, O. Schmitz, M. Cavedon, R. McDermott, R. Dux, M. Griener, and U. Stroth. Investigation of helium exhaust dynamics at the ASDEX Upgrade tokamak with full-tungsten wall. *Nucl. Fusion* **63**, 096027 (2023).

[39] J. Connor, G. Counsell, S. Erents, S. Fielding, B. LaBombard, and K. Morel. Comparison of theoretical models for scrape-off layer widths with data from COMPASS-D, JET and Alcator C-Mod. *Nucl. Fusion* **39**, 169–188 (1999).

[40] B. Lipschultz, B. LaBombard, C. S. Pitcher, and R. Boivin. Investigation of the origin of neutrals in the main chamber of Alcator C-Mod. *Plasma Phys. Control. Fusion* **44**, 733–748 (2002).

[41] S. I. Krasheninnikov, D. A. D'Ippolito, and J. R. Myra. Recent theoretical progress in understanding coherent structures in edge and SOL turbulence. *J. Plasma Phys.* **74**, 679–717 (2008).

[42] K. McCormick, G. Kyriakakis, J. Neuhauser, E. Kakoulidis, J. Schweinzer, and N. Tsois. Particle and energy transport scalings in the ASDEX scrape-off layer. *J. Nucl. Mater* **196-198**, 264–270 (1992).

[43] B. LaBombard, M. Umansky, R. Boivin, J. Goetz, J. Hughes, B. Lipschultz, D. Mossessian, C. Pitcher, J. Terry, and A. Group. Cross-field plasma transport and main-chamber recycling in diverted plasmas on Alcator C-Mod. *Nucl. Fusion* **40**, 2041–2060 (2000).

[44] J. A. Boedo, D. Rudakov, R. Moyer, S. Krasheninnikov, D. Whyte, G. McKee, G. Tynan, M. Schaffer, P. Stangeby, P. West, S. Allen, T. Evans, R. Fonck, E. Hollmann, A. Leonard, A. Mahdavi, G. Porter, M. Tillack, and G. Antar. Transport by intermittent convection in the boundary of the DIII-D tokamak. *Phys. Plasmas* **8**, 4826–4833 (2001).

[45] B. LaBombard, R. L. Boivin, M. Greenwald, J. Hughes, B. Lipschultz, D. Mossessian, C. S. Pitcher, J. L. Terry, S. J. Zweben, and Alcator Group. Particle transport in the scrape-off layer and its relationship to discharge density limit in Alcator C-Mod. *Phys. Plasmas* **8**, 2107–2117 (2001).

[46] D. L. Rudakov, J. A. Boedo, R. A. Moyer, S. Krasheninnikov, A. W. Leonard, M. A. Mahdavi, G. R. McKee, G. D. Porter, P. C. Stangeby, J. G. Watkins, W. P. West, D. G. Whyte, and G. Antar. Fluctuation-driven transport in the DIII-D boundary. *Plasma Phys. Control. Fusion* **44**, 717–731 (2002).

[47] J. L. Terry, S. J. Zweben, K. Hallatschek, B. LaBombard, R. J. Maqueda, B. Bai, C. J. Boswell, M. Greenwald, D. Kopon, W. M. Nevins, C. S. Pitcher, B. N. Rogers, D. P. Stotler, and X. Q. Xu. Observations of the turbulence in the scrape-off-layer of Alcator C-Mod and comparisons with simulationa.... *Phys. Plasmas* **10** (2003).

[48] B. Lipschultz, D. Whyte, and B. LaBombard. Comparison of particle transport in the scrape-off layer plasmas of Alcator C-Mod and DIII-D. *Plasma Phys. Control. Fusion* **47**, 1559–1578 (2005).

[49] D. Rudakov, J. Boedo, R. Moyer, N. Brooks, R. Doerner, T. Evans, M. Fenstermacher, M. Groth, E. Hollmann, S. Krasheninnikov, C. Lasnier, M. Mahdavi, G. McKee, A. McLean, P. Stangeby, W. Wampler, J. Watkins, W. West, D. Whyte, and C. Wong. Far scrape-off layer and near wall plasma studies in DIII-D. *J. Nucl. Mater* **337-339**, 717–721 (2005).

[50] O. E. Garcia, R. A. Pitts, J. Horacek, J. Madsen, V. Naulin, A. H. Nielsen, and J. J. Rasmussen. Collisionality dependent transport in TCV SOL plasmas. *Plasma Phys. Control. Fusion* **49**, B47–B57 (2007).

[51] J. L. Terry, B. LaBombard, B. Lipschultz, M. J. Greenwald, J. E. Rice, and S. J. Zweben. The Scrape-Off Layer in Alcator C-Mod: Transport, Turbulence, and Flows. *Fusion Sci. Technol.* **51**, 342–356 (2007).

[52] C. Silva, B. Gonçalves, C. Hidalgo, M. Pedrosa, W. Fundamenski, M. Stamp, and R. Pitts. Intermittent transport in the JET far-SOL. *J. Nucl. Mater* **390-391**, 355–358 (2009).

[53] D. Carralero, H. Müller, M. Groth, M. Komm, J. Adamek, G. Birkenmeier, M. Brix, F. Janky, P. Hacek, S. Marsen, F. Reimold, C. Silva, U. Stroth, M. Wischmeier, and E. Wolfrum. Implications of high density operation on SOL transport: A multimachine investigation. *J. Nucl. Mater* **463**, 123–127 (2015).

[54] F. Militello, L. Garzotti, J. Harrison, J. Omotani, R. Scannell, S. Allan, A. Kirk, I. Lupelli, and A. Thornton. Characterisation of the L-mode scrape off layer in MAST: decay lengths. *Nucl. Fusion* **56**, 016006 (2016).

[55] O. Garcia, R. Kube, A. Theodorsen, J.-G. Bak, S.-H. Hong, H.-S. Kim, Team, the KSTAR Project, and R. Pitts. SOL width and intermittent fluctuations in KSTAR. *Nucl. Mater. Energy* **12**, 36–43 (2017).

[56] N. R. Walkden, A. Wynn, F. Militello, B. Lipschultz, G. Matthews, C. Guillemaut, J. Harrison, D. Moulton, and JET Contributors. Interpretation of scrape-off layer profile evolution and first-wall ion flux statistics on JET using a stochastic framework based on fillamentary motion. *Plasma Phys. Control. Fusion* **59**, 085009 (2017).

[57] R. Kube, O. E. Garcia, A. Theodorsen, D. Brunner, A. Q. Kuang, B. LaBombard, and J. L. Terry. Intermittent electron density and temperature fluctuations and associated fluxes in the Alcator C-Mod scrape-off layer. *Plasma Phys. Control. Fusion* **60**, 065002 (2018).

[58] A. Wynn, B. Lipschultz, I. Cziegler, J. Harrison, A. Jaervinen, G. F. Matthews, J. Schmitz, B. Tal, M. Brix, C. Guillemaut, D. Frigione, A. Huber, E. Joffrin, U. Kruzei, F. Militello, A. Nielsen, N. Walkden, S. Wiesen, and JET Contributors. Investigation into the formation of the scrape-off layer density shoulder in JET ITER-like wall L-mode and H-mode plasmas. *Nucl. Fusion* **58**, 056001 (2018).

[59] A. Kuang, B. LaBombard, D. Brunner, O. Garcia, R. Kube, and A. Theodorsen. Plasma fluctuations in the scrape-off layer and at the divertor target in Alcator C-Mod and their relationship to divertor collisionality and density shoulder formation. *Nucl. Mater. Energy* **19**, 295–299 (2019).

[60] N. Vianello, D. Carralero, C. Tsui, V. Naulin, M. Agostini, I. Cziegler, B. Labit, C. Theiler, E. Wolfrum, D. Aguiam, S. Allan, M. Bernert, J. Boedo, S. Costea, H. De Oliveira, O. Fevrier, J. Galdon-Quiroga, G. Grenfell, A. Hakola, C. Ionita, H. Isliker, A. Karpushov, J. Kovacic, B. Lipschultz, R. Maurizio, K. McClements, F. Militello, A. Nielsen, J. Olsen, J. Rasmussen, T. Ravensbergen, H. Reimerdes, B. Schneider, R. Schrittwieser, E. Seliunin, M. Spolaore, K. Verhaegh, J. Vicente, N. Walkden, W. Zhang, the ASDEX Upgrade Team, the TCV Team, and the EUROfusion MST1 Team. Scrape-off layer transport and filament characteristics in high-density tokamak regimes. *Nucl. Fusion* **60** , 016001 (2020).

[61] A. Stagni, N. Vianello, C. Tsui, C. Colandrea, S. Gorno, M. Bernert, J. Boedo, D. Brida, G. Falchetto, A. Hakola, G. Harrer, H. Reimerdes, C. Theiler, E. Tsitrone, N. Walkden, The Tcv Team, and The EUROfusion Mst1 Team. Dependence of scrape-off layer profiles and turbulence on gas fuelling in high density H-mode regimes in TCV. *Nucl. Fusion* **62**, 096031 (2022).

[62] H. Sun, S. Silburn, I. Carvalho, D. King, C. Giroud, G. Fishpool, G. Matthews, R. Henriques, D. Keeling, F. Rimini, L. Garzotti, D. Frigione, D. Van Eester, M. Groth, J. Flanagan, D. Kos, B. Viola, A. Boboc, P. Shi, M.-L. Mayoral, J. Mailloux, C. Maggi, A. Huber, D. Douai, N. Vianello, P. Lomas, M. Lennholm, M. Maslov, K. Kirov, P. Jacquet, C. Lowry, M. Baruzzo, C. Stuart, J. Mitchell, L. Horvath, and D. McDonald. The broadening of SOL profiles in JET tritium plasma and its impact on machine operation. *Nucl. Fusion* **63**, 016021 (2023).

[63] M. Greenwald. Density limits in toroidal plasmas. *Plasma Phys. Control. Fusion* **44**, R27–R53 (2002).

[64] O. Garcia, R. Pitts, J. Horacek, A. Nielsen, W. Fundamenski, J. Graves, V. Naulin, and J. J. Rasmussen. Turbulent transport in the TCV SOL. *J. Nucl. Mater* **363-365**, 575–580 (2007).

[65] A. Y. Pigarov, S. I. Krasheninnikov, T. D. Rognlien, M. J. Schaffer, and W. P. West. Tokamak edge plasma simulation including anomalous cross-field convective transport. *Phys. Plasmas* **9**, 1287–1299 (2002).

[66] V. Naulin. Turbulent transport and the plasma edge. *J. Nucl. Mater* **363-365**, 24–31 (2007).

[67] S. Zweben, P. Liewer, and R. Gould. Edge plasma transport experiments in the Caltech Tokamak. *J. Nucl. Mater* **111-112**, 39–43 (1982).

[68] S. Zweben and R. Gould. Structure of edge-plasma turbulence in the Caltech tokamak. *Nucl. Fusion* **25**, 171–183 (1985).

[69] S. J. Zweben. Search for coherent structure within tokamak plasma turbulence. *Phys. Fluids* **28**, 974 (1985).

[70] A. J. Wootton, B. A. Carreras, H. Matsumoto, K. McGuire, W. A. Peebles, C. P. Ritz, P. W. Terry, and S. J. Zweben. Fluctuations and anomalous transport in tokamaks. *Phys. Fluids B: Plasma Physics* **2** , 2879–2903 (1990).

[71] O. Garcia, J. Horacek, R. Pitts, A. Nielsen, W. Fundamenski, V. Naulin, and J. J. Rasmussen. Fluctuations and transport in the TCV scrape-off layer. *Nucl. Fusion* **47**, 667–676 (2007).

[72] G. R. McKee, R. J. Fonck, D. K. Gupta, D. J. Schlossberg, M. W. Shafer, R. L. Boivin, and W. Solomon. Plasma turbulence imaging via beam emission spectroscopy in the core of the DIII-D tokamak. *Plasma Fusion Res.* **2**, S1025-S1025 (2007).

[73] A. Theodorsen. *Statistical properties of intermittent fluctuations in the boundary of fusion plasmas.* PhD thesis, UiT The Arctic University of Norway (2018).

[74] D. A. D'Ippolito, J. R. Myra, and S. J. Zweben. Convective transport by intermittent blob-filaments: Comparison of theory and experiment. *Phys. Plasmas* **18**, 060501 (2011).

[75] R. Maqueda, D. Stotler, and S. Zweben. Intermittency in the scrape-off layer of the National Spherical Torus Experiment during H-mode confinement. *J. Nucl. Mater* **415**, S459–S462 (2011).

[76] O. Grulke, J. L. Terry, B. LaBombard, and S. J. Zweben. Radially propagating fluctuation structures in the scrape-off layer of Alcator C-Mod. *Phys. Plasmas* **13**, 012306 (2006).

[77] A. Theodorsen, O. E. Garcia, J. Horacek, R. Kube, and R. A. Pitts. Scrape-off layer turbulence in TCV: evidence in support of stochastic modelling. *Plasma Phys. Control. Fusion* **58**, 044006 (2016).

[78] R. Kube, A. Theodorsen, O. E. Garcia, B. LaBombard, and J. L. Terry. Fluctuation statistics in the scrape-off layer of Alcator C-Mod. *Plasma Phys. Control. Fusion* **58**, 054001 (2016).

[79] J. Boedo, D. Rudakov, R. Colchin, R. Moyer, S. Krasheninnikov, D. Whyte, G. McKee, G. Porter, M. Schaffer, P. Stangeby, W. West, S. Allen, and A. Leonard. Intermittent convection in the boundary of DIII-D. *J. Nucl. Mater* **313-316**, 813–819 (2003).

[80] G. Y. Antar, G. Counsell, Y. Yu, B. Labombard, and P. Devynck. Universality of intermittent convective transport in the scrape-off layer of magnetically confined devices. *Physics of Plasmas* **10**, 419-428 (2003).

[81] D. Rudakov, J. Boedo, R. Moyer, P. Stangeby, J. Watkins, D. Whyte, L. Zeng, N. Brooks, R. Doerner, T. Evans, M. Fenstermacher, M. Groth, E. Hollmann, S. Krasheninnikov, C. Lasnier, A. Leonard, M. Mahdavi, G. McKee, A. McLean, A. Pigarov, W. Wampler, G. Wang, W. West, and C. Wong. Far SOL transport and main wall plasma interaction in DIII-D. *Nucl. Fusion* **45**, 1589–1599 (2005).

[82] G. Y. Antar. On the origin of "intermittency" in the scrape-off layer of linear magnetic confinement devices. *Phys. Plasmas* **10**, 3629–3634 (2003).

[83] J. Horacek, J. Adamek, H. Müller, J. Seidl, A. Nielsen, V. Rohde, F. Mehlmann, C. Ionita, and E. Havlíčková. Interpretation of fast measurements of plasma potential, temperature and density in SOL of ASDEX Upgrade. *Nucl. Fusion* **50**, 105001 (2010).

[84] L. Fattorini, Å. Fredriksen, H. L. Pécseli, C. Riccardi, and J. K. Trulsen. Turbulent transport in a toroidal magnetized plasma. *Plasma Phys. Control. Fusion* **54**, 085017 (2012).

[85] O. E. Garcia, S. M. Fritzner, R. Kube, I. Cziegler, B. LaBombard, and J. L. Terry. Intermittent fluctuations in the Alcator C-Mod scrape-off layer. *Phys. Plasmas* **20**, 055901 (2013).

[86] J. A. Boedo, J. R. Myra, S. Zweben, R. Maingi, R. J. Maqueda, V. A. Soukhanovskii, J. W. Ahn, J. Canik, N. Crocker, D. A. D'Ippolito, R. Bell, H. Kugel, B. Leblanc, L. A. Roquemore, D. L. Rudakov, and NSTX Team. Edge transport studies in the edge and scrape-off layer of the National Spherical Torus Experiment with Langmuir probes. *Phys. Plasmas* **21**, 042309 (2014).

[87] G. Birkenmeier, F. M. Laggner, M. Willensdorfer, T. Kobayashi, P. Manz, E. Wolfrum, D. Carralero, R. Fischer, B. Sieglin, G. Fuchert, U. Stroth, and the ASDEX Upgrade Team. Magnetic field dependence of the blob dynamics in the edge of ASDEX upgrade L-mode plasmas. *Plasma Phys. Control. Fusion* **56**, 075019 (2014).

[88] O. E. Garcia, R. Kube, A. Theodorsen, B. LaBombard, and J. L. Terry. Intermittent fluctuations in the Alcator C-Mod scrape-off layer for ohmic and high confinement mode plasmas. *Phys. Plasmas* **25**, 056103 (2018).

[89] B. LaBombard and L. Lyons. Mirror Langmuir probe: A technique for real-time measurement of magnetized plasma conditions using a single Langmuir electrode. *Rev. Sci. Instrum.* **78**, 073501 (2007).

[90] J. G. Bak, S. G. Lee, J. Y. Kim, and KSTAR Project Team. Electrical Probe Diagnostics for KSTAR. *Contrib. Plasma Phys.* **50**, 892–897 (2010).

[91] F. Militello, P. Tamain, W. Fundamenski, A. Kirk, V. Naulin, A. H. Nielsen, and the MAST team. Experimental and numerical characterization of the turbulence in the scrape-off layer of MAST. *Plasma Phys. Control. Fusion* **55**, 025005 (2013).

[92] B. LaBombard, T. Golfinopoulos, J. L. Terry, D. Brunner, E. Davis, M. Greenwald, J. W. Hughes, and Alcator C-Mod Team. New insights on boundary plasma turbulence and the quasi-coherent mode in Alcator C-Mod using a Mirror Langmuir Probe. *Phys. Plasmas* **21**, 056108 (2014).

[93] O. Garcia, J. Horacek, and R. Pitts. Intermittent fluctuations in the TCV scrape-off layer. *Nucl. Fusion* **55**, 062002 (2015).

[94] J. A. Boedo and D. L. Rudakov. Estimation of plasma ion saturation current and reduced tip arcing using Langmuir probe harmonics. *Rev. Sci. Instrum.* **88**, 033505 (2017).

[95] R. Kube, O. Garcia, A. Theodorsen, A. Kuang, B. LaBombard, J. Terry, and D. Brunner. Statistical properties of the plasma fluctuations and

turbulent cross-field fluxes in the outboard mid-plane scrape-off layer of Alcator C-Mod. *Nucl. Mater. Energy* **18**, 193–200 (2019).

[96] I. H. Hutchinson. *Principles of Plasma Diagnostics.* Cambridge University Press (2002).

[97] L. A. Lyons. Construction and operation of a mirror langmuir probe diagnostic for the Alcator C-Mod tokamak. Master's thesis, Massachusetts Institute of Technology (2007).

[98] J. A. Boedo, D. L. Rudakov, R. A. Moyer, G. R. McKee, R. J. Colchin, M. J. Schaffer, P. G. Stangeby, W. P. West, S. L. Allen, T. E. Evans, R. J. Fonck, E. M. Hollmann, S. Krasheninnikov, A. W. Leonard, W. Nevins, M. A. Mahdavi, G. D. Porter, G. R. Tynan, D. G. Whyte, and X. Xu. Transport by intermittency in the boundary of the DIII-D tokamak. *Phys. Plasmas* **10**, 1670–1677 (2003).

[99] G. Xu, V. Naulin, W. Fundamenski, C. Hidalgo, J. Alonso, C. Silva, B. Gonçalves, A. Nielsen, J. Juul Rasmussen, S. Krasheninnikov, B. Wan, and M. Stamp. Blob/hole formation and zonal-flow generation in the edge plasma of the JET tokamak. *Nucl. Fusion* **49**, 092002 (2009).

[100] J. Terry, R. Maqueda, C. Pitcher, S. Zweben, B. LaBombard, E. Marmar, A. Pigarov, and G. Wurden. Visible imaging of turbulence in the SOL of the Alcator C-Mod tokamak. *J. Nucl. Mater* **290-293**, 757–762 (2001).

[101] S. Zweben, J. Terry, B. LaBombard, M. Agostini, M. Greenwald, O. Grulke, J. Hughes, D. D'Ippolito, S. Krasheninnikov, J. Myra, D. Russell, D. Stotler, and M. Umansky. Estimate of convective radial transport due to SOL turbulence as measured by GPI in Alcator C-Mod. *J. Nucl. Mater* **415**, S463–S466 (2011).

[102] N. Offeddu, W. Han, C. Theiler, T. Golfinopoulos, J. Terry, E. Marmar, C. Wüthrich, C. Tsui, H. de Oliveira, B. Duval, D. Galassi, D. Oliveira, D. Mancini, and the TCV Team. Cross-field and parallel dynamics of SOL filaments in TCV. *Nucl. Fusion* **62**, 096014 (2022).

[103] S. J. Zweben, J. L. Terry, D. P. Stotler, and R. J. Maqueda. Invited Review Article: Gas puff imaging diagnostics of edge plasma turbulence in magnetic fusion devices. *Rev. Sci. Instrum.* **88**, 041101 (2017).

[104] M. Agostini, R. Cavazzana, P. Scarin, G. Serianni, Y. Yagi, H. Koguchi, S. Kiyama, H. Sakakita, and Y. Hirano. Electrostatic turbulence in the edge of TPE-RX and driving mechanisms. *Plasma Phys. Control. Fusion* **50**, 095004 (2008).

[105] D. Moulton, Y. Marandet, P. Tamain, P. Ghendrih, and R. Futtersack. Density and Temperature Correlations in the SOL; Implications for Gas Puff Imaging of Turbulence: Density and Temperature Correlations in the SOL; Implications for Gas Puff Imaging of Turbulence. *Contrib. Plasma Phys.* **54**, 575–579 (2014).

[106] J. Terry, S. Zweben, O. Grulke, M. Greenwald, and B. LaBombard. Velocity fields of edge/Scrape-Off-Layer turbulence in Alcator C-Mod. *J. Nucl. Mater* **337-339**, 322–326 (2005).

[107] J. Terry, S. Zweben, M. Umansky, I. Cziegler, O. Grulke, B. LaBombard, and D. Stotler. Spatial structure of scrape-off-layer filaments near the midplane and X-point regions of Alcator-C-Mod. *J. Nucl. Mater* **390-391**, 339–342 (2009).

[108] M. Agostini, J. Terry, P. Scarin, and S. Zweben. Edge turbulence in different density regimes in Alcator C-Mod experiment. *Nucl.r Fusion* **51**, 053020 (2011).

[109] S. J. Zweben, J. L. Terry, M. Agostini, R. Hager, J. W. Hughes, J. R. Myra, D. C. Pace, and the Alcator C-Mod Group. Search for zonal flows in the edge turbulence of Alcator C-Mod. *Plasma Phys. Control. Fusion* **54**, 025008 (2012).

[110] I. Cziegler, P. H. Diamond, N. Fedorczak, P. Manz, G. R. Tynan, M. Xu, R. M. Churchill, A. E. Hubbard, B. Lipschultz, J. M. Sierchio, J. L. Terry, and C. Theiler. Fluctuating zonal flows in the I-mode regime in Alcator C-Mod. *Phys. Plasmas* **20**, 055904 (2013).

[111] O. Grulke, J. Terry, I. Cziegler, B. LaBombard, and O. Garcia. Experimental investigation of the parallel structure of fluctuations in the scrape-off layer of Alcator C-Mod. *Nucl. Fusion* **54**, 043012 (2014).

[112] B. Cao, D. P. Stotler, S. J. Zweben, M. Bell, A. Diallo, and B. Leblanc. Comparison of gas puff imaging data in nstx with degas 2 simulations. *Fusion Sci. Technol.* **64**, 29-38 (2013).

[113] N. Walkden, A. Wynn, F. Militello, B. Lipschultz, G. Matthews, C. Guillemaut, J. Harrison, and D. Moulton. Statistical analysis of the ion flux to the JET outer wall. *Nucl. Fusion* **57**, 036016 (2017).

[114] D. A. D'Ippolito and J. R. Myra. Thermal transport catastrophe and the tokamak edge density limit. *Phys. Plasmas* **13**, 062503 (2006).

[115] S. Krasheninnikov. On scrape off layer plasma transport. *Phys. Lett. A* **283**, 368–370 (2001).

[116] O. E. Garcia. Blob Transport in the Plasma Edge: a Review. *Plasma Fusion Res.* **4**, 019–019 (2009).

[117] N. Bian, S. Benkadda, J.-V. Paulsen, and O. E. Garcia. Blobs and front propagation in the scrape-off layer of magnetic confinement devices. *Phys. Plasmas* **10**, 671–676 (2003).

[118] S. H. Müller, C. Theiler, A. Fasoli, I. Furno, B. Labit, G. R. Tynan, M. Xu, Z. Yan, and J. H. Yu. Studies of blob formation, propagation and transport mechanisms in basic experimental plasmas (TORPEX and CSDX). *Plasma Physics and Controlled Fusion* **51**, 055020 (2009).

[119] S. Zweben, R. Maqueda, D. Stotler, A. Keesee, J. Boedo, C. Bush, S. Kaye, B. LeBlanc, J. Lowrance, V. Mastrocola, R. Maingi, N. Nishino, G. Renda, D. Swain, J. Wilgen, and t. N. Team. High-speed imaging of edge turbulence in NSTX. *Nucl. Fusion* **44**, 134–153 (2004).

[120] N. Ben Ayed, A. Kirk, B. Dudson, S. Tallents, R. G. L. Vann, H. R. Wilson, and the MAST team. Inter-ELM filaments and turbulent transport in the Mega-Amp Spherical Tokamak. *Plasma Phys. Control. Fusion* **51** , 035016 (2009).

[121] A. Kirk, A. J. Thornton, J. R. Harrison, F. Militello, N. R. Walkden, and the MAST Team and the EUROfusion MST1 Team. L-mode filament characteristics on MAST as a function of plasma current measured using visible imaging. *Plasma Phys. Control. Fusion* **58**, 085008 (2016).

[122] J. Terry, S. Ballinger, D. Brunner, B. LaBombard, A. White, and S. Zweben. Fast imaging of filaments in the X-point region of Alcator C-Mod. *Nucl. Mater. Energy* **12**, 989–993 (2017).

[123] O. E. Garcia, N. H. Bian, V. Naulin, A. H. Nielsen, and J. J. Rasmussen. Mechanism and scaling for convection of isolated structures in nonuniformly magnetized plasmas. *Phys. Plasmas* **12**, 090701 (2005).

[124] J. R. Myra, D. A. Russell, and D. A. D'Ippolito. Collisionality and magnetic geometry effects on tokamak edge turbulent transport. I. A two-region model with application to blobs. *Phys. Plasmas* **13**, 112502 (2006).

[125] C. Theiler, I. Furno, P. Ricci, A. Fasoli, B. Labit, S. H. Müller, and G. Plyushchev. Cross-Field Motion of Plasma Blobs in an Open Magnetic Field Line Configuration. *Phys. Rev. Lett.* **103**, 065001 (2009).

[126] J. R. Myra, D. A. Russell, and S. J. Zweben. Theory based scaling of edge turbulence and implications for the scrape-off layer width. *Phys. Plasmas* **23**, 112502 (2016).

[127] D. Rudakov, J. Boedo, R. Pitts, G. Jackson, C. Lasnier, A. Leonard, R. Moyer, P. Stangeby, G. Tynan, and J. Watkins. SOL width in limited versus diverted discharges in DIII-D. *J. Nucl. Mater* **415**, S387–S390 (2011).

[128] N. Vianello, C. Tsui, C. Theiler, S. Allan, J. Boedo, B. Labit, H. Reimerdes, K. Verhaegh, W. Vijvers, N. Walkden, S. Costea, J. Kovacic, C. Ionita, V. Naulin, A. Nielsen, J. Juul Rasmussen, B. Schneider, R. Schrittwieser, M. Spolaore, D. Carralero, J. Madsen, B. Lipschultz, and F. Militello. Modification of SOL profiles and fluctuations with line-average density and divertor flux expansion in TCV. *Nucl. Fusion* **57** , 116014 (2017).

[129] D. Carralero, M. Siccinio, M. Komm, S. Artene, F. D'Isa, J. Adamek, L. Aho-Mantila, G. Birkenmeier, M. Brix, G. Fuchert, M. Groth, T. Lunt, P. Manz, J. Madsen, S. Marsen, H. Müller, U. Stroth, H. Sun, N. Vianello, M. Wischmeier, and E. Wolfrum. Recent progress towards a quantitative description of filamentary SOL transport. *Nucl. Fusion* **57**, 056044 (2017).

[130] A. S. Thrysøe, M. Løiten, J. Madsen, V. Naulin, A. H. Nielsen, and J. J. Rasmussen. Plasma particle sources due to interactions with neutrals in a turbulent scrape-off layer of a toroidally confined plasma. *Phys. Plasmas* **25**, 032307 (2018).

[131] C. K. Tsui, J. A. Boedo, D. Brida, O. Février, G. F. Harrer, A. Perek, H. Reimerdes, B. P. Duval, S. Gorno, U. A. Sheikh, C. Theiler, N. Vianello, N. Walkden, M. Wensing, M. Baquero-Ruiz, TCV Team, and MST1 Team. Evidence on the effects of main-chamber neutrals on density shoulder broadening. *Phys. Plasmas* **29**, 062507 (2022).

[132] J. Boedo. Edge turbulence and SOL transport in tokamaks. *J. Nucl. Mater* **390-391**, 29–37 (2009).

[133] J. L. Terry, M. L. Reinke, J. W. Hughes, B. LaBombard, C. Theiler, G. M. Wallace, S. G. Baek, D. Brunner, R. M. Churchill, E. Edlund, P. Ennever, I. Faust, T. Golfinopoulos, M. Greenwald, A. E. Hubbard, J. Irby, Y. Lin, R. R. Parker, J. E. Rice, S. Shiraiwa, J. R. Walk, S. J. Wukitch, P. Xu, and C-Mod Team. Improved confinement in high-density

H-modes via modification of the plasma boundary with lower hybrid waves. *Phys. Plasmas* **22**, 056114 (2015).

[134] J. J. Rasmussen, A. H. Nielsen, J. Madsen, V. Naulin, and G. S. Xu. Numerical modeling of the transition from low to high confinement in magnetically confined plasma. *Plasma Phys. Control. Fusion* **58** , 014031 (2016).

[135] R. Kube, O. Garcia, B. LaBombard, J. Terry, and S. Zweben. Blob sizes and velocities in the Alcator C-Mod scrape-off layer. *J. Nucl. Mater* **438** , S505–S508 (2013).

[136] D. Carralero, G. Birkenmeier, H. Müller, P. Manz, P. deMarne, S. Müller, F. Reimold, U. Stroth, M. Wischmeier, E. Wolfrum, and The ASDEX Upgrade Team. An experimental investigation of the high density transition of the scrape-off layer transport in ASDEX Upgrade. *Nucl. Fusion* **54**, 123005 (2014).

[137] S. Banerjee, H. Zushi, N. Nishino, K. Hanada, S. Sharma, H. Honma, S. Tashima, T. Inoue, K. Nakamura, H. Idei, M. Hasegawa, and A. Fujisawa. Statistical features of coherent structures at increasing magnetic field pitch investigated using fast imaging in QUEST. *Nucl. Fusion* **52** , 123016 (2012).

[138] W. Han, N. Offeddu, T. Golfinopoulos, C. Theiler, C. Tsui, J. Boedo, E. Marmar, and The TCV Team. Suppression of first-wall interaction in negative triangularity plasmas on TCV. *Nucl. Fusion* **61**, 034003 (2021).

[139] F. Riva, E. Lanti, S. Jolliet, and P. Ricci. Plasma shaping effects on tokamak scrape-off layer turbulence. *Plasma Phys. Control. Fusion* **59** , 035001 (2017).

[140] J. Horacek, R. A. Pitts, J. Adamek, G. Arnoux, J.-G. Bak, S. Brezinsek, M. Dimitrova, R. J. Goldston, J. P. Gunn, J. Havlicek, S.-H. Hong, F. Janky, B. LaBombard, S. Marsen, G. Maddaluno, L. Nie, V. Pericoli, T. Popov, R. Panek, D. Rudakov, J. Seidl, D. S. Seo, M. Shimada, C. Silva, P. C. Stangeby, B. Viola, P. Vondracek, H. Wang, G. S. Xu, Y. Xu, and JET Contributors. Multi-machine scaling of the main SOL parallel heat flux width in tokamak limiter plasmas. *Plasma Phys. Control. Fusion* **58**, 074005 (2016).

[141] A. Fasoli, B. Labit, M. McGrath, S. H. Müller, G. Plyushchev, M. Podestà, and F. M. Poli. Electrostatic turbulence and transport in a simple magnetized plasma. *Phys. Plasmas* **13**, 055902 (2006).

[142] F. Sattin, M. Agostini, R. Cavazzana, P. Scarin, and J. L. Terry. Fluctuations and power spectra in edge plasmas. *Plasma Phys. Control. Fusion* **51**, 095004 (2009).

[143] A. Theodorsen, O. Garcia, R. Kube, B. LaBombard, and J. Terry. Relationship between frequency power spectra and intermittent, large-amplitude bursts in the Alcator C-Mod scrape-off layer. *Nucl. Fusion* **57**, 114004 (2017).

[144] A. Theodorsen, O. E. Garcia, R. Kube, B. LaBombard, and J. L. Terry. Universality of Poisson-driven plasma fluctuations in the Alcator C-Mod scrape-off layer. *Phys. Plasmas* **25**, 122309 (2018).

[145] R. Kube, A. Theodorsen, O. E. Garcia, D. Brunner, B. LaBombard, and J. L. Terry. Comparison between mirror Langmuir probe and gas-puff imaging measurements of intermittent fluctuations in the Alcator C-Mod scrape-off layer. *J. Plasma Phys.* **86**, 905860519 (2020).

[146] M. A. Pedrosa, C. Hidalgo, B. A. Carreras, R. Balbín, I. García-Cortés, D. Newman, B. van Milligen, E. Sánchez, J. Bleuel, M. Endler, S. Davies, and G. F. Matthews. Empirical Similarity of Frequency Spectra of the Edge-Plasma Fluctuations in Toroidal Magnetic-Confinement Systems. *Phys. Rev. Lett.* **82**, 3621–3624 (1999).

[147] J. P. Graves, J. Horacek, R. A. Pitts, and K. I. Hopcraft. Self-similar density turbulence in the TCV tokamak scrape-off layer. *Plasma Phys. Control. Fusion* **47**, L1–L9 (2005).

[148] O. E. Garcia, J. Horacek, R. A. Pitts, A. H. Nielsen, W. Fundamenski, J. P. Graves, V. Naulin, and J. J. Rasmussen. Interchange turbulence in the TCV scrape-off layer. *Plasma Phys. Control. Fusion* **48** , L1–L10 (2006).

[149] D. L. Toufen, Z. O. Guimarães-Filho, I. L. Caldas, F. A. Marcus, and K. W. Gentle. Turbulence driven particle transport in Texas Helimak. *Phys. Plasmas* **19**, 012307 (2012).

[150] M. Zurita, W. A. Hernandez, C. Crepaldi, F. A. C. Pereira, and Z. O. Guimarães-Filho. Stochastic modeling of plasma fluctuations with bursts and correlated noise in TCABR. *Phys. Plasmas* **29**, 052303 (2022).

[151] O. Garcia, I. Cziegler, R. Kube, B. LaBombard, and J. Terry. Burst statistics in Alcator C-Mod SOL turbulence. *J. Nucl. Mater* **438**, S180–S183 (2013).

[152] B. Labit, I. Furno, A. Fasoli, A. Diallo, S. H. Müller, G. Plyushchev, M. Podestà, and F. M. Poli. Universal Statistical Properties of Drift-Interchange Turbulence in TORPEX Plasmas. *Phys. Rev. Lett.* **98** , 255002 (2007).

[153] F. Sattin, N. Vianello, and M. Valisa. On the probability distribution function of particle density at the edge of fusion devices. *Phys. Plasmas* **11**, 5032–5037 (2004).

[154] F. Sattin, M. Agostini, P. Scarin, N. Vianello, R. Cavazzana, L. Marrelli, G. Serianni, S. J. Zweben, R. J. Maqueda, Y. Yagi, H. Sakakita, H. Koguchi, S. Kiyama, Y. Hirano, and J. L. Terry. On the statistics of edge fluctuations: comparative study between various fusion devices. *Plasma Phys. Control. Fusion* **51**, 055013 (2009).

[155] J. Cheng, L. W. Yan, W. Y. Hong, K. J. Zhao, T. Lan, J. Qian, A. D. Liu, H. L. Zhao, Y. Liu, Q. W. Yang, J. Q. Dong, X. R. Duan, and Y. Liu. Statistical characterization of blob turbulence across the separatrix in HL-2A tokamak. *Plasma Phys. Control. Fusion* **52**, 055003 (2010).

[156] M. Agostini, S. J. Zweben, R. Cavazzana, P. Scarin, G. Serianni, R. J. Maqueda, and D. P. Stotler. Study of statistical properties of edge turbulence in the National Spherical Torus Experiment with the gas puff imaging diagnostic. *Phys. Plasmas* **14**, 102305 (2007).

[157] S. J. Zweben, D. P. Stotler, J. L. Terry, B. LaBombard, M. Greenwald, M. Muterspaugh, C. S. Pitcher, K. Hallatschek, R. J. Maqueda, B. Rogers, J. L. Lowrance, V. J. Mastrocola, and G. F. Renda. Edge turbulence imaging in the Alcator C-Mod tokamaka.... *Phys. Plasmas* **9** (2002).

[158] Y. H. Xu, S. Jachmich, R. R. Weynants, and t. T. team. On the properties of turbulence intermittency in the boundary of the TEXTOR tokamak. *Plasma Phys. Control. Fusion* **47**, 1841–1855 (2005).

[159] S. K. Saha and S. Chowdhury. Intermittency in the heat and particle transports in the SINP tokamak scrape-off layer. *Phys. Plasmas* **15** , 012305 (2008).

[160] H. Tanaka, N. Ohno, N. Asakura, Y. Tsuji, H. Kawashima, S. Takamura, and Y. Uesugi. Statistical analysis of fluctuation characteristics at high- and low-field sides in L-mode SOL plasmas of JT-60U. *Nucl. Fusion* **49** , 065017 (2009).

[161] L. Wang, G. R. Tynan, R. Hong, L. Nie, Y. Chen, R. Ke, T. Wu, T. Long, P. Zheng, M. Xu, and HL-2A Team. Edge turbulence evolution and intermittency development near the density limit on the HL-2A tokamak. *Phys. Plasmas* **26**, 092303 (2019).

[162] W. Han, R. A. Pietersen, R. Villamor-Lora, M. Beveridge, N. Offeddu, T. Golfinopoulos, C. Theiler, J. L. Terry, E. S. Marmar, and I. Drori. Tracking blobs in the turbulent edge plasma of a tokamak fusion device. *Sci Rep* **12**, 18142 (2022).

[163] R. A. B. Nilsen. Conditional averaging of overlapping pulses. Master's thesis, UiT The Arctic University of Norway (2023).

[164] N. R. Campbell. The study of discontinuous phenomena. *Proc. Cambr. Phil. Soc.* **15**, 117–136 (1909).

[165] S. O. Rice. Mathematical Analysis of Random Noise. *Bell Syst. Tech. J.* **23**, 282–332 (1944).

[166] S. O. Rice. Mathematical Analysis of Random Noise. *Bell Syst. Tech. J.* **24**, 46–156 (1945).

[167] O. E. Garcia. Stochastic Modeling of Intermittent Scrape-Off Layer Plasma Fluctuations. *Phys. Rev. Lett.* **108**, 265001 (2012).

[168] O. E. Garcia and A. Theodorsen. Auto-correlation function and frequency spectrum due to a super-position of uncorrelated exponential pulses. *Phys. Plasmas* **24**, 032309 (2017).

[169] O. E. Garcia, R. Kube, A. Theodorsen, and H. L. Pécseli. Stochastic modelling of intermittent fluctuations in the scrape-off layer: Correlations, distributions, level crossings, and moment estimation. *Phys. Plasmas* **23**, 052308 (2016).

[170] L. Bondesson. On simulation from infinitely divisible distributions. *Adv. Appl. Probab.* **14**, 855–869 (1982).

[171] A. Theodorsen, O. E. Garcia, and M. Rypdal. Statistical properties of a filtered Poisson process with additive random noise: distributions, correlations and moment estimation. *Phys. Scr.* **92**, 054002 (2017).

[172] F. A. C. Pereira, I. M. Sokolov, D. L. Toufen, Z. O. Guimarães-Filho, I. L. Caldas, and K. W. Gentle. Statistical properties of intermittent bursts in the Texas Helimak. *Phys. Plasmas* **26**, 052301 (2019).

[173] W. H. Richardson. Bayesian-Based Iterative Method of Image Restoration*. *J. Opt. Soc. Am.* **62**, 55 (1972).

[174] L. B. Lucy. An iterative technique for the rectification of observed distributions. *Astron. J.* **79**, 745 (1974).

[175] F. Benvenuto, R. Zanella, L. Zanni, and M. Bertero. Nonnegative least-squares image deblurring: improved gradient projection approaches. *Inverse Probl.* **26**, 025004 (2010).

[176] J. M. Losada, A. Theodorsen, and O. E. Garcia. Stochastic modeling of blob-like plasma filaments in the scrape-off layer: Theoretical foundation. *Phys. Plasmas* **30**, 042518 (2023).

[177] F. Militello and J. Omotani. Scrape off layer profiles interpreted with filament dynamics. *Nucl. Fusion* **56**, 104004 (2016).

[178] F. Militello and J. T. Omotani. On the relation between non-exponential scrape off layer profiles and the dynamics of filaments. *Plasma Phys. Control. Fusion* **58**, 125004 (2016).

[179] F. Militello, T. Farley, K. Mukhi, N. Walkden, and J. T. Omotani. A two-dimensional statistical framework connecting thermodynamic profiles with filaments in the scrape off layer and application to experiments. *Phys. Plasmas* **25**, 056112 (2018).

[180] C. Killer, B. Shanahan, O. Grulke, M. Endler, K. Hammond, and L. Rudischhauser. Plasma filaments in the scrape-off layer of Wendelstein 7-X. *Plasma Phys. Control. Fusion* **62**, 085003 (2020).

[181] G. Decristoforo, A. Theodorsen, J. Omotani, T. Nicholas, and O. E. Garcia. Numerical turbulence simulations of intermittent fluctuations in the scrape-off layer of magnetized plasmas. *Phys. Plasmas* **28**, 072301 (2021).

Paper I:
Reconstruction of intermittent time series as a superposition of pulses

S. Ahmed, O. E. Garcia and A. Theodorsen

Physical Review E **107**, 054222 (2023),
doi:10.1103/PhysRevE.107.054222

PHYSICAL REVIEW E **107**, 054222 (2023)

Reconstruction of intermittent time series as a superposition of pulses

Sajidah Ahmed[*], Odd Erik Garcia[†] and Audun Theodorsen[‡]
Department of Physics and Technology, UiT The Arctic University of Norway, N-9037 Tromsø, Norway

(Received 29 December 2022; accepted 27 April 2023; published 31 May 2023)

Fluctuations in a vast range of physical systems can be described as a superposition of uncorrelated pulses with a fixed shape, a process commonly referred to as a (generalized) shot noise or a filtered Poisson process. In this paper, we present a systematic study of a deconvolution method to estimate the arrival times and amplitudes of the pulses from realizations of such processes. The method shows that a time series can be reconstructed for various pulse amplitude and waiting time distributions. Despite a constraint on positive-definite amplitudes, it is shown that negative amplitudes may also be reconstructed by flipping the sign of the time series. The method performs well under moderate amounts of additive noise, both white noise and colored noise having the same correlation function as the process itself. The estimation of pulse shapes from the power spectrum is accurate except for excessively broad waiting time distributions. Although the method assumes constant pulse durations, it performs well under narrowly distributed pulse durations. The most important constraint on the reconstruction is information loss, which limits the method to intermittent processes. The ratio between the sampling time and the average waiting time between pulses must be about $1/20$ or smaller for a well-sampled signal. Finally, given the system forcing, the average pulse function may be recovered. This recovery is only weakly constrained by the intermittency of the process.

DOI: 10.1103/PhysRevE.107.054222

I. INTRODUCTION

Intermittent and seemingly random fluctuations of order unity compared to the mean value are found in a variety of nonlinear physical systems, such as turbulence in neutral fluids [1–4] and atmospheric winds [5,6], water resources and hydrology [7,8], complex fluids [9], fission chambers [10], physiology [11–13] and biophysics [14], and plasma turbulence—both simulations [15–18] and measurements from magnetically confined plasmas [19–27]. While such fluctuations may be extremely challenging to investigate from first-principles-based models, many fruitfully admit phenomenological modeling. One particularly useful reference model for time-series measurements from these systems is a stochastic model based on a superposition of localized pulses [4,7–10,13,14,18,22,25]. This model is called a shot noise process [28,29] or a filtered Poisson process (FPP) [30]. If all pulses have the same functional shape and duration, the process can be written as a convolution between the pulse function (which may be considered a system response) and a random forcing. In the simplest case, the random forcing is driven by a Poisson process, giving the FPP its name.

In many cases, it is of interest to extract amplitude and waiting-time statistics of the pulses or, alternatively, the average pulse function if the forcing is known. One popular family of methods is conditional averaging [31–33], used, for example, in Refs. [2,6,20,22,34–36]. Here, an amplitude threshold is set, and each time the signal crosses above this threshold, the time and amplitude of the peak are recorded along with the shape of the signal around the peak. Different authors use slightly different methods, and to the best of our knowledge, a systematic study of conditional averaging for the statistics of overlapping pulses in single-point time series is not available, although the case for nonoverlapping structures has been investigated [33,37] as has the case for two-dimensional structures with multipoint measurements [31,38]. It is clear that both pulses overlap, and threshold requirements may influence the results and applicability of the conditional averaging method.

If the pulse function is known or may be estimated, some form of deconvolution may be performed to recover the forcing from realizations of the process. A method based on iterative deconvolution of the FPP has been shown to be robust in this problem [4,23,39]. This algorithm, referred to as the Richardson-Lucy (RL) algorithm for Poissonian noise [40,41] or the iterative space reconstruction algorithm (ISRA) for normally distributed noise [42] is not new; it was originally developed for image data in astronomy [40,41] but has seen use in several other imaging applications [42–45]. This method requires a known or estimated common pulse function for all arrivals in the time series and reproduces the forcing in the maximum-likelihood sense under normally distributed and uncorrelated additive noise.

In this paper, we estimate pulse amplitudes and arrival times from the forcing by applying an iterative deconvolution on realizations of the process. Our main aim is to report accurately on the prospects and limitations of using this procedure as a tool for time-series analysis. A wide variety of assumptions regarding pulse overlap, pulse functions, amplitude and

---

[*] sajidah.ahmed@uit.no
[†] odd.erik.garcia@uit.no
[‡] audun.theodorsen@uit.no

waiting time distributions, additive noise, and correlations between these may be made in different contexts and applications. Further, noise, pulse superposition, and distribution of pulse shapes put limits on the estimation of pulse amplitudes and arrivals. To limit the scope of this paper, we will focus on assumptions relevant for time-series measurements in turbulent fluids and plasmas, and, in particular, at the boundary of magnetically confined fusion plasmas which are characterized by broad and positive definite amplitude distributions, close to Poisson distributed arrivals and asymmetric, positive, and exponentially decaying pulses [20–27,34,35,39].

We note that the deconvolution algorithm may also be used the other way around: If the forcing is known, the pulse function may be estimated using the same algorithm. In this way, it may be used to find the system response to a controlled input forcing, if the assumption of linearity is satisfied.

This contribution is structured as follows: In Sec. II, we review the stochastic model, define the base case of the model which will be modified during the following investigations, and present the deconvolution algorithm. In Sec. III, the limitations of the signal reconstruction from estimated amplitudes and arrival times due to sampling and pulse overlap are investigated. In Sec. IV, we assess the ability of the algorithm to reproduce various amplitude and arrival times for a known pulse function. Then, in Sec. V distortions due to additive noise, both uncorrelated and correlated, are investigated and a criterion for noise removal is established. Following this, in Sec. VI we report on the effect of estimating the pulse shape assuming a known functional form. Both the effects of over- and underestimating the pulse duration are considered, as well as the effect of a narrow distribution of pulse durations. Lastly, we turn the question around in Sec. VII and look at how well an unknown pulse function can be estimated if the pulse arrivals and amplitudes are known. Finally, we discuss the results and conclude in Sec. VIII. In this contribution, we will not consider the effects of statistical convergence: we will always use long time series to avoid large uncertainty or bias in parameter estimates and will always run the deconvolution algorithm to convergence. Effects of short time series on moment estimation were previously investigated in Refs. [46,47]. Sections III–VII are largely independent; the reader may consult the problem of particular interest. The numerical implementation of this method with its library of functions is openly available on the GitHub page of the UiT Complex Systems Modelling group [48].

II. THEORY

In this section, we first review the stochastic model given by a superposition of pulses with fixed shape and duration. This is followed by a presentation of the deconvolution algorithm. The section concludes by discussing how pulse amplitudes and arrival times can be recovered from realizations of the stochastic process using the deconvolution algorithm. Throughout this paper, we adopt the notation that angular brackets $\langle\cdot\rangle$ refer to a theoretical mean value, while an overline $\bar{\cdot}$ refers to a sample mean. Quantities estimated by the deconvolution method use the est-subscript $\cdot_{\text{est}}$.

A. The stochastic model

The basic stochastic model considered here is a superposition of pulses with a fixed shape defined as

$$\Phi_K(t) = \sum_{k=1}^{K(T)} A_k \varphi\left(\frac{t - s_k}{\tau_k}\right). \tag{1}$$

Here, $K(T)$ denotes a point process on the interval $[0, T)$ with sorted event arrival times s_k and waiting times $w_k = s_k - s_{k-1}$ with mean value $\langle w\rangle$. We will, in general, restrict $K(T)$ to be a *renewal* process, where the waiting times are independently and identically distributed [30]. The amplitudes A_k are randomly distributed with mean value $\langle A\rangle$ and, in general, assumed to be positive definite. The pulse function φ is assumed to be the same for all events but may have randomly distributed duration times τ_k. The average pulse duration time is denoted by $\tau_\text{d} = \langle\tau\rangle$. In the following, we take all A_k, w_k, and τ_k to be independent random variables, and each variable family is independently and identically distributed.

The fundamental parameter of the stochastic model is $\gamma = \tau_\text{d}/\langle w\rangle$, referred to as the *intermittency parameter*. It describes the degree of pulse overlap and quantifies how intermittent the fluctuations are through the skewness and flatness moments [49]. In general, the influence of γ on the qualitative appearance and features of the process is the following: For γ of order unity or smaller, pulses appear well separated due to the waiting times between pulses being long compared to the duration time. When $\gamma < 1$, the process Φ will thus have a small mean value compared to the mean pulse amplitude and large relative fluctuation levels. For γ much larger than one, there is a significant pulse overlap due to short waiting times and long pulse durations. This results in a process that is near normal distributed, where Φ will have a large mean value and small relative fluctuation levels [49]. In Sec. III, we will see that it is not the intermittency parameter which determines our ability to estimate the amplitudes and arrival times of the process but the ratio between the sampling time and the average waiting time. We write this ratio as $\gamma\theta$, where $\theta = \triangle_t/\tau_\text{d}$ is the sampling time $\triangle_t$ normalized by the average pulse duration.

Here, some care must be taken regarding the sampling process. If we consider a sampling method which instantaneously measures a value at regular intervals, pulses which are only a few sampling times in duration may be undersampled, such that the true amplitude of the pulse is not captured. Thus, the process may contain an artificially low number of pulses or have an artificially low mean value compared to an adequately sampled process. If the sampling time is an *integration time* such as a camera exposure time, all pulses will be identified. However, there may be distortions in the pulse shape due to the integration, as the integration smears out the pulse function. In either case, the deconvolution method described in Sec. II B reproduces the *sampled* time series and is not designed to make inferences regarding missing or distorted pulses. Thus, an accurate reconstruction of the true process also depends on a sufficiently high sampling rate to resolve the pulses. Our testing suggests that for the exponential pulse function in Eq. (2) (below), a sampling time of ten times the typical pulse duration time or better is sufficient, that is, $\triangle_t/\tau_\mathrm{d} \leqslant 10^{-1}$.

We take the following as the *base case*:

(1) $K(T)$ is a Poisson process. Therefore, it follows that the arrival times are independent and uniformly distributed on the interval $[0, T)$, and the waiting times $w_k = s_k - s_{k-1}$ are independently and exponentially distributed with mean value $\langle w\rangle$ [30]. The mean value of the Poisson process is then given by $\langle K(T)\rangle = T/\langle w\rangle$.

(2) Degenerate distribution of pulse durations, $\tau_\mathrm{d} P_\tau(\tau) = \delta(\tau - \tau_\mathrm{d})$, so all pulses have the same duration, $\tau_k = \tau_\mathrm{d}$.

(3) Fixed one-sided exponential pulse function for all events given by a jump followed by an exponential decay:

$$\varphi(x) = \begin{cases} 0, & x < 0 \\ \exp(-x), & x \geqslant 0. \end{cases} \tag{2}$$

(4) Exponentially distributed amplitudes with mean value $\langle A\rangle$, $\langle A\rangle P_A(A) = \exp\left(-A/\langle A\rangle\right)$ for $A > 0$.

Some consequences of this base case are of interest [49–52]:

(1) The probability distribution function (PDF) of Φ is a gamma distribution with shape parameter $\gamma = \tau_\mathrm{d}/\langle w\rangle$ and scale parameter $\langle A\rangle$:

$$P_\Phi(\Phi;\gamma,\langle A\rangle) = \frac{\Phi^{\gamma-1}}{\langle A\rangle^\gamma\Gamma(\gamma)}\exp\left(-\frac{\Phi}{\langle A\rangle}\right), \quad \Phi > 0. \tag{3}$$

(2) The four lowest order moments are the mean $\langle\Phi\rangle = \gamma\langle A\rangle$, variance $\Phi_\mathrm{rms}^2 = \gamma\langle A\rangle^2$, skewness $S_\Phi = \langle(\Phi - \langle\Phi\rangle)^3\rangle/\Phi_\mathrm{rms}^3 = 2/\sqrt{\gamma}$, and flatness (or excess kurtosis) $F_\Phi = \langle(\Phi - \langle\Phi\rangle)^4\rangle/\Phi_\mathrm{rms}^4 - 3 = K_\Phi - 3 = 6/\gamma$, where K_Φ is the kurtosis.

(3) The frequency power spectral density (PSD) of Φ has a Lorentzian shape:

$$\Omega_\Phi(\omega) = \Phi_\mathrm{rms}^2\frac{2\tau_\mathrm{d}}{1 + \tau_\mathrm{d}^2\omega^2} + 2\pi\langle\Phi\rangle^2\delta(\omega). \tag{4}$$

In the base case, there are three fundamental model parameters: γ, $\langle A\rangle$, and τ_d. From realizations of the process, the first two may be estimated from the PDF given by Eq. (3). From this follows the mean value and standard deviation of the process. The final parameter τ_d may be estimated from the autocorrelation function or from the frequency PSD given by Eq. (4).

In the case that all pulses have the same duration τ_d, we may express the stochastic model as a convolution between the pulse function φ and a forcing f_K,

$$\Phi_K(t) = [\varphi * f_K]\left(\frac{t}{\tau_\mathrm{d}}\right), \tag{5}$$

where f_K is given by

$$f_K(t) = \sum_{k=1}^{K(T)} A_k\delta\left(\frac{t - s_k}{\tau_\mathrm{d}}\right). \tag{6}$$

Hence, one can say that Φ_K is a train of delta pulses, given by f_K, arriving according to the point process $K(T)$ which is passed through a filter φ. The FPP may be considered a linear model for highly nonlinear phenomena, where the nonlinearity has been baked into the distributions of A and s and the pulse function φ. Given an estimate of the pulse function, it is therefore possible to estimate f_K by deconvolving a realization Φ_K with the pulse function φ. Further discussions on estimation of model parameters from realizations of the process are given in Refs. [39,46,47,50].

B. Deconvolution method

To estimate the pulse arrival times s_k and amplitudes A_k from realizations of the stochastic process, the "iterative image space reconstruction algorithm" (ISRA), is presented in Ref. [42], and we point the reader to this publication for a more thorough discussion of the details of the algorithm. Here, we consider Φ, φ, and f to be discretized with a uniform sampling time $\triangle_t$ and an odd number of data points N. Furthermore, Φ is assumed to be corrupted by uncorrelated white noise denoted X, so we may write for $0 \leqslant j < N$,

$$\Phi_j = (\varphi * f)_j + X_j, \tag{7}$$

where f_j is a sum of Kronecker deltas weighted by the pulse amplitudes, $f_j = \sum_{k=1}^{K(T)} A_k\delta_{j,j_k}$, and by abuse of notation $\varphi_j = \varphi(j\triangle_t/\tau_\mathrm{d})$. We have suppressed the subscript K on Φ and f for simplicity of notation and j_k is $s_k/\triangle_t$ rounded to the nearest integer. In the following, the hat symbol $\widehat{\cdot}$ is used to denote a flipped vector, $\widehat{\varphi}_j = \varphi_{N-1-j}$.

The maximum-likelihood estimation applied to the above model leads to the optimization problem

$$J_\Phi(f) = \tfrac{1}{2}\|\varphi * f - \Phi\|^2 \tag{8}$$

$$\text{subject to } f \geqslant 0. \tag{9}$$

The iteration scheme

$$f_j^{(n+1)} = f_j^{(n)}\frac{(\Phi * \widehat{\varphi})_j + b}{(f^{(n)} * \varphi * \widehat{\varphi})_j + b} \tag{10}$$

is known to converge asymptotically to the least-squares solution of the optimization problem under certain conditions on φ [42]. For our purposes, $\varphi(t) \geqslant 0$ and $\varphi(t = 0) > 0$ are sufficient conditions. Here, b is a free parameter chosen such that $(\Phi * \widehat{\varphi})_j + b > 0\,\forall\, j$. The method is designed to extract a *non-negative* signal f from a measurement described by Eq. (7), where the *only* negative parts of the signal are due to noise. The effect of negative pulse amplitudes is explored in Sec. IV. We note that the standard deviation of the noise X, or alternatively the signal-to-noise ratio, plays no role in the iteration scheme.

Numerical testing reveals that the choice of the initial guess $f^{(0)}$ as well as the exact value of b may play a role in the rate of convergence but do not affect the result of the iteration given by Eq. (10) if b is small compared to the mean signal value. Consequently, we set the initial guess to a positive constant and the b parameter to $b = 10^{-10} - b_\mathrm{min}$, where $b_\mathrm{min} = \min[0, \min(\Phi * \hat{\varphi})]$. The small constant 10^{-10} is added to avoid issues with the division of numbers close to zero in the denominator in Eq. (10).

C. Extracting amplitudes and arrival times

The result of the deconvolution is the maximum-likelihood estimate of the forcing, denoted f_res, where the subscript $\cdot_\mathrm{res}$

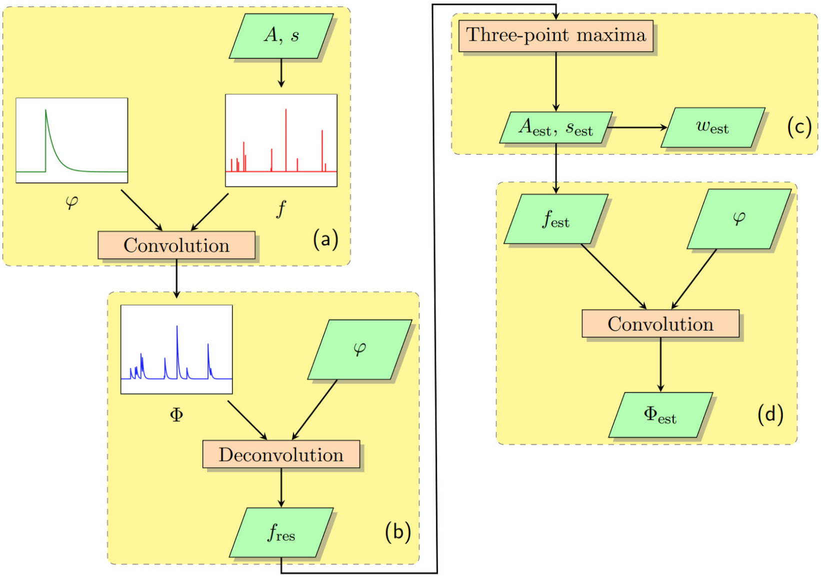

FIG. 1. Flow chart to show the procedure applied in this study of the deconvolution algorithm. The flow chart is detailed in the main text. For experimental data, the processes in (b)–(d) would be applied. In this contribution, the focus is on the effect of (c) and (d).

stands for result. In this paper, we are interested in estimating the amplitudes and arrival times that define the forcing f. For the realizations investigated in this paper, the delta-train forcing is estimated as a series of sharply localized peaks. Therefore, a peak-finding algorithm must be applied to recover the pulse arrival times and amplitudes. We have chosen to employ a simple three-point running maxima, so a data point $f_{\mathrm{res},j}$ is classified as a peak if it is larger than both neighboring points: $f_{\mathrm{res},j} > f_{\mathrm{res},j\pm1}$ for all $1 \leqslant j < N - 1$. The estimated arrival time s_{est} is the location of the maxima and the estimated amplitude A_{est} is the value of the maxima.

Using the found maxima directly leads to far too many detected events for small ($\gamma < 1$) intermittency parameters (six times the true number of events for $\gamma = 1/10$). This is due to numerical noise in sections of f_{res} without true pulses. To remove these spurious pulses, we introduce a small amplitude threshold equal to $10^{-2}\langle A\rangle$, which corresponds to the size of $|f_{\mathrm{res}} - f|$ for $\gamma = 1/10$. The presence of this threshold does not influence the results in the absence of additive noise, as investigated below. In the presence of additive noise, a stricter amplitude threshold is placed on local maxima. This amplitude threshold is discussed further in Sec. V.

The entire reconstruction process is described by the flow diagram in Fig. 1. In Fig. 1(a), the synthetic signal Φ is generated. The waiting times w are randomly drawn until their sum exceeds the specified signal duration T. The arrival times s are computed from the waiting times, and a number of amplitudes A matching the arrival times are randomly drawn. The synthetically generated forcing f consists of the amplitudes A and the arrival times s, and convolving this forcing with the specified pulse function φ gives the synthetic signal Φ. In Fig. 1(b), we perform the ISRA specified in Eq. (10), where f_{res} is the result of the deconvolution. Here, it may be necessary to estimate φ, for example, from the PSD as discussed in Sec. VI. In Fig. 1(c), A_{est}, s_{est}, and w_{est} refer to the amplitudes, arrival times, and waiting times extracted using the three-point maxima method described above. Finally, in Fig. 1(d), the signal is reconstructed. Here, f_{est} refers to forcing which consists of A_{est} and s_{est}. Φ_{est} refers to the signal reconstructed by using the estimated amplitudes and arrival times. For the model realizations considered in this paper, it will be shown that the process in Fig. 1(b) captures f very well. Thus, the focus of this contribution is the prospects and limitations of Figs. 1(c) and 1(d).

To check that the mean values of the estimated variables have converged, we employ a bootstrapping technique [53]. For a given data set X containing N samples, we first estimate the sample mean $\overline{X}$. Then we draw $3N/4$ random samples with replacement (that is, we are allowed to draw the same sample multiple times) and estimate the sample mean $\overline{X}_{3N/4}$. Repeating this procedure 100 times gives a data set containing 100 samples of $\overline{X}_{3N/4}$. Estimating the standard deviation of this data set gives a measure of how well $\overline{X}$ has converged. A large standard deviation would indicate that we have too few samples N, and should repeat our estimate with a larger data set. We chose $3N/4$ samples instead of N for the random draw to err on the side of overestimating the standard deviation. Estimates for higher moments proceed analogously. In all cases, this produced standard deviations within 6% of the corresponding mean values, indicating well-converged statistics.

Since the parameter values (in particular γ) are varied over an order of magnitude, we report the bias in the estimate as the *ratio* between the estimated value and the true value instead of the more common *difference* between the estimated value

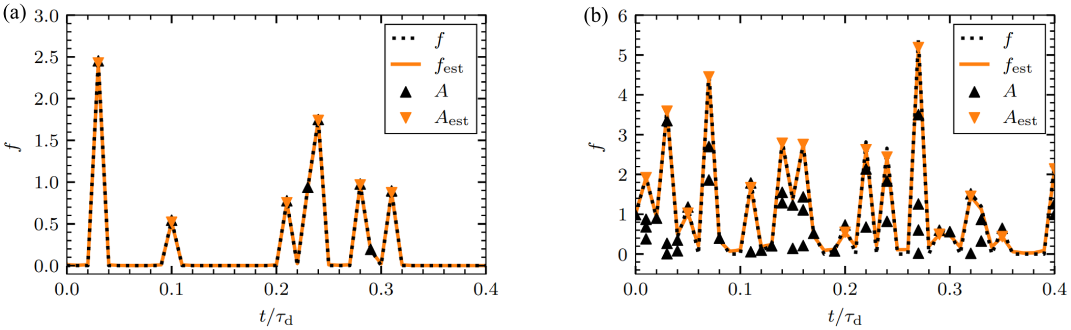

FIG. 2. Comparison between original forcing f and the estimated forcing $f_{\rm est}$ for two different intermittency parameters, (a) $\gamma = 10$ and (b) $\gamma = 10^2$, no noise $X = 0$, exponentially distributed pulse amplitudes, and a normalized sampling time of $\triangle_t/\tau_{\rm d} = 10^{-2}$. The exponential pulses are uncorrelated and have a uniform distribution of arrival times. The markers denote the original amplitudes A and the estimated amplitudes $A_{\rm est}$.

and the true value. This lets us compare estimates for different input parameters directly. In this contribution, a deviation of more than 10% from the true value is considered significant and is indicated with *italic* numbers in the tables. This will be the basis for our discussion of the results.

III. ESTIMATING AMPLITUDES AND WAITING TIMES

Two effects lead to loss of information of the true pulse arrivals in realizations of the process: (1) The point process $K(T)$ is continuous but, as we are working with discrete time series, pulses closer than a sampling time cannot be separated. These will be counted as one pulse arrival with amplitude equal to the sum of their amplitudes, corrupting the resulting estimated amplitude distribution and number of pulses. (2) As the peaks of $f_{\rm est}$ may have finite widths, a peak-finding algorithm must be employed. A straightforward and permissive method, a three-point maxima, compares each data point to its neighboring points and flags it as a peak if it is bigger than both neighbors. This method retains only the highest amplitude event if two or more pulses arrive closer than two sampling times to each other.

In Appendix A, it is shown that in the base case, the average number of three-point maxima M in f as compared to the average number of pulses $\langle K\rangle$ is given approximately by

$$\frac{\langle M\rangle}{\langle K\rangle} \approx \frac{1-\exp(-3\gamma\theta)}{3\gamma\theta}. \tag{11}$$

Here, $\theta = \triangle_t/\tau_{\rm d}$ is the normalized sampling time and $\gamma\theta = \triangle_t/\langle w\rangle$. To recover approximately 90% of the pulses using the three-point maxima, $\gamma\theta < 0.075$ is necessary, while to recover approximately 95% of the pulses, $\gamma\theta < 0.035$ is necessary. This suggests an approximate threshold of $\gamma\theta \leqslant 1/20$ to recover most (above 90%) of the pulses. In this paper, we have set $\triangle_t = 10^{-2}\tau_{\rm d}$, leading to an assumed approximate condition $\gamma < 5$ for reconstruction of amplitude and arrival time distributions within 10% variation in average values. We will see that, in general, $\gamma = 10$ gives too much overlap while, in some cases, $\gamma \leqslant 1$ is required, which corresponds to approximately 98.5% pulse recovery. This threshold should be seen as a guideline, dependent on the precision and objectives required for application of the method.

The sampling and local maxima issues are illustrated in Fig. 2, which shows results from deconvolution for fixed θ

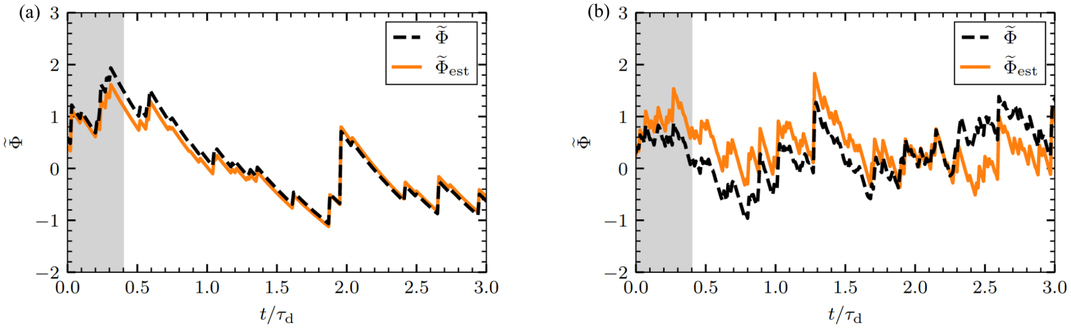

FIG. 3. Comparison between normalized original time series $\widetilde{\Phi}(t)$ and the normalized reconstructed time series $\widetilde{\Phi}_{\rm est}(t)$ for two different intermittency parameters, (a) $\gamma = 10$ and (b) $\gamma = 10^2$, using amplitudes and arrival times estimated with the deconvolution method. The forcing for the first 0.4 normalized time units is presented in Fig. 2 and is gray shaded here.

TABLE I. Table showing the sample moments of the reconstructed time series for various intermittency parameters γ as compared to the sample moments of the model realization. 10^5 iterations were used for parameters $\theta = 10^{-2}$, $T/\tau_d = 10^4$ and no noise was added. The theoretical expressions for the moments are given directly below Eq. (3).

	Moments			
γ	$\overline{\Phi}_{\text{est}}/\overline{\Phi}$	$\Phi^2_{\text{rms,est}}/\Phi^2_{\text{rms}}$	$S_{\Phi,\text{est}}/S_\Phi$	$(F_{\Phi,\text{est}}-3)/(F_\Phi-3)$
10^{-1}	1.00	0.99	1.00	1.00
1	0.99	0.97	0.99	0.99
5	0.97	0.94	0.99	0.97
10	0.94	*0.78*	0.98	0.94
50	*0.78*	*0.60*	1.02	*0.58*
10^2	*0.68*	*0.50*	*1.13*	*1.32*

and two different values of γ. Although the estimated forcing (the orange solid line) is a good approximation of the original forcing signal (the black dotted line), even for $\gamma = 10^2$, the same cannot be said of the estimated amplitudes (the orange triangles) when compared to the original amplitudes (the black triangles). In the case of $\gamma = 10$, the error is moderate and mainly caused by the three-point maxima not identifying arrivals at neighboring points. The effect is more severe in the case $\gamma = 10^2$, where it is evident that f_{est} is given by a superposition of multiple arrivals closer than one time step of each other.

The corresponding original and reconstructed time series are presented in Fig. 3 for one-sided exponential pulses and an exponential pulse amplitude distribution. Here and in the following, $\widetilde{\Phi}$ denotes the normalized variable $\widetilde{\Phi} = (\Phi - \langle\Phi\rangle)/\Phi_{\text{rms}}$. For these high γ values, the FPP resembles a normally distributed process. The reconstructed signal largely follows the overall path of the original signal but deviates in detail due to finite sampling rate and pulse overlap as described above. These differences may have a profound influence on the estimation of the amplitude and waiting time statistics, as investigated in detail below.

In Table I, the first four moments as estimated from the reconstructed time series are presented for various values of the intermittency parameter. The estimated moments are normalized by the sample moments of the original time series. In all cases, one-sided exponential pulses with an exponential amplitude distribution are used. For $\gamma \leqslant 5$, there is at most 6% disagreement between the estimated and sample moments, within our allowed tolerance. For $\gamma \geqslant 10$, both the mean value and standard deviation are underestimated, with values below the 10% threshold. The underestimation is worse for larger intermittency parameters. Higher-order moments are wrongly estimated for $\gamma \geqslant 50$, as evidenced by the three values in the lower right-hand corner of the table. Thus, we conclude that Table I provides evidence for the condition $\gamma\theta \leqslant 1/20$ for accurate reconstruction.

The deviation in the first two moments may be explained by the following: Due to pulse overlap and the three-point maxima, several true events are discounted. This leads to an underestimation of the mean value and the standard deviation, more severely for higher intermittency parameters. As the discounted events are preferentially small, the small-amplitude variations are decreased, leading to a lower overall rms-level of the signal. By taking the square root of the second column and dividing it by the first column, it is seen that the relative fluctuation level, however, is robust. The deviations in the higher moments are less systematic and a Monte Carlo study should be carried out to put reasonable error bars on these values. The important conclusion from this table is that it supports the approximate condition $\gamma\theta \leqslant 1/20$ and therefore a time-consuming Monte Carlo study for the largest intermittency parameters has not been performed here.

The effects of varying the sampling time are presented in Figs. 4 and 5. Here we keep $\gamma = 1$ fixed for various values of θ. In these figures, a realization of the FPP with normalized sampling time $\theta = 10^{-3}$ was downsampled by using only a portion of the data points in the time series. The downsampled signals were then deconvolved with a similarly downsampled pulse function, and the signals were reconstructed. In Fig. 4, the estimated forcing is presented. As expected, increasing the sampling time leads to fewer arrivals identified as not all pulses can be separated. The result is similar to the effect of keeping θ fixed and increasing γ, as expected from the theoretical prediction presented in Appendix A.

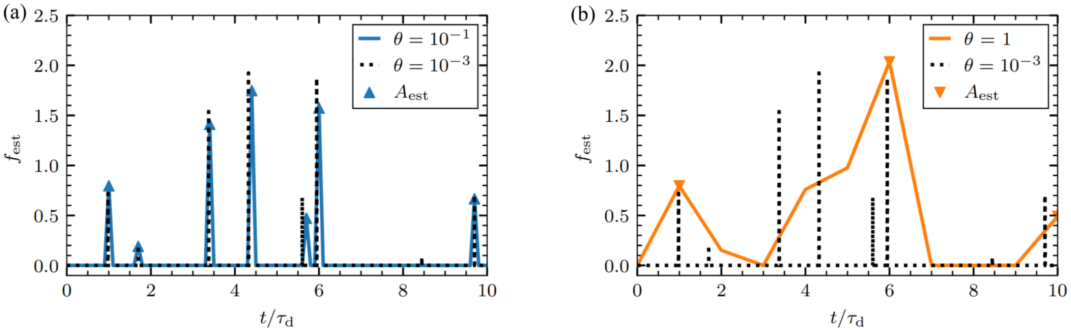

FIG. 4. Estimated forcing f_{est} (solid line) and estimated amplitudes (markers) for $\gamma = 1$ and two different normalized sampling times, (a) $\theta = 10^{-1}$ and (b) $\theta = 1$. The original forcing (black dotted line) with $\theta = 10^{-3}$ is shown for comparison.

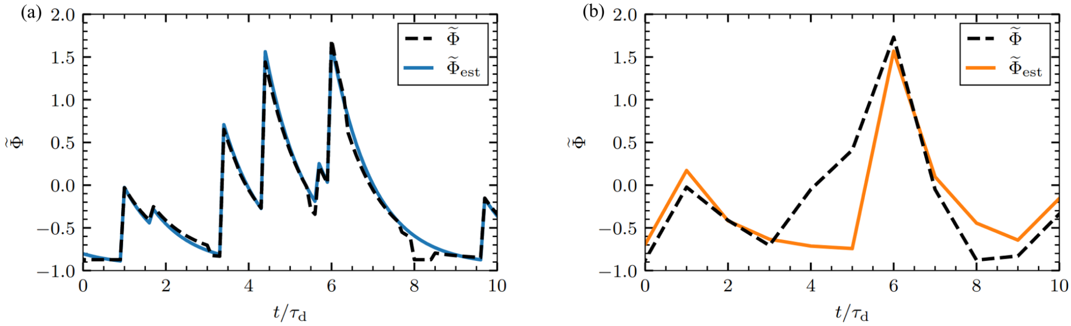

FIG. 5. Comparison between reconstructed time series using the estimated amplitudes and arrival times (solid line) and downsampled original signals (dashed line) for $\gamma = 1$ and two different normalized sampling times, (a) $\theta = 10^{-1}$ and (b) $\theta = 1$.

In Fig. 5, the reconstructed signals are compared to the downsampled original time series without noise, $X = 0$. Note that the downsampled time series with $\theta = 10^{-1}$ is here visually similar to the original time series with $\theta = 10^{-3}$. The reconstruction is reasonable, even for $\theta = 1$, when compared to the downsampled signal. However, while the amplitudes and arrival times might be reasonably estimated in the case $\theta = 10^{-1}$, this is obviously not possible in the case $\theta = 1$, as expected.

IV. AMPLITUDE AND WAITING TIME DISTRIBUTIONS

In this section, we investigate the ability of the deconvolution algorithm to reconstruct the amplitude and waiting time distributions for the case where the pulse function is known. In all the following cases, we use $\theta = 10^{-2}$, $T/\tau_{\mathrm{d}} = 10^4$ and we have not added any noise term. For this value of the sampling time, the condition $\gamma\theta \leqslant 1/20$ becomes $\gamma \leqslant 5$. The deconvolution ran for 10^5 iterations, leading to convergence for $\gamma < 10$ and marginal convergence for $\gamma \geqslant 10$.

A. Base case

First, we consider the effects of varying γ in the base case on the estimated amplitude and waiting time distributions from the deconvolved forcing. The plot symbols used for various intermittency parameters are presented in Fig. 6. The resulting distributions are presented in Fig. 7 and the estimated parameters are presented in Table II. Here, the found number of maxima, the estimated average amplitudes, and the estimated average waiting times are compared to the theoretical number of maxima in Eq. (A6) and the theoretical mean values of the process. In the figures, the distributions are well estimated for $\gamma \leqslant 10$, while the mean values are within 10% of their theoretic values for $\gamma \leqslant 5$. The expected number of maxima is well estimated by Eq. (A6).

For $\gamma = 50$, the mean amplitude and waiting time are significantly overestimated compared to the other cases. For the amplitudes, this effect is mainly due to multiple events being added as a result of being closer than a sampling time. The resulting distribution has a shallower slope and is more concave when compared to the original distribution. For the waiting times, a significant number of true waiting times are below one sampling time (the probability $\Pr[w < \theta] \approx 0.39$ for $\gamma = 50$). As the smallest waiting time resolvable by the deconvolution method is 2θ, this introduces a cutoff in the estimated distribution which increases the mean value of the estimated waiting times. Moreover, the waiting times only take values that are low-integer multiples of the sampling time. For consistency between different values of the intermittency parameter, we use the same bins for all distributions shown in these figures, chosen such that each bin contains a single integer multiple of the sampling time in the $\gamma = 50$ case. Although it is elevated, due to discounting the shortest waiting times, the distribution for $\gamma = 50$ decays with the same slope as the original distribution.

In the following, we will investigate the robustness of the method to nonexponential amplitude and waiting time distributions. We have chosen to test the Rayleigh distribution due to its Gaussian tail, the Pareto distribution as an example of a much broader distribution than the exponential, the uniform distribution for its discontinuous cutoff toward large values, and the extreme case of the degenerate distribution. Definitions of these distributions are presented in Appendix B.

B. Amplitude distributions

In Fig. 8, we present the amplitude distributions estimated from the deconvolution procedure for various pulse amplitude distributions and exponentially distributed waiting times. In all cases, the different symbols denote the estimated distributions corresponding to the intermittency parameter values given in Fig. 6. The black dashed line gives the analytical

γ	10^{-1}	1	5	10	50
Symbol	▼	♦	●	■	▲

FIG. 6. List of plot symbols for various intermittency parameters used for estimating pulse amplitude and waiting time statistics.

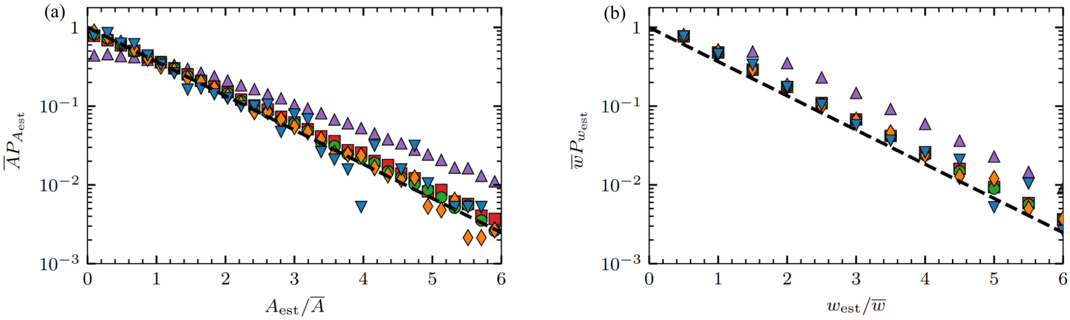

FIG. 7. Probability distributions of (a) estimated amplitudes and (b) estimated waiting times for various intermittency parameters in the base case with exponentially distributed pulse amplitudes and waiting times. In both cases, the distributions are normalized by the original sample mean values. The plot symbols are defined in Fig. 6.

distributions. Note that the Rayleigh distribution is presented with a semilogarithmic scale, the Pareto distribution is presented with a double-logarithmic scale, and the uniform and degenerate distributions are presented with a linear scale, with a semilogarithmic scale in the inset. Table III aggregates mean values for the distributions in Fig. 8.

We see that all distributions are well estimated for $\gamma \leqslant 1$. The estimates for Rayleigh distributed amplitudes are visibly affected by pulse overlap for $\gamma \geqslant 5$, showing elevated and close to exponential tails for large amplitudes. Pareto-distributed amplitudes are reliably identified for all tested intermittency parameters, likely due to the large range of probable values leading to little distortion due to pulse overlap. For uniformly distributed amplitudes, it is clear from the inset of Fig. 8(c) that while the implications of pulse overlap are visible even for $\gamma = 1$, there is a jump of order 10^{-2} from the originally allowed values to the larger values. As a consequence, the uniform distribution is well estimated and within the variation around the straight line expected for the uniform distribution. For a degenerate distribution of pulse amplitudes, the main contribution to the estimated amplitude distribution is the expected delta peak, with corrections at higher integer values, as seen in the inset. Only for $\gamma = 50$ is there a significant contribution of normalized amplitudes larger than two and for noninteger amplitudes.

TABLE II. Ratio of (top) number of maxima in the forcing estimated from the deconvolution to the theoretical number of maxima, (middle) mean estimated amplitudes to the original sample mean, and (bottom) mean estimated waiting times to the original sample waiting times. Results are from the base case and for various intermittency parameters. The corresponding distributions are presented in Fig. 7.

	Estimated averages	γ				
		10^{-1}	1	5	10	50
	$M/\langle M\rangle$	1.02	1.01	0.98	0.98	0.95
$A \sim$ exponential	$\overline{A}_{\mathrm{est}}/\overline{A}$	1.01	1.02	1.06	*1.11*	*1.58*
$w \sim$ exponential	$\overline{w}_{\mathrm{est}}/\overline{w}$	1.01	1.03	1.10	*1.19*	*2.03*

In Table III, the number of found maxima is very close to the expected number corrected by effects of discretization and taking the three-point maxima, as discussed in Sec. III. This distortion is reflected in the deviation of the average estimated waiting time from the theoretical waiting time. There is only a small effect on the average amplitudes for $\gamma \leqslant 10$, irrespective of amplitude distribution.

C. Waiting time distributions

Realizations of the process have also been made for various pulse waiting time distributions and intermittency parameters, with an exponential amplitude distribution in all cases. The estimated waiting time distributions from deconvolution of these realizations are presented in Fig. 9 and mean amplitudes and waiting times as well as the number of maxima in the forcing are presented in Table IV. For $\gamma \leqslant 10$, all distributions show agreement with the true distribution for low ($w_{\mathrm{est}} < 3\overline{w}$)

TABLE III. In each row: Ratio of (top) found number of maxima in the forcing estimated from the deconvolution to the theoretical number of maxima, (middle) mean estimated amplitudes to the original sample mean, and (bottom) mean estimated waiting times to the original sample waiting times. Results are for the various amplitude distributions used in Fig. 8, exponentially distributed waiting times, and for various intermittency parameters.

P_A	Estimated averages	γ				
		10^{-1}	1	5	10	50
Rayleigh	$M/\langle M\rangle$	1.03	1.02	1.00	1.00	0.99
	$\overline{A}_{\mathrm{est}}/\overline{A}$	1.00	1.01	1.03	1.07	*1.41*
	$\overline{w}_{\mathrm{est}}/\overline{w}$	1.00	1.02	1.08	*1.16*	*1.95*
Pareto(3)	$M/\langle M\rangle$	1.03	1.02	1.00	1.00	0.99
	$\overline{A}_{\mathrm{est}}/\overline{A}$	1.00	1.01	1.03	1.07	*1.45*
	$\overline{w}_{\mathrm{est}}/\overline{w}$	1.00	1.02	1.08	*1.16*	*1.95*
$\mathcal{U}(0, 2)$	$M/\langle M\rangle$	1.02	1.01	0.99	0.99	0.97
	$\overline{A}_{\mathrm{est}}/\overline{A}$	1.00	1.01	1.04	1.08	*1.46*
	$\overline{w}_{\mathrm{est}}/\overline{w}$	1.01	1.03	1.09	*1.17*	*1.99*
Degenerate	$M/\langle M\rangle$	1.03	1.02	1.00	1.00	0.96
	$\overline{A}_{\mathrm{est}}/\overline{A}$	1.00	1.00	1.02	1.04	*1.32*
	$\overline{w}_{\mathrm{est}}/\overline{w}$	1.00	1.02	1.08	*1.16*	*2.01*

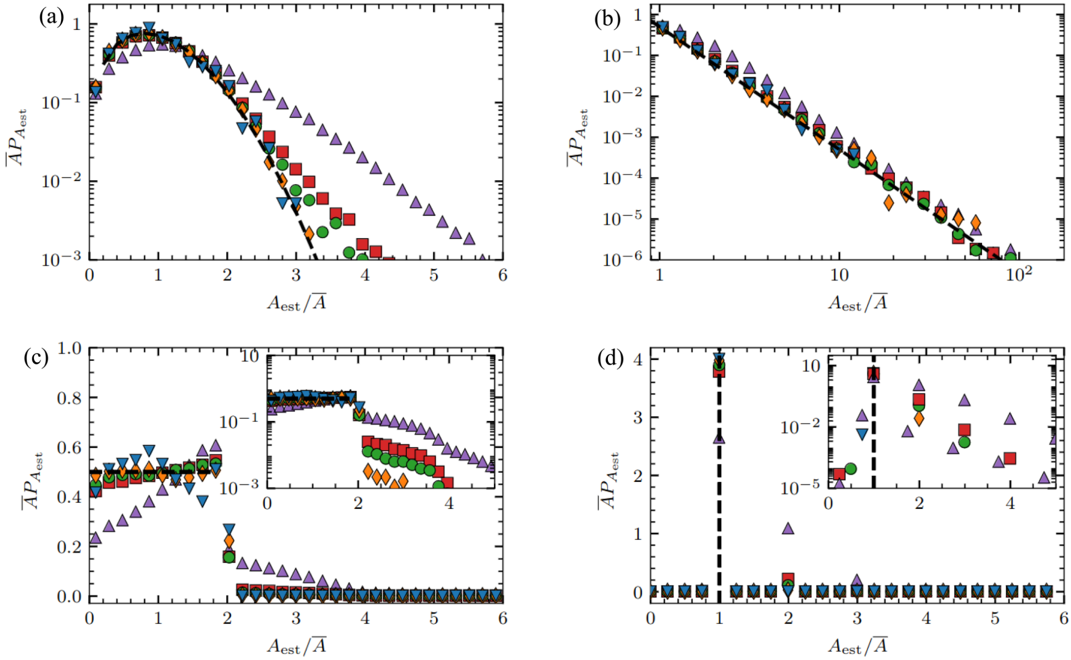

FIG. 8. Probability distributions of estimated pulse amplitudes normalized by the sample mean amplitude for various intermittency parameters and distributions of pulse amplitudes in realizations of the process. (a) $A \sim$ Rayleigh, (b) $A \sim$ Pareto(3), (c) $A \sim \mathcal{U}(0, 2)$, and (d) $A \sim$ degenerate. The insets in (c) and (d) show the distributions with semilogarithmic scaling. In all cases, exponentially distributed waiting times were used. The black dashed lines represent the analytical amplitude distribution of the various realizations. The plot symbols are defined in Fig. 6.

waiting times. The mean amplitudes and waiting times are well estimated for $\gamma \leqslant 10$, the largest deviation being a factor 1.11 increase for uniformly distributed waiting times and $\gamma = 10$.

Rayleigh distributed waiting times display an elevated, exponential-like tail toward large values. Despite this, the mean values are better estimated than in the base case, possibly due to the clear peak of the Rayleigh distribution, ensuring most events are well separated. The distortion to the Rayleigh distribution for $\gamma = 50$ follows the pattern seen for exponentially distributed waiting times, as discussed in the introduction to Sec. IV. Again, we have chosen bins such that each bin contains one integer multiple of the sampling time in the case $\gamma = 50$. We see that the tail of the distribution is elevated with respect to the original Rayleigh distribution and with respect to the lower γ cases. The inflated mean values in Table IV are due to the loss of waiting times shorter than two time steps and corresponding enhanced pulse overlap.

Pareto-distributed waiting times are identified in all cases, and the corresponding mean amplitudes and waiting times are almost perfectly estimated. This is due to pulse overlap not being a factor, even at these high intermittency levels: For $w \sim$ Pareto(3), there is a cutoff $w/\tau_{\rm d} \geqslant 1/2\gamma$, see Appendix B. With $\theta = 10^{-2}$, $\gamma = 50$ corresponds to a minimal waiting time of two data points. There is an arrival at least every second data point, and this can just about be resolved by the three-point maxima. A higher γ would result in an artificial cutoff in the same manner as for the Rayleigh distributed waiting times.

For the degenerate distribution, $\theta = 10^{-2}$ and $\gamma = 50$ corresponds to a (degenerate) waiting time of two data points, again just at the edge of resolvability. Here, the (small) probability of larger waiting times is likely due to very small amplitudes not being picked up by the deconvolution or being removed by the 10^{-2} numerical noise threshold. As seen in Table IV, this has some effect on the average waiting time, but hardly any effect on the average amplitudes.

For the uniform distribution, the deconvolution cutoff $w/\overline{w} \approx w/\langle w \rangle \geqslant 2\Delta_t/\langle w \rangle = 2\theta\gamma$. In the $\gamma = 50$ case, this condition is $w/\overline{w} \geqslant 1$ and is evident in Fig. 9(c): the probability of waiting times below this value is practically zero, and there is a corresponding positive probability for values larger than the original maximal value. The effect on the mean amplitude and waiting time is comparable to the effect in the case of Rayleigh-distributed waiting times.

Comparing Table IV to Table II, we see that the theoretical $\langle M \rangle$ is only valid for exponentially distributed waiting times, although the uniformly distributed waiting times are within the 10% margin for all γ. The most severe deviation is for Pareto-distributed waiting times, where the number of events found is wrong by approximately a factor $1/\gamma$. This error

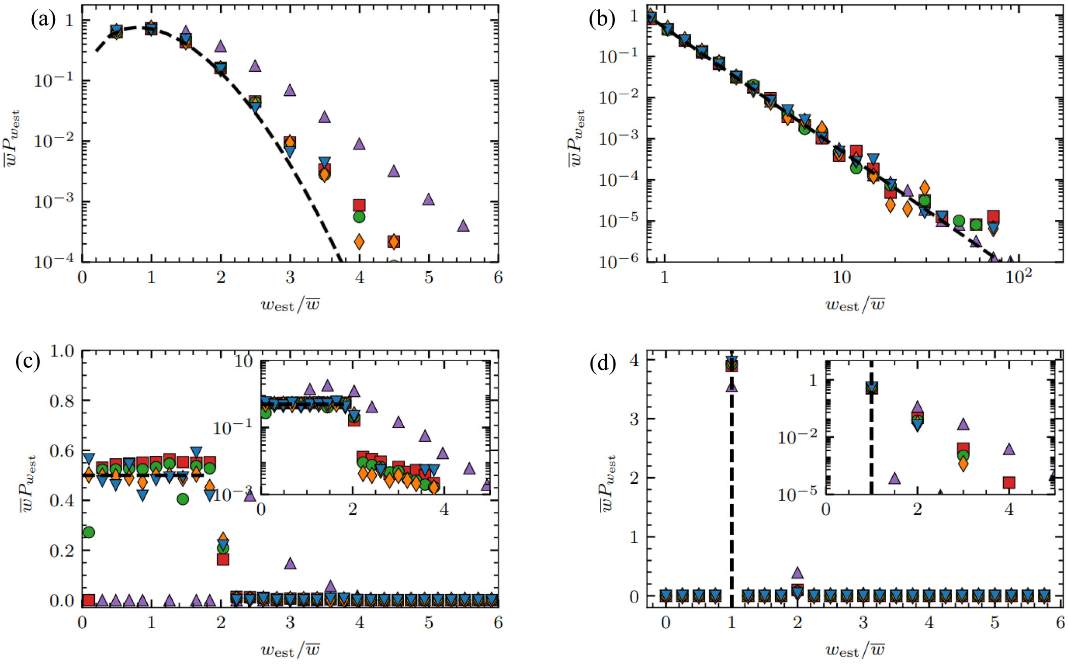

FIG. 9. Probability distributions of estimated waiting times normalized by the sample mean waiting time for various intermittency parameters and distributions of waiting times in realizations of the process. (a) $w \sim$ Rayleigh, (b) $w \sim$ Pareto(3), (c) $w \sim \mathcal{U}(0, 2)$, and (d) $w \sim$ degenerate. The insets in (c) and (d) show the distributions with semilogarithmic scaling. In all cases, exponentially distributed amplitudes were used. The black dashed lines represent the analytical waiting time distribution of the various realizations. The plot symbols are defined in VI.

is to be expected, as the exponential shape of the waiting time distribution, nonzero probability of evens closer than two time steps, and the memory-less property of the Poisson process were central to the calculations in Appendix A. For the nonexponential waiting time distributions, at least two of these assumptions are false.

These results may indicate that the deconvolution procedure distorts amplitudes more than waiting times. Even if a cluster of arrivals is counted as a single arrival by the estimation algorithm, the time between such clusters is not distorted much by the algorithm, and the tail in the waiting time distribution should be well estimated if there is no cutoff for large waiting times. The most significant source of error is the loss of events closer than two time steps.

D. Negative pulse amplitudes

All the amplitude distributions investigated above were positive definite. Now, we consider realizations with zero mean, normally distributed amplitudes to see if they are reproducible, and to investigate the robustness of the deconvolution to negative pulse amplitudes in the process. Symmetric Laplace-distributed amplitudes were also tested with similar results but are not presented here. As the deconvolution algorithm works under the constraint that the forcing is nonnegative, we first straightforwardly estimate the amplitudes and arrival times. This gives estimates of the positive amplitudes with corresponding arrival times. Then we multiply the signal by -1 and redo the deconvolution, giving estimates of the negative amplitudes with corresponding arrival times. In Fig. 10, the results are presented for normally distributed amplitudes. In Fig. 10(a), the resulting amplitude distributions are presented, where the vertical black line indicates the separation between positive and negative amplitudes. The overall shape of the normal distribution is well recovered. In Fig. 10(b), an example of the reconstructed signal is compared to the original signal. It is clear that while large pulse amplitudes, both positive and negative, are identified, the method struggles for small amplitudes. Adding positive and negative pulses in quick succession leads to a signal shape which cannot be recognized by the deconvolution as a sum of just positive or just negative amplitudes, and this effect is more severe for small amplitudes.

E. Conclusion

In this most favorable case of a known pulse function and no noise added, the deconvolution method performs well overall, only limited by pulse overlap, as expected from the theory. Different distributions of pulse amplitudes and waiting

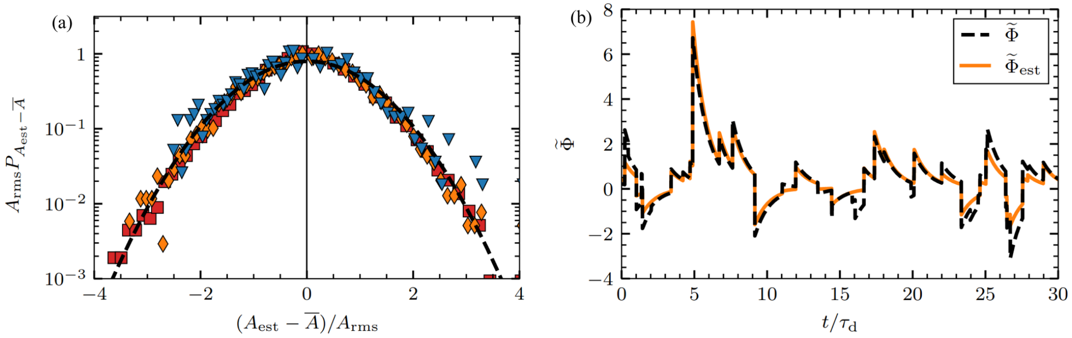

FIG. 10. Reconstruction of a realization with normally distributed pulse amplitudes. (a) Probability distribution function of the amplitudes of found events from the deconvolution. Refer to Fig. 6 for the legend. The analytical distribution (dashed line) is shown for reference, whereas the vertical solid lines show the separation between the negative found events and positive found events. (b) Reconstructed time series (solid line) using estimated amplitudes and arrival times for $\gamma = 1$. The original time series (dashed line) is shown for comparison.

times are well reproduced and mean amplitudes and waiting times are reliably estimated with an error of less than 10% for intermittent signals, $\gamma \leqslant 5$, lending credence to the approximate condition for pulse recovery $\gamma\theta \leqslant 1/20$. Even signals with both positive and negative pulse amplitudes allow reconstruction of large amplitude events.

V. EFFECTS OF NOISE

In this section, we investigate the effects of adding normally distributed noise to the FPP in two different ways. *Additive* noise consists of uncorrelated noise, while *dynamical* noise has the same correlation function as the base case FPP, achieved by convolving uncorrelated noise with the pulse function. Some effects of these forms of noise, including methods for estimating parameters, are discussed further in Refs. [50,52]. For both noise types, we use the base case FPP with uncorrelated, one-sided exponential pulses with exponentially distributed amplitudes. The noise-to-signal ratio is defined as $\epsilon = X_{\mathrm{rms}}^2/\Phi_{\mathrm{rms}}^2$, where X_{rms} is the standard deviation of the noise process. Here and in the following, X_{add} refers to additive noise, X_{dyn} refers to dynamic noise and $\Psi = \Phi + X$ refers to the process with noise.

TABLE IV. Each row shows the ratio of (top) found number of maxima in the forcing estimated from the deconvolution to the theoretical number of maxima, (middle) mean estimated amplitudes to the original sample mean and (bottom) mean estimated waiting times to the original sample waiting times. Results are for the various waiting time distributions used in Fig. 9, exponentially distributed amplitudes and for various intermittency parameters.

P_w	Estimated averages	γ				
		10^{-1}	1	5	10	50
Rayleigh	$M/\langle M\rangle$	1.01	1.02	1.05	*1.11*	*1.21*
	$\overline{A}_{\mathrm{est}}/\overline{A}$	1.01	1.01	1.01	1.02	*1.28*
	$\overline{w}_{\mathrm{est}}/\overline{w}$	1.01	1.01	1.02	1.05	*1.60*
Pareto(3)	$M/\langle M\rangle$	*9.76*	1.01	*0.21*	*0.11*	*0.04*
	$\overline{A}_{\mathrm{est}}/\overline{A}$	1.01	1.01	1.01	1.01	1.01
	$\overline{w}_{\mathrm{est}}/\overline{w}$	1.01	1.01	1.01	1.01	1.01
$\mathcal{U}(0, 2)$	$M/\langle M\rangle$	1.01	1.01	1.02	1.05	1.07
	$\overline{A}_{\mathrm{est}}/\overline{A}$	1.01	1.02	1.03	1.06	*1.33*
	$\overline{w}_{\mathrm{est}}/\overline{w}$	1.01	1.02	1.06	*1.11*	*1.64*
Degenerate	$M/\langle M\rangle$	0.99	1.00	1.06	*1.13*	*1.72*
	$\overline{A}_{\mathrm{est}}/\overline{A}$	1.01	1.01	1.01	1.01	1.03
	$\overline{w}_{\mathrm{est}}/\overline{w}$	1.01	1.01	1.02	1.03	*1.13*

In Fig. 11, we present excerpts of the original and reconstructed time series for both types of noise and the case with no noise. In all cases, the same realization of the FPP was used. It is evident that additive noise, at least for the given noise variance and FPP intermittency, does not lead to major distortions in the reconstruction. This is expected, as the deconvolution algorithm takes normally distributed, additive noise into account and does not depend on the noise level. In Fig. 11, a few small, spurious events can be seen, likely where the noise by chance approximately reproduces the pulse shape. For dynamical noise, we see more significant spurious events as the algorithm can no longer reliably separate the noise from the small amplitude pulses in the signal. This is seen in Fig. 12, where estimated amplitude and waiting time

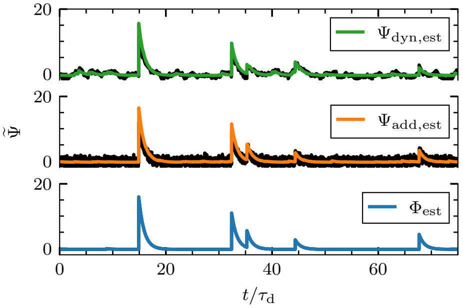

FIG. 11. Original time series (black lines) and reconstructed time series shown by the colored (gray) lines from the deconvolution for no noise (lower panel), additive noise (middle panel), and dynamical noise (upper panel). The intermittency parameter was set to $\gamma = 10^{-1}$, while the noise to signal ratio was set to $\epsilon = 1$.

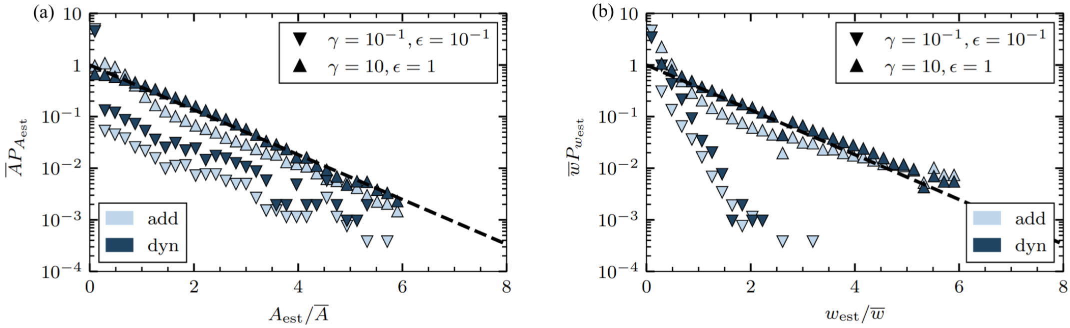

FIG. 12. Probability distributions of (a) estimated amplitudes and (b) estimated waiting times without thresholding. The black dashed line gives an exponential distribution. The symbols represent the values of γ and ϵ used, whereas the colors correspond to the noise type.

distributions are presented, using only the small amplitude threshold discussed in Sec. II C to avoid spurious arrivals. It is clear that many noise events are identified as pulses, and that this also influences the waiting time distribution. In all cases, the tail of the amplitude distribution follows the expected exponential decay. For low γ and ϵ, the effect of noise is largely concentrated in excessively many small-amplitude events, which is reflected in the sharper decay of the waiting time distributions as compared to the original exponential distribution. For high γ and ϵ, the estimated amplitudes and waiting times are moderately affected, and, in particular, dynamical noise has little effect on these distributions. In the following, we will discuss how to improve the results by removing the events with the smallest amplitudes.

Based on the exponential pulse amplitude and normal noise distributions, we have that $X_{\mathrm{rms}} = \sqrt{\gamma\epsilon}\langle A\rangle$, so we introduce a threshold where we reject all events with amplitude less than this value. From realizations of the process, these parameters may be estimated from the moments, probability distribution, or characteristic function as described in Refs. [50,52]. To simplify the analysis, we take γ, ϵ, and $\langle A\rangle$ as given for setting the threshold level. In Figs. 13 and 14, we present estimated amplitude and waiting time distributions after applying the amplitude criterion $A_{\mathrm{est}} > \sqrt{\gamma\epsilon}\langle A\rangle$, discarding all events with smaller amplitudes. Note that for these figures, we normalize by the sample mean of the estimated values instead of the sample mean of the original values to highlight the similarity in distribution. The result is that we have good agreement in distribution in all cases of pulse overlap and noise levels investigated. Removing the arrivals due to noise also realigns the waiting time distributions to the expected exponential.

In Tables V and VI, the estimated mean amplitudes and waiting times for all cases presented in Figs. 13 and 14 are presented. To accurately assess mean values of amplitudes and waiting times, the threshold must be taken into account. The mean value of the truncated amplitudes is, assuming exponentially distributed amplitudes, just the threshold subtracted from the sample mean value of the estimated amplitudes. Therefore, we report $(\overline{A}_{\mathrm{est}} - \sqrt{\gamma\epsilon}\langle A\rangle)/\overline{A}$. For waiting times, pulses are rejected if they have an amplitude $A < \sqrt{\gamma\epsilon}\langle A\rangle$, thus the number of found pulses after thresholding is reduced by a factor $1 - \Pr[A < \sqrt{\gamma\epsilon}\langle A\rangle] = \exp(-\sqrt{\gamma\epsilon})$. Here, the last equality holds for exponentially distributed amplitudes. This in turn implies that the estimated waiting time is prolonged and should be multiplied by this same factor, leading

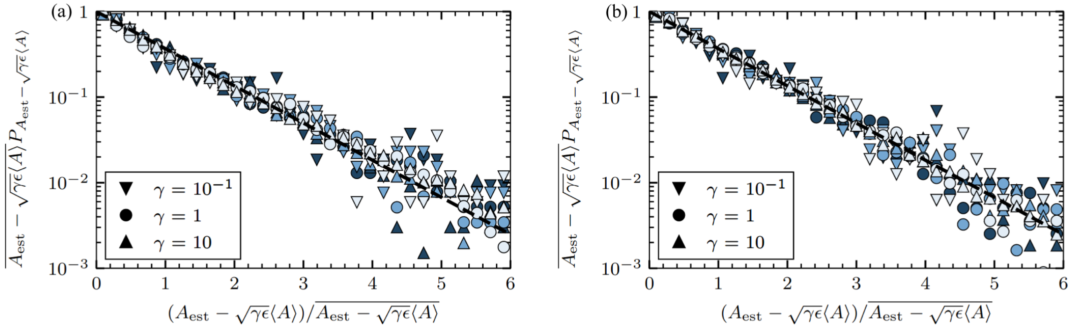

FIG. 13. Probability distributions of estimated amplitudes with thresholding in the presence of (a) additive noise and (b) dynamical noise. The colored markers represent the different noise-to-signal ratios ϵ, corresponding to different intermittency parameters γ represented by the shape of the markers. Light blue (light gray) refers to $\epsilon = 10^{-1}$, medium blue (medium gray) refers to $\epsilon = 1/2$, and dark blue (dark gray) represents $\epsilon = 1$. The black dashed line is an exponential distribution.

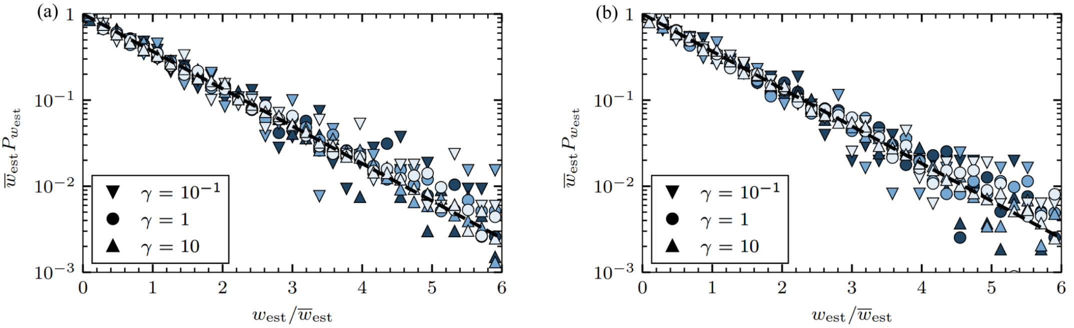

FIG. 14. Probability distributions of estimated waiting times with thresholding in the presence of (a) additive noise and (b) dynamical noise. The colored markers represent the different noise-to-signal ratios ϵ, corresponding to different intermittency parameters γ represented by the shape of the markers. Light blue (light gray) refers to $\epsilon = 10^{-1}$, medium blue (medium gray) refers to $\epsilon = 1/2$, and dark blue (dark gray) represents $\epsilon = 1$. The black dashed line is an exponential distribution.

us to report $\exp(-\sqrt{\gamma\epsilon})\overline{w}_{\mathrm{est}}/\overline{w}$. Note that this argument relies on an assumption of no pulse overlap and will be less accurate for intermittency parameters of order unity or larger.

In the case of the amplitudes, presented in Table V, we recover the mean value well when we correct for the threshold used, although additive noise leads to underestimation of the amplitudes while dynamic noise leads to overestimation of amplitudes in most cases investigated. The estimated waiting times, presented in Table VI, are, in general, much more affected by the noise than the amplitude distribution, reaching close to twice the original sample mean value. In both cases, it appears like moderate pulse overlap, $\gamma = 1$, is more affected by noise than either low or high pulse overlap. It may be that for low pulse overlap, noise is effectively filtered out, while for high degrees of pulse overlap, the threshold is so restrictive (see below) that only the largest amplitude pulses are identified. We also recall that $\overline{w}_{\mathrm{est}}/\overline{w} = 1.19$ is expected for $\gamma = 10$. Thus, the errors due to noise dominate for low and moderate γ, while for high γ, the errors due to pulse overlap are more significant.

In Fig. 15, we present the reconstructed time series from the deconvolution in the most extreme case considered, $\gamma = 10$ and $\epsilon = 1$. The original forcing (without noise) is compared to the forcing estimated from the signal with additive noise (orange dotted lines) and dynamical noise (green dashed lines) in Fig. 15(a). The horizontal black dashed line gives the amplitude threshold $\sqrt{\gamma\epsilon}$. It is clear that many small amplitude pulses are rejected as a result of the thresholding. Also note that additive noise appears to more severely affect large amplitudes than dynamical noise. In particular, note the large, spurious peak at normalized time 6.6. The reconstructed signals using the estimated forcing are compared to the original signal without noise in Fig. 15(b). It is clear that since only the largest amplitude pulses are identified, the method fails to reconstruct realizations of the process.

We have shown that the deconvolution recovers the forcing well in the case of normally distributed noise. To estimate amplitudes and arrival times, an amplitude threshold must be introduced. For high degrees of pulse overlap, this threshold significantly affects signal reconstruction, but, by properly taking the threshold into account, we may recover the tails of the amplitude and waiting time distributions as well as estimating their mean values. The mean amplitude is accurately recovered, while the mean of the estimated waiting times is within a factor 2 of the original sample waiting time, even for severe noise levels.

VI. ESTIMATING THE PULSE DURATION

For any given measurement time series, the pulse function and duration may not be known and so must be estimated to apply the deconvolution method. For pulses with fixed duration arriving in accordance to a Poisson process, the

TABLE V. Estimated average amplitudes in the case of amplitude noise thresholding corrected to $(\overline{A}_{\mathrm{est}} - \sqrt{\gamma\epsilon}\langle A\rangle)/\overline{A}$ corresponding to Fig. 13.

		γ		
	ϵ	10^{-1}	1	10
Additive	10^{-1}	0.90	0.90	*0.89*
	1/2	0.90	*0.87*	*0.89*
	1	0.92	*0.84*	0.94
Dynamic	10^{-1}	1.01	1.03	1.07
	1/2	1.00	1.02	1.05
	1	0.98	1.02	1.04

TABLE VI. Estimated average waiting times in the case of amplitude noise thresholding corrected to $\exp(-\sqrt{\gamma\epsilon})\overline{w}_{\mathrm{est}}/\overline{w}$ corresponding to Fig. 14.

		γ		
	ϵ	10^{-1}	1	10
Additive	10^{-1}	1.02	*1.24*	*1.36*
	1/2	*1.17*	*1.63*	*1.36*
	1	*1.32*	*1.89*	*1.22*
Dynamic	10^{-1}	*1.12*	*1.25*	*1.25*
	1/2	*1.25*	*1.55*	*1.41*
	1	*1.37*	*1.82*	*1.52*

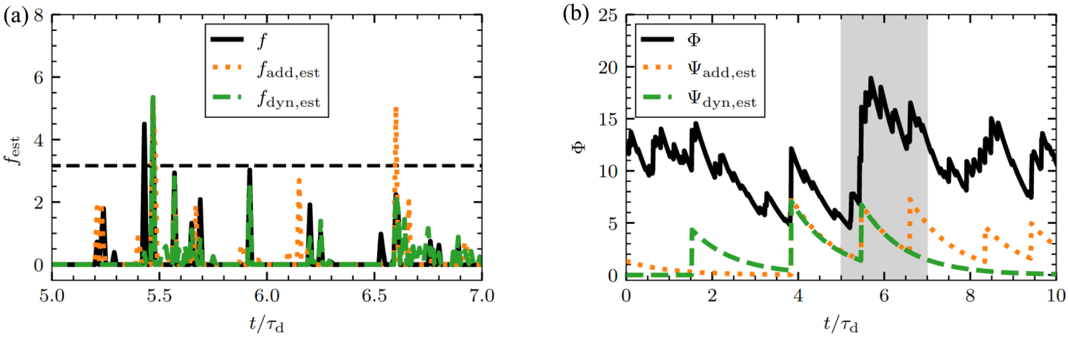

FIG. 15. (a) Excerpt of the original forcing (black solid line) with $\gamma = 10$ and $\epsilon = 1$, compared to the estimated forcing using additive noise (orange dotted line) and dynamical noise (green dashed line) where the noise threshold is shown (horizontal black dashed line). The reconstructed time series (b) is shown using the estimated amplitudes and arrival times from the three-point maxima. The shaded background corresponds to the time axis shown on the left.

pulse function can be obtained from the frequency PSD [51]. Alternatively, the conditionally averaging method for large-amplitude events may be used in the case of weak pulse overlap [22,39,54].

In this section, we investigate how different pulse duration and waiting time distributions distort the estimated pulse function and thereby the estimated amplitude and waiting time distributions. We will estimate the average duration from the frequency power spectra of the process, which, in contrast to the autocorrelation function, are very robust to a distribution of pulse durations [51]. We restrict ourselves to the one-sided exponential pulse function, as it has a clearly identifiable Lorentzian power spectrum. We further restrict ourselves to deviations from the base case which produce reasonable Lorentzian-like power spectra. This means that degenerate and uniform waiting time distributions are not considered, as they produce pronounced peaks in the spectra. Pareto-distributed waiting times produce mild deviations in the tail, which are considered acceptable. Exponentially distributed pulse durations will not be considered due to the significantly increased zero-frequency value in the PSD [51] and neither will Pareto-distributed durations due to their drastic effects on the power spectra [55]. Both uniformly distributed and Rayleigh-distributed durations give Lorenzian-like power spectra. To include a narrow (compared to the Rayleigh) unimodal distribution that is still positive definite, we use a gamma distribution with shape parameter 20.

In Fig. 16, we present the PSD of the normalized synthetic time series without added noise for the various selected distributions of durations and waiting times. The intermittency parameter has very little visible effect on the power spectra, so figures for other intermittency parameters are not presented. Indeed, for the base case with a degenerate distribution of pulse durations and an exponential waiting time distribution, the PSD of the normalized process $\widetilde{\Phi}$ does not depend on the intermittency parameter [51]. The theoretical expectation for the base case is apparently very close to the spectra for all cases presented in Fig. 16. This will be quantified by estimates of the average duration in Secs. VI B and VI C.

A. Wrongly estimated pulse duration

Before investigating the effect of a distribution of pulse durations and waiting times on the deconvolution method,

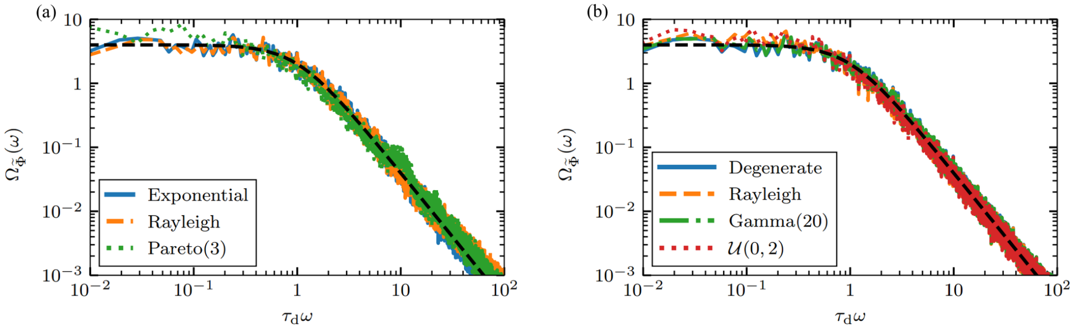

FIG. 16. Power spectral densities of normalized original time series for $\gamma = 10$ with (a) fixed pulse duration and different waiting time distributions and (b) exponential waiting time distribution and different pulse duration distributions. The black dashed line is the Lorentzian spectrum for the base case.

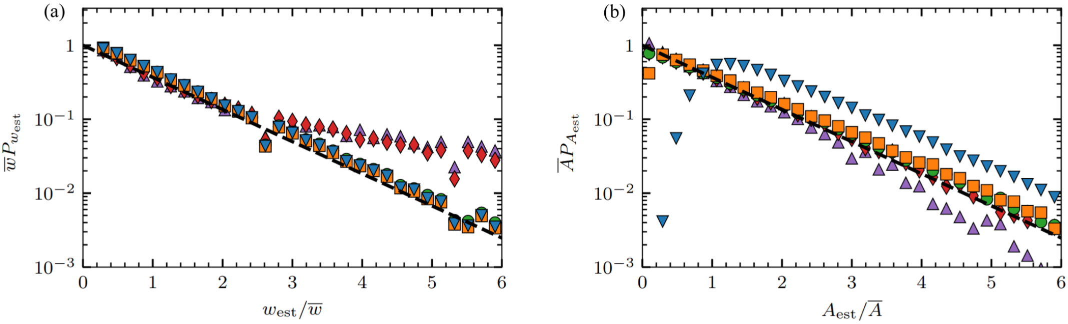

FIG. 17. Probability distribution function of estimated (a) waiting times and (b) amplitudes for $\gamma = 10$ and various assumed values of $\tau_{\mathrm{d,\,wrong}}$. The black dashed lines show an exponential distribution. ▼ represents $\tau_{\mathrm{d,\,wrong}}/\tau_\mathrm{d} = 1/10$, ■ shows the data for $\tau_{\mathrm{d,\,wrong}}/\tau_\mathrm{d} = 1/2$, ● shows the data for $\tau_{\mathrm{d,\,wrong}}/\tau_\mathrm{d} = 1$ ♦, shows the data for $\tau_{\mathrm{d,\,wrong}}/\tau_\mathrm{d} = 2$, and ▲ represents $\tau_{\mathrm{d,\,wrong}}/\tau_\mathrm{d} = 10$.

we consider the isolated effect of misidentifying the correct duration for the base case process. Here, we deconvolve a base case realization with a pulse function with a wrong duration time in the case of no noise added. We will keep the notation $\tau_\mathrm{d} = \langle\tau\rangle$ for the true duration of the process and use $\tau_{\mathrm{d,\,wrong}}$ for the assumed wrong duration.

In Fig. 17, the estimated amplitude and waiting time distributions are presented for various assumed $\tau_{\mathrm{d,\,wrong}}$. The intermittency parameter for all realizations is $\gamma = 10$. Similar results are present, but with a weaker effect, for $\gamma = 1$. We observe deviations from the exponential distribution of waiting times when $\tau_{\mathrm{d,\,wrong}} > \tau_\mathrm{d}$ and deviations for an exponential amplitude distribution for the two most extreme cases with $\tau_{\mathrm{d,\,wrong}}/\tau_\mathrm{d} = 1/10$ and $\tau_{\mathrm{d,\,wrong}}/\tau_\mathrm{d} = 10$. This is complemented by Tables VII and VIII, where the estimated average waiting time and amplitude are compared to their respective original sample mean values. Large $\tau_{\mathrm{d,\,wrong}}/\tau_\mathrm{d}$ leads to overestimation of the average waiting time and this is more pronounced for larger intermittency parameters. Large $\tau_{\mathrm{d,\,wrong}}/\tau_\mathrm{d}$ also leads to underestimation of the average amplitude and this is most pronounced for small intermittency parameters. Small $\tau_{\mathrm{d,\,wrong}}/\tau_\mathrm{d}$ has very little effect on the average waiting time but leads to overestimation of the average amplitude, in particular, for large intermittency parameters.

We interpret these results as follows. The deconvolution preserves the integral of the signal (at least before the three-point maxima is applied) and the integral of the pulse function is equal to the duration time. Therefore, overestimating or underestimating the pulse duration leads to decreased or increased mass in the estimated forcing, respectively. Increased mass in the forcing raises the zero level of the entire forcing, increasing the amplitudes but not causing any events to be lost. Decreased mass in the forcing can only be achieved by decreasing pulse amplitudes, which also eliminates some pulses entirely. Hence, overestimating the duration time leads to lost pulse arrivals, while underestimating the duration mainly leads to increased pulse amplitudes, which is moderate unless the underestimation is extreme or there is significant pulse overlap. These effects suggest that in application of the deconvolution method, where the pulse duration must be estimated, one should favor doing the deconvolution with a slightly lower duration than the estimated one. Noise, different distributions of amplitudes, waiting times, or durations, or correlations between these random variables could change this conclusion, however.

B. Effect of waiting time distribution

Here we will consider how various waiting time distributions affect the estimated pulse duration, and in turn how this influences the estimated amplitude and waiting time statistics using the deconvolution method. In Table IX, the estimated pulse duration for the cases in Fig. 16(a) are presented. These estimated durations were found by performing a least-square minimization using the curve_fit function of the SciPy module in Python, in the normalized frequency range $\tau_\mathrm{d}\omega$ between 10^{-1} to 10^2. The pulse duration is well estimated for the case of exponentially and Rayleigh distributed waiting times. The pulse amplitude and waiting time distributions estimated from the deconvolution method are not affected by the duration estimate in these cases, and are therefore not presented.

TABLE VII. Table of the estimated average pulse waiting times normalized by the mean of the sample waiting times, $\overline{w}_\mathrm{est}/\overline{w}$, for different pulse durations at different intermittency values.

	$\tau_{\mathrm{d,\,wrong}}/\tau_\mathrm{d}$							
γ	10^{-1}	1/2	1	11/10	5/4	3/2	2	10
10^{-1}	1.01	1.01	1.01	1.02	1.04	1.06	*1.12*	*1.78*
1	1.02	1.01	1.03	1.09	*1.18*	*1.33*	*1.60*	*4.53*
10	*1.17*	*1.16*	*1.19*	*1.28*	*1.44*	*1.71*	2.22	9.22

TABLE VIII. Table of the estimated average pulse amplitudes normalized by the sample mean amplitudes, $\overline{A}_\mathrm{est}/\overline{A}$, for different pulse durations at different intermittency values.

	$\tau_{\mathrm{d,\,wrong}}/\tau_\mathrm{d}$							
γ	10^{-1}	1/2	1	11/10	5/4	3/2	2	10
10^{-1}	1.02	1.01	1.01	0.97	0.91	*0.82*	*0.70*	*0.25*
1	1.10	1.01	1.02	1.00	0.97	0.93	*0.86*	*0.50*
10	*1.97*	*1.20*	*1.11*	*1.11*	1.10	1.09	1.07	*0.88*

TABLE IX. Ratio between estimated pulse duration $\tau_{\mathrm{d,\,est}}$ and the pulse τ_{d} for different waiting time distributions, corresponding to the spectra presented in Fig. 16(a).

	γ		
$\tau_{\mathrm{d,\,est}}/\tau_{\mathrm{d}}$	10^{-1}	1	10
$w \sim$ exponential	1.00	1.08	0.96
$w \sim$ Rayleigh	0.93	1.04	0.99
$w \sim$ Pareto(3)	*1.51*	*1.41*	*1.42*

Pareto-distributed waiting times gives an overestimation of the pulse duration, and we expect this to have effects on the subsequently estimated amplitude and waiting time distributions using the deconvolution method. The case $\gamma = 10^{-1}$ has the largest overestimation and will therefore be investigated in more detail. In Fig. 18, we present estimated amplitude and waiting time distributions from deconvolution for pulse durations τ_{d}, $\tau_{\mathrm{d,\,est}}$, and $\tau_{\mathrm{d,\,est}}/2$. The first is included as a baseline reference, while the third is included to demonstrate the effect of using a shorter duration than the estimated one. The amplitude distribution is not visibly affected, but the estimated waiting time distributions show elevated tails at large waiting times ($>10\overline{w}$) and in the case where we used $\tau_{\mathrm{d,\,est}}$, the distribution is elevated for waiting times greater than $\overline{w}$.

The mean values of all distributions presented in Fig. 18 are presented in Table X. The mean amplitudes are consistently underestimated, both for $\tau_{\mathrm{d,\,est}} > \tau_{\mathrm{d}}$ and for $\tau_{\mathrm{d,\,est}}/2 < \tau_{\mathrm{d}}$, in contrast to the results in Table VIII. We see that the deconvolution significantly overestimates $\overline{w}_{\mathrm{est}}$ for $\tau_{\mathrm{d,\,est}}$, and underestimates $\overline{w}_{\mathrm{est}}$ for $\tau_{\mathrm{d,\,est}}/2$. In agreement with the results reported in the previous section, using a slightly lower pulse duration than the estimated one improves the estimated average amplitude and waiting time.

TABLE X. Comparison of rescaled estimated parameters from Fig. 18 for Pareto waiting times, $\gamma = 10^{-1}$, using different duration time values in the deconvolution.

Estimated averages	τ_{d}	$\tau_{\mathrm{d,\,est}}/2$	$\tau_{\mathrm{d,\,est}}$
$\overline{A}_{\mathrm{est}}/\overline{A}$	1.01	0.91	*0.88*
$\overline{w}_{\mathrm{est}}/\overline{w}$	1.01	0.91	*1.28*

TABLE XI. Estimated averages of the amplitude and waiting times using different pulse duration distributions with the same average duration for all cases.

		γ		
P_{τ}	Estimated averages	10^{-1}	1	10
Rayleigh	$\overline{A}_{\mathrm{est}}/\overline{A}$	*0.86*	*0.88*	*0.88*
	$\overline{w}_{\mathrm{est}}/\overline{w}$	0.99	1.03	1.00
Gamma(20)	$\overline{A}_{\mathrm{est}}/\overline{A}$	0.96	0.97	1.06
	$\overline{w}_{\mathrm{est}}/\overline{w}$	1.02	1.05	*1.16*
$\mathcal{U}(0, 2)$	$\overline{A}_{\mathrm{est}}/\overline{A}$	*0.80*	*0.83*	*0.80*
	$\overline{w}_{\mathrm{est}}/\overline{w}$	1.00	1.01	0.92

C. Distribution of pulse durations

Consider now the situation where there is a distribution of pulse durations. The deconvolution method assumes all pulses to have the same duration, so it is of interest to investigate how it performs for a distribution of pulse durations. We first establish a baseline for the performance of the method using the theoretical average duration time. In Table XI, we present estimated average amplitudes and waiting times for three different pulse duration distributions. Table II describes the results for a degenerate distribution of pulse durations. While gamma-distributed durations with shape parameter 20 are narrow enough for the parameters to be well estimated, in both the Rayleigh and uniform cases, the amplitudes are underestimated for all intermittency parameters. For small intermittency parameters, this agrees with the results in Table VIII: the amplitudes of pulses with duration greater than τ_{d} are accurately reconstructed, while amplitudes of pulses with durations smaller than τ_{d} are underestimated. Pulse overlap modifies this relationship, leading to more robustly underestimated amplitudes for the case of randomly distributed durations.

The estimated average duration from fitting to the PSD is presented in Table XII for various duration distributions and

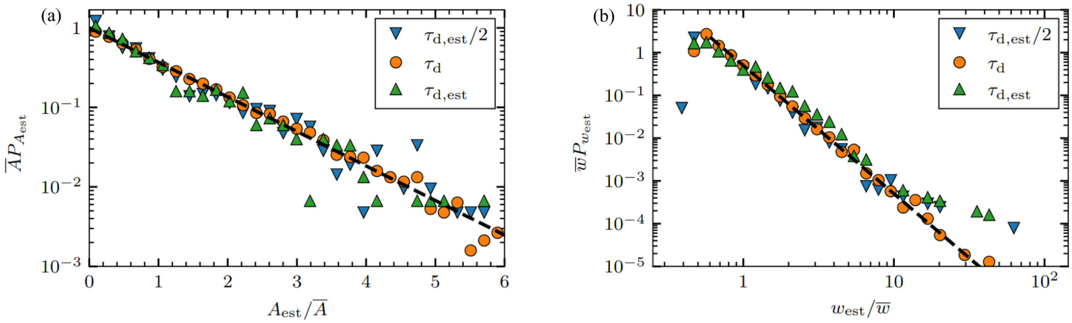

FIG. 18. Estimated (a) amplitude distributions and (b) waiting time distributions for Pareto-distributed waiting times, $w \sim$ Pareto(3), and $\gamma = 10^{-1}$. These plots compare the results from deconvolution performed using the true duration (orange circles) and the estimated duration (green triangles) from Table IX. The black dashed lines are the references of the input distributions.

TABLE XII. Ratio between estimated pulse duration $\tau_{\mathrm{d,est}}$ and sample mean of the durations $\overline{\tau}_{\mathrm{d}}$ using different duration time distributions.

	γ		
$\tau_{\mathrm{d,est}}/\overline{\tau_{\mathrm{d}}}$	10^{-1}	1	10
$\tau_{\mathrm{d}} \sim$ Rayleigh	*1.43*	*1.27*	*1.28*
$\tau_{\mathrm{d}} \sim$ gamma(20)	1.02	1.10	0.98
$\tau_{\mathrm{d}} \sim \mathcal{U}(0, 2)$	*1.54*	*1.45*	*1.39*

intermittency parameters. The case of degenerately distributed pulse durations is equivalent to the case of exponentially distributed waiting times presented in Table IX. Again, a gamma(20) distribution of durations does not appear to significantly affect the results, but the average pulse duration is overestimated in both the other cases. The case of uniformly distributed durations give the largest deviation in the estimated average pulse duration and will again be investigated in more detail.

The estimated pulse amplitude and waiting time distributions for the case of uniformly distributed durations are presented in Fig. 19, and the estimated average amplitudes and waiting times are presented in Table XIII. Again, we compare results from deconvolution with pulses using τ_{d}, $\tau_{\mathrm{d,\,est}}$, and $\tau_{\mathrm{d,\,est}}/2$ as pulse duration. Both the amplitude and waiting time distributions are well estimated. The estimated average waiting time is within 10% of the original sample mean value for both estimated pulse durations used for deconvolution. However, the deconvolution with the reduced estimated pulse duration captures the average amplitude better than the full estimated duration time, consistent with the previous cases.

D. Conclusion

In this section, we have investigated the effect of estimating the pulse duration time from the PSD in the case of nonexponentially distributed waiting times, as well as for a distribution of pulse durations. If the shape of the power spectrum is similar to that of a single pulse (as it will be for uncorrelated pulses with an exponential waiting time distribution), the pulse duration is accurately estimated and there are no issues in applying the deconvolution method. Likewise, a narrow distribution of pulse durations [gamma(20) in our case] gives reliable estimates of amplitudes and waiting times. However, broadly distributed pulse durations will lead to errors in the estimated averages, even if the average duration time is known exactly. It is again demonstrated that using a smaller duration time than the one estimated from the frequency spectrum is preferable, but did not improve on using the mean duration time.

TABLE XIII. Table showing the rescaled estimated parameters from Fig. 19 for uniformly distributed pulse durations using different average duration values in the deconvolution for $\gamma = 10^{-1}$. The corresponding estimated duration can be found in Table XII.

Estimated averages	τ_{d}	$\tau_{\mathrm{d,est}}/2$	$\tau_{\mathrm{d,est}}$
$\overline{A}_{\mathrm{est}}/\overline{A}$	*0.80*	*0.80*	*0.72*
$\overline{w}_{\mathrm{est}}/\overline{w}$	1.00	0.93	1.08

VII. RECONSTRUCTION OF THE PULSE FUNCTION

In some applications, the forcing is known or may be estimated, while the pulse function (or system response to the forcing) is unknown. It is clear from Eq. (7) and the iteration scheme given by Eq. (10) that the particular interpretation of the vectors f and φ does not affect the deconvolution algorithm if the known vector satisfies the conditions of nonnegativity and a positive value at $t = 0$. As such, we may consider f a known forcing and φ an unknown pulse function and obtain the deconvolution algorithm by switching the symbols f and φ in Eq. (10):

$$\varphi_j^{(n+1)} = \varphi_j^{(n)} \frac{(\Phi * \widehat{f})_j + b}{(\varphi^{(n)} * f * \widehat{f})_j + b}. \tag{12}$$

Here, we are interested in the direct result of the deconvolution, and so we do not expect the value of the intermittency parameter to significantly influence the result. This is confirmed by Fig. 20, where we present reconstructions of the one-sided exponential pulse for different intermittency parameters from realizations of the model in the base case. In all cases with a finite intermittency parameter, the pulse recon-

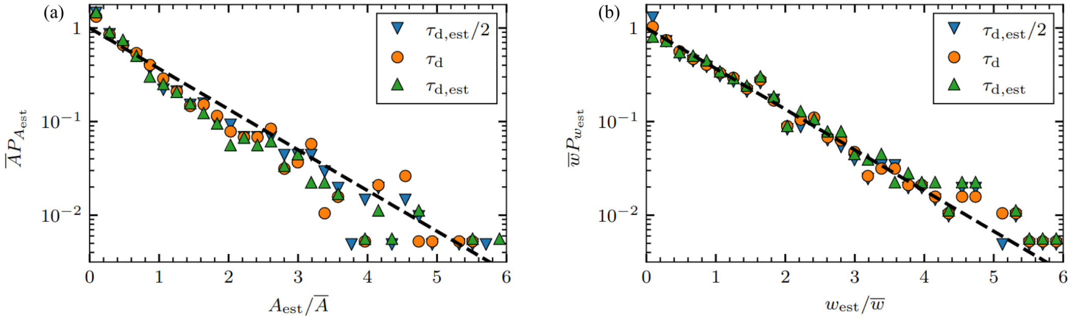

FIG. 19. Estimated (a) amplitude distributions and (b) waiting time distributions for uniformly distributed duration times, $\tau \sim \mathcal{U}(0, 2)$ and $\gamma = 10^{-1}$, using various assumed constant duration times. The black dashed lines are the references of the input distributions.

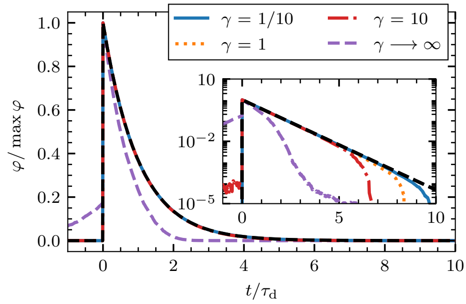

FIG. 20. Reconstruction of a one-side exponential pulse function with different intermittency parameters without noise added. The inset shows the differences between the pulse reconstructions with semilogarithmic axes. The black dashed line shows the true one-sided exponential pulse function.

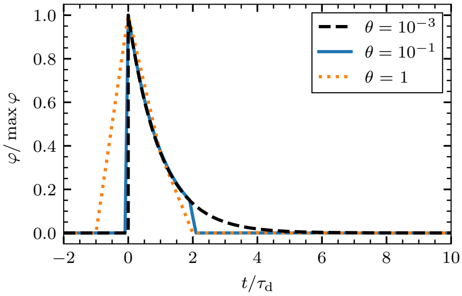

FIG. 21. Reconstruction of a one-sided exponential pulse function (solid colored line and dotted colored line) for variously downsampled signals with intermittency parameter $\gamma = 1$ and no noise added. The black dashed line shows the true one-sided exponential pulse.

struction is reliable, although in the inset it is seen how a lager intermittency parameter pushes up the noise floor, thereby decreasing the time window of accurate reconstruction. Still, for $\gamma = 10$, the effects are only seen two decades below the maximal pulse value. In Fig. 20, we have also indicated the case $\gamma \to \infty$ by letting the forcing signal consist of independently and identically normally distributed random variables, with a constant added to make the forcing positive. In this most severe case, the pulse function is significantly affected, with a slight rise before the peak and correspondingly a faster decay after the peak. In the following, we will only consider the case of moderate pulse overlap, given by $\gamma = 1$. For the results presented in this section, we use a portion of the synthetic time series and its known forcing, where both have a length of $2^{19} + 1$ data points. The initial guess for estimating the pulse function is an array, also of size $2^{19} + 1$ data points, containing a boxcar function centered at zero with an amplitude of one and a width of $2^{17} + 1$ data points, equivalent to about 1300 pulse duration times. All values outside the boxcar are set to zero. The boxcar is used to improve stability; allowing positive values over the entire estimated pulse function array can sometimes lead to spurious positive values at the far ends with a corresponding degradation of the pulse function in the center. Since zeros remain zero during the iteration of the algorithm, such effects are removed by the boxcar. Note that the boxcar is still huge compared to the expected size of the pulse it contains.

In Fig. 21, reconstructed pulse functions from deconvolution of downsampled model realizations using down-sampled forcing is presented. Here it is seen that the pulse function is not accurately reproduced if the process is undersampled. Note that for the comparison, the pulse functions have been rescaled to match the amplitude of the original pulse function. For $\theta = 10^{-1}$, the maximum value is 0.93 and, for $\theta = 1$, the maximum value is 0.62. Thus, the reconstructed amplitude is affected as well as the pulse function. We note, however, that this result is sensitive to how undersampling affects the forcing, and, in particular, whether undersampling leads to losses of entire pulses or not. In the case presented here, loss of pulses in the forcing but not the signal is the major discrepancy between the original down-sampled forcing and the forcing estimated from the down-sampled signals.

We consider the effect of noise in Fig. 22. Additive noise leads to noise in the tail, worse for higher ϵ. Still, we reach noise rms two times the signal rms without significant deviations from the pulse function. Dynamical noise also distorts the pulse function, but not significantly, likely due to the noise in this case being convolved with the same pulse function as the forcing.

In Fig. 23, we present reconstruction of the pulse function in the case of broad distribution of durations. The deconvolution method assumes all pulses have the same duration, but is shown to accurately reproduce the pulse function with largely the correct average duration. Narrower duration distributions [Rayleigh, gamma(20)] were also attempted, but gave results indistinguishable from the true pulse function. Attempting to fit the result of the Pareto case to a single exponential on a linear scale gives $\tau_{\mathrm{d,\,est}} = 0.85$, which is easily seen in the inset not to capture the correct pulse function.

In conclusion, the deconvolution method can be used reliably to recover the pulse function from a given forcing. Only severe noise, undersampling, or excessively broad pulse duration distributions lead to significant deviations from the average pulse function.

VIII. DISCUSSION AND CONCLUSIONS

In this paper, we have presented a method for extracting pulse amplitudes and arrival times from realizations of a stochastic process given by a superposition of pulses with fixed shape. The method relies on the ISRA deconvolution algorithm,which produces the maximum-likelihood solution to the deconvolution problem $\Phi = \varphi * f + X$, where Φ is a known signal, φ is a known pulse or kernel function, f is the forcing to be estimated, and X is normally distributed noise. Since the result of the deconvolution algorithm is the forcing time series f, a three-point maxima is used to estimate pulse amplitudes and arrival times.

For realizations of an intermittent process with high temporal resolution (sampling time 1/20 times the average time between pulses or better and 1/10 times the average pulse

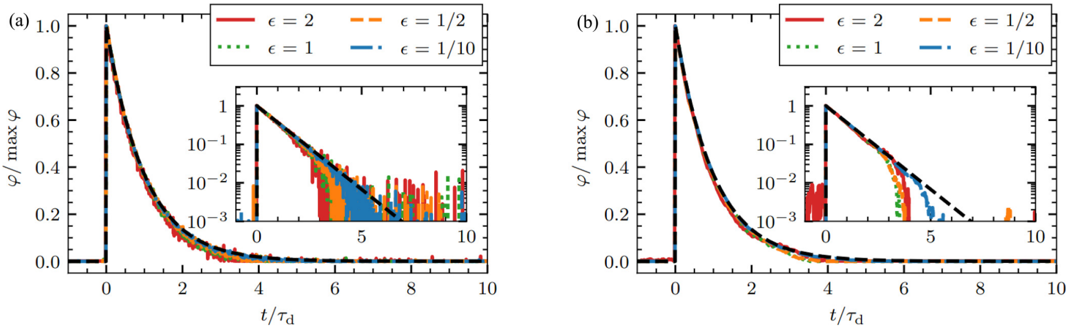

FIG. 22. Reconstruction of a one-sided exponential pulse function using the modified RL-deconvolution for $\gamma = 1$ and different values of the noise to signal ratio ϵ. (a) Additive noise. (b) Dynamic noise. The black dashed lines represent the true one-sided exponential pulse function.

duration time or better), amplitude and waiting time distributions are well recovered in a variety of cases. Coarser sampling or more pulse overlap both lead to several pulses being counted as one, which distorts the estimated amplitude distribution and leads to overestimation of the average amplitude and waiting time. We note that this condition on the sampling time still allows for pulse overlap and pulses which are separated by two sampling times or more robustly separated by the algorithm. Based on studies of numerous model realizations, it is recommend to use the approximate conditions $\gamma\theta = \triangle_t/\langle w\rangle \leqslant 1/20$ and $\theta \leqslant 1/10$ to determine if the deconvolution will give reasonable estimates of mean values of pulse amplitudes and waiting times, and $\gamma\theta \leqslant 1/10$ if only the functional shape of the corresponding distributions are desired.

While the deconvolution method is only designed for positive valued signals and forcings, negative signal values may be accounted for by a straightforward modification of the algorithm. If negative values are present, we may recover both positive and negative parts by using the method on both the signal and its sign reversed version separately, and combine the results. While the method is not able to accurately resolve parts of data time series where fluctuations of different sign arrive close together, parts of the signal where one sign dominates are well reconstructed.

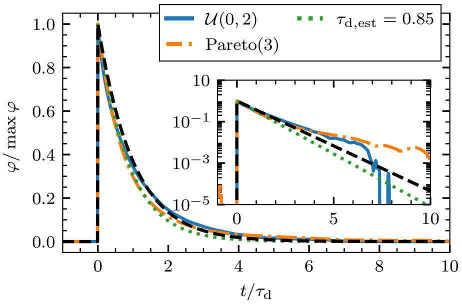

FIG. 23. Pulse reconstruction with randomly distributed pulse durations for $\gamma = 1$ and no added noise. The inset shows the same with semi-logarithmic axes. The dotted line gives the best fit to the pulse function in the Pareto case. The black dashed line is the true one-sided exponential case.

Noise may be handled, and relies at present on introducing an amplitude threshold in the three-point maxima. The threshold performs well recovering the tail of the amplitude and waiting time distributions. Average pulse amplitudes are estimated to within 15% of their true value, while mean waiting times are estimated to within a factor of 2.

If the pulse duration is not known before applying the deconvolution method, it may be estimated from the frequency PSD of the process. The spectrum is insensitive to pulse overlap and amplitude distribution and robust to nonexponential waiting time distributions as well as distributions of the pulse duration. It is demonstrated that for intermittent processes, underestimation of the pulse duration has little to no effect on the estimation of pulse amplitudes and arrivals, while overestimation of the pulse duration has significant implications. Broad distributions in waiting times or durations lead to overestimation of the average duration, which in turn distorts average amplitude and waiting time estimated from the deconvolution. It is shown that in these cases, performing the deconvolution with a pulse duration half the estimated value from the PSD improves the results.

Lastly, if the forcing is known but the pulse function is unknown, the ISRA algorithm may be employed straightforwardly. We have demonstrated that the reproduction of the pulse function is excellent for all but the most severe undersampling or noise. Even if there is a narrow distribution of the pulse durations, the algorithm recovers the pulse function with the average duration time.

For real data, we advise a procedure as in Refs. [23,39]. First, the analysis leading to estimates of the stochastic model parameters is performed. Then, the deconvolution is performed on the empirical data. Finally, synthetic data from model realizations with the estimated model parameters is made and analyzed in the same manner as the empirical data. Results from analysis of the synthetic data should then be compared to the results of the measurement time series. Ideally, this should be carried out as a Monte Carlo study with multiple model realizations, demonstrating that the results of the deconvolution are within the expected errors for synthetic data.

In conclusion, the deconvolution algorithm is shown to recover amplitude and waiting time distributions from realizations of an intermittent process even in the presence of significant pulse overlap, addition of noise, and deviations from the expected pulse function. For all signals considered in this contribution, the underlying ISRA method recovers the forcing admirably and only the basic information loss associated with the finite sampling of a continuous signal affects the reconstruction of amplitude and waiting time distributions.

ACKNOWLEDGMENTS

This work was supported by Tromsø Research Foundation under Grant No. 19_SG_AT and the UiT Aurora Centre Program, UiT The Arctic University of Norway (2020).

APPENDIX A: EFFECT OF SAMPLING ON EVENT RECOLLECTION

In this Appendix, we investigate the information loss associated with poor sampling of the FPP. Consider a Poisson point process $K(T)$ on the interval $[0, T)$ with rate parameter $1/\gamma$. For a given realization, the arrivals of K events are uniformly distributed on the interval. The interval is discretized into N time steps of size $\triangle_t = T/N$. For reference, we note that

$$\langle K\rangle = \gamma\theta N, \tag{A1}$$

where $\theta = \triangle_t/\tau_\mathrm{d}$. We only record if events occur in a given time step, not how many events occur. We therefore move from the process $K(T)$ to the process $F(N)$, denoting locations with events. By necessity, $F \leqslant K$ and $F \leqslant N$. For each of the N time steps, the probability of receiving events is $1 - \mathrm{Pr}[\text{No events in time } \theta]$, which from the Poisson distribution of K is $1 - \exp(-\gamma\theta)$. Therefore, the probability mass function of F is a Binomial distribution over N trials with success probability $1 - \exp(-\gamma\theta)$:

$$P_F(f; \gamma, \theta, N) = \binom{N}{f} \exp(-\gamma\theta)^{N-f}[1 - \exp(-\gamma\theta)]^f. \tag{A2}$$

The mean value is given by

$$\langle F\rangle = N[1 - \exp(-\gamma\theta)]. \tag{A3}$$

For $\gamma\theta \ll 1$, the exponential in Eq. (A3) can be expanded and $\langle F\rangle \approx \langle K\rangle$. However, $\gamma \approx 1/\theta$ gives $\langle K\rangle \approx N$ but $\langle F\rangle \approx 0.6N$ as many events arrive at the same discrete time location.

Let us now investigate the effect of the three-point maxima peak finding algorithm. Letting M denote the number of maxima, we do the following approximation (here, cluster of size k means k consecutive filled time steps with empty time steps at each end):

$$\begin{aligned} M &= \sum_c \sum_m (\text{number of maxima in cluster } m \text{ of size } c),\\ \langle M\rangle &\approx N \sum_c \mathrm{Pr}[\text{cluster of size } c]\\ &\quad \times \langle\text{number of maxima in clusters of size } c\rangle. \end{aligned} \tag{A4}$$

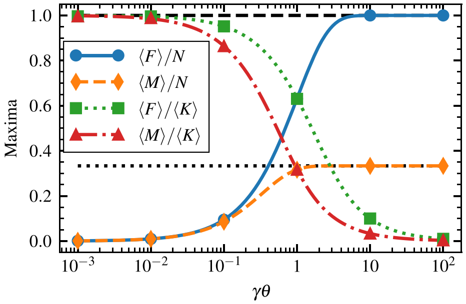

FIG. 24. Comparison of the expected number of events $\langle K\rangle$, the expected number of time steps with events $\langle F\rangle$ and the expected number of events found after a three-point maxima $\langle M\rangle$ as a function of $\gamma\theta$. In all cases, the number of data points was $N = 10^5$ and the normalized time step was $\theta = 10^{-2}$. The lines give analytical approximations, and the symbols are results from numerical simulations.

Letting C be the cluster size, the probability of having a cluster of size c is given by

$$\mathrm{Pr}[\text{cluster of size } c] = \mathrm{Pr}[C = c] = (1 - e^{-\gamma\theta})^c (e^{-\gamma\theta})^2. \tag{A5}$$

To find the number of maxima per cluster, we argue as follows: As the amplitudes are independently and identically distributed, so are the values of the forcing at neighboring time steps. As such, all permutations of the forcing values in a cluster are equally likely. For $c = 1$ and $c = 2$, there is obviously just one maximum. For $c = 3$, there are six permutations, two of which give two maxima and the rest give one, for an average of 4/3 maxima in the cluster. By going from two to three data points, we had a 1/3 chance of adding an extra maximum. Adding further data points to the end of the sequence, each time gives an additional 1/3 chance of a new maxima, so the average number of maxima should increase by 1/3 per new data point. Aided by brute force investigation of all ordered sequences up to $c = 10$, we guess that the average number of maxima in an ordered sequence of size $c \geqslant 2$ is $(c + 1)/3$, including the end points. Adding 1/3 to this gives $((c + 1) + 1)/3$, the average number of maxima in a sequence of $c + 1$ data points. We therefore have that the approximation in Eq. (A4) can be written as

$$\begin{aligned} \frac{\langle M\rangle}{N} &\approx \mathrm{Pr}[C = 1] + \sum_{c=2}^{\infty} \mathrm{Pr}[C = c]\frac{c + 1}{3},\\ \frac{\langle M\rangle}{N} &\approx \frac{1 - e^{-\gamma\theta}}{3}[1 + e^{-\gamma\theta} + (e^{-\gamma\theta})^2], \end{aligned} \tag{A6}$$

where we have used $\mathrm{Pr}[C = c]$ from Eq. (A5). This expression fits our expectations: For very small $\gamma\theta$, we mainly expect clusters of size 1, and Eq. (A6) approaches Eq. (A3). For very large $\gamma\theta$, the entire time series is likely to be filled, so we expect about $N/3$ maxima following the discussion above.

In Fig. 24, we compare the analytical results of this section with results from a Monte Carlo study. The lines give the analytical predictions, while the points give mean values of 20 realizations of the base case with $N = 10^5$ and $\theta = 10^{-2}$

for various γ. One standard deviation would give error bars smaller than the plot symbols. Equation (A6) is an excellent approximation to the average number of maxima for large N, and that the full distribution of the number of events is narrow, justifying the use of $\langle M\rangle$ instead of the full distribution.

For the deconvolution method, $\langle M\rangle/\langle K\rangle$ is the most significant number, as this gives a measure of how well we may hope to recreate the individual pulses in the time series. The lower this ratio is, the more separate pulses are counted as one. If we had a way of avoiding the three-point maxima, we would still have the coarse-graining introduced by discretizing the time series. In this ideal case, $\langle F\rangle/\langle K\rangle$ is the important ratio.

APPENDIX B: DEFINITION OF DISTRIBUTIONS

In this Appendix, we list the distributions used in this paper. In all cases, we give the distributions in terms of their mean value $\langle X\rangle = \mu$, so for any realization $\{X_k\}_{k=1}^{K}$ listed here, we may get amplitudes, waiting times, or pulse durations by setting $\mu = \langle A\rangle$, $\mu = \tau_\mathrm{w}$, or $\mu = \tau_\mathrm{d}$, respectively. Unless otherwise noted, all distributions used are positive definite, so we only give the distributions for $x > 0$. For $x < 0$, we have $P_X(x) = 0$.

(a) The exponential distribution is given by

$$P_X(x) = \frac{1}{\mu}\exp\left(-\frac{x}{\mu}\right). \tag{B1}$$

We denote an exponentially distributed random variable by $X \sim$ exponential

(b) The gamma distribution is given by

$$P_X(x;k) = \frac{k^k}{\Gamma(k)\mu^k}x^{k-1}\exp\left(-\frac{kx}{\mu}\right). \tag{B2}$$

This distribution has one free parameter, the shape parameter k. For $k = 1$, this coincides with the exponential distribution. In the main text, the gamma distribution is denoted by $X \sim \mathrm{gamma}(k)$.

(c) The Rayleigh distribution is given by

$$P_X(x) = \frac{\pi x}{2\mu^2}\exp\left(-\frac{\pi x^2}{4\mu^2}\right). \tag{B3}$$

We denote a Rayleigh distributed random variable by $X \sim$ Rayleigh

(d) The Pareto distribution is given by

$$P_X(x) = \frac{(\alpha-2)^{\alpha-1}}{(\alpha-1)^{\alpha-2}}\frac{\mu^{\alpha-1}}{x^\alpha}, \quad x \geqslant \frac{\alpha-2}{\alpha-1}\mu. \tag{B4}$$

As we require a well-defined mean for all random variables, we demand $\alpha > 2$. We denote a Pareto distributed random variable by $X \sim \mathrm{Pareto}(\alpha)$. Note that following this definition, the PDF decays as $x^{-\alpha}$, while in the standard definition, it is the cumulative distribution function which decays as $x^{-\alpha}$.

(e) The degenerate distribution is given by

$$P_X(x) = \delta(x-\mu). \tag{B5}$$

We denote a degenerately distributed random variable by $X \sim$degenerate.

(f) The uniform distribution is given by

$$P_X(x) = \begin{cases} \frac{1}{2\mu}, & 0 \leqslant x \leqslant 2\mu \\ 0, & \text{else.} \end{cases} \tag{B6}$$

Note that this is the broadest possible non-negative uniform distribution with mean μ. We denote the uniform distribution by $X \sim \mathcal{U}(0, 2)$.

APPENDIX C: PEARSON CORRELATION COEFFICIENTS

In Tables XIV–XIX, we present Pearson correlation coefficients between the true forcing f and the forcing f_est from estimated amplitudes and arrival times. These results are presented for completion; in general, the conclusions that may be drawn from these tables are the same as may be drawn from the distributions and mean values in the main text. To guide the eye and highlight this correspondence, we have marked correlations below 0.9 in italics.

Comparing Tables XVII (for noisy signals without thresholding) and XVIII (for noisy signals with thresholding), we see that the thresholding, although it improves the estimate of the amplitude- and waiting time distributions, uniformly lead to larger differences between f and f_est. If the thresholding were able to separate between events and noise, we would expect the thresholding to improve the correlation. From the tables, it is evident that it removes many true events as well.

TABLE XIV. Table of the Pearson correlation coefficients between the true forcing and the forcing from estimated amplitudes and arrivals corresponding to the the base case, Fig. 7 and Table II.

	γ				
	1/10	1	5	10	50
$A \sim$ exponential	0.95	0.93	0.92	0.91	*0.86*
$w \sim$ exponential	0.95	0.93	0.92	0.91	*0.86*

TABLE XV. Pearson correlation coefficients between the true forcing and the forcing from estimated amplitudes and arrivals for different amplitude distributions, corresponding to Fig. 8 and Table III.

	γ				
	10^{-1}	1	5	10	50
Rayleigh	0.94	0.92	0.91	0.90	*0.82*
Pareto(3)	0.92	0.93	0.96	0.92	0.90
$\mathcal{U}(0, 2)$	0.94	0.92	0.91	0.90	*0.82*
Degenerate	0.93	0.92	0.90	*0.88*	*0.77*

TABLE XVI. Pearson correlation coefficients between the true forcing and the forcing from estimated amplitudes and arrivals for different waiting time distributions, corresponding to Fig. 9 and Table IV

	γ				
	10^{-1}	1	5	10	50
Rayleigh	0.90	0.93	0.92	0.92	*0.87*
Pareto(3)	0.92	0.93	0.92	0.92	0.91
$\mathcal{U}(0, 2)$	0.91	0.93	0.91	0.91	*0.87*
Degenerate	1.00	1.00	0.93	0.93	0.90

TABLE XVII. Table showing the values of the Pearson correlation coefficients between the true forcing and the estimate forcing for different noise to signal ratios, corresponding to Fig. 12.

		γ		
	ϵ	10^{-1}	1	10
Additive	10^{-1}	0.99	0.95	*0.74*
	1/2	0.97	*0.83*	*0.43*
	1	0.95	*0.73*	*0.30*
Dynamic	10^{-1}	1.00	0.99	0.97
	1/2	0.98	0.93	*0.88*
	1	0.96	*0.88*	*0.78*

TABLE XVIII. Pearson correlation coefficients between the true forcing and the forcing using estimated amplitudes and arrival times with thresholding, for various intermittency parameters and noise to signal ratios corresponding to Figs. 13 and 14 and Tables V and VI.

		γ		
	ϵ	10^{-1}	1	10
Additive	10^{-1}	0.95	*0.89*	*0.67*
	1/2	0.93	*0.77*	*0.37*
	1	0.92	*0.68*	*0.24*
Dynamic	10^{-1}	0.95	0.91	*0.85*
	1/2	0.94	*0.85*	*0.65*
	1	0.93	*0.78*	*0.49*

TABLE XIX. Pearson correlation coefficients between the true forcing and the estimated amplitudes and arrival times using three-point maxima for various pulse duration times and intermittency values. This table corresponds to Fig. 17 and Tables VII and VIII.

	$\tau_{\mathrm{d,\,wrong}}/\tau_{\mathrm{d}}$				
γ	10^{-1}	1/2	1	2	10
10^{-1}	0.95	0.95	0.95	0.94	*0.77*
1	0.92	0.93	0.93	*0.88*	*0.61*
10	*0.87*	0.91	0.91	*0.84*	*0.53*

---

[1] P. F. Salipante, S. E. Meek, and S. D. Hudson, Soft Matter **14**, 9020 (2018).

[2] S.-S. Ding, H.-M. Li, W.-D. Yan, and J.-Q. Zhong, Phys. Rev. Fluids **4**, 023501 (2019).

[3] Y. Wang, X. He, and P. Tong, J. Fluid Mech. **874**, 263 (2019).

[4] G. Decristoforo, A. Theodorsen, and O. E. Garcia, Phys. Fluids **32**, 085102 (2020).

[5] L. Kristensen, M. Casanova, M. S. Courtney, and I. Troen, Boundary-Layer Meteorol. **55**, 91 (1991).

[6] R. Narasimha, S. R. Kumar, A. Prabhu, and S. V. Kailas, Philos. Trans. A. Math. Phys. Eng. Sci. **365**, 841 (2007).

[7] P. Claps, A. Giordano, and F. Laio, Adv. Water Resour. **28**, 992 (2005).

[8] M. Lefebvre, Stat. Probab. Lett. **78**, 3274 (2008).

[9] J.-B. Thomazo, B. Le Révérend, L.-L. Pontani, A. M. Prevost, and E. Wandersman, Proc. Natl. Acad. Sci. **118**, e2020402118 (2021).

[10] Z. Elter, C. Jammes, I. Pázsit, L. Pál, and P. Filliatre, Nucl. Instrum. Methods Phys. Res., Sect. A **774**, 60 (2015).

[11] J. R. Segal, B. Ceccarelli, R. Fesce, and W. P. Hurlbut, Biophys. J. **47**, 183 (1985).

[12] R. Fesce, J. R. Segal, and W. P. Hurlbut, J. Gen. Physiol. **88**, 25 (1986).

[13] M. J. E. Richardson, Phys. Rev. E **98**, 042405 (2018).

[14] V. Hakim and J. Ranft, Phys. Rev. E **101**, 012411 (2020).

[15] O. E. Garcia, V. Naulin, A. H. Nielsen, and J. Juul Rasmussen, Phys. Plasmas **12**, 062309 (2005).

[16] H. Karimabadi, V. Roytershteyn, M. Wan, W. H. Matthaeus, W. Daughton, P. Wu, M. Shay, B. Loring, J. Borovsky, E. Leonardis, S. C. Chapman, and T. K. M. Nakamura, Phys. Plasmas **20**, 012303 (2013).

[17] J. Anderson and B. Hnat, Phys. Plasmas **24**, 062301 (2017).

[18] G. Decristoforo, F. Militello, T. Nicholas, J. Omotani, C. Marsden, N. Walkden, and O. E. Garcia, Phys. Plasmas **27**, 122301 (2020).

[19] A. J. Wootton, J. Nucl. Mater. **176-177**, 77 (1990).

[20] G. Y. Antar, G. Counsell, Y. Yu, B. Labombard, and P. Devynck, Phys. Plasmas **10**, 419 (2003).

[21] D. A. D'Ippolito, J. R. Myra, and S. J. Zweben, Phys. Plasmas **18**, 060501 (2011).

[22] O. E. Garcia, R. Kube, A. Theodorsen, J.-G. Bak, S.-H. Hong, H.-S. Kim, the KSTAR Project Team, and R. A. Pitts, Nucl. Mater. Energy **12**, 36 (2017).

[23] R. Kube, A. Theodorsen, O. E. Garcia, D. Brunner, B. LaBombard, and J. L. Terry, J. Plasma Phys. **86**, 905860519 (2020).

[24] F. Militello, P. Tamain, W. Fundamenski, A. Kirk, V. Naulin, and A. H. Nielsen, Plasma Phys. Control. Fusion **55**, 025005 (2013).

[25] A. Theodorsen, O. E. Garcia, J. Horacek, R. Kube, and R. A. Pitts, Plasma Phys. Control. Fusion **58**, 044006 (2016).

[26] A. Theodorsen, O. E. Garcia, R. Kube, B. LaBombard, and J. L. Terry, Nucl. Fusion **57**, 114004 (2017).

[27] N. R. Walkden, A. Wynn, F. Militello, B. Lipschultz, G. Matthews, C. Guillemaut, J. Harrison, and D. Moulton, Nucl. Fusion **57**, 036016 (2017).

[28] S. O. Rice, Bell Syst. Tech. J. **23**, 282 (1944).

[29] S. O. Rice, Bell Syst. Tech. J. **24**, 46 (1945).

[30] E. Parzen, *Stochastic Processes* (Society for Industrial and Applied Mathematics, Philadelphia, 1999).

[31] H. L. Pécseli and J. Trulsen, Phys. Fluids B: Plasma Phys. **1**, 1616 (1989).

[32] F. J. Øynes, H. L. Pécseli, and K. Rypdal, Phys. Rev. Lett. **75**, 81 (1995).

[33] D. Block, I. Teliban, F. Greiner, and A. Piel, Phys. Scr. **T122**, 25 (2006).

[34] D. Rudakov, J. Boedo, R. Moyer, P. Stangeby, J. Watkins, D. Whyte, L. Zeng, N. Brooks, R. Doerner, T. Evans, M. Fenstermacher, M. Groth, E. Hollmann, S. Krasheninnikov, C. Lasnier, A. Leonard, M. Mahdavi, G. McKee, A. McLean, A. Pigarov *et al.*, Nucl. Fusion **45**, 1589 (2005).

[35] J. A. Boedo, J. R. Myra, S. Zweben, R. Maingi, R. J. Maqueda, V. A. Soukhanovskii, J. W. Ahn, J. Canik, N. Crocker, D. A. D'Ippolito, R. Bell, H. Kugel, B. Leblanc, L. A. Roquemore, and D. L. Rudakov, Phys. Plasmas **21**, 042309 (2014).

[36] R. Kube, O. E. Garcia, A. Theodorsen, D. Brunner, A. Q. Kuang, B. LaBombard, and J. L. Terry, Plasma Phys. Control. Fusion **60**, 065002 (2018).

[37] I. Teliban, D. Block, A. Piel, and F. Greiner, Plasma Phys. Control. Fusion **49**, 485 (2007).

[38] H. Johnsen, H. L. Pécseli, and J. Trulsen, Phys. Fluids **30**, 2239 (1987).

[39] A. Theodorsen, O. E. Garcia, R. Kube, B. LaBombard, and J. L. Terry, Phys. Plasmas **25**, 122309 (2018).

[40] W. H. Richardson, J. Opt. Soc. Am. **62**, 55 (1972).

[41] L. B. Lucy, Astron. J. **79**, 745 (1974).

[42] F. Benvenuto, R. Zanella, L. Zanni, and M. Bertero, Inverse Probl. **26**, 025004 (2010).

[43] F. Dell'Acqua, G. Rizzo, P. Scifo, R. A. Clarke, G. Scotti, and F. Fazio, IEEE Trans. Biomed. Eng. **54**, 462 (2007).

[44] F. Dell'Acqua, P. Scifo, G. Rizzo, M. Catani, A. Simmons, G. Scotti, and F. Fazio, NeuroImage **49**, 1446 (2010).

[45] N. Dey, L. Blanc-Feraud, C. Zimmer, P. Roux, Z. Kam, J.-C. Olivo-Marin, and J. Zerubia, Microsc. Res. Tech. **69**, 260 (2006).

[46] R. Kube and O. E. Garcia, Phys. Plasmas **22**, 012502 (2015).

[47] O. E. Garcia, R. Kube, A. Theodorsen, and H. L. Pécseli, Phys. Plasmas **23**, 052308 (2016).

[48] https://github.com/uit-cosmo/.

[49] O. E. Garcia, Phys. Rev. Lett. **108**, 265001 (2012).

[50] A. Theodorsen, O. E. Garcia, and M. Rypdal, Phys. Scr. **92**, 054002 (2017).

[51] O. E. Garcia and A. Theodorsen, Phys. Plasmas **24**, 032309 (2017).

[52] A. Theodorsen and O. E. Garcia, Plasma Phys. Control. Fusion **60**, 034006 (2018).

[53] A. C. Davison and D. V. Hinkley, *Bootstrap Methods and their Application*, Cambridge Series in Statistical and Probabilistic Mathematics (Cambridge University Press, Cambridge, 1997).

[54] O. E. Garcia, R. Kube, A. Theodorsen, B. LaBombard, and J. L. Terry, Phys. Plasmas **25**, 056103 (2018).

[55] M. A. Korzeniowska, A. Theodorsen, M. W. Rypdal, and O. E. Garcia (unpublished).

Paper II:
Strongly intermittent far scrape-off layer fluctuations in Alcator C-Mod plasmas close to the empirical discharge density limit

S. Ahmed, O. E. Garcia, A. Q. Kuang, B. LaBombard, J. L. Terry
and A. Theodorsen
Submitted to Plasma Physics and Controlled Fusion on 14.04.2023
Available online on arXiv:2304.06785

Strongly intermittent far scrape-off layer fluctuations in Alcator C-Mod plasmas close to the empirical discharge density limit

Sajidah Ahmed,[1] Odd Erik Garcia,[1] Adam Q Kuang[2], Brian LaBombard,[3] James L Terry[3] and Audun Theodorsen[1]

[1] Department of Physics and Technology, UiT The Arctic University of Norway, N-9037 Tromsø, Norway
[2] Commonwealth Fusion Systems, 117 Hospital Road, Devens, MA 01434, United States of America
[3] MIT Plasma Science and Fusion Center, Cambridge, MA 02139, United States of America

E-mail: `sajidah.ahmed@uit.com`

19 September 2023

Abstract. Intermittent plasma fluctuations in the boundary region of the Alcator C-Mod device were comprehensively investigated using data time-series from gas puff imaging and mirror Langmuir probe diagnostics. Fluctuations were sampled during stationary plasma conditions in ohmically heated, lower single null diverted configurations with scans in both line-averaged density and plasma current, with Greenwald density fractions up to 0.85. Utilizing a stochastic model, we describe the plasma fluctuations as a super-position of uncorrelated pulses, with large-amplitude events corresponding to blob-like filaments moving through the scrape-off layer. A deconvolution method is used to estimate the pulse arrival times and amplitudes. The analysis reveals a significant increase of pulse amplitudes and waiting times as the line-averaged density approaches the empirical discharge density limit. Broadened and flattened average radial profiles are thus accompanied by strongly intermittent and large-amplitude fluctuations. Although these filaments are arriving less frequently at high line-averaged densities, we show that there are significant increases in radial far-SOL particle and heat fluxes which will further enhance plasma–wall interactions. The stochastic model has been used as a framework for study of the scalings in the intermittency parameter, flux and mean amplitude and waiting times, and is being used to inform predictive capability for the effects of filamentary transport as a function of Greenwald fraction.

Keywords: scrape-off layer, intermittency, filament, blobs, stochastic modelling, turbulence, plasma–wall interactions

Submitted to: *Plasma Phys. Control. Fusion*

1. Introduction

The boundary of magnetically confined fusion plasmas plays an imperative role in determining the heat flux density onto the material surfaces. The open field line region, known as the scrape-off layer (SOL), is riddled with turbulent flows mainly in the form of blob-like filaments that propagate radially toward the vessel walls [1–4]. These are believed to be the dominant contributors to the cross-field transport of particles and heat in the SOL, which can lead to enhanced erosion rates of the wall materials and threaten the quality of plasma confinement [2, 5–8]. For reactor-relevant devices, reliable predictions of the expected plasma–wall interactions are necessary to mitigate the deleterious effects on the wall and the inevitable sputtering of material atoms. Therefore, the statistical properties of the plasma fluctuations are of great interest in order to predict and monitor the far-SOL transport, in particular the amplitudes of these far-SOL plasma fluctuations, their frequency of occurence and the duration times.

Filaments are coherent pressure perturbations with order-unity relative fluctuation amplitudes, elongated along and localized perpendicular to the magnetic field lines [9–16]. They are believed to originate in the vicinity of the last closed magnetic flux surface (LCFS), and are observed in all magnetic configurations and confinement states [12, 15, 17–23]. On the low-field side of the SOL, magnetic gradient and curvature drifts lead to electric polarization of these filaments, resulting in a radial propagation towards the vessel walls [24–28].

In single-point measurements of SOL plasma fluctuations, filaments are observed as large-amplitude bursts, and have been shown to exhibit several robust statistical properties [19, 29–39]. These include skewed and flattenened probability density functions (PDFs) with elevated tails for large amplitudes and frequency spectra which are flat for low frequecies and power-law like for high frequencies [12, 40–50]. Conditional averaging revealed exponentially distributed pulse amplitudes and waiting times as well as the waveform of the bursts to be well described by a two-sided exponential function [16, 30, 31, 34, 35, 37, 46, 50–52].

To describe the statistical properties of the SOL fluctuations, a stochastic model based on a super-position of uncorrelated exponential pulses with constant duration has been introduced [53–58]. It can be shown that exponentially distributed amplitudes and waiting times between consecutive events lead to frequency power spectral densities (PSDs) with a Lorentzian shape and Gamma probability density functions (PDFs) [44, 53, 54, 56–59]. Both of these properties have been shown to be in excellent agreement with Langmuir probe and gas puff imaging (GPI) measurements in various confinement regimes and fusion devices [37, 44–46, 52]. Operating at a sampling rate of a few megahertz, these diagnostics have sampling times relevant for studying SOL turbulence dynamics. Further, the stochastic model has been used to validate numerical simulations of SOL turbulence, which reveal the same statistical properties of the fluctuations as found from experimental measurements [60].

The stochastic model describes the fluctuations at any given position in the SOL as only due to blob-like filaments. This notion probably does not apply in the vicinity of the LCFS and near-SOL region due to the presence of drift waves and a shear layer where poloidal velocities may be significant [14,61–66]. However, the focus of this investigation is large-amplitude fluctuations in the far-SOL where we expect low poloidal velocities and radial motion of the blob structures to dominate [14,61,64,65,67,68]. Moreover, the distinction between the near and the far-SOL regions disappears at high line-averaged densities, supporting the assumption that the most dominant process leading to these flat and broad profiles are the filaments [43, 51, 69–76]. Measurements from various fusion devices suggest that edge and SOL transport appears to be strongly related to the empirical discharge density limit, as seen by the broadening and flattening of the radial SOL density and temperature profiles [1, 19, 34, 35, 63, 77, 78]. As one approaches the density limit, these filamentary structures are observed on closed-field line regions as a result of the far-SOL extending all the way inside the LCFS [12].

In this contribution, exceptionally long fluctuation time series from the GPI and the mirror Langmuir probe (MLP) on Alcator C-Mod were analyzed in order to carry out a study of the stochastic model parameters with the line-averaged density of the main plasma and the plasma current. From the measurement data, the parameters of the stochastic model are estimated, comprising the mean pulse amplitude and the average pulse duration and waiting times. By reformulating the stochastic model as a convolution of the pulse function with a train of delta pulses, the Richardson–Lucy (RL) deconvolution algorithm was used to recover the pulse amplitudes and their arrival times from the measurement time series [79–81]. This provides an accurate determination of these quantities for both small and large-amplitude events [45, 82], as opposed to the much-used conditional averaging technique that selectively measures properties only of the large-amplitude events. Concerns about using the conditional averaging technique arise from choice of amplitude threshold and the struggle to deal with significant pulse overlap and noise consistently. The application of the deconvolution method was initially used to analyze GPI data from Alcator C-Mod [45]. Subsequently, this method underwent theoretical investigations in reference [82], resulting in significant improvements. In our present study, we employ this enhanced version of the deconvolution method for the first time, showcasing its effectiveness in our analyses. Further, in previous studies using the deconvolution algorithm, the method contained a free parameter chosen to make the mean estimated waiting time from the deconvolution as close as possible to the mean waiting time estimated from γ/τ_d [45,48]. This application of the deconvolution method on the measurement time-series in this study does not employ this free parameter.

Estimating various blob velocity scaling regimes and connection to the divertor target is beyond the scope of this study. This is because there is no consensus in the literature about the role that the divertor conditions play in the main plasma SOL. References that address this issue, but with conflicting conclusions, are [49, 51, 83–85]. Here we restrict the study to the main plasma SOL alone since existing work on Alcator C-Mod in reference [49] has shown no obvious effect of the divertor state on the SOL.

Blob regimes have previously been studied in Alcator C-Mod, assessing the role of the Greenwald density fraction [49, 67, 86]. It was found that local plasma parameters appeared to have a strong influence on radial propagation, which is not captured well by blob theory. Furthermore, the results of the tracking of blob-structures from reference [67] suggest that the blob size changes little with line-averaged density.

Here, results are presented from detailed time series analyses of far-SOL fluctuation data in ohmically heated, lower single null (LSN) diverted Alcator C-Mod plasmas with a wide range of line-averaged densities ($0.46 \times 10^{20} - 2.8 \times 10^{20}\,\mathrm{m}^{-3}$) and plasma currents ($0.53 - 1.1\,\mathrm{MA}$). These line-averaged densities and plasma currents will be quoted in terms of the Greenwald fraction, $f_{\mathrm{GW}} = \overline{n}_{\mathrm{e}}/n_{\mathrm{G}}$, where $\overline{n}_{\mathrm{e}}$ is the line-averaged density and the empirical Greenwald density limit is defined as $n_{\mathrm{G}} = (I_{\mathrm{P}}/\pi a^2) \times 10^{20}\ \mathrm{m}^{-3}$, where a is the minor radius of the plasma in units of meters and I_{P} is the plasma current in units of mega-Amperes [87]. The study by reference [1] demonstrated that as the empirical density limit was approached in Alcator C-Mod, there was a noticeable increase in the radial particle and heat fluxes within the scrape-off layer (SOL). This finding serves as additional motivation for utilizing the Greenwald density fraction as a parameter of interest. Incorporating the Greenwald fraction enables comparisons between different machines and facilitates predictive capabilities, both of which are key benefits of this work. In this study, we present new findings that focus on the exploration of Greenwald fractions within the range of $0.48 < f_{\mathrm{GW}} \leq 0.85$ in the framework of stochastic modeling. Previous studies [38, 44, 67, 88] have not investigated this specific range. We provide explicit evidence illustrating the changes in fluctuation statistics across a wide range of Greenwald fractions. These findings are subsequently employed to interpret flux measurements in the far-SOL region. Although a discrepancy has been indicated in reference [48] between the GPI and the MLP, we emphasize the discrepancies between these two diagnostics across a wide density scan range, showing that distinct trends exist with the fluctuation statistics. We show that it is the functional dependence itself which is different, not just the parameter values. Despite these differences, both diagnostics show that strongly intermittent fluctuations are observed as the density limit is approached.

This contribution is structured in the following way: Section 2 gives details of the experimental setup and a brief overview of the GPI and MLP diagnostic systems. In section 3, we review the stochastic model and the base case (that is, exponentially distributed pulse amplitudes and waiting times) used to interpret the measurement time series, as well as the deconvolution algorithm used to recover the pulse arrival times and amplitudes. In addition, we discuss the quality of the parameter estimation. The results of the density and plasma current scans are presented in section 4, revealing the fluctuation statistics and demonstrating how the stochastic model parameters change with the Alcator C-Mod plasma parameters. Finally, we discuss the results and conclude the study in section 5. Appendix A presents the fluctuation statistics estimated from the plasma current scan in terms of I_{P} and Appendix B discusses methodology for estimating model parameters.

2. Experimental setup

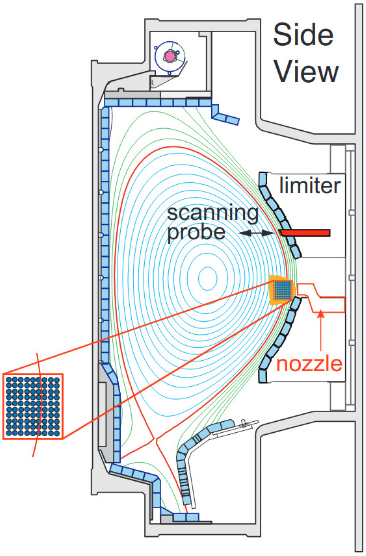

Figure 1. Poloidal cross-section of the Alcator C-Mod tokamak in lower diverted single-null configuration, showcasing the diagnostic set up. The mirror-Langmuir probe (MLP) and the gas puff imaging (GPI) were used to diagnose SOL plasma fluctuations [38]. The blow-up of the GPI field-of-view illustrates the 9 × 10 viewing-spots and the LCFS passing through the field-of-view. This figure is reproduced from O. E. Garcia, *et al.* "Intermittent fluctuations in the Alcator C-Mod scrape-off layer." *Phys. Plasmas* **20** 055901 2013, with the permission of AIP Publishing.

Alcator C-Mod is a compact high-field (toroidal field B_T from 2 to 8 T) tokamak with major radius $R = 0.68\,\mathrm{m}$ and minor radius $a = 0.21\,\mathrm{m}$. We study the statistical properties of the time series from GPI and the MLP diagnostics measuring far-SOL fluctuations at the outboard side of ohmically heated plasma discharges fuelled by deuterium. All plasma discharges analyzed here were in a diverted LSN magnetic configuration, as shown in figure 1.

2.1. Diagnostic systems

The GPI diagnostic provides two-dimensional images of emitted line radiation from a neutral gas with high temporal resolution. This diagnostic consists of two essential parts. A gas nozzle puffs a contrast gas into the boundary plasma. The puffed gas atoms are excited by local plasma electrons and emit characteristic line radiation modulated on fast time scales by fluctuations in the local electron density and temperature. This local emission is sampled in a favorable viewing geometry by an optical system comprising either a fast-framing camera or an array of avalanche photodiodes (APDs).

The APD-based GPI diagnostic on Alcator C-Mod was used for this study, and it consists of a 9×10 APD array of toroidally-directed views of a localized gas puff. The GPI system was puffing helium and imaging the He I 587 nm emission line, where the signals are digitized at a rate of 2×10^6 frames per second. The viewing area spans the outboard edge and SOL plasma near the midplane, covering the major radius from 88.00 to 91.08 cm and the vertical distance, relative to the $Z = 0$ midplane, from -4.51 to -1.08 cm. The in-focus spot size of the imaging optics is 3.8 mm for each of the individual views. For each discharge analyzed here, the GPI diagnostic yields at least 100 milliseconds of usable time series data during which both plasma current and line-averaged density were approximately constant. More information on this APD-based GPI system on the Alcator C-Mod device can be found in reference [23]. Since the absolute value of the GPI light intensity is a function of the (unmeasured) local density of neutral gas, it is of secondary significance, and we only consider normalized GPI signals in this study.

The MLP digitization system allows for fast sampling of ion saturation current I_{sat}, floating potential V_{f}, and electron temperature T_{e} with $0.9\,\mu$s time resolution on a single electrode. The plasma parameters are obtained by fitting digitized $I - V$ data, sampled at a rate of 3.3 MHz. Due to its capability of real-time plasma temperature determination to optimize voltage bias states at sampling frequencies in the range of megahertz, it is therefore called a “mirror” Langmuir probe. Four probe tips are embedded in a Mach probe head that is mounted on a linear servomotor probe drive system. These four MLP electrodes are arranged in a pyramidal dome geometry on the probe head so that they sample approximately the same magnetic flux surface. A diagram of the MLP can be seen in reference [89], and more details can be found in reference [90]. The probe was scanned horizontally or dwelled in a position just inside of the limiter radius 11 cm above the outboard midplane location. The MLP and the GPI diagnostics did not share the same magnetic flux tube. We focus on the dwell probe measurements in the far-SOL, as we want to investigate the statistical properties of turbulence there. Accordingly, only GPI and scanning probe data from the far-SOL are analyzed in order to make a direct comparison.

2.2. Data preprocessing

Measurement data is rarely sampled under perfectly stationary conditions. This may be due to small changes in the LCFS location or small drifts in the main plasma density. Before analyzing the time series, measurements were therefore rescaled to have a locally vanishing mean and unit standard deviation,

$$\widetilde{\Phi}_{\text{mv}} = \frac{\Phi - \langle\Phi\rangle_{\text{mv}}}{\Phi_{\text{rms,mv}}}, \tag{1}$$

where

$$\langle\Phi\rangle_{\text{mv}}(t_i) = \frac{1}{2r+1}\sum_{k=-r}^{r} \Phi(t_{i+k}) \tag{2}$$

and

$$\Phi_{\mathrm{rms,mv}}(t_i) = \left[\frac{1}{2r+1} \sum_{k=-r}^{r} \left(\Phi(t_{i+k}) - \langle \Phi(t_i) \rangle_{\mathrm{mv}} \right)^2 \right]^{1/2} \tag{3}$$

denote the moving average and the moving root mean square, respectively, of the time series signal $\Phi(t)$ [47]. For the GPI diagnostic, the sampling time was $\triangle_{\mathrm{t}} = 0.5\,\mu$s and the moving filter radius used was $r = 8192$ samples, which corresponds to 4 ms. For the MLP diagnostic, the sampling time of the fitted I_{sat} data was $\triangle_{\mathrm{t}} = 0.3\,\mu$s where the filter radius was $r = 16384$ samples, which corresponds to a moving window of 5 ms. Detrending the raw time-series measurements according to equation (1) ensures that slow variations in the mean and variance due to slowly changing plasma conditions are removed. Absorbing these variations into the normalization of the time series allows for the comparison of as many samples as possible to ensure well-converged statistical estimates.

The estimators of the radial electric drift velocity U, particle flux Γ_n and heat flux Γ_T estimated using the MLP data are given by,

$$U = \frac{1}{2} \frac{V^{\mathrm{S}} - V^{\mathrm{N}}}{B_{\mathrm{MLP}} \triangle_Z}, \tag{4}$$

$$\Gamma_{n,\widetilde{n}_{\mathrm{e}}} = \widetilde{n}_{\mathrm{e}} \widetilde{U}, \tag{5}$$

$$\Gamma_{n,\widetilde{I}_{\mathrm{sat}}} = \widetilde{I}_{\mathrm{sat}} \widetilde{U}, \tag{6}$$

$$\Gamma_T = \frac{\langle T_{\mathrm{e}} \rangle}{T_{\mathrm{e,rms}}} \widetilde{U} \widetilde{n}_{\mathrm{e}} + \frac{\langle n_{\mathrm{e}} \rangle}{n_{\mathrm{e,rms}}} \widetilde{U} \widetilde{T}_{\mathrm{e}} + \widetilde{n}_{\mathrm{e}} \widetilde{T}_{\mathrm{e}} \widetilde{U}, \tag{7}$$

respectively. Here, B_{MLP} is the magnetic field at the position of the probe head and $(V^{\mathrm{S}} - V^{\mathrm{N}})/\triangle_Z$ is used to estimate the poloidal electric field, where $\Delta_Z = 2.24$ mm is the separation between the electrodes. 'N' and 'S' denote the "north" and "south" vertically-spaced electrodes, and $V^{\mathrm{N/S}} = ({V_{\mathrm{p}}}^{\mathrm{NE/SE}} + {V_{\mathrm{p}}}^{\mathrm{NW/SW}})/2$ [47]. The particle flux is calculated using detrended and normalized time series according to (1), thus postulating that there is no stationary convection in the SOL. $\Gamma_{n,\widetilde{I}_{\mathrm{sat}}}$ and $\Gamma_{n,\widetilde{n}_{\mathrm{e}}}$ denote the particle flux calculated using $\widetilde{n}_{\mathrm{e}}$ and $\widetilde{I}_{\mathrm{sat}}$ measurements, respectively. For the heat flux measurements, the contribution comes from a convective part, a conductive part and of a part due to triple correlations [91]. It is noted that the study in reference [91] investigates the MLP measurements in scanning mode and elucidates the relative contribution of each part to the total heat flux with Greenwald fraction up to $f_{\mathrm{GW}} \approx 0.5$ from the same runday on the Alcator C-Mod device.

3. Statistical framework

In this section, we discuss the stochastic model used as the data analysis framework, as well as data processing methods. Implementations of analytical functions and analysis routines can be found in the UiT Complex Systems Modelling group GitHub repository [92].

3.1. The stochastic model

Previous work has shown that the statistical properties of SOL plasma fluctuations in various fusion devices and confinement modes have been accurately described by means of stochastic modeling [37, 46, 52]. This stochastic model known as a filtered Poisson process (FPP) describes single-point measurements in the SOL as a super-position of uncorrelated pulses with a fixed shape and duration,

$$\Phi_K(t) = \sum_{k=1}^{K(T)} A_k \varphi\left(\frac{t-s_k}{\tau_\mathrm{d}}\right). \tag{8}$$

Here, $K(T)$ is a Poisson process in the interval $[0, T]$ with intensity $T/\langle w\rangle$, where T is the duration of the process and K is the number of pulses. Consequently, pulse arrival times s_k are independent and uniformly distributed on the interval, and waiting times w_k are independent and exponentially distributed with mean value $\langle w\rangle$. All pulses are assumed to have the same duration time τ_d. The amplitudes A_k are taken to be exponentially distributed with the mean value $\langle A\rangle$. We assume that the pulse function is given by a two-sided exponential,

$$\varphi\left(x\right) = \begin{cases} \exp(-x/(1-\lambda)), & x \geq 0, \\ \exp(-x/\lambda), & x < 0, \end{cases} \tag{9}$$

where the pulse asymmetry parameter is described by λ and x is a dimensionless variable.

The fundamental parameter of the stochastic model is the *intermittency parameter* defined by $\gamma = \tau_\mathrm{d}/\langle w\rangle$, which determines the degree of pulse overlap. When γ is small, the pulses appear isolated in the realizations of the process, resulting in a strong intermittency. When γ is large, there is significant overlap of pulses, resulting in a weakly intermittent process. For $\gamma \rightarrow \infty$, the FPP approaches a normally distributed process [53]. By averaging over all random variables, it can be shown that the four lowest order moments are the mean $\langle\Phi\rangle = \gamma\langle A\rangle$, variance $\Phi_\mathrm{rms}^2 = \gamma\langle A\rangle^2$, skewness $S_\Phi = 2/\sqrt{\gamma}$ and flatness $F_\Phi = 3 + 6/\gamma$ [53]. The PDF, and therefore the moments, do not depend on the pulse asymmetry parameter λ [54]. It follows that the PDF of Φ is a Gamma distribution,

$$P_\Phi(\Phi) = \frac{1}{\langle A\rangle\Gamma(\gamma)}\left(\frac{\Phi}{\langle A\rangle}\right)^{\gamma-1} \exp\left(-\frac{\Phi}{\langle A\rangle}\right), \tag{10}$$

where the shape parameter for the PDF is γ, the intermittency parameter, Γ here denotes the Gamma function and $\langle A\rangle$ is the scale parameter of the PDF.

Since all experimental measurement signals are normalized to have zero mean and unit standard deviation, the stationary process in (8) is scaled to $\widetilde{\Phi} = (\Phi - \langle\Phi\rangle)/\Phi_\mathrm{rms}$. The frequency power spectral density (PSD) of the FPP is the product of two Lorenztian spectra, where the analytical expression is [56]

$$\Omega_{\widetilde{\Phi}}(\omega) = \frac{2\tau_\mathrm{d}}{\left[1 + (1-\lambda)^2(\tau_\mathrm{d}\omega)^2\right]\left[1 + \lambda^2(\tau_\mathrm{d}\omega)^2\right]}, \tag{11}$$

where ω is the angular frequency. The PSD of the normalized process $\widetilde{\Phi}$ is the same as that of a single pulse due to the assumption of independently and uniformly distributed pulse arrivals and fixed pulse duration. The PSD features a flat part for low frequencies and a power-law decay for high frequencies. The intermittency parameter does not influence the shape of the power spectral density [56].

3.2. Noise and parameter estimation

Blob dispersion, small background fluctuations and measurement noise may all contribute to deviations from predictions by the FPP for experimental signal values close to the mean value. We model all these fluctuations as an additional normally distributed noise process X with zero mean and variance X_{rms}^2. We define the noise parameter ε as the ratio between the root mean square of the noise and the root mean square of the signal, $\varepsilon = (X_{\mathrm{rms}}/\Phi_{\mathrm{rms}})^2$. The combined process $\Phi + X$ has mean value $\langle \Phi + X \rangle = \gamma \langle A \rangle$, variance $(\Phi + X)_{\mathrm{rms}}^2 = (1+\varepsilon)\gamma\langle A \rangle^2$, skewness $S_{\Phi+X} = 2/\gamma^{1/2}(1+\varepsilon)^{3/2}$ and flatness $F_{\Phi+X} = 3 + 6/\gamma(1+\varepsilon)^2$.

The PDF of the combined process is a convolution between a Gamma distribution and a normal distribution. By assuming correlated noise which is noise connected to the pulse, the PSD is exactly the same as the expression in (11). If the noise is uncorrelated, also known as observational noise, the PSD is given by equation (35*b*) in reference [57]. We assume correlated noise and utilize (11) for the spectrum in this study. Finally, the expression for the PDF of the normalized signal with the noise parameter can be found in equation (A9) in reference [57].

For the MLP measurement data, the shape of the PSD is influenced by the preprocessing, which filters the signal through a 12-point boxcar window [48]. Figure 7(b) shows the resulting PSD. Therefore, the expected PSD of the MLP data time series is the product of the function in equation (11) and the PSD of a boxcar window [48],

$$\Omega_{\widetilde{\Phi},\mathrm{MLP}}(\omega) = \Omega_{\widetilde{\Phi}}(\omega) \left[\frac{1}{6\Delta_{\mathrm{t}}\omega} \sin(6\Delta_{\mathrm{t}}\omega) \right]^2 . \tag{12}$$

The boxcar filtering results in an estimated pulse function that is highly asymmetric with λ close to zero.

The parameters of the stochastic model are $\langle A \rangle$, τ_{d}, λ, $\langle w \rangle$ and ε, which can all be estimated from realizations of the process. The parameters γ and ε, can be estimated from the PDF of realizations of the process or alternatively from the empirical characteristic function (ECF) of the normalized signal [57]. The average pulse amplitude $\langle A \rangle$ can then be estimated from γ and the sample mean of the realization. The pulse duration τ_{d} and asymmetry parameter λ can be estimated from the auto-correlation function or the PSD [56]. From γ and τ_{d}, the average waiting time $\langle w \rangle$ can be estimated. Finally, the deconvolution method can then be used to unravel the pulse arrival times and amplitudes, which allows to estimate the amplitude and waiting time distributions and the mean values of these directly, as will be discussed in section 3.3. Furthermore, in section 4.3 we provide a consistency check between these distribution parameters and the mean values $\langle A\rangle$ and $\langle w\rangle$ estimated from the moments.

3.3. Deconvolution algorithm

The RL deconvolution algorithm is a point-wise iterative procedure used to recover the amplitude forcing given a known pulse function [79–81]. This was done to achieve a broader range of waiting-time and amplitude statistics compared to the conditional averaging method and to relate them to plasma parameters. A detailed description and investigation of the deconvolution method is presented in reference [82]. Figure 2 shows how the deconvolution algorithm in incorporated into the study.

The full (un-normalized) FPP can be expressed as a convolution between the pulse function φ and a forcing signal $\mathcal{F}_K$,

$$\Phi_K\left(t\right) = \left[\varphi * \mathcal{F}_K\right]\left(\frac{t}{\tau_\mathrm{d}}\right), \tag{13}$$

where $\mathcal{F}_K$ consists of a train of delta-function pulses,

$$\mathcal{F}_K\left(t\right) = \sum_{k=1}^{K(T)} A_k \delta\left(\frac{t-s_k}{\tau_\mathrm{d}}\right). \tag{14}$$

Given an estimate of φ, we estimate $\mathcal{F}_K$ according to the iterative procedure

$$\mathcal{F}_j^{(n+1)} = \mathcal{F}_j^{(n)} \frac{\left(\Phi * \widehat{\varphi}\right)_j + b}{\left(\mathcal{F}^{(n)} * \varphi * \widehat{\varphi}\right)_j + b}, \tag{15}$$

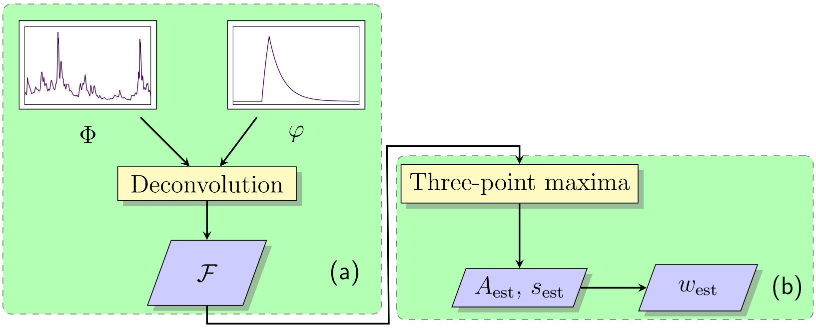

Figure 2. A schematic diagram showing how the RL deconvolution is utilized [82]. Firstly, (a) shows a measurement time-series Φ. Here, this is an excerpt of $\widetilde{I}_\mathrm{sat}$ from a Greenwald fraction of $f_\mathrm{GW} = 0.80$. The pulse function φ estimated from the PSD is deconvolved out to estimate $\mathcal{F}$. Finally in (b), a three-point maxima peak-finding algorithm is employed to find the estimated amplitudes A_est, arrival times s_est and hence the estimated waiting times w_est. The estimated amplitudes and waiting times are then used to estimate their respective distributions.

where the hat symbol $\widehat{\cdot}$ is used to denote a flipped vector, $\widehat{\varphi}_j = \widehat{\varphi}_{-j}$. The parameter b ensures positivity of the deconvolved signal: For $b = 0$, positive definite Φ, and positive definite initial guess $\mathcal{F}^{(0)}$, all subsequent iterations $\mathcal{F}^{(n)}$ are also positive definite. To maintain this property in the presence of noise, b is chosen such that $\left(\Phi * \widehat{\varphi}\right)_j + b > 0 \,\forall\, j$ [81]. The iteration in (15) is known to converge, minimizing $\Phi - \varphi * \mathcal{F}^{(n)}$ in the least-square sense under Gaussian noise. The choice of the initial guess $\mathcal{F}^{(0)}$ as well as the exact value of b may affect the rate of convergence, but does not influence the result as long as b is small compared to the mean signal value.

The outcome of the deconvolution process yields a time series consisting of pulses that are highly localized. However, it is important to note that the deconvolution does not typically reduce each pulse to the width of a single data point. To recover the pulses and to remove spurious events in parts of the signal without pulses, we apply a simple three-point running maxima with a threshold, tagging each data point as a pulse if it is larger than each of its neighbors and larger than $10^{-3}\langle A\rangle$.‡

The primary focus is to investigate the statistical properties of the fluctuations where the analysis is performed on normalized signals. However, it is not feasible to utilize a normalized signal as input for the deconvolution algorithm. This is because the normalized signal can result in a decay to an incorrect zero level, leading to a distorted representation of the pulse function. To address this issue, we rescale the normalized time series and perform the RL deconvolution algorithm on $\sqrt{\gamma(1+\varepsilon)}\widetilde{\Phi} + \gamma$. Here, γ and ε are estimated from either the PDF or the ECF of the signal. By incorporating this rescaling approach, we ensure that the deconvolution accurately captures the pulse function without being influenced by the normalization process.

The experimental measurement data reported in the following reveal a bi-exponential distribution of pulse amplitudes and waiting times. Such a bi-exponential pulse amplitude distribution follows from the assumption of a discrete uniform distribution of pulse velocities [93]. The bi-exponential amplitude distribution is mathematically described as

$$P_A(A) = \frac{q}{\langle A_<\rangle}\exp\left(-\frac{A}{\langle A_<\rangle}\right) + \frac{1-q}{\langle A_>\rangle}\exp\left(-\frac{A}{\langle A_>\rangle}\right). \tag{16}$$

Here, $0 < q < 1$ represents the probability that an event corresponds to a small-amplitude fluctuation. $\langle A_<\rangle$ denotes the mean of small-amplitude fluctuations, while $\langle A_>\rangle$ represents the mean of large-amplitude fluctuations. The average amplitude is given by $\langle A\rangle = q\langle A_<\rangle + (1-q)\langle A_>\rangle$. It is assumed that the amplitudes of these fluctuations correlate with the velocity, where larger-amplitude fluctuations are impacted the least by parallel drainage to the sheaths compared to smaller-amplitude fluctuations [93]. Consequently, the tail of the signal amplitude distribution

---

‡ In reference [82], a specific threshold relating to γ and ε was used on synthetic realizations of the process with noise which led to exponentially distributed amplitudes and waiting times. We move away from this threshold as it was found to be quite harsh when applied to these experimental measurement time series.

is predominantly influenced by the contribution of large-amplitude fluctuations. To estimate the mean values $\langle A_> \rangle$ and $\langle w_> \rangle$, we utilize the expression of the bi-exponential distribution rather than employing a tail fit in order to prevent any imposed hard limits. These mean values are later compared to $\langle A \rangle$ and $\langle w \rangle$ estimated from the statistical properties of the measurements in section 4.3.

4. Results

Here, we present results from the analysis performed on GPI and MLP measurement data from a line-averaged density scan and a plasma current scan. Tables 1 and 2 provide details of the duration of time windows considered for the analysis, line-averaged density, plasma current, and toroidal magnetic field considering these time windows, as well as shot numbers. The time windows are chosen such that both the plasma parameters and the fluctuation measurement time series are reasonably stationary.

Long time series measurements of at least several hundreds of milliseconds allow us to resolve the tails of the PDF so that γ is revealed, as are the flat, low frequency part of the PSDs, which aids in determining τ_d. In figure 3, un-normalized excerpts of ion saturation current time series are shown for $f_\mathrm{GW} = 0.12$ and $f_\mathrm{GW} = 0.81$. The upper panel of figure 3 shows larger signal amplitudes where the bursts appear more intermittent for $f_\mathrm{GW} = 0.81$ compared to $f_\mathrm{GW} = 0.12$ shown in the lower panel, indicating strongly intermittent, large-amplitude fluctuations at high line-averaged densities. It is worth noting that the background appears to be insignificant compared to the large bursts in both time series.

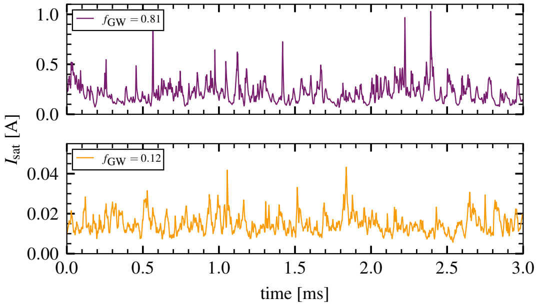

Figure 3. Excerpts of ion saturation current measurements from the MLP dwelling the the far-SOL. The upper panel shows measurements from the highest Greenwald fraction case of the density scan $f_\mathrm{GW} = 0.81$, whereas the lower panel shows the time series from the lowest Greenwald fraction $f_\mathrm{GW} = 0.12$. Note the different scales on the y-axes for both time series.

While the data for the scan in particle density comes from a dedicated experiment executed on a single runday, the data for the current scan were gathered from other

Table 1. Plasma discharges considered for the density scan using the GPI fluctuation measurements. We present the start time of the GPI time series analysis t_{start} and the duration of the time window considered T. In addition, we show the line-averaged densities $\overline{n}_{\mathrm{e}}$ and the associated Greenwald fraction f_{GW} averaged over the analysis time window. The plasma current I_{P} is in the range $0.51 - 0.55\,\mathrm{MA}$ and the toroidal magnetic field B_{T} is approximately $5.4\,\mathrm{T}$. The time averaged ρ-position is in the range $2.3 - 2.7\,\mathrm{cm}$, where ρ is the radial distance outside the LCFS after magnetically mapping the measurement location to the outboard midplane using EFIT. All of these discharges are from the same runday. These are all LSN except for the last $20 - 90\,\mathrm{ms}$ in the time series from shots 1160616025 and 1160616026, which are double null according to EFIT. Excluding these parts of the time series did not make a difference to the fluctuation statistics.

shot	t_{start} [s]	T [s]	$\overline{n}_{\mathrm{e}}$ [$\times 10^{20}\,\mathrm{m}^{-3}$]	f_{GW}
1160616009	1.25	0.2	0.86	0.24
1160616011	1.15	0.3	1.07	0.30
1160616016	1.15	0.3	1.60	0.45
1160616017	1.15	0.3	1.56	0.45
1160616018	1.15	0.3	1.65	0.47
1160616022	1.15	0.3	2.29	0.67
1160616025	1.15	0.3	2.76	0.82
1160616026	1.15	0.3	2.83	0.85

experiments on different rundays and under conditions over which the line-averaged density was not exactly the same. Tables 3 and 4 show the plasma parameters considered for this scan, for the GPI and MLP data respectively.

For the current scan, the MLP was operated in scanning mode, and a rather large radial bin in the far-SOL was chosen in order to calculate relevant statistical averages and distributions. Therefore, the time windows used on the MLP in this plasma current scan are shorter than the ones used in the other parameter scans, giving larger uncertainty in the parameter estimation and deconvolved amplitudes and waiting times in particular.

The GPI signals of interest were taken from diode view positions in the far-SOL. The time windows for the analyses were chosen so that the plasma parameters were steady and to ensure sufficient duration of the time series for estimating the FPP model parameters and distributions.

To assess the quality of the parameter fitting, we take samples from several GPI view positions at similar radial positions ρ in the far-SOL. Here, ρ is the radial distance outside the LCFS after magnetically mapping the measurement location to the outboard midplane by applying the magnetical equilibrium reconstruction calculated using EFIT. The position of the LCFS is thus at $\rho = 0$. The position of the LCFS may change slowly relative to the fixed locations of the views; therefore, the flux surfaces may move slightly relative to the GPI views. However, we will only consider fixed view positions.

We emphasize that the positions of the GPI and MLP in dwell mode are measuring fluctuations at different ρ values, where the MLP measurements are inside of those of the GPI. Power balance correction was applied to the GPI and MLP ρ positions in all of

Table 2. Plasma discharges considered for the density scan using the MLP in dwell mode. We present the start time of the MLP time series analysis t_{start} and the duration of the time window considered T. In addition, we show the same parameters that are given in table 1, together with the time-averaged position of the probe dwelling to take these measurements, which are quoted in terms of the relative distance from the LCFS, ρ. In machine coordinates, the probe is dwelling in the range $86.4 - 86.9\,\text{cm}$ across all of these plasma discharges. The plasma current I_{P}, is in the range $0.51 - 0.56\,\text{MA}$ and the toroidal magnetic field B_{T} is approximately $5.4\,\text{T}$. All of these discharges are from the same runday as in table 1. The connection length for the density scan is in the range $8 - 10\,\text{m}$. All of these plasma discharges were in LSN.

shot	t_{start} [s]	T [s]	$\overline{n}_{\text{e}}$ [$\times 10^{20}\,\text{m}^{-3}$]	f_{GW}	ρ [cm]
1160616007	1.03	0.27	0.46	0.12	1.23
1160616008	0.83	0.67	0.45	0.13	1.05
1160616010	0.5	1.0	0.76	0.21	1.25
1160616012	0.7	0.8	1.00	0.27	1.41
1160616015	0.75	0.35	1.29	0.36	1.40
1160616019	0.7	0.8	1.58	0.45	1.38
1160616018	0.7	0.8	1.63	0.47	1.28
1160616021	0.65	0.4	1.86	0.58	1.02
1160616020	1.0	0.5	2.12	0.60	1.17
1160616023	1.0	0.5	2.05	0.62	0.97
1160616024	1.0	0.5	2.09	0.63	0.76
1160616027	1.0	0.35	2.70	0.80	0.86
1160616026	1.0	0.35	2.73	0.81	0.88

Table 3. Plasma discharges considered for the plasma current scan using the GPI fluctuation measurements. We present the start time of the GPI time series analysis t_{start}, the length of the time window considered T, the plasma current I_{P} and toroidal magnetic field B_{T}. Divertor configurations for these discharges were all in LSN.

shot	t_{start} [s]	T [ms]	$\overline{n}_{\text{e}}$ [$\times 10^{20}\text{m}^{-3}$]	I_{P} [MA]	B_{T} [T]	f_{GW}
1160629026	1.22	0.28	1.87	1.07	5.40	0.27
1160629031	1.22	0.28	1.88	1.07	5.40	0.27
1160927003	0.78	0.61	1.44	0.79	5.36	0.28
1160616017	1.15	0.30	1.56	0.53	5.41	0.45
1160616016	1.15	0.30	1.60	0.53	5.40	0.46

the results shown in the study. Such corrections were made in order to mitigate possible EFIT errors in the location of the LCFS [94].

We focus mainly on the analysis performed on the ion saturation current from the MLP, as this is a widely measured plasma quantity across various devices. We point the reader to references [47] and [95], where data analysis has been performed on n_{e} and T_{e} fluctuation measurements.

Table 4. Plasma discharges considered for the plasma current scan using the ion saturation current data from the scanning MLP. We present the start time of the GPI time series analysis t_{start}, the length of the time window considered T, the plasma current I_{P} and toroidal magnetic field B_{T}. Divertor configurations for these discharges were all in LSN.

shot	t_{start} [s]	T [ms]	$\overline{n}_{\mathrm{e}}$ [$\times 10^{20}\mathrm{m}^{-3}$]	I_{P} [MA]	B_{T} [T]	f_{GW}
1160629031	1.3011	20	1.74	1.07	5.41	0.25
1140730018	1.1869	13	1.60	0.80	5.40	0.27
1160616016	1.2583	14	1.62	0.53	5.40	0.46

4.1. Radial profiles

The time-averaged radial profiles of the I_{sat} measurements from the scanning MLP in the density scan are presented in figure 4. These were averaged over 1 mm radial bins. The profiles are normalized to their respective separatrix values. The location of the limiter shadow, which is always fixed in major radius coordinates, is represented by the gray-shaded region in the ρ-coordinate space. When presenting this position relative to the LCFS, the ρ coordinate could change by approximately 5 mm during the pulse as noted above. For that reason, we show an approximate flux-position location of the limiter in figures 4(a) and 4(b) as a gray-shaded region that is not fixed relative to the LCFS. In machine coordinates, the probe was always 2 cm inside of the limiter radius for all discharges in the density scan. The time-averaged radial profiles in figures 4(a) and 5(a) are normalized by the separatrix value to emphasize the profile shape. However, as seen later in figure 10(a), there is no discontinuous jump in the mean values of the far-SOL quantities, I_{sat}, n_{e} and T_{e}, over the full density and f_{GW} scan.

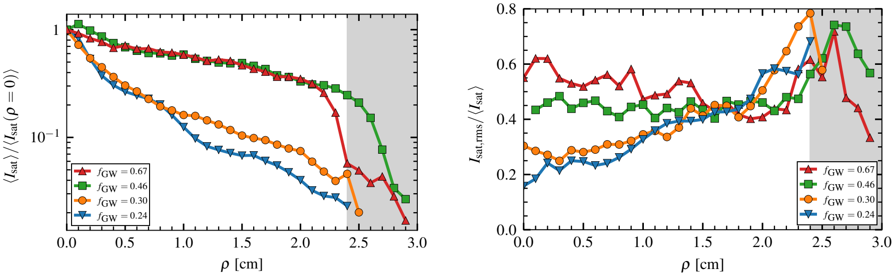

(a) (b)

Figure 4. Radial profiles of plasma parameters from the density scan: (a) $\langle I_{\mathrm{sat}}\rangle$ normalized by its estimated separatrix value and (b) I_{sat} relative fluctuations. The local limiter location at $Z = 11$ cm above the midplane is $R = 88.4$ cm (in local machine coordinates). The approximate flux-position location of the limiter using EFIT magnetic reconstruction is presented by the gray-shaded region.

Focusing on the lower Greenwald fraction cases in figure 4(a), a well-known two-layer structure can be seen from the radial profile of $\langle I_{\mathrm{sat}}\rangle$. Closer to the separatrix,

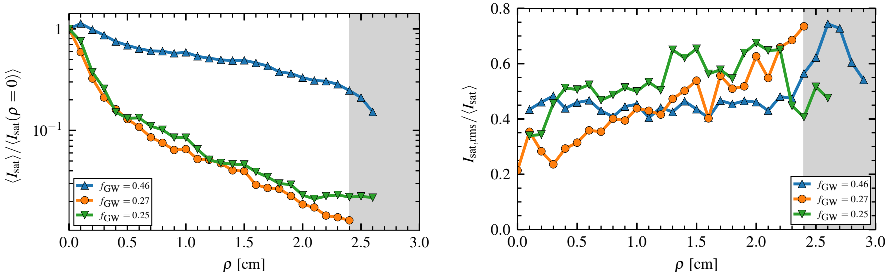

(a) (b)

Figure 5. Radial profiles of plasma paramters from the plasma current scan: (a) $\langle I_{\mathrm{sat}}\rangle$ normalized by its estimated separatrix value and (b) I_{sat} relative fluctuation levels. The local limiter location at $Z = 11\,\mathrm{cm}$ above the midplane is $R = 88.4\,\mathrm{cm}$. We show the approximate ρ location of the limiter using EFIT magnetic reconstruction represented by the gray-shaded region.

the near-SOL region shows a steep decay length with moderate fluctuation levels for these measurements. In comparison, the far-SOL exhibits longer scale lengths and a fluctuation level of order unity. As the line-averaged density increases, for Greenwald fractions $f_{\mathrm{GW}} \geq 0.46$, the far-SOL profile becomes broader and flatter, so that the far-SOL profile effectively extends all the way to the separatrix. The significant change in the mean profile can be attributed to the amplitudes becoming larger as well as intermittent, which impacts the nature of the cross-field transport in the SOL.

The radial variation in the I_{sat} relative fluctuations levels is presented in figure 4(b). Once again, the time-averaged quantities were calculated over 1 mm bins. The I_{sat} relative fluctuation levels are estimated as the ratio between the standard deviation and the sample mean. Near the separatrix, the relative fluctuation levels are low, resulting in significant pulse overlap for $f_{\mathrm{GW}} \leq 0.46$. For $f_{\mathrm{GW}} = 0.24$ the I_{sat} relative fluctuation levels increase from approximately 0.15 to 0.6 from the LCFS into the far-SOL, but are considerably higher for $f_{\mathrm{GW}} = 0.67$ and are around 0.5 over the entire SOL. The far-SOL scale lengths for radial $\langle I_{\mathrm{sat}}\rangle$ profiles were found to be 2.8 cm for $f_{\mathrm{GW}} = 0.67$, 2.2 cm for $f_{\mathrm{GW}} = 0.46$, 1.2 cm for $f_{\mathrm{GW}} = 0.30$ and 1.0 cm for $f_{\mathrm{GW}} = 0.24$, hence these scale lengths getting longer with line-averaged density. Overall, this suggests that for the highest line-averaged density studied, the whole SOL is dominated by large-amplitude fluctuations, suggesting that the cross-field transport comes mainly from the filaments.

These time-averaged radial profiles and relative fluctuation levels of the electron density and electron temperature have been previously reported in reference [91] for $0.1 \leq f_{\mathrm{GW}} \leq 0.5$, and are therefore not shown here. The mean n_{e} radial profile behaves similarly to the I_{sat} mean profile in figure 4(a). The mean T_{e} profiles decay strongly for the highest-density case, indicating that at higher densities the temperature drains faster. For low densities, this is similar to the time-averaged I_{sat} radial profile. The n_{e} relative fluctuation levels for the same discharges in figure 4 were found to vary little with radial distance for all Greenwald fractions. Furthermore, the T_e relative fluctuation levels were found to be consistently higher for $f_\mathrm{GW} \geq 0.46$ across the entire SOL compared to $f_\mathrm{GW} \leq 0.30$ but once again, varies little with radial position. Radial profiles of the relative fluctuation levels for the Greenwald fraction ranges $0.15 \leq f_\mathrm{GW} \leq 0.30$ have been previously demonstrated to increase radially outward for all line-averaged densities using the GPI [44].

The time-averaged radial profiles for the I_sat measurements are presented in figure 5 for various plasma currents and these are quoted in terms of Greenwald fractions. At large I_P values ($f_\mathrm{GW} = 0.25$ and $f_\mathrm{GW} = 0.27$), the distinct two-layer structure between the near- and far-SOL is again obvious, as was observed in figure 5(a), but there is no significant difference between these two profiles. The I_sat mean profile shows a broad and flat profile at the lowest I_P ($f_\mathrm{GW} = 0.46$), decreasing to 70 % of the reference value $\langle I_\mathrm{sat}(\rho = 0)\rangle$ at the limiter, as shown in figure 5(a). This is the same data from the same probe reciprocation as the one shown in figure 4(a). The far-SOL scale lengths from the radial $\langle I_\mathrm{sat}\rangle$ profiles were found to be 2.4 cm for $f_\mathrm{GW} = 0.46$, 0.9 cm for $f_\mathrm{GW} = 0.27$ and 1.0 cm for $f_\mathrm{GW} = 0.25$, therefore a decrease in the far-SOL scale length as the I_P is increases. The radial profiles with mean values of n_e and T_e show similar behavior to that for I_sat displayed in figure 5.

We now focus on the relative fluctuation levels of I_sat in figure 5(b). Here, $f_\mathrm{GW} = 0.27$ (high I_P) is comparable to both $f_\mathrm{GW} = 0.24$ and $f_\mathrm{GW} = 0.30$ in figure 4(b). Again $f_\mathrm{GW} = 0.46$ is the same in both figures 4(b) and 5(b). The highest I_P case, $f_\mathrm{GW} = 0.25$, behaves differently, but this discrepancy does not seem to affect the far-SOL statistics discussed in section 4.3. It does, however, prevent us from drawing firm conclusions about the effect of high I_P on the SOL profiles.

4.2. Fluctuation statistics

We present a detailed analysis of PDFs and PSDs for $\widetilde{I}_\mathrm{sat}$ signals from the MLP when dwelling in the far-SOL and for the GPI signals across the density scan. For this parameter scan we have long time series measurements from both diagnostics. We will focus on three different density/Greenwald-fraction cases, $f_\mathrm{GW} = 0.24$, 0.67 and 0.85 for the GPI measurements and $f_\mathrm{GW} = 0.21$, 0.47 and 0.80 for the MLP measurements. For simplicity and ease of interpretation, the figures of PDFs and PSDs from GPI will focus on time series measurements from the same APD view $(R, Z) = (90.68, -1.57)$ cm in machine coordinates, where $\rho = 2.3$ cm for $f_\mathrm{GW} = 0.24$, $\rho = 2.4$ cm for $f_\mathrm{GW} = 0.67$ and $\rho = 2.6$ cm for $f_\mathrm{GW} = 0.85$. Figures showing the parameters of the stochastic model as a function of all Greenwald fractions showing all the views considered are presented in section 4.3.

Probability distributions We present the histograms of the time-series measurements in figure 6. The PDFs of the GPI measurement data for various densities are shown in figure 6(a), while the MLP measurements are exhibited in figure 6(b). The parameters

γ and ε are estimated from the ECF of the normalized time series [57]. In all cases, the PDFs are positively skewed and flattened, indicating intermittent fluctuations even at low densities. The tails of the PDFs lift as the density increases for both GPI and MLP measurements, indicating increasingly intermittent time series. The noise ratio ε is low for all cases considered; the highest attained values are 0.12 and 0.08 for the MLP and GPI, respectively. Both of these maximal values were attained at the highest density.

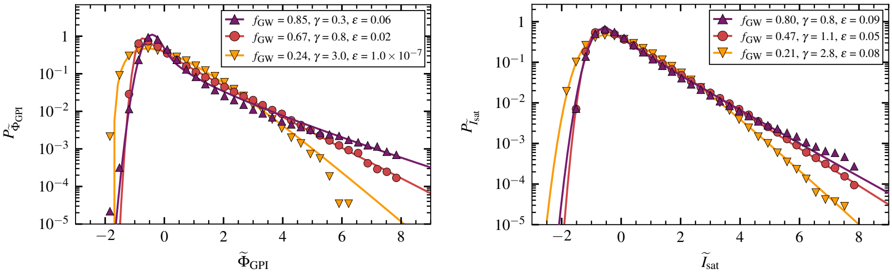

(a) (b)

Figure 6. The PDFs of the normalized time series of (a) the GPI light intensity measurements and (b) the MLP $\widetilde{I}_{\mathrm{sat}}$ fluctuation measurements for various line-averaged densities. The markers represent the measurement data. The solid lines represent the corresponding agreement of the measurement data with the stochastic model where the values for the intermittency and the noise-to-signal ratio ε, are quoted.

Power spectral densities As noted in section 3, the shape of the pulse function is reflected in the frequency dependence of the power spectral density. Assuming a two-sided exponential pulse function as described by (9), the parameters τ_{d} and λ can be estimated from the PSD of the normalized time series. The PSDs of the GPI and MLP time series for various line-averaged densities are presented in figures 7(a) and 7(b), respectively. The fits in figure 7(a) use (9) directly, while the fits in figure 7(b) use the spectrum of the pulse function convolved by the 12-point boxcar, shown in (12). As seen previously [44, 46], the power spectra of the GPI time series collapse to a similar shape. At $f_{\mathrm{GW}} = 0.85$, the relative noise floor of the spectra, evident above about 300 kHz, increases significantly. This apparent increase in the noise floor is actually due to the signal normalization, as seen in (1), and the fact that the overall GPI signal is lower at the highest densities relative to the electronic noise. This apparent increase in noise is consistent with the highest density having the highest ε-value, as discussed in the previous paragraph. For the MLP spectra, the ringing effect at high frequencies is clearly seen due to the preprocessing of the MLP data. The lowest density case has a significantly shorter duration than the higher density cases, as is visible in the spectra.

It is worth noting the differences in the estimates τ_{d} and λ of the two diagnostics. The pulse asymmetry parameter estimated from the GPI measurement of the light fluctuations is larger compared to the asymmetry parameter estimated from the MLP

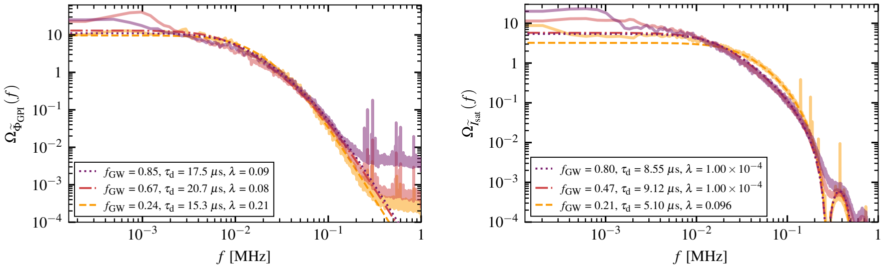

(a) (b)

Figure 7. The PSDs of the normalized time series from (a) the GPI and (b) the MLP ion saturation current measurements for various line-averaged densities. The measurement datasets are represented by the solid lines with lighter colors whereas best fits of the stochastic model are represented by the textured lines of the same colors. Appendix B discusses how these fits were made.

$\widetilde{I}_{\mathrm{sat}}$ measurements. Extremely small λ values estimated for the MLP for $f_{\mathrm{GW}} > 0.21$ seem to be hitting the lower limit of the fitting function. Overall, λ seems to get smaller as the density increases revealing highly asymmetric average pulse shapes. Furthermore, the τ_{d} estimates of the MLP measurements are smaller compared to those of the GPI. This will be discussed further in connection with figure 13(c).

Deconvolved pulse amplitude distributions The pulse amplitude and waiting time distributions estimated from the deconvolution algorithm for various line-averaged densities are presented in figures 8 and 9. Here, we show some of the Greenwald density fraction discharges meeting the criterion of deconvolution where $\gamma\theta \leq 1/20$, where $\theta = \triangle_{\mathrm{t}}/\tau_{\mathrm{d}}$ is the sampling time normalized by the duration time [82]. These means were estimated by performing a bi-exponential fit to the estimated amplitude distribution using (16) and using the exponential that describes the larger events. Further details of this can be found in Appendix B describing the challenges with fitting a bi-exponential to the GPI amplitude distribution. A cross-correlation analysis between pulse amplitudes and both preceding and following waiting times reveals that there are no such correlations, consistent with the assumption of uncorrelated pulses in the FPP model.

We present the estimated distributions from the deconvolution algorithm applied to the normalized GPI time series in figure 8. The estimated amplitude distributions for various Greenwald fractions on the GPI time series are presented in figure 8(a). The lack of a readily apparent density dependence can be attributed to the fact that the amplitude distribution depicted is derived from normalized signals. The deviation for large amplitudes from an exponential is due to the single data points in the histograms. The relative scarcity of data points did not allow high confidence in the bi-exponential fits to the GPI amplitudes, hence we do not quote their mean values as well as their fits. Instead, we show a gray-dashed line through the large amplitudes to emphasize

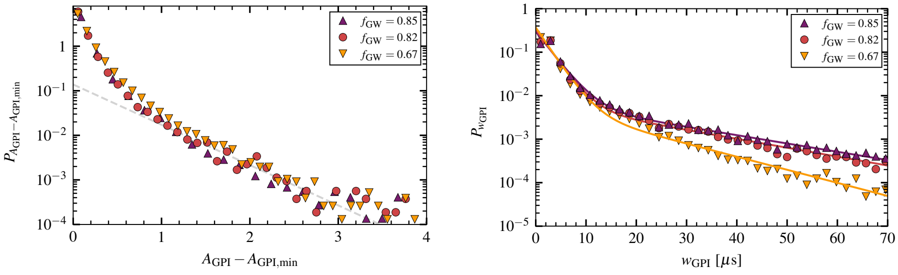

(a) (b)

Figure 8. Estimated distributions from the deconvolution algorithm applied to the normalized GPI time series. (a) Amplitude distribution of the normalized time series and (b) shows the waiting time distribution. The markers represent the histogram of the measurements for various densities. The gray-dashed line in (a) highlights an exponential decay. The solid lines show the bi-exponential fits to the waiting time distributions.

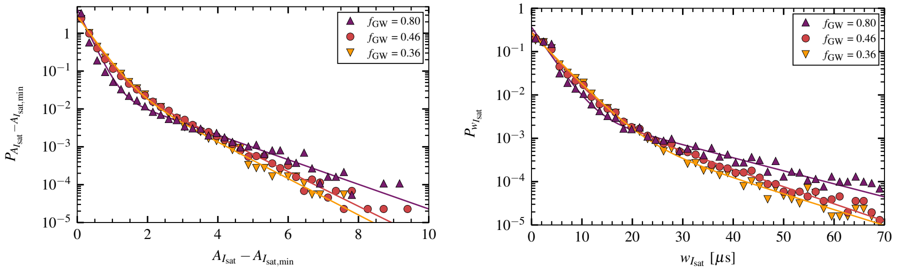

(a) (b)

Figure 9. Estimated distributions from the RL deconvolution applied to the normalized MLP ion saturation current measurements $\widetilde{I}_{\mathrm{sat}}$, where (a) shows the amplitudes and (b) are the waiting times for various densities. The markers in the legend represent the measurement data whereas the solid lines show the bi-exponential fits to these waiting time distributions.

the exponential decay. In figure 8(b), the estimated waiting time distribution for the GPI is shown. The estimated mean waiting times from the GPI measurements $\langle w_{>,\mathrm{GPI}}\rangle$ are 14.4 μs for $f_{\mathrm{GW}} = 0.67$, 21.8 μs for $f_{\mathrm{GW}} = 0.82$ and 22.7 μs for $f_{\mathrm{GW}} = 0.85$. This shows that as the line-averaged density is increased, the waiting times on average are becoming longer and the fluctuations are becoming increasingly intermittent in the GPI signal.

The RL deconvolution was applied to $\widetilde{I}_{\mathrm{sat}}$ measurements where the results are shown in figure 9. The functional shape seen in figure 9(a) indicates a density dependence in the amplitude distributions as the density limit is approached. The pulse amplitudes are approximately bi-exponentially distributed for all signals analyzed. For the distributions of the Greenwald fraction cases shown here, the mean of the estimated large amplitudes for the $\widetilde{I}_{\mathrm{sat}}$ measurements $\langle A_{>,I_{\mathrm{sat}}}\rangle$ in dimensional units are 0.09 A for $f_{\mathrm{GW}} = 0.36$, 0.12 A for $f_{\mathrm{GW}} = 0.46$ and 0.29 A for $f_{\mathrm{GW}} = 0.80$. In section 4.3, we show a consistency check of these means to $\langle A\rangle$ estimated from the sample mean Φ/γ. For the MLP $\widetilde{I}_{\mathrm{sat}}$ measurements, the estimated waiting time distribution is shown in figure 9(b). The mean of the estimated waiting times $\langle w_{>,I_{\mathrm{sat}}}\rangle$ for these densities are 11.7 μs for $f_{\mathrm{GW}} = 0.36$, 11.3 μs for $f_{\mathrm{GW}} = 0.46$ and 15.4 μs for $f_{\mathrm{GW}} = 0.80$. This shows that as the density limit is approached, longer waiting times are expected due to increasingly intermittent fluctuations.

4.3. Parametric analysis

Here, we investigate how fluctuating quantities measured by the MLP change in the line-averaged density scan in order to explain later the overall results from the estimations of the stochastic model's parameters.

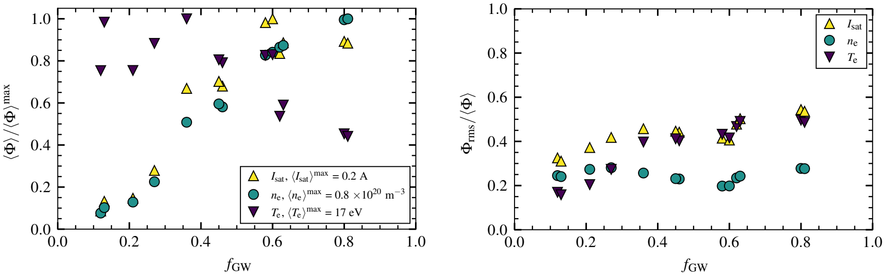

(a) (b)

Figure 10. Plasma parameters (shown in the legend with the maximal value across all Greenwald fractions), as a function of Greenwald fraction from the dwell MLP density scan, where (a) shows the normalized mean value of the plasma parameter and (b) shows the relative fluctuation levels of the plasma parameter for the length of the time windows shown in table 2.

The mean plasma parameters in the far-SOL versus Greenwald fraction, as measured by the MLP in dwell mode, are shown on the left-hand side of figure 10. In figure 10(a), $\langle I_{\mathrm{sat}}\rangle$ and $\langle n_{\mathrm{e}}\rangle$ increase with the Greenwald fraction, but saturate at high densities where $f_{\mathrm{GW}} > 0.6$. $\langle T_{\mathrm{e}}\rangle$ shows the opposite dependence, decreasing with the line-average density. This is expected if the power flow to the far-SOL does not increase in the same proportion as the density increase. The relative fluctuations estimated as a ratio between the root mean square of the plasma parameter and the mean plasma parameter are shown in figure 10(b). The I_{sat} relative fluctuations increase by a factor of two while the n_{e} relative fluctuations are roughly constant. Although $\langle T_{\mathrm{e}}\rangle$ decreases with Greenwald fraction, the relative fluctuation levels in T_{e} increase with density by a factor of more than two.

The Pearson correlation coefficients R of the plasma parameter fluctuations are shown in figure 11(a). Once again, these are from the MLP in dwell mode. For

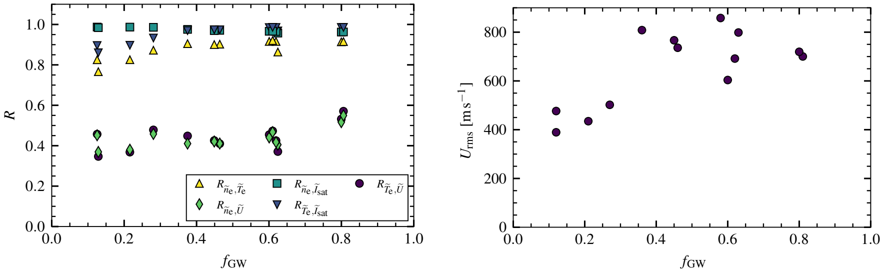

(a) (b)

Figure 11. Pearson correlation coefficients R of (a) the normalized electron density fluctuations and the normalized electron temperature fluctuations $R_{\widetilde{n}_\mathrm{e},\widetilde{T}_\mathrm{e}}$; the normalized electron density fluctuations and the normalized ion saturation current fluctuations $R_{\widetilde{n}_\mathrm{e},\widetilde{I}_\mathrm{sat}}$; the normalized electron temperature fluctuations and the normalized radial velocity fluctuations $R_{\widetilde{T}_\mathrm{e},\widetilde{U}}$; the normalized electron density fluctuations and the normalized radial velocity fluctuations $R_{\widetilde{T}_\mathrm{e},\widetilde{U}}$; the normalized electron temperature fluctuations and the normalized ion saturation current fluctuations $R_{\widetilde{T}_\mathrm{e},\widetilde{I}_\mathrm{sat}}$ and (b) the root mean square of the radial velocity fluctuations U_{rms} as a function of Greenwald fraction from the density scan.

the reader's interest, the joint PDFs of these plasma discharges using the MLP from this runday have already been shown in a previous study [91]. The $\widetilde{n}_\mathrm{e}$, $\widetilde{T}_\mathrm{e}$ and $\widetilde{I}_\mathrm{sat}$ fluctuations are seen to be strongly correlated for all Greenwald fractions, and the correlation coefficient is practically independent of Greenwald fraction. Normalized radial velocity fluctuations $\widetilde{U}$ were calculated using the plasma potential as described by (4). Fluctuations in particle density and electron temperature are both positively correlated with fluctuations in the radial velocity, and the correlation coefficients are practicaly identical and independent of Greenwald fraction. These correlations are not as strong as the correlation between particle density and temperature. While the correlations do not change significantly with density, the root mean square of the radial velocity fluctuations U_{rms}, shows a weakly increasing dependence, as shown in figure 11(b). By relating the average size of the velocity to $\tau_\mathrm{d}/U_{\mathrm{rms}}$, this suggests that on average, the sizes of these filaments are also weakly increasing since τ_d remains constant. The radial velocity of fluctuations increasing with line-average density have been reported previously in Alcator C-Mod [65, 67]. Considered together, these correlations suggest that large fluctuations in particle density are associated with large fluctuations in electron temperature as well as positive radial velocities.

We explore the radial particle flux using the n_e and I_sat fluctuation measurements and the total heat flux and how this scales using the stochastic model parameters in figure 12 as a function of the Greenwald fraction from the density scan. We present the mean values of the particle density flux using the electron density measurements $\langle \Gamma_{n,n_\mathrm{e}} \rangle$, the mean values of particle flux using the ion saturation current measurements $\langle \Gamma_{n,I_\mathrm{sat}} \rangle$

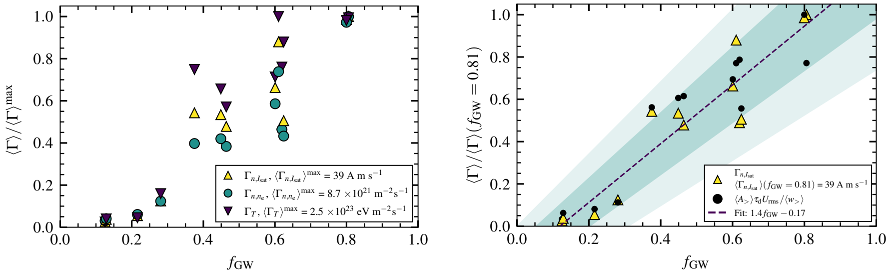

(a) (b)

Figure 12. The radial fluxes measures for varying Greenwald fraction from the density scan where (a) shows the mean radial particle flux using $n_{\rm e}$ fluctuation data, $I_{\rm sat}$ fluctuation data and the mean heat flux and (b) shows the how the flux scales with $\langle A_>\rangle\tau_{\rm d}U_{\rm rms}/\langle w_>\rangle$ (black circles) where $\langle A_>\rangle$ and $\langle w_>\rangle$ are estimated from the deconvolution (see figure 13) and $\tau_{\rm d}$ is estimated from the PSD. The dashed line is the linear fit to the statistical estimates of the flux. The shaded region shows the confidence intervals of 1σ and 2σ from the linear fit.

and the mean heat flux $\langle\Gamma_T\rangle$ which are calculated as

$$\langle\Gamma_{n,n_{\rm e}}\rangle = n_{\rm e,rms}U_{\rm rms}\langle\widetilde{n}_{\rm e}\widetilde{U}\rangle, \tag{17}$$

$$\langle\Gamma_{n,I_{\rm sat}}\rangle = I_{\rm sat,rms}U_{\rm rms}\langle\widetilde{I}_{\rm sat}\widetilde{U}\rangle, \tag{18}$$

$$\langle\Gamma_T\rangle = U_{\rm rms}\left\langle\widetilde{U}\left[\langle T_{\rm e}\rangle\widetilde{n}_{\rm e}n_{\rm e,rms} + \langle n_{\rm e}\rangle\widetilde{T}_{\rm e}T_{\rm e,rms} + \widetilde{n}_{\rm e}n_{\rm e,rms}\widetilde{T}_{\rm e}T_{\rm e,rms}\right]\right\rangle. \tag{19}$$

In figure 12(a), as expected, the radial particle flux increases with line-averaged density, indicating more transport where the filaments are hotter and larger in amplitude. The mean of the total heat flux, as calculated from (7), increases with density. Figure 12(b) shows the scaling of $\langle\Gamma_{n,I_{\rm sat}}\rangle$ calculated using $\langle\Gamma_{n,I_{\rm sat}}\rangle \approx \langle A\rangle\tau_{\rm d}U_{\rm rms}/\langle w\rangle$ since this combination of statistical quantities should be approximately proportional to the particle flux resulting from the radial motion of the filaments. We compare estimates of $\langle A_>\rangle\tau_{\rm d}U_{\rm rms}/\langle w_>\rangle$ to $\langle\Gamma_{n,I_{\rm sat}}\rangle$ as we have estimated the mean amplitudes and mean waiting times from the deconvolution of the $\widetilde{I}_{\rm sat}$ and estimate $\tau_{\rm d}$ from the PSD of the $\widetilde{I}_{\rm sat}$ measurements as shown in figure 7(b). The strong similarity in the scaling of these independently arrived at quantities serves as a consistency check and to increase confidence in the measurements. The minimum mean flux measurements were found to be all at $f_{\rm GW} = 0.13$ where this was $\langle\Gamma_{n,n_{\rm e}}\rangle = 2.3 \times 10^{20}\,{\rm m^{-2}s^{-1}}$, $\langle\Gamma_{n,I_{\rm sat}}\rangle = 1.0\,{\rm A\,m\,s^{-1}}$ and $\langle\Gamma_T\rangle = 6.3 \times 10^{21}\,{\rm eV\,m^{-2}s^{-1}}$; to avoid confusion that these markers in figure 12(a) appear to be at zero. These are all approximately 1/40 times their respective maximal values.

To summarize figures 10, 11, and 12, the largest filaments are hot, dense and fast compared to the background values, and their velocities appear to be increasing with Greenwald fraction. Although $\tau_{\rm d}$ remains approximately constant, increasing velocity indicates that the filaments are becoming larger in size. The independence of the correlations on the Greenwald fraction suggests that the physical mechanism of the blobs in the far-SOL is robust with Greenwald fraction.

The stochastic model parameters estimated from the line-averaged density and plasma current scans are presented in figure 13 and are plotted against Greenwald fraction. The intermittency parameter γ is shown in figures 13(a) and 13(b) for the MLP and GPI, respectively. We also show the average duration time τ_d in figure 13(c), the mean of the estimated waiting time $\langle w_> \rangle$ in figure 13(f) and the mean of the estimated amplitudes $\langle A_> \rangle$ in figure 13(e). The mean amplitudes are dimensionalized by $\langle I_\mathrm{sat} \rangle / \gamma$. The legend in figures 13(a) and 13(b) refers to the estimated parameters from the type of diagnostic and parameter scan. For the reader's interest, results showing how the fluctuation statistics change with respect to I_P instead of Greenwald fraction can be found in Appendix A.

Firstly, it is clearly shown from the line-averaged density scan that as the core density is increased, the fluctuations become increasingly intermittent for both the GPI (green squares) and the MLP (yellow triangles) for $f_\mathrm{GW} \gtrsim 0.45$ as shown in figures 13(a) and 13(b). The MLP shows an asymptotic decrease in the value of γ. A parabolic fit predicts an increase which is not seen in the data, therefore we employ an asymptotic regression on the MLP γ results revealing an approximate scaling of $1/f_\mathrm{GW}$. The MLP plasma current scan (purple inverted triangles) also shows that the fluctuations become strongly intermittent with increasing Greenwald fraction (decreasing I_P) but this dependence appears somewhat weaker than that resulting from an increase in density. Nonetheless, this result aligns well with the line-averaged density scan using the MLP.

However, the intermittency parameter estimated from the GPI plasma current scan (blue circles) increases from $f_\mathrm{GW} = 0.27$ to $f_\mathrm{GW} = 0.46$. This increase in the intermittency parameter (where fluctuations are becoming weakly intermittent) between low-intermediate Greenwald fractions has also been seen in previous results [38]. The GPI measurements from the density scan and plasma current scan show a spread in the estimated parameters. The diode views considered are nominally from similar flux positions and show some variation in the PDFs. These scans show similar trends where the intermittency increases with Greenwald fraction (that is, fluctuations becoming weakly intermittent). We utilize an asymptotic regression for the GPI γ results in figure 13(b) from $f_\mathrm{GW} \approx 0.46$ to describe the decrease in γ, which revealed an approximate scaling of $\sim 1/f_\mathrm{GW}^2$.

There is a spread in the intermittency parameter estimated from the GPI measurements for intermediate Greenwald fractions around $f_\mathrm{GW} \approx 0.46$. Note that for shot 1160616018 ($f_\mathrm{GW} \approx 0.47$) the MLP and the GPI were operational, and it is striking to see the differences in the estimated intermittency parameter. For shots 1160616026 and 1160616027 ($f_\mathrm{GW} \approx 0.81$), the MLP and GPI were also operational but there are little differences in the intermittency parameters. This discrepancy in the intermittency parameter between the GPI and the MLP ion saturation current is also reported in [48], where the same discharge from Alcator C-Mod was analyzed. In Appendix B, we investigate the quality of the fits to the GPI measurements from the

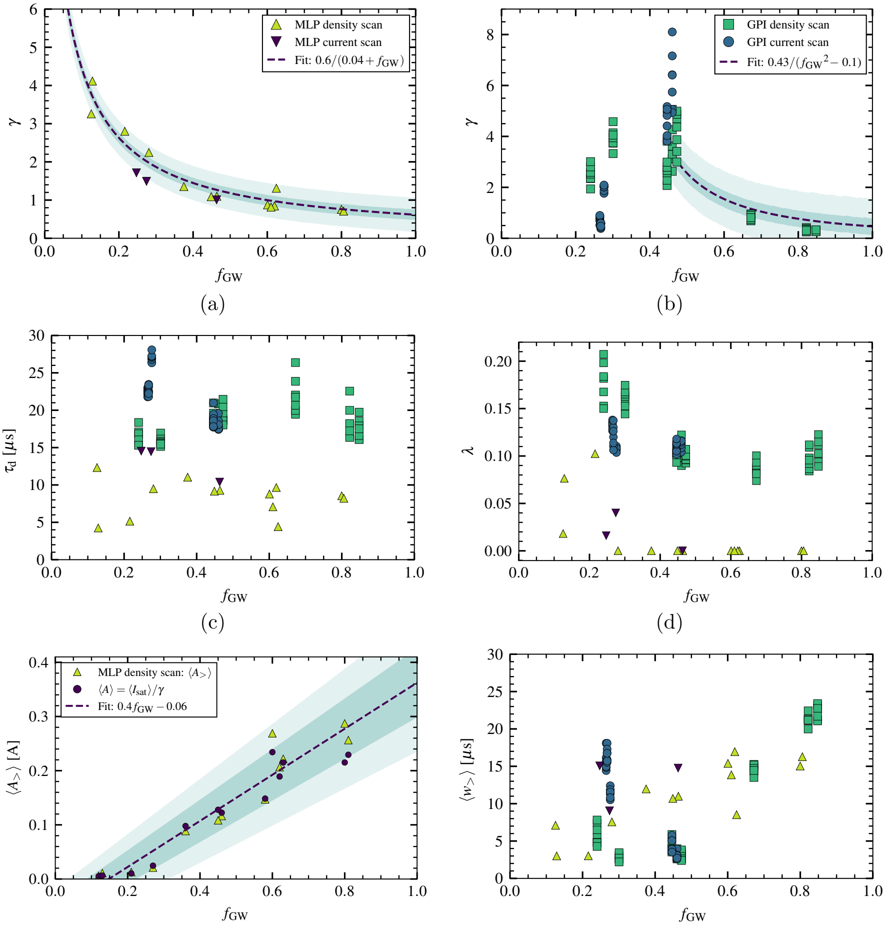

(a) (b)

(c) (d)

(e) (f)

Figure 13. Summary of figures showing how the stochastic model parameters, estimated from the density scan and plasma current scan, change with Greenwald fraction: (a) Intermittency parameter from the MLP density and current scan where we employ an asymptotic fit (purple dashed-line); (b) Intermittency parameter from the GPI density and current scan showing a reciprocal square fit (purple dashed-line) for $f_{GW} > 0.45$; (c) the duration time; (d) asymmetry parameter; (e) estimated mean amplitude $\langle A_> \rangle$ shown are only from the MLP $\widetilde{I}_{sat}$ density scan as a function of Greenwald fraction. These are compared to $\langle A \rangle = \langle I_{sat} \rangle / \gamma$ (purple circles) where we show the linear fit (purple dashed-line). (f) shows the estimated mean waiting time $\langle w_> \rangle$, from the bi-exponential fit. The markers represent which diagnostic and the type of scan in which the model parameters are estimated which can be inferred to the legends in (a) and (b). The shaded regions show confidence intervals of 1σ and 2σ.

mid-Greenwald fraction discharges $f_{\mathrm{GW}} = 0.47$ and found that these GPI measurements do not have an elevated tail and show poor agreement with the stochastic model. Thus the fitted values of γ depend heavily on the fit ranges, explaining some of the spread in the results. In contrast, the distributions of the GPI normalized time series for $f_{\mathrm{GW}} > 0.6$ are well fitted. The MLP $\widetilde{I}_{\mathrm{sat}}$ measurements show good agreement for all Greenwald fractions.

Next, in figure 13(c), the duration times estimated from the far-SOL GPI and MLP measurements seem robust against changes in line-averaged density. On average, the duration times estimated from the GPI measurements are larger than those found the MLP measurements. The small duration times seen from some of the MLP measurements may be due to strong poloidal velocities present in the SOL as also discussed in reference [65]. The larger estimates of the pulse duration times from the GPI is due, at least in part, to spatial averaging. For example, a $1\,\mathrm{cm}$ filament moving past a probe tip at $1\,\mathrm{km\,s^{-1}}$, will have a $\tau_{\mathrm{d}} \approx 10\,\mu\mathrm{s}$. If a single GPI view averages over a $0.7\,\mathrm{cm}$ radial region, then it will measure a $\tau_{\mathrm{d}} \approx 17\,\mu\mathrm{s}$ for the same $1\,\mathrm{cm}, 1\,\mathrm{km\,s^{-1}}$ filament. A $0.7\,\mathrm{cm}$ spatial smoothing, while larger than the $0.38\,\mathrm{cm}$ optical in-focus spot size, can easily result from the finite size of the gas cloud and the $\sim 8^\circ$ angle of the viewing chord relative to the local fieldline and provide a likely reason for the difference in the estimated τ_{d} values measured by the two diagnostics. The effects of spatial averaging would also impact the estimated λ, resulting in larger values, and hence a more symmetric pulse shape compared to the MLP. The observation that the discrepancies in the GPI and MLP evaluations of τ_{d} and λ are likely due to the poorer GPI spatial resolution is not surprising since, as demonstrated, spatial resolution can enter into the evaluations if it is not significantly smaller than the typical blob-size. It is therefore important that this effect be considered when performing detailed fluctuation analyses. However, it does not render the finite-resolution GPI measurements unsuitable for such analyses since GPI measurements still provide valuable long time-series data over the GPI field-of-view and under edge plasma conditions where heat-fluxes are too large for a scanning probe.

Although the plasma current scan shows far fewer data points than the density scan, there seems to be no significant trend in τ_{d} with Greenwald fraction. The MLP current scan points are within the scatter of the MLP density scan. Once again, the duration times estimated from the GPI plasma current scan are larger compared to those estimated from the MLP plasma current scan.

The asymmetry parameter for the various scans is shown in figure 13(d). λ values between 0.02 and 0.1 are measured by the MLP for $f_{\mathrm{GW}} < 0.3$. The very small λ values estimated at higher Greenwald fractions are due to reaching the lower limits of the fitting technique, suggesting a pulse shape that is close to a one-side exponential with a very fast initial rise. The λ evaluations from the GPI data show a decrease in λ as f_{GW} increases to approximately 0.45. Above that Greenwald fraction, λ is essentially constant. This suggests that the shape of the fluctuations, on average, appear more asymmteric at higher densities. The results from the GPI plasma current results are

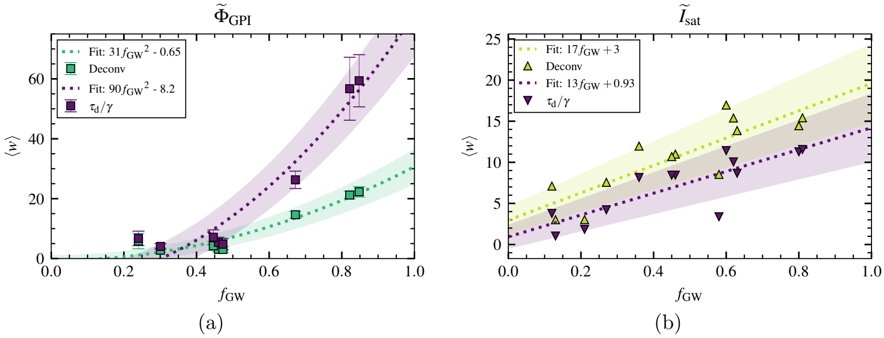

(a) (b)

Figure 14. Comparison of the mean waiting times from the fluctuation statistics (τ_{d}/γ) and the RL deconvolution algorithm represented by the markers. Focusing on results from the density scan, (a) GPI shows the average of the mean waiting times for all diode view positions considered where the error bars correspond to the maximum and minimum mean waiting times. The dotted lines show a non-linear regression for the GPI. (b) shows the mean waiting time estimated from the MLP $\widetilde{I}_{\mathrm{sat}}$ measurements. The dotted lines for the MLP scaling represent a linear regression. The shaded regions correspond to 1σ intervals of the results.

within the scatter of the GPI density scan.

In figure 13(e), the mean amplitudes of the ion saturation current fluctuations are presented in physical units for all densities considered. These mean values were achieved by performing bi-exponential fits to the estimated amplitude distribution using (16) to get $\langle A_{>} \rangle$ which is then multiplied by $\langle I_{\mathrm{sat}} \rangle / \gamma$. Since we are interested in the large-amplitude fluctuations under the reasonable assumption that they dominate the cross-field transport, we present the estimated mean amplitude of these fluctuations. As expected, the mean amplitudes of the fluctuations increase with the core density, indicating that these strongly intermittent fluctuations become increasingly large. In conjunction with the flux of the particle density shown previously in figure 12, at high Greenwald fractions there is a higher level of particle transport with fluctuations in the far-SOL, driven by large-amplitude events.

The mean waiting times in figure 13(f) are estimated by performing a bi-exponential fit to the deconvolved waiting time distribution to avoid the effects of noise and blob dissipation, which affect the smaller waiting times the most. We focus on the mean of the larger waiting times. In figure 13(f), the mean waiting times from the two diagnostics are roughly similar at similar Greenwald fractions for both scans, except at $f_{\mathrm{GW}} = 0.3$ and 0.45, where the GPI-measured waiting times are smaller than those measured by the MLP. The reason for this is not known and is confusing since we expect that the GPI-measured waiting times should be greater than or equal to those from the MLP since the GPI measures at ρ values larger than those for the MLP, as will be discussed below. Nevertheless, the overall trend with Greenwald fraction is similar and notable.

We look at a comparison of the mean waiting times in figure 14 between the estimation from the fluctuation statistics (i.e. $\langle w \rangle = \tau_\mathrm{d}/\gamma$, where τ_d is evaluated from the PSD and γ is evaluated from the ECF) and from the deconvolution algorithm. The methods used to estimate γ and τ_d involve no thresholding which will lead to shorter mean waiting times. For the GPI mean waiting times, we employ a non-linear regression $\langle w \rangle = \alpha f_\mathrm{GW}^2 + c_1$, where the slope of this regression is α and c_1 is the intercept. In contrast, a linear regression $\langle w \rangle = \beta f_\mathrm{GW} + c_2$, was performed on the MLP mean waiting times where the slope of this scaling is referred to and β and the intercept it given by c_2.

We present these scalings for the GPI in figure 14(a) showing the mean waiting times estimated from the deconvolution algorithm and the mean waiting times estimated from the fluctuation statistics. We see a divergence of these results for $f_\mathrm{GW} > 0.5$ where these mean waiting times are unequal. The regression reveals a scaling of $\alpha_{\tau_\mathrm{d}/\gamma} = 90$ for $\langle w \rangle = \tau_\mathrm{d}/\gamma$ and $\alpha_\mathrm{Deconv} = 31$ for $\langle w_> \rangle$ estimated from the bi-exponential fit to the deconvolved waiting times. We will present the MLP results before discussing this discrepancy.

For the MLP $\widetilde{I}_\mathrm{sat}$ measurements, shown in figure 14(b), the regression reveals a scaling of $\beta_{\tau_\mathrm{d}/\gamma} = 13$ for $\langle w \rangle = \tau_\mathrm{d}/\gamma$ and $\beta_\mathrm{Deconv} = 17$ for $\langle w_> \rangle$ estimated from the bi-exponential fit to the deconvolved waiting times. However, the mean waiting times calculated from τ_d/γ are lower than the mean waiting time estimated from the bi-exponential fit on the deconvolved waiting time distribution. This is due to the threshold-independent estimation of γ and τ_d taking into account all of the fluctuations in the time series, which will naturally lead to slightly lower mean waiting times.

We now turn to the discrepancy between $\langle w \rangle$ and $\langle w_> \rangle$ seen for the GPI but not for the MLP in figure 14. For the MLP, figure 9 shows that the large amplitudes and waiting times indeed follow exponential distributions consistent with the FPP. That is corroborated by the favorable comparison in figure 14(b) and indicates that the small amplitudes and waiting times are mainly due to the noise process. For the GPI, figure 8 shows the same exponentially distributed large waiting times, but we did not produce convincing fits to the amplitude distribution in figure 8(a). Using the non-exponential amplitude distribution of the GPI as a working hypothesis, the discrepancy between $\langle w \rangle$ and $\langle w_> \rangle$ for the GPI may be explained as follows: Numerical testing suggests that a positive definite amplitude distribution with higher flatness than an exponential distribution leads us to underestimate γ, if we make a fit using the Gamma distribution from the standard FPP with exponential amplitudes. If this is the case, as it is for the amplitudes in figure 8(a), γ has been underestimated for the GPI leading to an overestimate of $\langle w \rangle = \tau_\mathrm{d}/\gamma$, consistent with figure 14(a). The opposite effect, that a positive definite amplitude distribution with lower flatness than the exponential distribution leads us to underestimate γ, is seen in figure 3 in reference [58]. This explanation remains tentative, however, as a wrong estimate of γ leads to an incorrect rescaling $\sqrt{\gamma(1+\varepsilon)}\widetilde{\Phi} + \gamma$, it also influences the deconvolution and in turn the deconvolved amplitude distribution. A consistent estimate requires further modelling work.

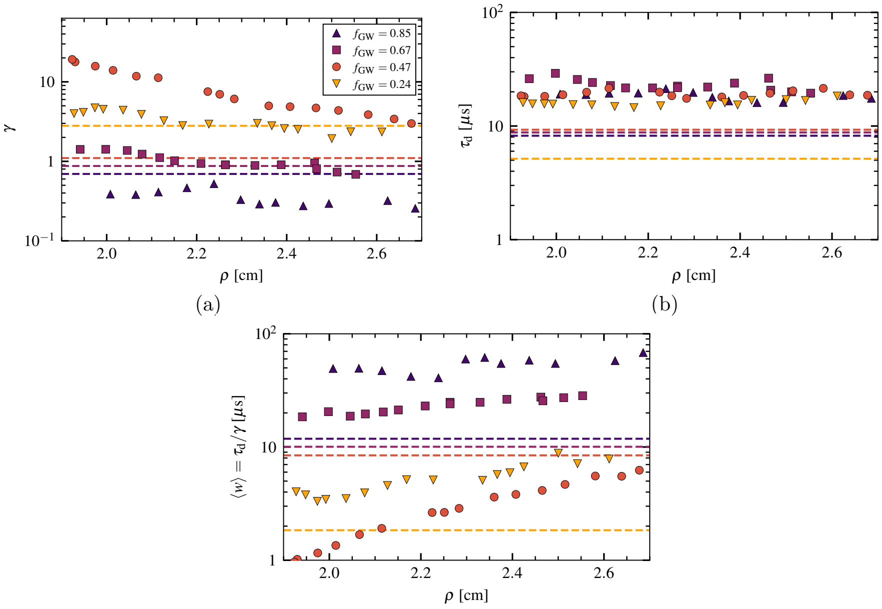

(a) (b)

(c)

Figure 15. The stochastic model parameters estimated from the GPI square markers) where (a) γ, (b) τ_{d} and (c) $\langle w \rangle = \tau_{\mathrm{d}}/\gamma$ are plotted as a function of the GPI view location in terms of ρ. Here, we take into consideration a larger range of views compared to what is shown in previous figures to demonstrate how the statistics change with ρ. The legend is shown in (a) where the colors represent the Greenwald fractions from the GPI density scan. The MLP results are plotted as dashed lines at similar Greenwald fractions to the GPI results, indicated by the same colors as shown in the legend. The MLP measures the fluctuations at a significantly smaller ρ ($\approx 0.9 - 1.4$ cm, see table 2) compared to the GPI, but is shown here for comparison.

Investigating the GPI measurements further, we present how ρ may influence the statistics at various Greenwald fraction densities. This is presented in figure 15 where we also show the MLP results at similar densities to the GPI as colored dashed lines for comparison and we recognize that these fluctuations measured by the MLP were taken at a lower ρ location, as seen in table 2. γ as a function of ρ is presented in figure 15(a) for all of the diode views considered in this study. For $f_{\mathrm{GW}} \leq 0.47$, the value of γ decreases (becomes more intermittent) as ρ increases which is consistent with previous results [44]. The other Greenwald fraction cases are decreasing in the ranges of ρ shown in figure 15(a) but not as strongly as $f_{\mathrm{GW}} = 0.47$. As ρ increases, filaments experience dissipation through parallel transport as they propagate through the SOL. As we approach higher line-averaged densities where $f_{\mathrm{GW}} \geq 0.67$, we have strongly intermittent fluctuations where $\gamma < 1$ across the ρ-space presented in figure 15(a) [54]. This is due to the flattening and broadening of the SOL profiles observed in figure 4. The range of MLP γ values shows that these are smaller compared to the GPI estimate at $f_{\mathrm{GW}} = 0.47$. However, for the highest density case, variation in ρ makes little difference to the intermittency values from both diagnostics.

The pulse duration times as a function of ρ in figure 15(b) seem to vary little, consistent with previous results [44]. We have explained earlier the differences in the estimation of τ_{d} between the MLP and GPI. In figure 15(c) where $\langle w \rangle = \tau_{\mathrm{d}}/\gamma$, these means increase with ρ for the Greenwald fractions presented here which is indicative of the effects of pulse overlap shown in figure 15(a). In particular, $f_{\mathrm{GW}} = 0.85$ shows that the values for $\langle w \rangle$ remain constant with ρ due to flat profiles, as previously discussed. For $f_{\mathrm{GW}} \geq 0.67$, $\langle w \rangle$ from the MLP are lower overall compared to the high density GPI results. The GPI views are seeing fluctuations at a larger ρ location, hence larger $\langle w \rangle$.

In general, figure 13 summarizes the parametric analysis when it comes to changing the line-averaged density and plasma current in Alcator C-Mod. From both diagnostics, we see the same trends with fluctuations becoming strongly intermittent, increasing mean waiting times, and no change in the average duration times with increasing Greenwald fraction. At some values of f_{GW}, the actual values $\langle w_{>} \rangle$ and γ are similar, while at others they disagree but within a factor of two. The actual values of τ_{d} differ consistently by a factor of approximately two.

5. Discussion and conclusions

The fluctuation statistics for various plasma parameters in ohmic, diverted single-null configurations are presented, using time-series data from GPI and the MLP. The profiles of the relative fluctuation levels with increasing main-plasma line-averaged density suggest that fluctuations become more intermittent. As the densities increase, the observed shift in shape of the histograms obtained from the normalized time series can be attributed to the reduced occurrence of filaments with higher mean amplitudes and velocities. The agreement with the stochastic model at low line-averaged densities is well established [38, 44–46]. Here we demonstrate that this agreement continues to hold for high line-averaged densities, indicating that the mechanism behind generating these filaments does not change with density.

The deconvolution algorithm was used to recover the pulse amplitudes and arrival times, as opposed to the conditional averaging technique, in order to provide statistics for a much more inclusive range of fluctuation amplitudes. Large filaments are believed to have an outsized contribution to plasma–wall interactions. Therefore, we only consider the large amplitudes and large waiting times in the analysis of the deconvolution. The deconvolution shows that the mean amplitudes and the mean waiting times increase for the ion saturation current measurements at increasing line-average densities. Increasing mean waiting times is contrary to the idea that the filaments occur more frequently as the density is increased which was an observation made from GPI measurements at low densities [38, 44, 46]. However, our analysis shows that this is not the case for the MLP. Despite the fluctuations occuring less frequently at high densities, the particle and heat fluxes increase significantly where the filament amplitudes are considerably large, thereby amplifying plasma-wall interactions.

The shape of normalized frequency power spectra appears independent of the Greenwald fraction. This means that the temporal scale of these fluctuations, as parameterized by the quantity, τ_d, stays roughly constant as the density increases. Inferring from the fluctuation statistics at lower Greenwald fractions, signals from both the GPI and the MLP show more pulse overlap compared to higher Greenwald fraction cases where the pulses appear more isolated and larger in amplitude.

Differences in duration times and mean amplitudes between GPI and MLP can be attributed to the effects of spatial averaging as explained in the previous section. The factor of two difference between the GPI and MLP estimated duration times are reasonable. The MLP shows shorter duration times estimated from the frequency power spectral density of the far-SOL measurements with no dependence on the Greenwald fraction. Furthermore, absolute values of the amplitudes can be recovered from the MLP measurements.

In references [38] and [46] it was shown that γ increases with line-averaged density up to $f_\mathrm{GW} = 0.35$. Observing these time series from the outermost diode view only, reference [38] used a four-point density scan up to $f_\mathrm{GW} = 0.35$ and showed the same trends as shown in figure 13(b). There was not enough from the two-point density scan in reference [46] to see a clear trend. These studies did not go to high enough Greenwald fractions in density to see that the value of the intermittency parameter decreases with Greenwald fraction. It remains unclear as to why the γ value peaks at $f_\mathrm{GW} \approx 0.46$ for the GPI where these observations are not seen in the MLP γ scaling with Greenwald fraction.

There are strong correlations between the $\widetilde{n}_\mathrm{e}$, $\widetilde{U}$ and $\widetilde{T}_\mathrm{e}$ fluctuations. These correlations are constant throughout the line-average density scan, indicating that the physics behind filament propagation at increasing line-averaged densities is not changing. However, the U_rms increases with the line-average density, suggesting that the size of the filaments is increasing since the durations times are constant. Consequently, at higher line-average densities, intermittent and large-amplitude fluctuations of the electron density and temperatures at high velocities will increase plasma-wall interaction. Density and velocity fluctuations that appear in phase, as demonstrated by the correlation study, lead to large particle flux events. This is consistent with the observation that the midplane neutral pressure increases with line-average density [18].

5.1. Comparison to other devices

Previously, scans in plasma current were performed in TCV, MAST and DIII-D. In TCV, it was seen that the plasma current does not make a difference in the shape of the probability density functions of the Langmuir probe time series and the conditionally averaged waveforms [34]. Also, at lower plasma currents, the mean profile becomes broader. Despite the change in collisionality in the study presented in reference [34], this feature did not make a difference in the shape of the probability density functions and hence the intermittency. In MAST, a plasma current scan revealed that the radial velocity and radial size of L-mode filaments decrease with increasing plasma current, thus decreasing radial transport [96]. In DIII-D, similar results were also observed in which plasma ion fluxes to the low-field side increased with decreasing plasma current [33]. The radial mean profiles from the Alcator C-Mod plasma current analysis is in agreement with these previous findings.

Alcator C-Mod and TCV are most similar in machine size, but differ when it comes to divertor design [97]. It was found in TCV that as the line-averaged density increases, the filament velocities become increasingly larger and the profiles become flatter and broader; features also exhibited in Alcator C-Mod [35, 67, 68, 91]. Interestingly, it was found in TCV for various line-averaged densities in ohmic, diverted single-null plasmas that the PDFs of the probe measurements at the wall radius do not change as shown in reference [35] which is in disagreement with the Alcator C-Mod density scan results.

The SPARC tokamak ($R = 1.85\,\mathrm{m}$ and $a = 0.57\,\mathrm{m}$) is planning to operate initially in L-mode [98]. Despite this study being a single-machine scan, we utilized the scalings presented in this study, and extrapolate to the outer limiters that SPARC will have a particle wall flux of approximately $7 \times 10^{18}\,\mathrm{m}^{-2}\mathrm{s}^{-1}$. This is a decrease of two orders of magnitude compared to Alcator C-Mod at similar Greenwald fractions.

5.2. Conclusion

Radially propagating far-SOL fluctuations become increasingly intermittent with Greenwald fraction. Notably, however, there exist significant differences between the results from GPI time-series (as measured at ρ between 2.3 and 2.7 cm) and MLP time-series (as measured at ρ between 0.8 and 1.4 cm) in terms of the average duration times across all Greenwald fractions, as well as the intermittency found at low-intermediate Greenwald fractions. These findings are intriguing and warrant further investigation in future research. Nonetheless, for $f_{\mathrm{GW}} \gtrsim 0.45$ it is worth noting that both diagnostics demonstrate strongly intermittent fluctuations with similar intermittency parameters. The continuous change in all statistical properties of the mirror-Langmuir probe data with Greenwald fraction indicates that there is no new physics mechanism as the empirical discharge density limit is approached.

We clarify the scalings of the stochastic model parameters with a wider range of Greenwald fractions which we have found for γ, $\langle A \rangle$, $\langle w \rangle$ and the particle flux. As a result of increasing line-averaged density, we see increasing temperatures of these fluctuations where filaments are getting hotter and move with increased radial velocities and amplitudes. Even though the mean waiting times between consecutive fluctuations get longer with increasing density, the filaments observed in the far-SOL are larger in amplitude, carrying radially most of the particle and heat. This leads to a significant increase in the plasma density at the wall. In turn, this will lead to increased plasma–wall interactions which will threaten the life-time of the first wall for future fusion devices and high duty cycle confinement experiments that plan to operate at high densities. Motivated by the scalings unraveled in order to inform predictive capability, we made some initial estimates for SPARC on the expected particle wall flux for an L-mode scenario.

Further work will focus on how the statistics on intermittent plasma fluctuations in the far-SOL change with machine size across various fusion devices, i.e. Alcator C-Mod, DIII-D, TCV and MAST. In addition, investigations are also underway on how profiles change with the Greenwald fraction, other plasma parameters, and confinement modes. This would use an extended version of the stochastic model recently developed by the UiT group that includes the radial position and the parallel drainage time [93].

Data availability statement

The data cannot be made publicly available upon publication because no suitable repository exists for hosting data in this field of study. The data that support the findings of this study are available upon reasonable request from the authors.

Acknowledgments

This work was supported by the Tromsø Research Foundation under grant number 19_SG_AT and the UiT Aurora Centre Program, UiT The Arctic University of Norway (2020). Alcator C-Mod data were generated and maintained under US Department of Energy awards DE-FC02-99ER54512 and DE-SC0014264. Support for A.Q.K. was provided by Commonwealth Fusion System under the grant number RPP-022. Support for J.L.T. was provided by the US Department of Energy, Fusion Energy Sciences, award DE-SC0014251. The first author thanks the MIT Plasma Science and Fusion Center for their generous hospitality where this work was conducted. Finally, discussions with Gregor Decristoforo are gratefully acknowledged.

Appendix A. Plasma current scan

The parameters of the FPP model are plotted against I_P in figure A1 for both the GPI and the scanning MLP data. The means of the estimated amplitudes are not plotted because of the short time series of the scanning MLP data and questionable absolute values of the GPI light intensity measurements. For the GPI results shown here, we present all the diode views considered at time-averaged ρ values ranging between $1.6 - 2.0\,\mathrm{cm}$. The GPI shows that as I_P is changed, the parameters of the FPP model estimated from the time series are impacted. In particular, we observe stronger intermittency in the time series with increasing I_P shown in figure 1(a). In contrast, the MLP $\widetilde{I}_\mathrm{sat}$ measurements do not show such trends between the γ and I_P. This is consolidated by the profiles of the relative fluctuation levels showing indifference to the change in I_P, as shown in figure 5. The contradiction between these two diagnostics

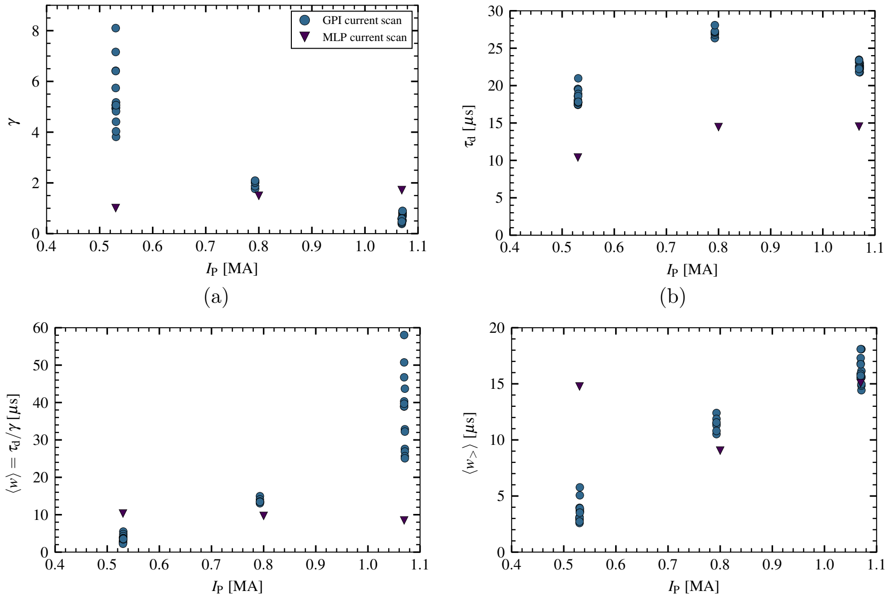

(a) (b)

(c) (d)

Figure A1. The stochastic model parameters plotted against plasma current. (a) Intermittency parameter, (b) the duration time, (c) mean waiting time from τ_d/γ and (d) estimated mean waiting time from the deconvolution, all as a function of plasma current showing estimated parameters from the GPI (blue circles) and the MLP $\widetilde{I}_\mathrm{sat}$ data (purple inverted triangles).

highlights the differences between them for fluctuation analysis, where the MLP is more of a localized measurement of plasma parameters compared to the GPI which is strongly impacted by spatial averaging.

In figure 1(b) for both diagnostics, τ_d seems independent of I_P where the MLP duration times are shorter compared to the GPI, which we also observe in the line-averaged density scan in figure 13(c). The GPI τ_d estimates are consistently a factor of approximately two larger than the MLP τ_d estimates, once again due to spatial averaging. These results imply that the plasma current does not impact the filament duration times estimated from the GPI and MLP.

The mean values of the estimated waiting time for both diagnostics are presented in figure 1(d). The GPI shows an increase in the mean estimated waiting time with I_P, further suggesting that fluctuations become more intermittent with I_P. This is consistent with decreasing intermittency (fluctuations becoming strongly intermittent) as seen in figure 1(a). However, for the MLP, no such trends are observed and the values for $\langle w_> \rangle$ seem to be higher compared to the GPI. Compared to the mean waiting time estimated from $\langle w \rangle = \tau_\mathrm{d}/\gamma$ as shown in figure 1(c), the MLP $\langle w \rangle$ also shows no change with I_P. The GPI shows an increasing trend when it comes to the mean waiting times.

There is a notable spread for $\langle w \rangle$ in the GPI data for $I_{\mathrm{P}} = 1.07\,\mathrm{MA}$. In any case, the GPI results with $\langle w \rangle < 30\ \mu\mathrm{s}$ show agreement within a factor of two with $\langle w_{>} \rangle$ in figure 1(d).

Appendix B. Issues with fit results

As an example, we will thoroughly describe the data analysis performed on GPI light intensity measurements from plasma discharges with Greenwald fractions of $f_{\mathrm{GW}} = 0.47$ and $f_{\mathrm{GW}} = 0.67$. We use the LMFIT module, which is a non-linear least squares optimization method in order to estimate the parameters of the stochastic model [99]. These will be then compared to synthetic realizations from the stochastic model, where we randomly generate around 10 realizations using the estimated γ and ε from the ECF and the estimated τ_{d} and λ from the PSD. These realizations assume observational noise.

In figure B1 we show the histogram of the normalized measurements from the GPI for one pixel, for simplicity. We estimate γ and ε from the empirical characteristic function, as it does not rely on the binning procedure. We will address the implications of this compared to the PDF estimate of the intermittency parameter later on. For the $f_{\mathrm{GW}} = 0.47$ plasma discharge in figure 1(a), the PDF of the measurement data lacks an elevated tail. This makes it challenging to perform a parameter estimation. The FPP histograms in figure 1(a) agree with the measurement data for approximately two decades in probability, but show an elevated tail in the PDF. However, for the Greenwald fraction-case of $f_{\mathrm{GW}} = 0.67$ in figure 1(b), we see an elevated tail of the distribution and the agreement of the FPP histograms aligns well with the histogram of the measurement data. This demonstrates that the onus is on the quality of these fits, which can impact later results – in particular for the intermediate Greenwald fraction discharges where these non-elevated tails are present, despite performing the analysis on long time-series measurements.

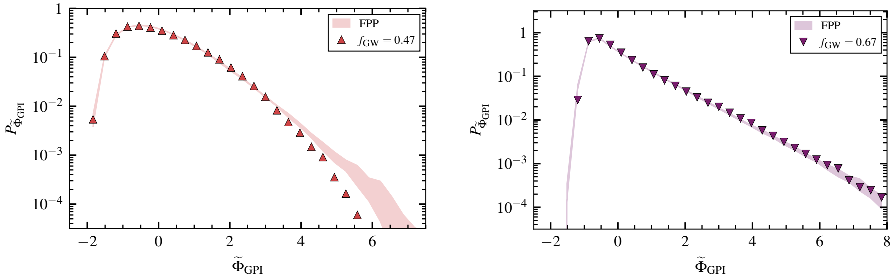

(a) (b)

Figure B1. Histograms of the normalized GPI measurements for (a) $f_{\mathrm{GW}} = 0.47$ and (b) $f_{\mathrm{GW}} = 0.67$. The markers show the measurement data whereas the shaded regions show the minimum and maximum of the FPP histograms.

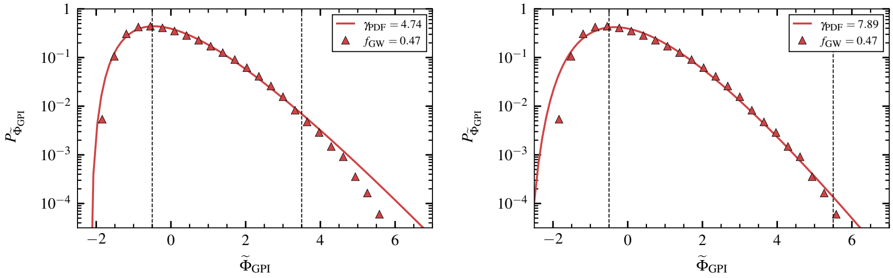

(a) (b)

Figure B2. Histogram of the normalized GPI measurements for $f_{\mathrm{GW}} = 0.47$ showing the fits based on the intervals chosen. Smaller fitting range is shown in (a) whereas in (b) a larger fitting range is used. The solid lines show the fits, the black dashed lines show the interval shown for performing the fit and the triangular markers represent the measurement data.

Additionally, placing the weight on the tail impacts the way the fit agrees with the peak of the distribution. Figure B2 demonstrates this issue. Once again, we focus on the same pixel as before. Other pixels considered in the analysis later also show non-elevated tails in the PDF of the normalized signal. Here we use the analytical expression of the PDF from Equation (A9) in [57]. Considering the fit in figure 2(a), where some of the tail is not included in the fitting procedure. Figure 2(b) considers a wide range of values to fit the histogram. It is noticable that the peak is not well described by the fit using a large range, and hence the intermittency parameter being larger. We present these intermittency parameters and noise parameters from the PDF fits as γ_{PDF} and $\varepsilon_{\mathrm{PDF}}$, respectively. For this reason, we chose to use the ECF to perform a parameter estimation for the intermittency and noise parameters in the rest of the study.

Figure B3 shows the estimation of the intermittency parameter with the ECF compared to the analytical expression of the PDF for the GPI measurements (only to the tail as seen in figure 2(b)) and the MLP $\widetilde{I}_{\mathrm{sat}}$ measurements (fitting ranges similar to figure 2(a)). The expression of the PDF can be found in equation A9 of [57]. For GPI measurements, a similar spread was also observed in the estimated intermittency parameter using the PDF as shown in figure B3, where these values are larger compared to the ECF estimates. The intermittency parameter estimated from the MLP $\widetilde{I}_{\mathrm{sat}}$ measurements shows better agreement between both methods. Some variation can be observed between the two at lower densities. Therefore, to treat the GPI and MLP data in the same way, the ECF is used as opposed to the PDF since the intermittency parameter estimate is not sensitive to the number of bins. Overall, our impression of this study suggests that the estimation of parameters on the GPI data for $0.3 \leq f_{\mathrm{GW}} \leq 0.47$ is questionable due to the non-existent tails seen from the histograms. Otherwise, the intermitency parameters between the GPI and the MLP $\widetilde{I}_{\mathrm{sat}}$ align well for $f_{\mathrm{GW}} > 0.6$.

We show the frequency power spectral densities (darker solid lines) of the normalized GPI measurements in figure B4 as well as the agreement with the parameters

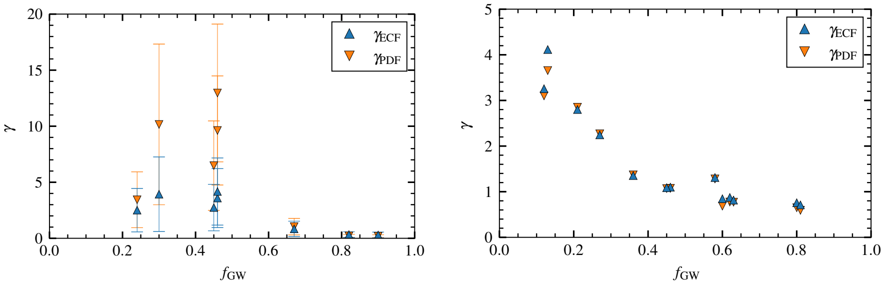

(a) (b)

Figure B3. Comparison of the intermittency parameter estimate using the empirical characteristic function γ_{ECF} (blue triangles) and the PDF expression of the normalized time series γ_{PDF} (orange inverted triangles), applied to (a) the GPI measurements, where γ_{PDF} is estimated through a tail fit and (b) the MLP $\widetilde{I}_{\mathrm{sat}}$ data where γ_{PDF} is estimated with a similar fit range to figure 2(a). The markers represent the average γ of all the APD views considered, whereas the errors bars are the minimum and maximum values of the estimated γ.

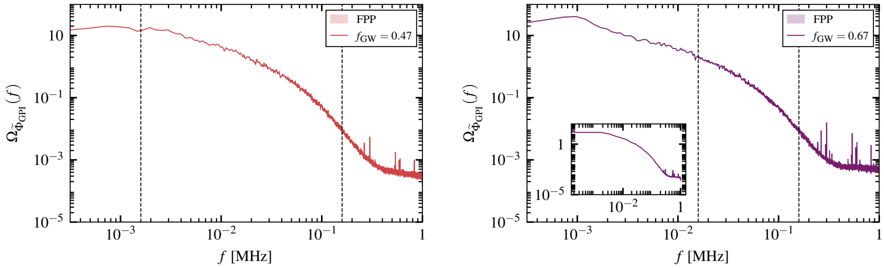

(a) (b)

Figure B4. PSDs of the normalized GPI measurements for (a) $f_{\mathrm{GW}} = 0.47$ and (b) $f_{\mathrm{GW}} = 0.67$, represented by the solid darker lines. The shaded regions are the minimum and maximum of the PSD of the FPP realizations. The dashed lines show the range considered for performing the fits.

estimated from these FPP realizations, shown by the shaded regions. Welch's method was used to produce these spectra, which can be readily accessed through Python's SciPy package [100]. The number of samples per segment (nperseg) for Welch's method on all discharges using the GPI was kept the same, which was nperseg = 8196. In figure 4(a), the PSD of the measurement data from the $f_{\mathrm{GW}} = 0.47$-case agrees well with the realizations of the stochastic model. We see a clear bump in the power spectra in figure 4(b) for the $f_{\mathrm{GW}} = 0.67$ plasma discharge, which is located at $\approx 1\,\mathrm{kHz}$. This bump becomes prominent as the core density increases. The slope of the spectra is captured well by the fitting function, but struggles for the low-frequency part. In order to estimate τ_{d} without the influence of the bump, we lower nperseg to a point where the bump has been averaged out where this is shown in the inset of figure 4(b). Indeed, it

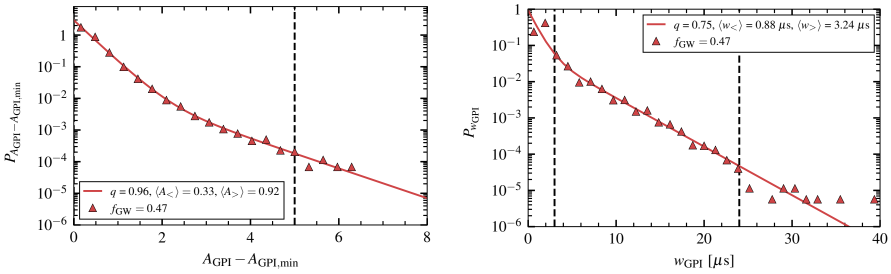

(a) (b)

Figure B5. Bi-exponential fits to (a) the estimated amplitude distribution and (b) waiting time distribution of the GPI measurements for $f_{\mathrm{GW}} = 0.47$. The markers represents the deconvolved data. The black-dashed lines show the ranges taken into consideration for the fitting prodecude. The solid line represents the fits with the bi-exponential expression found in (16).

can be seen that the bump in the flat part of the spectra is substantially reduced and agrees well with the PSDs of the FPP realizations. We do not use such a low nperseg in the actual analysis since much of the data is smoothed away. Furthermore, a shorter fit range is used for $f_{\mathrm{GW}} = 0.67$ since the fit will overestimate τ_{d}. We have discussed the consequences of overestimating τ_{d} for the pulse function in the deconvolution algorithm in reference [82].

In addition, we present in the figure B5, the bi-exponential fits to the amplitude distribution and the waiting time distribution from the RL deconvolution on the GPI measurements for $f_{\mathrm{GW}} = 0.47$ only. The bi-exponential fits shown by the solid lines were made to non-rescaled distributions in order to extract the mean of the estimated amplitude and estimated waiting time. As explained above, we are interested in large-amplitude events, and therefore we consider the mean of the estimated large amplitudes $\langle A_> \rangle$. Bear in mind that we do not trust these values to be the true mean amplitudes of the GPI measurements, since the measurements are not a proxy for plasma parameters. We see from figure Appendix B, the bi-exponential fit to the non-rescaled amplitude distribution. We present the parameters estimated for the partition between small and large amplitudes $q = 0.96$, the mean of the small amplitudes $\langle A_< \rangle = 0.33$ as well as $\langle A_> \rangle = 0.92$. q changes little with Greenwald fraction, therefore no results are shown for this. In figure B5, we present the bi-exponential fit to the estimated waiting time distribution using the RL deconvolution algorithm on the GPI measurement. The mean of the short waiting times was estimated to be $\langle w_< \rangle = 0.88$ μs and the mean of the long waiting times was found to be $\langle w_> \rangle = 3.24$ μs.

References

[1] LaBombard B, Boivin R L, Greenwald M, Hughes J, Lipschultz B, Mossessian D, Pitcher C S, Terry J L, Zweben S J and the Alcator C-Mod Group (Alcator Group) 2001 *Phys. Plasmas* **8**

2107–2117

[2] Pitts R A *et al.* 2005 *Plasma Phys. Control. Fusion* **47** B303

[3] D'Ippolito D A, Russell D A, Myra J R, Thakur S C, Tynan G R and Holland C 2012 *Phys. Plasmas* **19** 102301

[4] Birkenmeier G *et al.* 2015 *Nucl. Fusion* **55**

[5] Stangeby P C 2000 *The Plasma Boundary Of Magnetic Fusion Devices* (IoP Publishing)

[6] Krasheninnikov S, Smolyakov A and Kukushkin A 2020 *On the edge of magnetic fusion devices* (Springer Nature)

[7] Lipschultz B *et al.* 2007 *Nucl. Fusion* **47** 1189

[8] Marandet Y *et al.* 2011 *Nucl. Fusion* **51**

[9] Zweben S J 1985 *Physics of Fluids (1958-1988)* **28** 974–982

[10] Grulke O, Terry J L, LaBombard B and Zweben S J 2006 *Phys. Plasmas* **13** 012306

[11] Zweben S J *et al.* 2002 *Phys. Plasmas* **9** 1981–1989

[12] Terry J L *et al.* 2003 *Phys. Plasmas* **10** 1739–1747

[13] Zweben S *et al.* 2004 *Nucl. Fusion* **44** 134

[14] Terry J L, Zweben S J, Grulke O, Greenwald M J and Labombard B 2005 *J. Nucl. Mater.* **337-339** 322–326

[15] Maqueda R, Stotler D and Zweben S 2011 *J. Nucl. Mater.* **415** S459 – S462

[16] Banerjee S *et al.* 2012 *Nucl. Fusion* **52** 123016

[17] Endler M 1999 *J. Nucl. Mater.* **266–269** 84 – 90

[18] LaBombard B, Umansky M, Boivin R, Goetz J, Hughes J, Lipschultz B, Mossessian D, Pitcher C, Terry J and Alcator Group 2000 *Nucl. Fusion* **40** 2041

[19] Boedo J A *et al.* 2001 *Phys. Plasmas* **8** 4826–4833

[20] Antar G Y, Krasheninnikov S I, Devynck P, Doerner R P, Hollmann E M, Boedo J A, Luckhardt S C and Conn R W 2001 *Phys. Rev. Lett.* **87**(6) 065001

[21] Zweben S J, Boedo J A, Grulke O, Hidalgo C, LaBombard B, Maqueda R J, Scarin P and Terry J L 2007 *Plasma Phys. Control. Fusion* **49** S1

[22] Xu G S *et al.* 2009 *Nucl. Fusion* **49** 092002

[23] Cziegler I, Terry J L, Hughes J W and LaBombard B 2010 *Phys. Plasmas* **17** 056120 (pages 8)

[24] Krasheninnikov S I 2001 *Physics Letters A* **283** 368 – 370

[25] Bian N, Benkadda S, Paulsen J V and Garcia O E 2003 *Phys. Plasmas* **10** 671–676

[26] Bisai N, Das A, Deshpande S, Jha R, Kaw P, Sen A and Singh R 2005 *Phys. Plasmas* **12** 102515

[27] Garcia O E, Bian N H and Fundamenski W 2006 *Phys. Plasmas* **13** 082309 (pages 16)

[28] Garcia O E, Bian N H, Naulin V, Nielsen A H and Rasmussen J J 2006 *Phys. Scr.* **2006** 104

[29] Antar G Y, Devynck P, Garbet X and Luckhardt S C 2001 *Phys. Plasmas* **8** 1612–1624

[30] Rudakov D L *et al.* 2002 *Plasma Phys. Control. Fusion* **44** 717

[31] Boedo J A *et al.* 2003 *Phys. Plasmas* **10** 1670–1677

[32] Graves J P, Horacek J, Pitts R A and Hopcraft K I 2005 *Plasma Phys. Control. Fusion* **47** L1

[33] Rudakov D *et al.* 2005 *Nucl. Fusion* **45** 1589

[34] Garcia O E, Pitts R A, Horacek J, Madsen J, Naulin V, Nielsen A H and Rasmussen J J 2007 *Plasma Phys. Control. Fusion* **49** B47

[35] Garcia O E, Horacek J, Pitts R A, Nielsen A H, Fundamenski W, Naulin V and Rasmussen J J 2007 *Nucl. Fusion* **47** 667

[36] Garcia O E, Horacek J and Pitts R A 2015 *Nucl. Fusion* **55** 062002

[37] Theodorsen A, Garcia O E, Horacek J, Kube R and Pitts R A 2016 *Plasma Phys. Control. Fusion* **58** 044006

[38] Garcia O E, Fritzner S M, Kube R, Cziegler I, LaBombard B and Terry J L 2013 *Phys. Plasmas* **20** 055901

[39] Garcia O E, Cziegler I, Kube R, LaBombard B and Terry J L 2013 *J. Nucl. Mater.* **438** S180 – S183

[40] Antar G Y, Counsell G, Yu Y, LaBombard B and Devynck P 2003 *Phys. Plasmas* **10** 419–428

[41] Horacek J, Pitts R A and Graves J P 2005 *Czechoslov. J. Phys.* **55** 271–283

[42] Agostini M, Zweben S J, Cavazzana R, Scarin P, Serianni G, Maqueda R J and Stotler D P 2007 *Phys. Plasmas* **14** 1–9

[43] Walkden N, Wynn A, Militello F, Lipschultz B, Matthews G, Guillemaut C, Harrison J, Moulton D and JET Contributors 2017 *Nucl. Fusion* **57** 036016

[44] Theodorsen A, Garcia O E, Kube R, LaBombard B and Terry J 2017 *Nucl. Fusion* **57** 114004

[45] Theodorsen A, Garcia O E, Kube R, LaBombard B and Terry J L 2018 *Phys. Plasmas* **25** 122309

[46] Garcia O E, Kube R, Theodorsen A, LaBombard B and Terry J L 2018 *Phys. Plasmas* **25** 056103

[47] Kube R, Garcia O E, Theodorsen A, Brunner D, Kuang A Q, LaBombard B and Terry J L 2018 *Plasma Phys. Control. Fusion* **60** 065002

[48] Kube R, Theodorsen A, Garcia O E, Brunner D, Labombard B and Terry J L 2020 *J. Plasma Phys.*

[49] Kuang A Q, LaBombard B, Brunner D, Garcia O E, Kube R and Theodorsen A 2019 *Nucl. Mater. Energy* **19** 295 – 299

[50] Zurita M, Hernandez W, Crepaldi C, Pereira F A C and Guimarães-Filho Z 2022 *Phys. Plasmas* **29** 052303

[51] Carralero D *et al.* 2014 *Nucl. Fusion* **54** 123005

[52] Garcia O, Kube R, Theodorsen A, Bak J G, Hong S H, Kim H S, the KSTAR Project Team and Pitts R 2017 *Nucl. Mater. Energy* **12** 36 – 43

[53] Garcia O E 2012 *Phys. Rev. Lett.* **108**(26) 265001

[54] Garcia O E, Kube R, Theodorsen A and Pécseli H L 2016 *Phys. Plasmas* **23** 052308

[55] Militello F and Omotani J 2016 *Nucl. Fusion* **56** 104004

[56] Garcia O E and Theodorsen A 2017 *Phys. Plasmas* **24** 032309

[57] Theodorsen A, Garcia O E and Rypdal M 2017 *Phys. Scr.* **92** 054002

[58] Theodorsen A and Garcia O E 2018 *Plasma Phys. Control. Fusion* **60** 034006

[59] Garcia O E and Theodorsen A 2017 *Phys. Plasmas* **24** 020704

[60] Decristoforo G, Theodorsen A, Omotani J, Nicholas T and Garcia O E 2021 *Phys. Plasmas* **28** 072301

[61] Terry J, Maqueda R, Pitcher C, Zweben S, LaBombard B, Marmar E, Pigarov A and Wurden G 2001 *J. Nucl. Mater.* **290–293** 757 – 762

[62] LaBombard B, Gangadhara S, Lipschultz B and Pitcher C 2003 *J. Nucl. Mater.* **313** 995–999

[63] LaBombard B, Hughes J, Mossessian D, Greenwald M, Lipschultz B, Terry J and the Alcator C-Mod Team 2005 *Nucl. Fusion* **45** 1658

[64] Zweben S *et al.* 2011 *J. Nucl. Mater.* **415** S463 – S466

[65] Agostini M, Terry J, Scarin P and Zweben S 2011 *Nucl. Fusion* **51** 053020

[66] Russell D A, Myra J R, D'Ippolito D A, LaBombard B, Hughes J W, Terry J L and Zweben S J 2016 *Physics of Plasmas* **23** 1–10

[67] Kube R, Garcia O, LaBombard B, Terry J and Zweben S 2013 *J. Nucl. Mater.* **438, Supplement** S505 – S508

[68] Offeddu N *et al.* 2022 *Nucl. Fusion* **62** 96014

[69] Rudakov D L, Boedo J A, Moyer R A, Lehmer R D, Gunner G and Watkins J G 2001 *Rev. Sci. Instrum* **72** 453–456

[70] LaBombard B 2002 *Phys. Plasmas* **9** 1300–1311

[71] Whyte D G, Lipschultz B L, Stangeby P C, Boedo J, Rudakov D L, Watkins J G and West W P 2005 *Plasma Phys. Control. Fusion* **47** 1579–1607

[72] Asakura N 2007 *J. Nucl. Mater.* **363–365** 41–51

[73] Vianello N, Spolaore M, Martines E, Cavazzana R, Serianni G, Zuin M, Spada E and Antoni V 2010 *Nucl. Fusion* **50** 042002

[74] D'Ippolito D A, Myra J R and Zweben S J 2011 *Phys. Plasmas* **18** 060501

[75] McCormick K, Kyriakakis G, Neuhauser J, Kakoulidis E, Schweinzer J and Tsois N 1992 *J. Nucl. Mater.* **196–198** 264 – 270

[76] Militello F, Garzotti L, Harrison J, Omotani J T, Scannell R, Allan S, Kirk A, Lupelli I and Thornton A J 2016 *Nucl. Fusion* **56** 8–10

[77] Antar G Y, Counsell G and Ahn J W 2005 *Phys. Plasmas* **12** 1–11

[78] Guzdar P, Kleva R, Kaw P, Singh R, LaBombard B and Greenwald M 2007 *Phys. Plasmas* **14** 020701

[79] Richardson W H 1972 *J. Opt. Soc. Am.* **62** 55

[80] Lucy L B 1974 *Astron. J.* **79** 745

[81] Benvenuto F, Zanella R, Zanni L and Bertero M 2010 *Inverse Probl.* **26** 025004

[82] Ahmed S, Garcia O E and Theodorsen A 2023 *Phys. Rev. E* **107** 54222

[83] Carralero D, Manz P, Aho-Mantila L, Birkenmeier G, Brix M, Groth M, Müller H W, Stroth U, Vianello N and Wolfrum E 2015 *Phys. Rev. Lett.* **115** 1–5

[84] Carralero D *et al.* 2017 *Nucl. Fusion* **57** 056044

[85] Wynn A *et al.* 2018 *Nucl. Fusion* **58** 056001

[86] Kube R, Garcia O E and Wiesenberger M 2016 *Phys. Plasmas* **23** 122302

[87] Greenwald M 2002 *Plasma Phys. Control. Fusion* **44** R27

[88] Kuang A Q 2019 *Measurements of divertor target plate conditions and their relationship to scrape-off layer transport* Ph.D. thesis Massachusetts Institute of Technology

[89] Kube R, Theodorsen A, Garcia O E, LaBombard B and Terry J L 2016 *Plasma Phys. Control. Fusion* **58** 054001

[90] Labombard B and Lyons L 2007 *Rev. Sci. Instrum* **78** 073501–073501–9

[91] Kube R, Garcia O E, Theodorsen A, Kuang A Q, LaBombard B, Terry J L and Brunner D 2019 *Nucl. Mater. Energy* **18** 193 – 200

[92] 2022 https://github.com/uit-cosmo/

[93] Losada J M, Theodorsen A and Garcia O E 2023 *Phys. Plasmas* **30**

[94] LaBombard B, Golfinopoulos T, Terry J L, Brunner D, Davis E, Greenwald M and Hughes J W 2014 *Phys. Plasmas* **21** 056108

[95] Kube R, Bianchi F M, Brunner D and LaBombard B 2019 *Rev. Sci. Instrum* **90** 013505

[96] Kirk A, Thornton A J, Harrison J R, Militello F and Walkden N R 2016 *Plasma Phys. Control. Fusion* **58** 085008

[97] Vianello N *et al.* 2019 *Nucl. Fusion* **60** 16001

[98] Creely A J *et al.* 2020 *J. Plasma Phys.* **86** 865860502

[99] Newville M, Stensitzki T, Allen D B, Rawlik M, Ingargiola A and Nelson A 2016 *Astrophysics Source Code Library* ascl–1606

[100] Welch P 1967 *IEEE trans. audio electroacoust.* **15** 70–73

Paper III:
Multimachine analysis of intermittent scrape-off layer fluctuations in ohmically heated plasmas fluctuations

S. Ahmed, S. Allan, J. G. Bak, J. A. Boedo, W. G. Fuller, O. E Garcia, W. Han, J. Horacek, A. Kirk, H. S. Kim, A. Q. Kuang, B. LaBombard, M. Lampert, F. Militello, Y. U. Nam, N. Offeddu, R. A. Pitts, P. Ryan, J. L. Terry, P. Tamain, C. Theiler and A. Theodorsen

Multimachine analysis of intermittent scrape-off layer fluctuations in ohmically heated plasmas

Sajidah Ahmed,[1] Scott Allan,[2] Jun-Gyo Bak,[3] Jose A. Boedo,[4] William G. Fuller,[2] Odd Erik Garcia,[1] Woonghee Han,[5] Jan Horacek,[6] Andrew Kirk,[2] Heung Su Kim,[3] Adam Q. Kuang,[7] Brian LaBombard,[5] Máté Lampert,[8] Fulvio Militello,[2] Yong Un Nam,[3] Nicola Offeddu,[9] Richard A. Pitts,[10] Peter Ryan,[2] James L. Terry,[5] Patrick Tamain,[11] Christian Theiler[8] and Audun Theodorsen[1]

[1] Department of Physics and Technology, UiT The Arctic University of Norway, N-9037 Tromsø, Norway
[2] UKAEA-CCFE, Culham Science Centre, Abingdon OX14 3DB, United Kingdom of Great Britain and Northern Ireland
[3] National Fusion Research Institute, Daejeon, Republic of Korea
[4] Center for Energy Research, University of California, San Diego, La Jolla, CA 92093-0417, United States of America
[5] MIT Plasma Science and Fusion Center, 167 Albany St, Cambridge, MA 02139, United States of America
[6] Institute of Plasma Physics of the CAS, Prague, Czech Republic
[7] Commonwealth Fusion Systems, 148 Sidney Street, Cambridge, MA 02139, United States of America
[8] Princeton Plasma Physics Laboratory, Princeton, New Jersey 08540, USA
[9] Ecole Polytechnique Federale de Lausanne (EPFL), Swiss Plasma Center (SPC), CH-1015 Lausanne, Switzerland
[10] ITER Organization, Route de Vinon-sur-Verdon, CS 90 046, 13067 St. Paul Lez Durance Cedex, France
[11] IRFM, CEA Cadarache, F-13108 St. Paul-lez-Durance, France

E-mail: `sajidah.ahmed@uit.com`

19 September 2023

Abstract. Far scrape-off layer (SOL) fluctuations from six separate tokamaks have been analyzed in the context of stochastic modeling, describing the fluctuations as a superposition of uncorrelated two-sided exponential pulses with a fixed shape and duration. The observed fluctuations from all devices investigated are well described by the stochastic model. Therefore we explore the characteristics of far-SOL fluctuations using the parameters of this model which are the mean waiting times between consecutive pulses, the pulse duration times and the mean of the pulse amplitudes. For the first time, a multimachine comparison of fluctuation statistics is made from time-series measurements of six tokamaks, Alcator C-Mod, DIII-D, TCV, KSTAR, MAST and MAST-U, in low confinement mode scenarios. The multimachine analysis reveals dependencies on the line-averaged density and the plasma current. The duration times and waiting times are affected. The strength of the intermittency parameter defined by pulse overlap, and mean amplitudes are also impacted by these parameters. No dependencies were found with minor radius. Changes in the dimensionless device parameters such as the aspect ratio and elongation are also presented. The study highlights the differences between conventional and spherical tokamaks, where the far-SOL fluctuations have higher amplitudes and longer durations, as well as

longer mean waiting times. In conventional tokamaks, the duration times, waiting times, and amplitudes show clear trends with respect to the aspect ratio.

1. Introduction

For successful operation of future fusion devices at high densities, it is crucial to predict the expected particle-wall fluxes [1–6]. Fluctuation-induced transport, characterized by blob-like filaments, is commonly observed in the boundary region of fusion devices and are elongated along the field lines [7–14]. These coherent structures dominate the scrape-off layer (SOL) as these propagate radially toward the first wall [15–18]. Interactions between fluctuation-induced particle flux and the surface of the main wall material will result in increased erosion rates and sputtering [1, 3–6, 19, 20].

In many fusion devices, the SOL profile exhibits a distinctive two-layer structure known as a density shoulder [2, 16, 21–39]. This profile is relatively steep in the near-SOL, extending outward from the magnetic separatrix. At a certain break point, the profile scale length becomes longer, forming the "shoulder" in what is commonly referred to as the far-SOL. As the main plasma density increases, the break point between the near- and far-SOL moves radially inward, leading to broadening of the radial density profile, which is called profile broadening. At the same time, the scale length of the profile increases, a phenomenon commonly referred to as flattening. As a result of gradual flattening, there is a significant increase in the particle and heat carried by the filaments that arrive at the main chamber wall [16]. This strongly supports the idea that cross-field transport is correlated with the Greenwald fraction, which serves as a measure of how close the plasma is to the operational limit [40]. Observations indicate that as a fusion device approaches its empirical discharge density limit, the interactions between plasma and the vessel wall become increasingly significant [2, 16, 21–39, 41].

Several studies have shown that time-series measurements of far-SOL plasma fluctuations, characterized as large-amplitude bursts, exhibit universal statistical properties [21, 23, 27–30, 33, 35, 37, 42–62]. It is commonly observed that probability density functions (PDFs) for the plasma density are skewed and flattened with raised tails for large signal amplitudes, and the conditionally averaged waveform is well described by a two-sided exponential pulse shape with a fast rise and a slow decay. Additionally, the power spectral densities (PSDs) of such time series are constant for low frequencies and have a power-law-like behavior for high frequencies, consistent with the two-sided exponential pulse shape.

The impact of global and engineering parameters on the SOL or bursty transport in other regimes is scarce but has been addressed in previous multimachine studies [3, 38, 63, 64]. It was indicated that the size of the flucutations across several fusion devices scales with the minor radii of these machines, despite the study being performed on edge-localised modes [63]. It is not clear whether filaments in low-confiment mode regimes would follow the same trends. Reference [31] compared the evolution of the SOL in ASDEX-Upgrade (AUG) and the Joint European Torus (JET) and observed that the onset of profile broadening and flattening occurred at approximately 50% of their density limits. Recent filament-tracking results from the Tokamak á Configuration Variable (TCV) highlighted the effect of triangularity from a single machine scan that demonstrated suppression of turbulent structures in negative triangularity plasmas [65, 66].

We review the stochastic model that describes SOL fluctuations as a superposition of uncorrelated pulses [67]. Previous studies have demonstrated excellent agreement between observations from exceptionally long time series from gas puff imaging (GPI) and Langmuir probe (LP) measurements with the predictions of the stochastic model [33–35, 53, 54, 57–59, 68–70], and our results also show the model describes the measurements very well. Further, a recent study on Alcator C-Mod has shown that the stochastic model parameters strongly depend on the plasma parameters that involve line-averaged densities and plasma current [62].

This contribution strictly focuses on analyzing far-SOL fluctuations in low confinement mode (L-mode) plasmas from the following five tokamaks: Alcator C-Mod, DIII-D, TCV, the Mega-Amp Spherical Tokamak (MAST) and its successor, MAST-U. We investigate how the statistics of these fluctuations compare from their respective line-averaged density scans. For the first time, measurements from MAST-U and DIII-D LPs, as well as from the TCV GPI, are interpreted in the framework of the stochastic model. The extraction of fluctuation amplitudes and waiting times was achieved by performing a Richardson-Lucy (RL) deconvolution algorithm on most of the time-series measurements from DIII-D, TCV, MAST, and MAST-U time series. The mean waiting times ranged from $5 - 30\,\mu$s across the devices. Using analyses performed previously on stationary LP data from Alcator C-Mod [62], KSTAR [33] and TCV [57] we present how far-SOL fluctuation statistics change with machine parameters which have not been shown before. Although previous studies such as those in reference [38] investigate how blob regimes differ between tokamaks, we examine the dependencies within the statistical framework and present how its model parameters change with plasma and engineering parameters.

The results highlight that the intermittency parameter of the fluctuations, which determines the degree of pulse overlap, do not change as the line-averaged density is increased in DIII-D, TCV, MAST and MAST-U. C-Mod is the only fusion device in this study that shows the intermittency parameter decreases as the density limit is approached, and this is demonstrated over a much wider range of line-averaged densities. This suggests that the C-Mod far-SOL fluctuations are becoming strongly intermittent with density. The range of plasma currents investigated across of these devices indicates that duration times and mean waiting times between the fluctuations are impacted with increasing plasma current. This result is also indicative of the impact of the poloidal magnetic field on these parameters, further strengthening the strong influence of the plasma current on profile flattening. No dependencies were observed with minor radius, which questions the choice of using the Greenwald fraction as a parameter to describe L-mode far-SOL fluctuations across devices. There is a significant difference between spherical tokamaks and conventional tokamaks, in particular, when the duration times, mean waiting times, and mean amplitudes trend with aspect ratio and elongation, alluding to plasma shaping as playing a significant role. We remind the reader that edge-localized modes are not studied here and would require a different set of assumptions for the stochastic model.

The study is organized as follows: Section 2 discusses the experimental setup of the L-mode plasmas in all devices and the diagnostics involved. In Section 3, we review the stochastic model and describe its parameters. The extraction of amplitude and waiting time using the deconvolution algorithm is explained. Results are shown in Section 4 where fluctuation statistics for DIII-D, TCV, C-Mod, MAST and MAST-U. A parametric analysis for the LP and GPI results is demonstrated as a function of the Greenwald fraction. Further, machine parameters are shown with the addition of KSTAR and TCV LP data, and how the stochastic model parameters depend on them. Finally, we end the study with a discussion of the results and with concluding remarks in Section 5.

2. Experiments

Ion saturation current I_{sat} measurements from the LPs and light intensity measurements from the GPI were analysed in this study. Thanks to the high temporal resolution for their measurements, I_{sat} of SOL fluctuations is one of the variables routinely measured by LPs, and for this reason, these time series were analyzed from the LPs instead of other parameters such as the electron density and temperature.

For DIII-D, KSTAR, MAST, and MAST-U LP measurements only are considered, while for C-Mod and TCV, both LP and GPI are analyzed. In the C-Mod LP case, the measurements are actually from the “mirror” Langmuir probe [71, 72]. Details of these C-Mod diagnostic systems can be viewed in reference [62]. We only look at a single KSTAR shot which was previously report in reference [33].

LPs used are all on reciprocating heads which rapidly enter then exit the plasma so to minimize the impact of perturbations to the local plasma or they are dwelling in the far-SOL. Furthermore, the positions of the probe measuring fluctuations of I_{sat} are quoted in terms of $\rho = r - r_{\mathrm{sep}}$, where this is the midplane distance relative to the separatrix. The ion $B \times \nabla B$ drift for all experiments was pointing towards the lower X-point. The Greenwald fraction is dependent on three parameters, the line-averaged density $\overline{n}_{\mathrm{e}}$, plasma current I_{P}, and the minor radius a, according to $f_{\mathrm{GW}} = \overline{n}_{\mathrm{e}}[\times 10^{20}\,\mathrm{m}^{-3}]/(\pi a\,[\mathrm{m}]^2/I_{\mathrm{P}}\,[\mathrm{MA}])$ [40]. The data from each fusion device comes from scans of the line-averaged density, and will be parameterized by the Greenwald fraction in this study. The devices in which the far-SOL data was taken from dwelled LPs are mentioned in table 1. The devices which used reciprocating LPs are noted in table 2. Lastly, those which used GPI to diagnose far-SOL fluctuations are shown in table 3.

Table 1. Dwelled LP measurements taken at the far-SOL from some fusion devices considered. Machine and L-mode plasma parameters are listed for these devices. R_0 is the major radius in meters, a is the minor radius in meters, R_0/a is the aspect ratio, $\overline{n}_{\mathrm{e}}$ is the line-averaged density where the ranges are shown in units of $\times 10^{20}\,\mathrm{m}^{-3}$, f_{GW} is the Greenwald fraction where the ranges are quoted below, I_{P} is the plasma current during in units of mega-Amperes, and the axial toroidal magnetic field B_{T} is in units of Tesla. The divertor configuration is either lower single null (LSN) magnetic equilibrium or in double null (DN). The ion $B \times \nabla B$ drift for all experiments was pointing towards the lower X-point.

	C-Mod	TCV	MAST-U	KSTAR
R_0 [m]	0.68	0.89	0.7	1.9
a [m]	0.22	0.25	0.5	0.5
R_0/a	3.09	3.52	1.4	3.8
$\overline{n}_{\mathrm{e}}$ [$\times 10^{20}\,\mathrm{m}^{-3}$]	0.46 - 2.8	0.48, 0.85	0.13 - 0.27	0.23
f_{GW}	0.12 - 0.85	0.26, 0.49	0.28 - 0.56	0.30
I_{P} [MA]	0.55	0.34	0.45	0.6
B_{T} [T]	5.4	1.4	0.50	2.0
Divertor	LSN	LSN	DN	LSN

TCV has a major radius $R_0 = 0.89\,\mathrm{m}$ and a minor radius $a = 0.25\,\mathrm{m}$. In TCV, LP and GPI fluctuation measurements were taken from deuterium-fueled plasmas from two different rundays. The GPI system in TCV is a 12×10 arrangement of views coupled to avalanche diodes (APDs), measuring light intensity fluctuations at a sampling frequency of 2 MHz. The deuterium gas was puffed at the outer midplane, recording time series measurements of D_α light emission. Time-series measurements

Table 2. Fusion devices shown in the study using reciprocating LP measurements taken at the far-SOL. Machine and L-mode plasma parameters are listed below. R_0 is the major radius in meters, a is the minor radius in meters, R_0/a is the aspect ratio, $\overline{n}_\mathrm{e}$ is the line-averaged density where the ranges are shown in units of $\times 10^{20}\,\mathrm{m}^{-3}$, f_GW is the Greenwald fraction where the ranges are quoted below, I_P is the plasma current during in units of mega-Amperes, and the axial toroidal magnetic field B_T is in units of Tesla. The divertor configuration is either lower single null (LSN) magnetic equilibrium or in double null (DN). The ion $B \times \nabla B$ drift for all experiments was pointing towards the lower X-point.

	DIII-D	MAST
R_0 [m]	1.67	0.85
a [m]	0.67	0.65
R_0/a	2.49	1.31
$\overline{n}_\mathrm{e}$ [$\times 10^{20}\,\mathrm{m}^{-3}$]	0.09 - 0.34	0.09 - 0.16
f_GW	0.12 - 0.49	0.23 - 0.43
I_P [MA]	0.98	0.41 - 0.43
B_T [T]	2.05	0.48 - 0.53
Divertor	LSN	DN

Table 3. Machine and L-mode plasma parameters listed for fusion devices considered where the GPI measurements were analysed. R_0 is the major radius in meters, a is the minor radius in meters, R_0/a is the aspect ratio, $\overline{n}_\mathrm{e}$ is the line-averaged density where the ranges are shown in units of $\times 10^{20}\,\mathrm{m}^{-3}$, f_GW is the Greenwald fraction where the ranges are quoted below, I_P is the plasma current during in units of mega-Amperes, and the axial toroidal magnetic field B_T is in units of Tesla. The divertor configuration is either lower single null (LSN) magnetic equilibrium or in double null (DN). The ion $B \times \nabla B$ drift for all experiments was pointing towards the lower X-point.

	C-Mod	TCV
R_0 [m]	0.68	0.89
a [m]	0.22	0.25
R_0/a	3.09	3.52
$\overline{n}_\mathrm{e}$ [$\times 10^{20}\,\mathrm{m}^{-3}$]	0.46 - 2.8	0.20 - 0.81
f_GW	0.12 - 0.85	0.16 - 0.66
I_P [MA]	0.55	0.24
B_T [T]	5.4	1.4
Divertor	LSN	LSN

considered for this analysis were from multiple views piercing the puffed-gas-cloud at positions having similar far-SOL flux positions. This was done to ensure that the estimated statistics were indeed reproducible. Experiments were performed on LSN, ohmically heated L-mode plasmas with stepwise density scans at constant $I_\mathrm{P} = 0.34\,\mathrm{MA}$ and $B_\mathrm{T} = 1.42\,\mathrm{T}$. The line-averaged density scan was performed in over the range $\overline{n}_\mathrm{e} \approx [0.20 - 0.81] \times 10^{20}\,\mathrm{m}^{-3}$, leading to a Greenwald fraction range of $f_\mathrm{GW} = [0.16 - 0.66]$ with GPI measurements. The TCV LP measurements were made from a five-tip probe system that was at a fixed position centered at approximately $Z = -0.01\,\mathrm{m}$, hence a small distance below the midplane. The I_sat was measured in the far-SOL roughly 20 mm from the LCFS. The middle pin, as labeled in figure 1(a), recorded I_sat, while the pins on either side recorded the floating potential V_f at a rate of 6 MHz. In addition to the previously studied dwell LP measurements studied in reference [57], which was at $\overline{n}_\mathrm{e} \approx 0.45 \times 10^{20}\,\mathrm{m}^{-3}$, we also examined a TCV

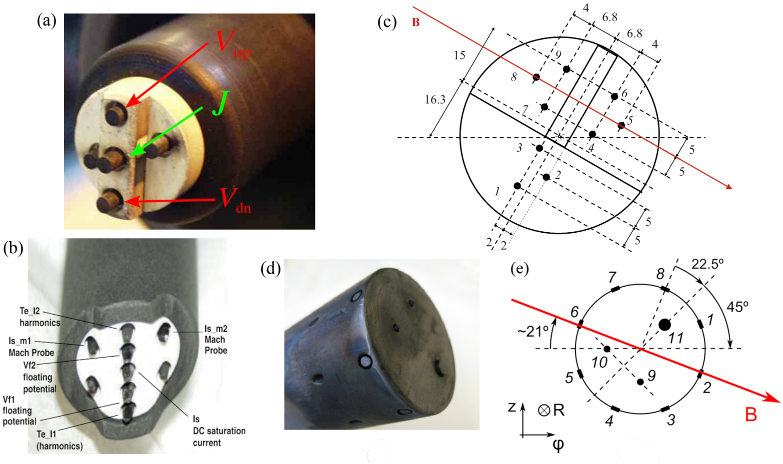

Figure 1. Probe diagnostics from various fusion devices from which $I_{\rm sat}$ measurements were collected for this study. (a) Five-point probe in TCV; (b) nine-pin probe in DIII-D showing the pin labels; (c) Schematic of Mach probe used in MAST and MAST-U (for MAST-U, electron saturation was measured) where the distances between the pins are presented (units of millimeters); (d) photograph of the Gundestrup probe in MAST; and (e) is the schematic of the Gundestrup probe. [Figure 1(b) is reproduced from J. A. Boedo and D. L. Rudakov, "Estimation of plasma ion saturation current and reduced tip arcing using Langmuir probe harmonics." *Rev. Sci. Instrum.* **88** (3) 2017 with the permission of AIP Publishing. Figure 1(a) is reprinted from A. Theodorsen, *et al.* "Scrape-off layer turbulence in TCV: evidence in support of stochastic modelling." *Plasma Phys. Control. Fusion* **58** (4) 2016. ©IOP Publishing. Reproduced with permission. All rights reserved. Figure 1(c) is from B. Hnat, *et al.* "Experimental constraint on the radial mode number of the geodesic acoustic mode from multi-point Langmuir probe measurements in MAST Ohmic plasma." *Plasma Phys. Control. Fusion* **60** (8) 2018. ©IOP Publishing. Reproduced with permission. All rights reserved. Finally, figures 1(d) and 1(e) are from P. Tamain, *et al.* "Edge turbulence and flows in the presence of resonant magnetic perturbations on MAST." *Plasma Phys. Control. Fusion* **52** (7) 2010. ©IOP Publishing. Reproduced with permission. All rights reserved].

discharge with $\overline{n}_{\rm e} \approx 0.85 \times 10^{20}\,{\rm m}^{-3}$. Therefore, the Greenwald fractions for the LP measurements are $f_{\rm GW} = 0.26$ and $f_{\rm GW} = 0.49$. The connection length on average to the divertor target was $L_{\|} \approx 10\,{\rm m}$ from the probe position [57].

DIII-D is a medium-sized tokamak with a major radius of $R_0 = 1.67\,{\rm m}$ and a minor radius of $a = 0.67\,{\rm m}$. A dedicated line-averaged density scan was performed in LSN, deuterium-fueled plasma where the density ranged from $\overline{n}_{\rm e} \approx [0.09 - 0.34] \times 10^{20}\,{\rm m}^{-3}$. The plasma current and the toroidal magnetic field were kept constant and set to $I_{\rm P} = 0.98\,{\rm MA}$ and $B_{\rm T} = 2.05\,{\rm T}$. This leads to a Greenwald fraction of $f_{\rm GW} = [0.12 - 0.49]$. The outer midplane LP is a nine-tip probe system, all of which are made of graphite tips embedded onto a boron nitride matrix. Figure 1(b) shows a photo of the midplane LP where the pin labels are indicated. Sampling up to frequencies of 4 MHz, this study uses I_{sat} fluctuations measured at the DC-biased pin, which prevents the presence of arcs in the analysis. The probe is on a reciprocating arm which, within 250 ms, enters then exits the plasma – hence a short measurement period. Reference [73] discusses in more detail the outer-midplane probe system in DIII-D. For radial velocity estimates, we consider V_{f} measurements from 'Vf2' and 'Vf1'. The probe was approximately $Z = -0.18\,\mathrm{m}$ below the midplane. To ensure enough samples for fluctuation analysis, radial bins of 2 cm were used, while avoiding data points from the wall shadow and near-SOL. The measurement locations in the flux space are on average $\rho \approx 2.4\,\mathrm{cm}$, which corresponds to the far-SOL and ρ is the relative distance to the LCFS at the midplane. Therefore, on average, $L_{\|}$ from the probe position to the divertor target is approximately 14 m.

The MAST device is a spherical tokamak with a major and minor radius of $R_0 = 0.85\,\mathrm{m}$ and $a = 0.65\,\mathrm{m}$, respectively, and a toroidal magnetic field strength of up to approximately 0.55 T. Time series of I_{sat} were recorded in double null (DN) configurations from two different campaigns. The fluctuation analysis was performed on discharges from a line-averaged density scan $\overline{n}_{\mathrm{e}} \approx [0.09 - 0.16] \times 10^{20}\,\mathrm{m}^{-3}$. We allow the plasma current and toroidal field at the magnetic axis to vary, where these take the range of $I_{\mathrm{P}} = [0.41 - 0.43]\,\mathrm{MA}$ and $B_{\mathrm{T}} = [0.48 - 0.53]\,\mathrm{T}$, respectively, to ensure enough discharges in the study. The corresponding Greenwald fractions are $f_{\mathrm{GW}} = [0.23 - 0.43]$. No heating was used to ensure that the analysis was carried out on L-mode plasmas. In earlier campaigns, a Gundestrup probe and a Mach probe were used to measure fluctuations in the SOL, both sampling measurements at a frequency of 1 MHz. Both of these diagnostics were directly on the midplane, $Z = 0\,\mathrm{m}$. Most of the plasma discharges analyzed in this study use I_{sat} measurements from the Gundestrup probe. This probe consists of 11 pins, as shown in figures 1(d) and 1(e) where pins 1-8 are uniformly distributed around a boron nitride cylinder. We focus on I_{sat} measurements collected by pin 1. The floating potential V_{f} was measured by pins 9-11. Three of the discharges studied here are from the MAST Mach probe, figure 1(c). Pins 2, 5 and 8 measured I_{sat} fluctuations. In this analysis, we focus only on pin 5. Pins 1, 3, 4, 6, 7 and 9 measure V_{f}. Both probes were being scanned at a slower rate compared to DIII-D; therefore, a smaller radial bin of 1 cm in the far-SOL was chosen. The far-SOL was taken to be at $\rho = 3 - 4\,\mathrm{cm}$ from the LCFS. Across the discharges used here, the connection length from the reciprocating probe at the midplane to the lower target was on average $L_{\|} \approx 12\,\mathrm{m}$.

MAST-U is also a spherical tokamak ($R_0 = 0.7\,\mathrm{m}$ and $a = 0.5\,\mathrm{m}$) with an aspect ratio similar to its predecessor, $R_0/a \approx 1.4$. A dedicated density scan was performed in L-mode and a DN configuration with constant $I_{\mathrm{P}} = 0.45\,\mathrm{MA}$ and $B_{\mathrm{T}} = 0.5\,\mathrm{T}$. The density ranged from $\overline{n}_{\mathrm{e}} = [0.13 - 0.27] \times 10^{20}\,\mathrm{m}^{-3}$ providing a Greenwald fraction range of $f_{\mathrm{GW}} = [0.28 - 0.56]$. The Mach probe, shown in figure 1(c), sampled measurements at 0.5 MHz. The data contained some noise of around 0.1 MHz that was removed using a lowpass filter. Unfortunately, the probe was biased incorrectly and measured the electron saturation current E_{sat} as a result. Situated directly at the midplane, the probe was dwelling at $\rho \approx 3\,\mathrm{cm}$ collecting at least a hundred milliseconds of measurement data. We analyze pin 2 which measured E_{sat}. We continue to analyse this measurement as this is proportional to the plasma density. Since the data are usually normalized before analysis, E_{sat} may still be used as a representative. Although the MAST-U data are included in the comparison, they are only used to confirm the existing trends in MAST.

3. Stochastic modeling of fluctuations

3.1. Filtered Poisson Process

The analysis of SOL single-point measurements in the framework of stochastic modeling has been successfully applied to various fusion devices [33, 35, 53, 54, 57, 59, 61, 70]. Fluctuations in this region can be well-described as a superposition of uncorrelated pulses in

$$\Phi_K(t) = \sum_{k=1}^{K(T)} A_k \varphi\left(\frac{t - s_k}{\tau_\mathrm{d}}\right). \tag{1}$$

The pulses arrive according to a Poisson process denoted $K(T)$ that occurs within the time interval from $[0, T]$. The pulse shape function is given by φ. As a result of the Poisson process, the arrival times of each pulse, labeled s_k, are independent and uniformly distributed over the given interval. Similarly, the time between fluctuation events, or waiting times between pulses, referred to as w_k, are independent and follow an exponential distribution with an average value of τ_w [67]. All pulses are assumed to have the same duration, indicated as τ_d. The pulse amplitudes, denoted A_k, are exponentially distributed with a mean amplitude value given by $\langle A \rangle$. The stochastic model may also be written as a convolution between the pulse function and a random forcing function [59, 61, 74] in

$$\Phi_K(t) = [\varphi * \mathcal{F}_K]\left(\frac{t}{\tau_\mathrm{d}}\right), \tag{2}$$

where $\mathcal{F}_K$ is a train of delta-function pulses,

$$\mathcal{F}_K(t) = \sum_{k=1}^{K(T)} A_k \delta\left(\frac{t - s_k}{\tau_\mathrm{d}}\right). \tag{3}$$

Thus, the stochastic model is referred to as a *filtered Poisson process*, where a train of delta-function pulses are filtered though the pulse shape function φ.

The main parameter in the stochastic model is the intermittency parameter, denoted as γ, which is defined as the ratio of pulse duration τ_d to the average waiting time τ_w. This parameter determines the level of pulse overlap. When γ is small, the pulses appear isolated during the process, leading to a strong intermittency. On the other hand, when γ is large, there is a significant overlap between pulses, resulting in a weakly intermittent process. As γ approaches infinity, the filtered Poisson process (FPP) tends to resemble a normally distributed process. The four lowest-order moments can be derived by averaging over all random variables: The mean $\langle \Phi \rangle = \gamma \langle A \rangle$, variance $\Phi_\mathrm{rms}^2 = \gamma \langle A \rangle^2$, skewness $S_\Phi = 2/\sqrt{\gamma}$ and flatness $F_\Phi = 3 + 6/\gamma$ [67]. The symbol $\cdot_\mathrm{rms}$ denotes the root mean square value. It is assumed that the pulse function is described by a two-sided exponential distribution given by,

$$\varphi(x) = \begin{cases} \exp(-x/(1-\lambda)), & x \geq 0, \\ \exp(-x/\lambda), & x < 0, \end{cases} \tag{4}$$

where the parameter describing the asymmetry of the pulse is represented by λ, and x denotes a dimensionless variable. PDFs and, consequently, statistical moments remain unaffected by λ. As a result, the PDF of Φ follows a Gamma distribution given by

$$P_\Phi(\Phi) = \frac{1}{\langle A\rangle\Gamma(\gamma)}\left(\frac{\Phi}{\langle A\rangle}\right)^{\gamma-1}\exp\left(-\frac{\Phi}{\langle A\rangle}\right), \tag{5}$$

where Γ denotes the Gamma function. In this study, the measurement time series will be normalized to have zero mean and a standard deviation of unity to eliminate trends in the measurements, for example, caused by a shifitng plasma column. Therefore, the time series are scaled to $\widetilde{\Phi} = (\Phi - \langle\Phi\rangle)/\Phi_{\mathrm{rms}}$. The frequency power spectral density (PSD) of the FPP is given by the analytical expression

$$\Omega_{\widetilde{\Phi}}(\omega) = \frac{2\tau_\mathrm{d}}{\left[1+(1-\lambda)^2(\tau_\mathrm{d}\omega)^2\right]\left[1+\lambda^2(\tau_\mathrm{d}\omega)^2\right]}, \tag{6}$$

a product of two Lorenztian spectra where ω is the angular frequency [75]. The PSD exhibits a flat region at low frequencies providing an estimate for τ_d and then follows a power-law decay at high frequencies, giving an estimate for λ. The shape of the PSD is not affected by the intermittency of the process. As a result of assuming independently and uniformly distributed pulse arrivals and fixed pulse duration, the PSD of the normalized process $\widetilde{\Phi}$ is the same as that of a single pulse.

The FPP can include fluctuations due to noise that are modeled as a normally distributed noise process X with a vanishing mean and a variance X_{rms}^2 [76]. A noise parameter ε may be defined as the square ratio between the root mean square of the noise and the root mean square of the signal, $\varepsilon = (X_{\mathrm{rms}}/\Phi_{\mathrm{rms}})^2$. The combined process $\Phi + X$ has mean value $\langle\Phi + X\rangle = \gamma\langle A\rangle$, variance $(\Phi + X)_{\mathrm{rms}}^2 = (1+\varepsilon)\gamma\langle A\rangle^2$, skewness $S_{\Phi+X} = 2/\gamma^{1/2}(1+\varepsilon)^{3/2}$ and flatness $F_{\Phi+X} = 3 + 6/\gamma(1+\varepsilon)^2$. We model the fluctuations to have noise that is correlated; therefore, the PSD of this process would be equivalent to (6) [76].

In summary, the parameters of the stochastic model are τ_d, τ_w, $\langle A\rangle$, λ and ε. From the PDF or the empirical characteristic function (ECF) of the process, γ and ε can be estimated [76]. The PSD of the time series can provide us with estimates of τ_d and λ [75]. Using those parameters estimated from the PSD, a pulse function of fixed shape and constant duration can be used to estimate $\mathcal{F}$, thus determining τ_w and $\langle A\rangle$. We therefore have two independent methods for determining τ_w and $\langle A\rangle$, either from the PDF and PSD or from the deconvolution. Comparing these estimates provides a check on the validity of the stochastic model.

3.2. Deconvolution

In many previous studies, the extraction of amplitudes and waiting times has generally been performed using the conditional averaging technique. The study presented here moves away from the traditional method to achieve improved amplitude and waiting-time statistics. Here, the Richarson-Lucy (RL) deconvolution method is employed to estimate the forcing described by (3) [77, 78]. Since φ is estimated from (6) due to the assumption of uncorrelated pulses, a maximum likelihood estimate of $\mathcal{F}_K$ can be achieved according to the iterative procedure

$$\mathcal{F}_j^{(n+1)} = \mathcal{F}_j^{(n)}\frac{(\Phi * \widehat{\varphi})_j + b}{\left(\mathcal{F}^{(n)} * \varphi * \widehat{\varphi}\right)_j + b}, \tag{7}$$

where the hat symbol $\widehat{\cdot}$ is used to denote a flipped vector, $\widehat{\varphi}_j = \widehat{\varphi}_{-j}$. Constant τ_d is a requirement for performing deconvolution and ensures that not every fluctuation present in the time series is due to a filament. The parameter b ensures positive definite events throughout iterations [74]. To maintain this, b is chosen so that $\left(\Phi * \widehat{\varphi}\right)_j + b > 0 \, \forall \, j$ in the presence of noise. The iteration in (7) is known to converge to a least squares solution, minimizing $\Phi - \varphi * \mathcal{F}^{(n)}$ under Gaussian noise. The choice of the initial guess $\mathcal{F}^{(0)}$ and the exact value of b does not affect the result of the deconvolution, provided that b is small compared to the mean value of the signal. A detailed study of the strengths and weaknesses of the deconvolution method can be viewed in reference [74].

The estimated forcing may contain spurious pulses caused by noise; therefore, a three-point running maxima method is used as a peak-finding method to extract pulse arrivals and amplitudes where the threshold is set to $10^{-3}\langle A\rangle$. Usually, it is best to investigate the statistical properties of fluctuations in normalized signals. However, normalized signals cannot be used as inputs for the deconvolution algorithm. The algorithm assumes a positive definite input signal, so using a normalized signal results in distorted or missing pulse amplitudes. To address this problem, we scale the normalized time series and perform the RL deconvolution algorithm on $\sqrt{\gamma(1+\varepsilon)}\widetilde{\Phi} + \gamma$. Here, γ and ε are estimated from either the PDF or the ECF of the signal. By incorporating this scaling approach, we ensure that deconvolution accurately captures the pulse function without being affected by the normalization process.

The experimental measurements described in the following reveal a sum of two exponential distributions of pulse amplitude and waiting time. Such a bi-exponential pulse amplitude distribution is based on the assumption of a discrete uniform distribution of pulse velocities [79]. The bi-exponential amplitude distribution is mathematically described as

$$P_A(A) = \frac{q}{\langle A_<\rangle} \exp\left(-\frac{A}{\langle A_<\rangle}\right) + \frac{1-q}{\langle A_>\rangle} \exp\left(-\frac{A}{\langle A_>\rangle}\right). \tag{8}$$

The probability that an event corresponds to a small-amplitude fluctuation is represented by $0 < q < 1$. $\langle A_<\rangle$ and $\langle A_>\rangle$ denote the mean of small-amplitude fluctuations and the mean of large-amplitude fluctuations, respectively. It is assumed that the amplitude of these fluctuations correlates with the velocity, where the lower amplitude fluctuations are mainly affected by parallel drainage, while the higher amplitude fluctuations remain unimpeded [79]. Therefore, the tail of the signal amplitude distribution is primarily influenced by the contribution of large-amplitude fluctuations. In a similar fashion, the mean of the long waiting times between consecutive pulses are given by $\langle w_>\rangle$, whereas its short counterpart is due to noise. Therefore, to estimate the mean values $\langle A_>\rangle$ and $\langle w_>\rangle$, we use the expression of the bi-exponential distribution, not the tail fit, to prevent any hard limits. Later, these will be compared with the ones estimated from the moments of the process.

4. Results

4.1. Fluctuation statistics

Here we present the fluctuation analysis applied to the normalized I_sat measurements from the DIII-D and MAST midplane LPs as well as the normalized brightness time series from the TCV GPI diagnostic. MAST-U analysis was performed on E_{sat} measurements as a result of a wrongly biased potential applied to the probe. The data presented in this section come from scans of the line-averaged density and are parameterized by the Greenwald fraction.

Probability density functions The PDFs of the normalized time-series measurements from TCV, DIII-D, MAST and MAST-U are presented in figure 2. Note that the MAST-U analysis was performed on electron saturation measurements.

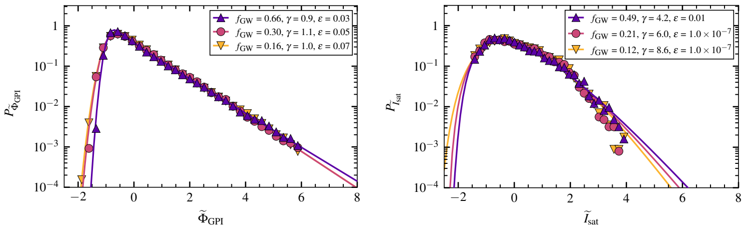

(a) TCV

(b) DIII-D

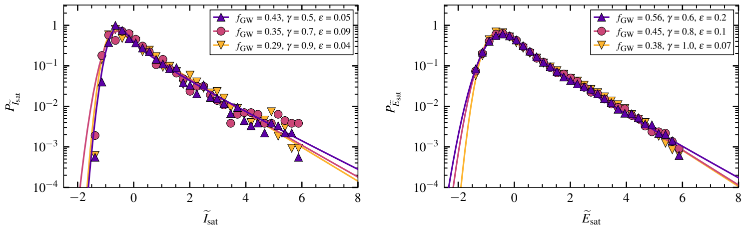

(c) MAST

(d) MAST-U

Figure 2. Histograms of the normalized time-series measurements from (a) TCV GPI data as well as LP data from (b) DIII-D, (c) MAST and (d) MAST-U. Markers represent the data collected at different Greenwald fractions from these machines. The corresponding fitted lines show the agreement with the FPP. The estimated parameters of the stochastic model are presented for the intermittency and the noise-to-signal ratio in the legends. Note that MAST-U results are from E_{sat} measurements.

Focusing on the results of the TCV GPI diagnostic shown in figure 2(a), we note that as the line-averaged density/Greenwald fraction increases, the PDFs remain essentially unchanged over the scan range, showing a skewed Gamma distribution where the tails are toward large values of the signal amplitude. This is consistent with previous results from measurements of the TCV scanning probe in the LSN configuration, showing that the PDFs collapse to a similar shape irrespective of line-averaged density [55]. Similarly, in figure 2(b), the ion saturation current measurements from the DIII-D device also show PDFs all exhibit a similar shape, even though the γ's from the fits differ. We believe that the differences are due to having such short time series at each density which makes the fits very sensitive to the sparse large amplitude events. The DIII-D data have a smaller y-range showcasing less than three decades in probability. If we assume that the overall shape of the PDFs of the DIII-D $\widetilde{I}_{\mathrm{sat}}$ data is not a function of density and use all of the DIII-D normalized time series data, then we get a much larger data set and estimate the intermittency parameter from this, which is $\gamma = 4.2$. Note that this value is the same as the DIII-D dataset for the highest Greenwald fraction. We assign this as the actual value for DIII-D in the later multimachine comparisons. Similar values of the intermittency parameters at different f_{GW} in DIII-D is not surprising, as previous results [26] have suggested that the relative fluctuation levels in the far-SOL are independent with increasing line-averaged density. This is also the case for the spherical tokamaks, MAST and MAST-U, as seen in figures 2(c) and 2(d) where the PDFs exhibit very similar skewed Gamma distributions as line-averaged density is increased, but γ does not appear to significantly change. Recalling from Section 3, a small γ implies highly intermittent, isolated fluctuations in time, while a large γ implies overlapping fluctuation events with little to no time between them. Our primary conclusions from these data are that over the range $0.1 \lesssim f_{\mathrm{GW}} \lesssim 0.6$ in L-mode plasmas, the intermittency does not depend strongly on density and that at similar Greenwald fraction densities, the far-SOL fluctuations from TCV, MAST and MAST-U appear more intermittent compared to DIII-D.

Frequency power spectral densities The results of the PSDs for various line-averaged densities in TCV, DIII-D, MAST, and MAST-U are shown in figure 3. In all cases, the PSDs of the experimental data show good agreement with the FPP, showcasing a Lorentzian. It is worth noting from the TCV GPI measurements that the duration time estimates are implemented on several decades of frequency spectra, highlighting the importance of long time-series measurements and good sampling frequencies. The aforementioned conditions allow us to reliably estimate τ_{d} and λ, respectively. This is not the case for some of the reciprocationg LPs, in particular, DIII-D in figure 3(b) where the flat part of the spectra suffers as a result of short time series.

Previously it was found from the TCV reciprocating LPs in reference [55] that the conditionally averaged waveform appears independent of density, hence the duration times do not change. However, for the TCV GPI time series in figure 3(a), it is observed that as the line-averaged density increases, the τ_{d} of the fluctuations also increases. Applying the conditional averaging to a single GPI diode view looking at the far-SOL shows the waveforms becoming broader with density, indicating an increase in the duration time, but we do not show them here. To further confirm the validity of the τ_{d} results from the TCV GPI measurements, the size and velocity estimates from reference [80] can be used to find the duration time. Note that reference [80] utilized conditional average sampling across the field of view to estimate velocities. By estimating the duration times as a ratio of size and velocity, where the total velocity is taken as the norm of its radial and poloidal components, this showcases that the duration times do indeed increase with Greenwald fraction density. These differences between the LP and GPI have also been observed in C-Mod where further details can be seen in reference [62].

Similarly in MAST and MAST-U, the duration times, τ_{d}, do indeed increase with density, as seen in figures 3(c) and 3(d). The raised tails at frequencies approximately above 0.06 MHz in the MAST-U spectra are artifacts of stray currents in the probe electronics, which possibly impact the electron saturation current measurements,

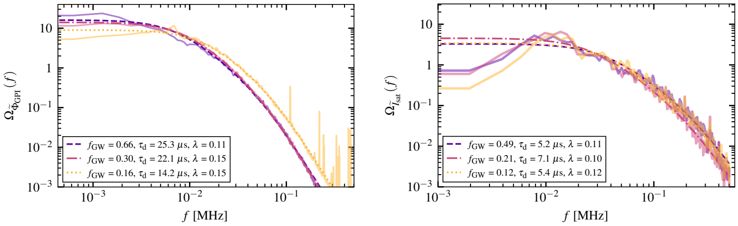

(a) TCV (b) DIII-D

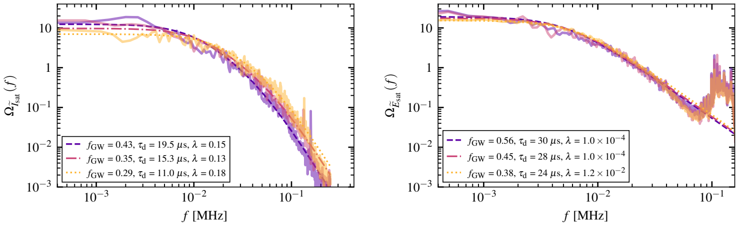

(c) MAST (d) MAST-U

Figure 3. Power spectral densities of the normalized time-series measurements from (a) TCV GPI data as well as LP data from (b) DIII-D, (c) MAST and (d) MAST-U. Solid lines represent the data collected at different Greenwald fractions. The corresponding fitted lines, which are textured, show agreement with the FPP. The estimated parameters of the stochastic model are presented for the duration times and the asymmetry parameter. Note that MAST-U results are from E_{sat} measurements.

causing a higher relative standard deviation. A low-pass filter was implemented to remove most of this effect. The two decades in frequency power spectra is result of low sampling frequencies of the MAST-U probe in figure 3(d). In figure 3(b), the duration times in DIII-D appear to be independent of the line-averaged density and are significantly smaller than those found in TCV, MAST, and MAST-U. Conditional averaging results also yield short duration times from the DIII-D measurements [26,81], but for these measurements we do not show them here. The low-frequency parts of the spectra are the result of the short time series obtained by the reciprocating probe. Although the τ_{d} of DII-D is smaller on average than that of TCV, MAST, and MAST-U, small τ_{d} values similar to those of DIII-D and independent of density were found in the C-Mod far-SOL as reported in reference [62]. The λ parameter that describes the asymmetry of the pulse seems approximately similar in TCV, DIII-D, and MAST indicating a fast rise and a slow decay of the pulse waveform. However, in MAST-U, the estimated asymmetry is smaller with λ values less than what can be extracted from the data, suggesting an even faster rise and resembling a one-sided exponential pulse function. A similar asymmetry was found using probe measurements from C-Mod [62].

4.2. Parametric analysis

We now examine how the stochastic model parameters change with Greenwald fraction, utilizing the respective core density scans from each machine. Results are included from the C-Mod GPI and LP diagnostics, examining the stochastic model parameters over a wider density scan range $0.12 < f_{\mathrm{GW}} < 0.85$, which we have recently studied in detail in reference [62]. Note that C-Mod has a much higher toroidal field compared to the other devices. The results from the previous section are included for all devices, plotting those parameter values as a function of f_{GW}. The C-Mod data span the other devices, showcasing the large range in Greenwald fraction densities. We also present the results of the GPI data analysis separately from the LP data analysis, as diagnostic differences have been highlighted in reference [62].

In order to estimate the waiting time statistics from the time series, the criterion for the deconvolution must be met. The product of the intermittency and the normalized sampling time must be less than and equal to 1/20 in order to execute a reliable deconvolution [74]. This criterion was not met for some of the time series measurements, in particular, the data from DIII-D since the intermittency values are larger compared to the other devices. Therefore, in this section, only the mean waiting times estimated from the fluctuation statistics, i.e. $\tau_{\mathrm{w}} = \tau_{\mathrm{d}}/\gamma$, will be shown for DIII-D. Extracting absolute values of the amplitudes from the GPI measurements will not be provided, as the GPI signal level which is proportional to the line brightness is impacted by the neutral density of the puffed gas.

Results from Langmuir Probes The results of the LP fluctuation analyses as a function of Greenwald fraction are presented in figure 4. In all cases, the C-Mod results appear to span the two other sets of data - DIII-D and that of MAST and MAST-U. Figure 4(a) shows the variation in intermittency of the far-SOL fluctuations over their respective density scans. As discussed previously, for DIII-D the same γ value was chosen for all f_{GW} due to the robust PDFs shown in figure 2(b). For MAST-U, γ appears to be unchanging with f_{GW}. For MAST, there is a slight decrease in γ with f_{GW} which seems to scatter across the Greenwald fraction range studied. The small variations in γ at similar Greenwald fractions in MAST are notable, possibly due to the ability of the fitting or due to the fact that there is a variation in the plasma current and toroidal field. But we conclude for MAST and therefore MAST-U that γ appears to be independent of the Greenwald fraction given the available data. C-Mod does indicate a stronger change with Greenwald fraction, through its dependence on line-averaged density. The γ values found in C-Mod agree with MAST and MAST-U for $0.2 < f_{\mathrm{GW}} < 0.4$ and roughly agree with DIII-D at $f_{\mathrm{GW}} \approx 0.12$. Repeats of the plasma discharges at similar Greenwald fractions would be required to see if the statistics are consistent.

The variation in the duration times versus the Greenwald fraction is presented in figure 4(b). For C-Mod and DIII-D, the duration times over their respective f_{GW} ranges appear to be independent of the Greenwald fraction. These also have similar values (within the scatter) for similar Greenwald fraction ranges. In reference [82], it is indicated that, on average in C-Mod, filament size and radial velocity increase with line-averaged density, therefore τ_{d} in the far-SOL is expected to remain constant, as shown in figure 4(b). However, the duration times in MAST and MAST-U seem to increase with the line-averaged density.

The mean amplitudes $\langle A \rangle$, estimated from the I_{sat} measurement time-series are

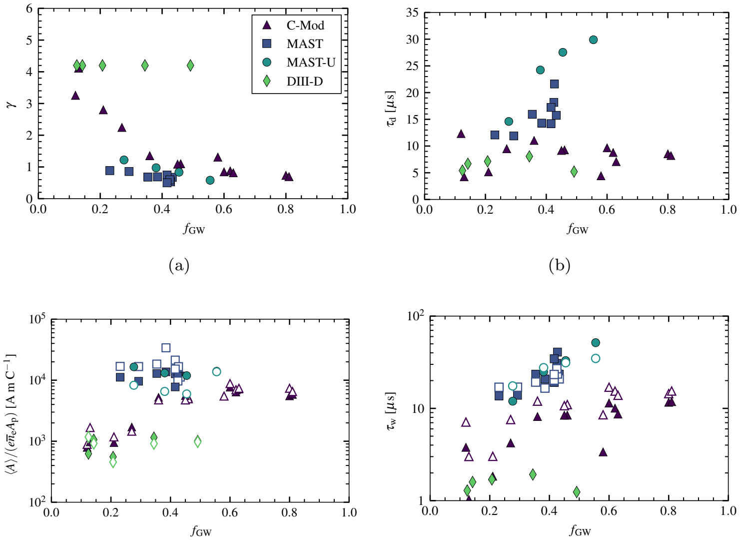

(a) (b)

(c) (d)

Figure 4. Stochastic model parameters as a function of Greenwald fraction from LP diagnostics of C-Mod, MAST, MAST-U and DIII-D taken in L-mode plasmas. (a) Intermittency parameter, (b) duration time, (c) mean amplitudes normalized by $e\overline{n}_\mathrm{e}A_\mathrm{p}$, and (d) mean waiting times are shown for each fusion device are presented. The legend in figure (a) shows which marker is assigned to which fusion device. In figures (c) and (d), the filled-in markers show the means estimated from the moments, i.e. $\langle A\rangle = \langle I_\mathrm{sat}\rangle/\gamma$ and $\tau_\mathrm{w} = \tau_\mathrm{d}/\gamma$, where as the hollow markers with corresponding colors are the estimated means from the RL deconvolution. Note that MAST-U results are from E_sat measurements.

shown in figure 4(c). For a fair comparison, the mean amplitudes are normalized by $e\overline{n}_\mathrm{e}A_\mathrm{p}$ where the projected area of the probe pin is given by A_p measuring I_sat and e is the electron charge. The hollow markers show the estimated mean amplitudes from the deconvolution estimated from (8). For low Greenwald fractions between $0.1 < f_\mathrm{GW} \leq 0.3$, the mean normalized amplitudes appear to have similar values for C-Mod and DIII-D. MAST and MAST-U seem to have larger $\langle A\rangle$ compared to DIII-D and C-Mod. C-Mod is the only dataset showing a significant change in $\langle A\rangle$ of the ion saturation current where the mean values increase by two orders of magnitudes from $f_\mathrm{GW} \approx 0.12$ to $f_\mathrm{GW} \approx 0.8$. These results overall showcase linearly increasing mean amplitudes for DIII-D, MAST and MAST-U, but a considerable increase of approximately two orders of magnitude in the mean amplitudes for C-Mod.

In figure 4(d) we present the mean waiting times, τ_w. The mean waiting times calculated from $\tau_\mathrm{w} = \tau_\mathrm{d}/\gamma$ are presented with filled-in markers, where the hollow markers represent the results of the deconvolution for C-Mod, MAST, and MAST-U. The results of deconvolution agree within a factor of two compared to the mean waiting times estimated from τ_d/γ for C-Mod, but in most cases for MAST and MAST-U. As mentioned above, the DIII-D ion saturation current data did not meet the deconvolution criterion; instead, only the values from $\tau_\mathrm{w} = \tau_\mathrm{d}/\gamma$ are presented. The results of DIII-D show that the τ_w's do not change with the Greenwald fraction and are noticeably smaller in comparison to those of the other devices. The independence of τ_w over f_GW is consistent with the fact that the intermittency parameter and duration times are independent of line-averaged density for DIII-D. In C-Mod, τ_w shows a linear increase with f_GW as discussed previously [62]. In MAST and MAST-U, the mean waiting times appear to increase with f_GW. These τ_w's seem significantly longer compared to those in C-Mod and DIII-D at similar Greenwald fraction ranges $0.3 \lesssim f_\mathrm{GW} \lesssim 0.5$. This suggests that the fluctuations in MAST-U and MAST occur less frequently compared to those of C-Mod and DIII-D at low-intermediate Greenwald fractions.

Results from Gas puff imaging We present the stochastic model parameters estimated from the GPI diagnostics in C-Mod and TCV in figure 5. Time series from several

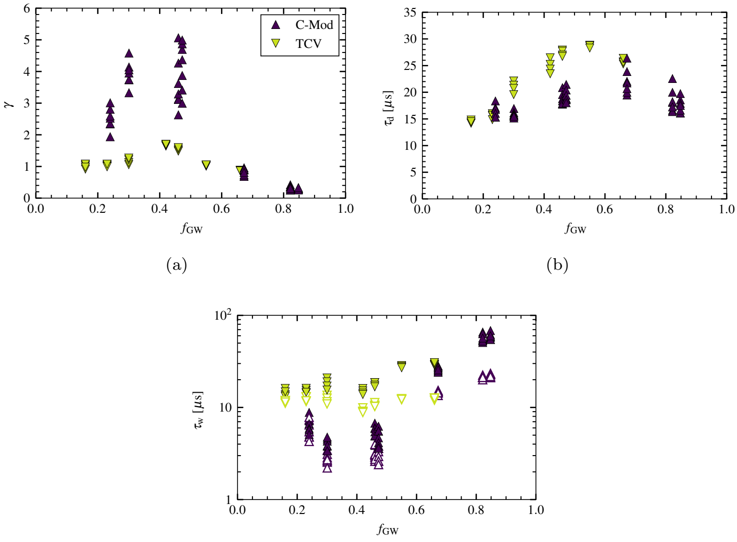

(a)

(b)

(c)

Figure 5. Stochastic model parameters as a function of Greenwald fraction analyzed from the GPI diagnostics of C-Mod and TCV taken in L-mode plasmas. (a) Intermittency, (b) duration times, and (c) mean waiting times are shown for both fusion devices. In figure (c), the filled-in markers show the means estimated from the moments, i.e. $\tau_\mathrm{w} = \tau_\mathrm{d}/\gamma$, while the hollow markers with corresponding colors are the estimated means from the RL deconvolution. The legend in figure (a) shows which marker is assigned to which fusion device.

diode view positions at similar flux surface positions for each device were analyzed to ensure the statistics were reproducible. Absolute values of the amplitudes from the GPI measurements are not presented, as the GPI signal level is impacted by the neutral density of the puffed gas.

The results for the intermittency parameter against the Greenwald fraction are shown in figure 5(a). In C-Mod we observe two trends where the value of γ increases with the Greenwald fraction until $f_{\mathrm{GW}} \approx 0.46$ and then decreases. It is not clear why there are two different trends. The considerable variation for $f_{\mathrm{GW}} \approx 0.46$ is discussed in reference [62]. The stochastic model parameters were assessed using the C-Mod GPI measurements in order to investigate whether the large scatter in γ could be attributed to the radial dependence. We concluded that the radial variation was not responsible for it. As part of that study, we found that any radial dependence in the far-SOL is reduced for $f_{\mathrm{GW}} \geq 0.67$. This is consistent with the flattened and broadened profiles seen in C-Mod at those higher Greenwald fractions [62].

However, the GPI results from the TCV experiments show a smaller variation in intermittency across the density scan compared to the C-Mod result. It is worth noting that a less prominent bump is found for TCV around 50% of its density limit, but the trend in γ is qualitatively similar to that of the C-Mod GPI density scan. Interestingly, around this Greenwald fraction for both devices, detachment occurs for TCV [80] and C-Mod [83]. However, the LP data for C-Mod as well as the DIII-D show no inflection, which goes from attached to detached divertor. However, it is not known how divertor detachment affects the fluctuation statistics measured by the GPI at the plasma midplane.

Next, the duration times are plotted as a function of f_{GW} in figure 5(b). It should be noted that the GPI systems in TCV [84] and C-Mod [8] have a similar spatial resolution of approximately 5 mm. Again, there are quantitative differences in the τ_{d} values, with the TCV values being roughly 1.4× larger than those from C-Mod for $0.3 \lesssim f_{\mathrm{GW}} \lesssim 0.66$. In TCV, an increasing dependence between τ_{d} and line-averaged density is consistent with the trend for τ_{d} found from analysis of the PSDs, shown in figure 3(a) and discussed there. We attribute the larger τ_{d} and λ estimated from the GPI diagnostics compared to those estimated from the LPs to be due to the spatial averaging inherent in the finite-resolution of the GPI views. These attributes are discussed in reference [62].

We present the mean waiting times estimated from the moments (filled-in markers) as well as the RL deconvolution (hollow markers) in figure 5(c). From the C-Mod analysis, the τ_{w} estimated from τ_{d}/γ and from the deconvolution increase with the Greenwald fraction, although those from the deconvolution are smaller by up to a factor of 3. This discrepancy increases as f_{GW} increases. It is not observed in the C-Mod LP measurements (see figure 4(d)), as also highlighted in [62]. Further modeling work is required to understand why this is the case. In TCV, the τ_{w} estimated from the moments also increases with f_{GW}, but this is a weaker increase compared to C-Mod. For $f_{\mathrm{GW}} < 0.6$, the mean waiting times extracted from both methods are longer compared to the C-Mod GPI results. The deconvolved waiting times from the TCV GPI time series are approximately 1.3× higher than those from the moments for small f_{GW}, but become relatively larger as the Greenwald fraction increases, becoming roughly 2.8× higher at $f_{\mathrm{GW}} = 0.66$. Although the results for $\tau_{\mathrm{w}} = \tau_{\mathrm{d}}/\gamma$ show an increasing trend with density, this is not observed in the deconvolved mean waiting times.

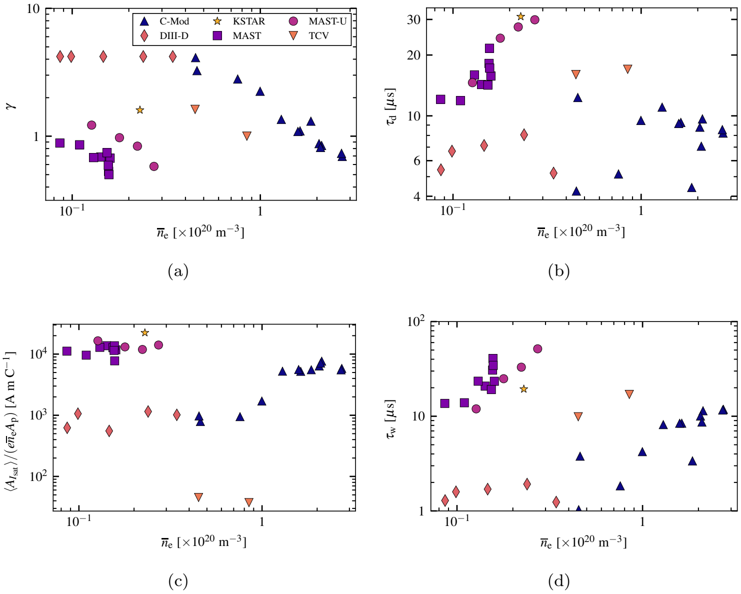

(a) (b)

(c) (d)

Figure 6. Fluctuation statistics as a function of line-averaged densnity analyzed from the LP diagnostics. (a) Intermittency parameter, (b) duration times, (c) mean amplitudes normalized by $e\overline{n}_\mathrm{e}A_\mathrm{p}$, and (d) mean waiting times are shown for all devices. The markers indicate the device and is found in figure (a). The subfigures are given here are all plotted on logarithmic scales.

Machine parameters Hitherto, it has been shown how the stochastic model parameters change with the Greenwald fraction by varying $\overline{n}_\mathrm{e}$. We use the entire LP database and combine results from previous TCV [57] and KSTAR [33] studies that analyzed time series from outboard midplane LPs, dwelling in the far-SOL. The fluctuation measurements using the TCV LP were not under the same experimental conditions as the TCV GPI measurements. We do not show GPI results here since τ_d estimates cannot be compared to LPs due to spatial averaging effects.

Since the Greenwald fraction depends on three parameters, $\overline{n}_\mathrm{e}$, I_P and a, here we study each dependence individually. For the first case we show how the stochastic model parameters change with $\overline{n}_\mathrm{e}$ in figure 6. The variation between γ and $\overline{n}_\mathrm{e}$ is shown in figure 6(a) for all devices considered. It is apparent that as $\overline{n}_\mathrm{e}$ increases, the intermittency parameter of the far-SOL fluctuations in C-Mod reduces thereby the fluctuation becoming strongly intermittent. However, this trend is weak from the TCV LP measurements as there are only two data points and this conclusion contradicts previous TCV work [55]. For the available DIII-D datapoints, the values of γ for the observed densities lower than $\overline{n}_\mathrm{e} < 0.4 \times 10^{20}\,\mathrm{m}^{-3}$ were set to the same value as previously described. The MAST and MAST-U results seem to cluster in the lower-left corner and both show that γ decreases weakly with increasing $\overline{n}_\mathrm{e}$. For

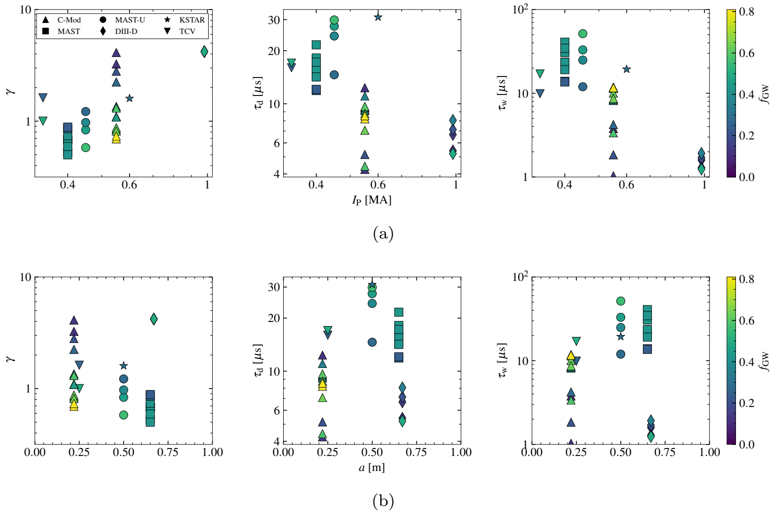

(a)

(b)

Figure 7. Indicative trends from the multimachine scan showcasing the parameters estimated from the LP I_{sat} time-series measurements from C-Mod, MAST, MAST-U, DIII-D, KSTAR and TCV, represented by the markers in the legend of (a). The intermittency parameter γ, the duration time τ_{d} and the mean waiting times τ_{w} are plotted against (a) the plasma current I_{P} and (b) minor radius a. The color bars indicate the Greenwald fraction f_{GW}.

MAST-U, the estimated γ is from E_{sat} not I_{sat}.

Next, the variation of τ_{d} with $\overline{n}_{\mathrm{e}}$ is shown in figure 6(b). These results show no obvious trend for DIII-D, C-Mod and TCV. MAST and MAST-U show increasing duration times with $\overline{n}_{\mathrm{e}}$. This leads to the strong conclusion that τ_{d} is independent of $\overline{n}_{\mathrm{e}}$ across machines. The mean amplitudes normalized by $e\overline{n}_{\mathrm{e}}A_{\mathrm{p}}$ in figure 6(c). The constant values in figure 6(c) apart from C-Mod, correspond to $\langle A\rangle \sim \overline{n}_{\mathrm{e}}$. Thus, the amplitudes are increasing with line-averaged density which is not surprising, since denser core plasmas probably shed denser filaments. The significant increase is notable for C-Mod. As discussed before, the mean waiting times shown in figure 6(d) increase with $\overline{n}_{\mathrm{e}}$ for C-Mod, MAST, MAST-U, and TCV. The large spread in τ_{w} can be observed across the devices when plotted as a function of $\overline{n}_{\mathrm{e}}$. Although τ_{w} appears to trend with $\overline{n}_{\mathrm{e}}$, the spread across the machines suggests that $\overline{n}_{\mathrm{e}}$ is not the only factor. The same may be true for most of the results displayed in this section as shall be demonstrated.

Next, the variation of the far-SOL fluctuation statistics with engineering parameters are presented in the following figures. The variation with I_{P} and a are shown in figure 7 in which f_{GW} is dependent on. The color bar indicates the range of Greenwald fractions that are present in each device. The dependencies with I_{P} are clear in figure 7(a). The γ estimated from the time-series measurements of LPs appears to increase with I_{P}. This is a consequence of the reduction in τ_{d} and τ_{w} also seen in figure 7(a). There is no variation of the stochastic model parameters with

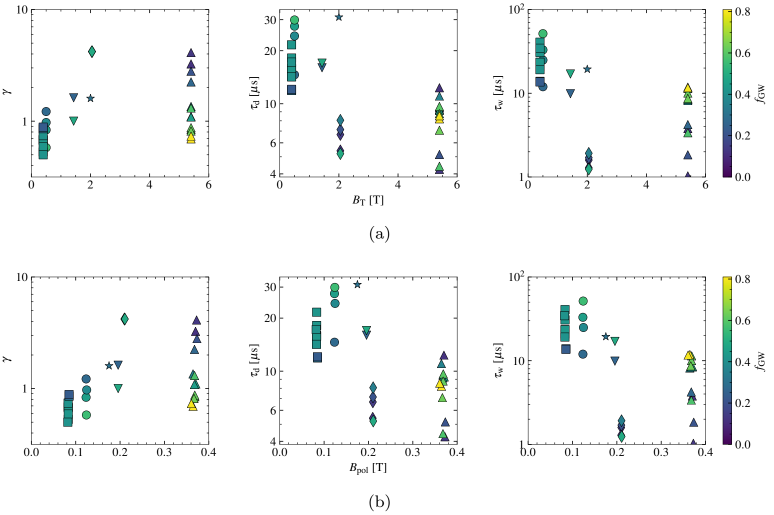

(a)

(b)

Figure 8. Indicative trends from the multimachine scan showcasing the parameters estimated from the LP I_{sat} time-series measurements from C-Mod, MAST, MAST-U, DIII-D, KSTAR and TCV, represented by the markers in the legend of figure 7(a). The intermittency parameter γ, the duration time τ_{d} and the mean waiting times τ_{w} are plotted against (a) on-axis toroidal magentic field B_{T} and (b) the poloidal magnetic field B_{pol} (definition of B_{pol} found in reference [64]). The color bars indicate the Greenwald fraction f_{GW}.

either a as seen in figure 7(b) or with R_0; hence we do not show these results for R_0. Contributing the most to the Greenwald fraction, we conclude that $\overline{n}_{\mathrm{e}}$, I_{P}, and hence the poloidal magnetic field B_{pol} (shown in figure 8(b)), plays a role in the far-SOL statistics across these devices. The lack of dependence of the a suggests that the Greenwald fraction may not be the parameter when it comes to describing far-SOL statistics across the devices.

The impact of the magnetic fields B_{T} and B_{pol} are shown in figure 8. The toroidal fields across devices can be seen in figure 8(a). γ seems to be independent of B_{T}, but a possible trend is presented in the duration times and the mean waiting times where both appear to decrease with B_{T}. The plot of these results as functions of the toroidal field in the outboard midplane did not make a difference and showed a trend similar to those presented in figure 8(a).

The statistics as a function of B_{pol} are presented in figure 8(b). The definition of B_{pol} used is the same as that found in [64]. Although dependent on I_{P}, a and elongation κ (shown in figure 9(b)), it seems that I_{P} is the dominant factor for the results shown here. We see a weak increase, arguably no change in γ with poloidal magnetic field. It follows from γ that τ_{d} and τ_{w} show some dependencies with B_{pol} indicating a decrease. This implies that the effect of κ as seen in figure 9(b) does not counteract the effects of I_{P} as shown in figure 7(a). Equally, the short range of κ may also be a contributing factor to the latter.

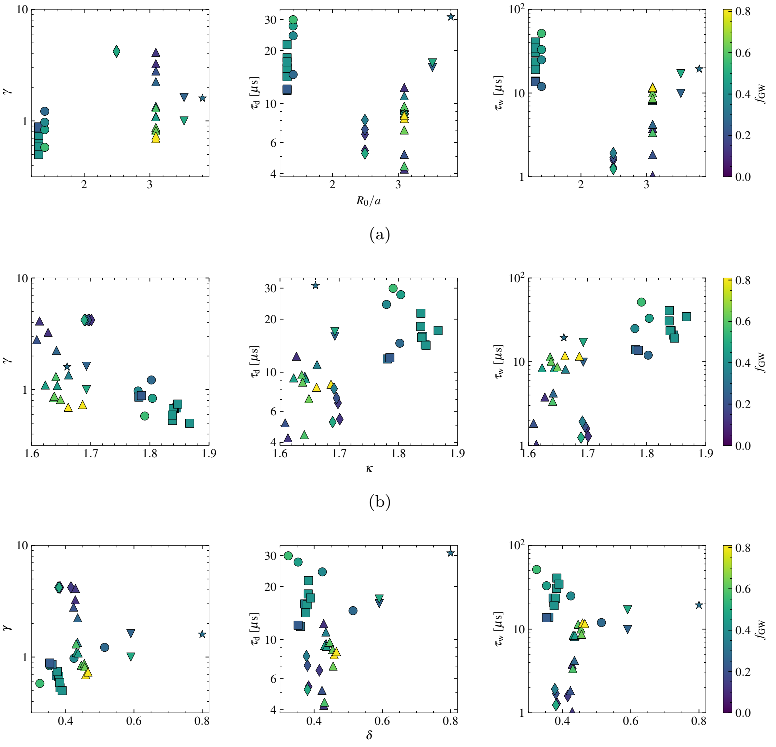

(a)

(b)

(c)

Figure 9. Trends from the multimachine scan of the parameters estimated from the LP I_sat time-series measurements from C-Mod, MAST, MAST-U, DIII-D, KSTAR and TCV, represented by the markers in the legend of figure 7(a). The intermittency parameter γ, the duration time τ_d and the mean waiting times τ_w are plotted as a function of (a) aspect ratio R_0/a, (b) elongation κ, and (c) δ. The color bars indicate the Greenwald fraction f_GW.

The effects of plasma shaping on the far-SOL fluctuation statistics are shown in figure 9. Considering that the outboard sides of magnetically confined fusion devices are locally interchange unstable, we chose to examine how the aspect ratio R_0/a, *kappa* and triangularity δ, affects the stochastic model parameters found for the far-SOL fluctuations [85].

We present these results in figure 9(a). γ is plotted as a function of R_0/a for a range of Greenwald fraction cases studied. The results indicate that the far-SOL intermittency is not strongly dependent on R_0/a, however, in all cases, the fluctuations across all devices are intermittent. The estimated duration times from the time series of all devices are plotted against the aspect ratio in figure 9(a). For conventional

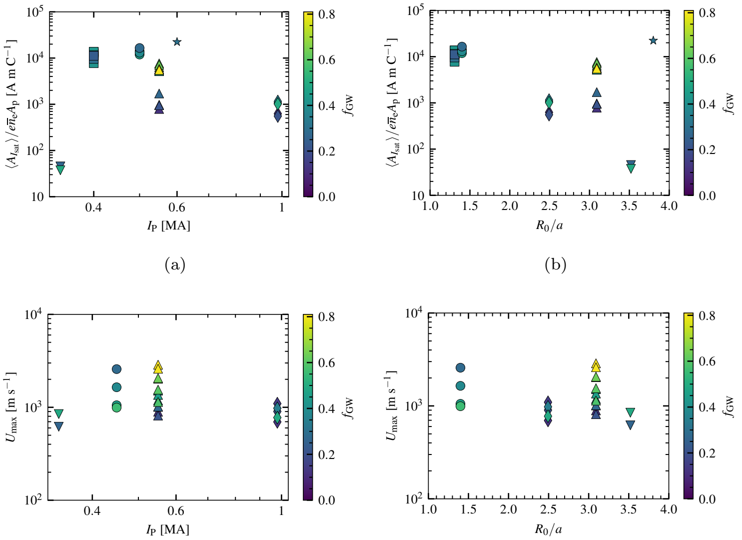

(a) (b)

(c) (d)

Figure 10. Mean amplitudes normalized by $e\overline{n}_{\rm e}A_{\rm p}$ plotted as function of (a) $I_{\rm P}$ and (b) aspect ratio. Maximum of the cross-conditionally averaged velocity $U_{\rm max}$ as a function of $I_{\rm P}$ in (c) and the aspect ratio in (d). The legend in figure 7(a) shows which marker belongs to which fusion device. The color bar indicates the Greenwald fraction.

tokamaks, the trend shows a dependence with R_0/a where $\tau_{\rm d}$ increases, and therefore the fluctuations in the far-SOL become longer, on average. Of the conventional tokamaks considered in this study, KSTAR shows the longest duration time around $30\,\mu$s and DIII-D shows the shortest duration times, on average $8\,\mu$s. However, for the smallest aspect ratio, large durations are also observed. The trend exhibits a dependence on R_0/a where $\tau_{\rm d}$ appears to be the minimum at $R_0/a \approx 2.5-3$. The trend for $\tau_{\rm w}$ also appears to show a minimum in the similar range of R_0/a.

The results of how the elongation, κ, affects the statistics are shown in 9(b). Note that this is κ at the LCFS. There is a dependency for γ, where there appears to be a general decrease with elongation. The duration times and mean waiting times tend to increase with κ. Due to the small range of κ, these conclusions may not hold in general. Model parameters as a function of triangularity δ, are shown in figure 9(c) and there appears to be no obvious trend.

The absolute values of the mean amplitudes normalized by $e\overline{n}_{\rm e}A_{\rm p}$ are shown in figure 10 as a function of a few engineering parameters. First, it is clear that the plasma current has an impact on the far-SOL fluctuations, as seen in figure 10(a). The spread of the data points is due to the impact of the line-averaged density of the amplitude of the fluctuations, as previously highlighted in figure 6(c). Overall, the mean normalized amplitudes of the I_{sat} measurements depend on I_{P}.

The effect of I_{P} on the maximum of the cross-conditionally averaged radial velocities U_{max} is presented in figure 10(c). It is further recognized that the velocities measured from the E_{sat} measurements from the MAST-U device may indicate a different behaviour compared to I_{sat} due to small mass and if the maxima in E_{sat} do not coincide systematically with the maxima in I_{sat}. The variation with Greenwald fraction for each presented device is clear where for C-Mod U_{max} shows an increase with density. One may consider a slight increase in radial velocities with the Greenwald fraction for the TCV LP. However, in DIII-D it appears that the radial velocities are independent of the density for $I_{\mathrm{P}} = 1\,\mathrm{MA}$. This has also been observed in reference [26] for $I_{\mathrm{P}} = 0.8\,\mathrm{MA}$. The variation of U_{max} with I_{P} between these devices is unclear since it is obvious that $\overline{n}_{\mathrm{e}}$ affects the radial velocity of some of these devices more than others. The mean particle flux was also investigated; however, the I_{sat} data for MAST-U are required to make suitable conclusions and are therefore not shown.

The effect of the aspect ratio on the mean amplitudes is presented in figure 10(b). A dependency can be observed with the aspect ratio for conventional tokamaks as was observed for τ_{d} and τ_{w} in figure 9(a). Furthermore, it also seems unclear that U_{max} in figure 10(d) changes with aspect ratio, but the dependence with line-averaged density is notable for C-Mod and TCV.

In summary, the stochastic model parameters as a function of f_{GW} show different trends for the fusion devices studied here, as illustrated in figures 4 and 5. C-Mod is the only device that seems to show a significant variation in the intermittency parameter values and mean amplitudes across a wide range of f_{GW} and $\overline{n}_{\mathrm{e}}$. The intermittency parameter shows no definitive trend as a function of the Greenwald fraction density across C-Mod, TCV, DIII-D, MAST and MAST-U. The machine parameter scan shows a strong dependence with I_{P} but no dependence with a. This suggests that f_{GW} may not be the right choice in describing far-SOL fluctuation statistics across devices. Nonetheless, it is evident that the mean amplitudes of the fluctuations increase with $\overline{n}_{\mathrm{e}}$ for all of the devices presented here. Although these mean amplitudes are influenced by I_{P} overall, no observable trend is found for the radial velocity, as shown in figure 10. Moreover, the results in figure 9 showing changes in far-SOL fluctuation statistics with aspect ratio, elongation, and triangularity indicate some dependencies on plasma shaping. To highlight, τ_{d} and τ_{w} clearly trend with aspect ratio of the conventional tokamaks.

5. Discussion and conclusion

We have described the diagnostic measurements, the measurement conditions, and the framework(s) for the analyses of the measurements in the preceding Sections. Further, we have demonstrated that far-SOL fluctuations analysed from the LP measurements taken from DIII-D, MAST and MAST-U as well as the TCV GPI measurements are well portrayed as a superposition of uncorrelated two-sided exponential pulses with fixed shape and constant duration. The intermittency parameter of these fluctuations appears to be independent of the line-averaged density in DIII-D and TCV, as was previously seen in the relative fluctuation level profiles in references [26, 86], respectively. Despite this, these earlier studies observed that the I_{sat} profiles exhibit broadening, indicating an increase in the amplitudes of the fluctuations.

Over the relatively small range of Greenwald fractions studied in MAST and MAST-U, we observed that γ of the far-SOL fluctuations do not change. C-Mod stands out as the only fusion device in this study that demonstrates a significant change in the shape of the PDF from a near-Gaussian distribution to a strongly skewed-Gamma distribution as the Greenwald fraction increases [62]. This shape alteration indicates not only a rise in intermittency but also an increase in amplitudes, as clearly shown by the elevated tails in reference [62]. References [86] and [33], which investigate the dependence of the profile with the density on TCV and KSTAR using reciprocating LPs, respectively, show that $\overline{n}_\mathrm{e}$ does not influence the relative fluctuation levels in the far-SOL. The robustness of this result suggests that there is no change in the intermittency parameter.

The estimates of τ_d show no change with $\overline{n}_\mathrm{e}$ for DIII-D and C-Mod. This is not the case for MAST and MAST-U, although this may be due to the small range in Greenwald fractions. The TCV GPI results show an increase in τ_d with density, which is contrary to previous results that used reciprocating LPs [29]. The mean waiting times between consecutive fluctuations vary little with $\overline{n}_\mathrm{e}$ in DIII-D, but vary in C-Mod, TCV, MAST, and MAST-U. Although f_GW has been used as a parameter for single machine scans where trends have been observed in previous studies for fluctuation analysis [33, 35, 53, 54, 58, 59, 61, 62, 70], the suitability of f_GW as a dimensionless parameter for cross-machine comparison is questionable due to the interplay between $\overline{n}_\mathrm{e}$ and I_P.

For the first time, the study presents how these fluctuation statistics change with machine and engineering parameters covered by the available database in L-mode plasmas. The Greenwald fraction depends on $\overline{n}_\mathrm{e}$, I_P, and a. The size of the device, in particular a, seems to have no effect on the fluctuation statistics across machines. We found that the statistics vary strongly with I_P as seen in figure 7(a) and, therefore, B_pol as presented in figure 8(b). The results in figure 8(b) suggest that the effects of I_P dominate over any dependence on κ. The effect of I_P on SOL profiles has previously been addressed in single machine scans [26, 28, 32, 38, 62, 87]. In particular, references [26, 28] show a broadening and flattening of the radial particle density profiles with decreasing I_P for DIII-D and TCV, respectively. This suggests that although the PDFs are independent of Greenwald fraction as indicated by reference [28], the mean amplitudes of the filaments are increasing with decreasing I_P. In addition, as is clearly shown in reference [26], for the same plasma conditions, there are stark differences in the signal amplitudes where these are higher for $I_\mathrm{P} = 0.8\,\mathrm{MA}$ than for $I_\mathrm{P} = 1.0\,\mathrm{MA}$. This is consistent with the results from the DIII-D measurements shown here. On the basis of the available data, it was found that the mean amplitudes across devices are impacted by I_P.

The multimachine database reveals little differences in the radial velocities across different devices with varying I_P, hence B_pol. Within the DIII-D density scan, the radial velocity varies little, as previously reported in [26]. Changes in radial velocities are noticeable with increasing Greenwald fraction density as shown in figure 10(c), but this is not the case in the DIII-D density scan. Unlike DIII-D, the radial velocity decreases with increasing I_P in previous TCV results [28]. These differences between machines may be attributed to the combined effects of the density and B_pol. This would explain why a correlation between radial velocities and f_GW is not apparent in the multimachine analysis. Another single-machine scan looked at the effect of the magnetic field pitch angle [88], where the findings showed that PDFs of the burst amplitude and frequency are skewed and flattened with elevated tails as the pitch angle increased. This suggests that filaments are more frequent at higher pitch angles, where B_T remained fixed. However, it was shown that there was no significant variation in radial velocities with pitch angle. This lack of change in velocities across devices can also be seen in figure 10(c), hence no variation with B_{pol}.

The scan in B_{T}, as seen in figure 8(a), suggests that fluctuations are less intermittent at higher toroidal fields and lower densities. These results show a similar trend to the results for B_{pol} in figure 8(b). A higher B_{T} suggests smaller radial $\mathbf{E}\times\mathbf{B}$ drifts, which is one of the reasons for reducing the amount of cross-field transport in the SOL [89, 90]. Reference [91] investigated the magnetic field dependence of L-mode filaments in AUG, showing that the number of blobs detected by lithium beam emission spectroscopy decreases with increasing B_{T} at constant I_{P}. However, this was not observed at constant q_{95}. As highlighted by reference [91], this suggests that B_{T} cannot be the only factor that affects the frequency of the fluctuations. The results of the present multimachine scan show that machines with higher B_{T} have smaller τ_{d} and τ_{w}, thus an increase in the blob frequency.

The effects of plasma shaping on the model parameters are investigated. First, the impact of triangularity on the far-SOL fluctuation statistics across devices with δ is inconclusive, as seen in figure 9(c). Although we study a smaller range of δ here, this observation is consistent with the notion that a higher δ suggests greater significance of filaments, as highlighted in simulations of inner-wall limited plasmas [85]. Recently, a triangularity scan was performed on TCV, demonstrating the reduction of SOL fluctuations in negative triangularity plasmas [65]. This study found that the relative fluctuation levels decreased in more negative δ regimes. Furthermore, the reference [65] showed that a strong decrease in the connection length in negative triangularity plasmas is intrinsic to suppressing first-wall interactions, thus minimizing cross-field transport. However, reference [66] noted that the radial velocities of the filaments are reduced even in regions where the connection length is not reduced in negative δ plasmas, suggesting that connection length may not be the only factor. LP measurements from strongly negative delta plasmas would be very valuable in clarifying the multimachine results for δ.

It is difficult to interpret the results found for the effect of κ and R_0/a on far-SOL fluctuations in figures 9(b) and 9(a), respectively. Little prior experimental work has been performed to investigate these effects on SOL, in addition to what has been studied in references [64, 85]. From the nonlinear simulation work presented in reference [85], it was suggested that plasma shaping has an impact on the growth rate of resistive ballooning modes. These were found to be stable with R_0/a, κ, and $\delta < 0$. Furthermore, it was implied that the SOL pressure scale length decreases with κ, consistent with the narrowing of the heat flux width presented in reference [64]. On the basis of this notion, it would suggest that shoulder formation is not prominent in strongly elongated plasmas. From reference [79], it is noted that the radial velocity and the parallel drainage time of the filaments are known to drive the formation of the density shoulder. Therefore, κ must be inversely proportional to the radial velocity and the drainage time, where the drainage time scales with the connection length. The multimachine scan shows a clear separation between the conventional and spherical tokamaks for κ and R_0/a. It can be concluded that smaller aspect ratio devices (also having the highest elongation) have far-SOL fluctuations with longer duration times and mean waiting times compared to conventional tokamaks based on the available database. More devices with sufficiently long time-series measurements are required to conduct a dedicated scan of all of the engineering parameters studied here and should be explored in more detail.

Divertor closure has previously been indicated to play a role in influencing the characteristics of filaments [38]. We did not pinpoint whether this effect was present in this study, although it is recognized that this is indeed different between the devices. Also, we do not study the effects of divertor collisionality here, since other investigations in JET, C-Mod and AUG have implied that this was insufficient to explain upstream conditions in the SOL [36, 37, 92]. Instead, the role of neutrals was suggested as one of the candidates for shoulder formation due to modifying ionization rates [36, 92]. It is acknowledged that the main chamber recycling may behave differently between these devices. In C-Mod, this increases with line-averaged density, and the neutral density also increases [16,24]. In TCV, the presence of divertor baffles and a large inner wall gap were indicated to reduce the recycling of main chamber neutrals as well as the density shoulder amplitude [93]. This feature was also highlighted in AUG high confinement mode (H-mode) scenarios showing that larger filaments are observed at higher neutral pressures [38]. We do not study these effects since the main focus of this work is to characterize the far-SOL fluctuations using the stochastic model that is agnostic to such effects.

Looking towards next-step fusion devices such as SPARC and ITER, one can tentatively infer from this L-mode study what the characteristics of far-SOL fluctuations may be. For the SPARC device, the L-mode scenario at $I_\mathrm{P} = 8.7\,\mathrm{MA}$ and $B_\mathrm{T} = 12.2\,\mathrm{T}$ at $f_\mathrm{GW} = 0.12$ is provided in reference [94]. The main plasma parameters for ITER are $I_\mathrm{P} = 12\,\mathrm{MA}$, $B_\mathrm{T} = 5.3\,\mathrm{T}$ before a transition from L-mode to H-mode at $f_\mathrm{GW} = 0.33$, based on a simulation is mentioned in reference [95]. These large I_P values are responsible for such low f_GW. From the results of this study, despite being limited to an L-mode database, we expect the combination of strong magnetic fields and large plasma currents to result in weakly intermittent far-SOL fluctuations. It is indicated that the strong toroidal fields drive the duration times and waiting times lower. In view of this, weakly intermittent fluctuations close to the first wall suggests one is approaching Gaussian distributions, resulting in sputtering rates based on mean electron density and temperature becoming increasingly relevant. Since f_GW is low in SPARC due to such large plasma currents, the radial velocity may be further hindered by strong magnetic fields, reducing the expected wall fluxes, as stated in reference [62].

In conclusion, this study demonstrates the applicability of the FPP to far-SOL statistics across DIII-D, TCV, KSTAR, MAST, MAST-U, and C-Mod. The intermittency parameter of the fluctuations appears to be independent of $\overline{n}_\mathrm{e}$ in all of the devices studied here, except for C-Mod which is indisputably a function of Greenwald fraction density. Throughout, the mean amplitudes increase with $\overline{n}_\mathrm{e}$ in all devices. In compact devices such as C-Mod, MAST, and MAST-U, waiting times increase with $\overline{n}_\mathrm{e}$. In conventional tokamaks, τ_d is independent of $\overline{n}_\mathrm{e}$, whereas this is not the case for spherical tokamaks. The multimachine analysis shows a dependence of the plasma current and therefore the poloidal magnetic field on the fluctuation statistics. Higher magnetic fields suggest weak intermittency at low densities as a result of smaller radial velocities and decreased cross-field particle transport. From this study, the use of parameterizing fluctuation statistics with f_GW for cross-machine comparison is debatable due to the different statistical behaviours seen with $\overline{n}_\mathrm{e}$ and that there was no dependence on the minor radius. This motivates a fundamental investigation in how the fluctuation statistics change with the variable quantities of Greenwald fraction. Limited experimental work has been conducted on the effects of elongation and aspect ratio on far-SOL fluctuations. Here, we present for the first time how this impacts the statistical properties of filaments in L-mode using the stochastic model, showing a clear distinction between conventional and spherical tokamaks. The filaments appear bigger in amplitude, longer in waiting times, and longer in duration times in spherical tokamaks. The duration times, mean waiting times and amplitudes trend with aspect ratio for conventional tokamaks. Overall, the study highlights the influence of machine and engineering parameters on L-mode far-SOL fluctuation statistics, thereby providing an insight for future devices.

Further work would benefit from the inclusion of other fusion devices. This also includes employing the analysis on I_{sat} measurements from the MAST-U Mach probe and incorporating reciprocating LP measurements from KSTAR [33] and TCV [29] to increase the current LP database for these devices. Additionally, larger scans of the presented parameters, in particular dedicated experiments, are probably required to make fully conclusive statements on the role of κ. The examination of effects from different divertor configurations such as the Super-X, and investigation into the effects of neutral pressure would be fruitful. It would also be interesting to include another high-field device such as COMPASS-U to determine whether similar trends to C-Mod are observed.

Acknowledgments

Discussions with G. Decristoforo, T. Golfinopoulos, E. Marmar and C. K. Tsui are gratefully acknowledged. The first author thanks the DIII-D reviewers, A. McLean and M. Shafer for their comments. This work was supported by the Tromsø Research Foundation under grant number 19_SG_AT and the UiT Aurora Centre Program, UiT The Arctic University of Norway (2020). Alcator C-Mod data were generated and maintained under US Department of Energy awards DE-FC02-99ER54512 and DE-SC0014264. Support for A. Q. Kuang was provided by Commonwealth Fusion System under the grant number RPP-022. Support for J. L. Terry was provided by the US Department of Energy, Fusion Energy Sciences, award DE-SC0014251. The first author thanks the MIT Plasma Science and Fusion Center for their generous hospitality where this work was conducted. M. Lampert was provided by the Princeton Plasma Physics Laboratory (PPPL) under the grant number DE-AC02-09CH11466. MAST-U data collection was funded by the EPSRC Energy Programme [grant number EP/W006839/1]. MAST data collection was funded by the RCUK Energy Programme [grant number EP/I501045]. Work related to the TCV data was supported in part by the Swiss National Science Foundation. Further, this work has been carried out within the framework of the EUROfusion Consortium, via the Euratom Research and Training Programme (Grant Agreement No 101052200 — EUROfusion) and funded by the Swiss State Secretariat for Education, Research and Innovation (SERI). Views and opinions expressed are however those of the author(s) only and do not necessarily reflect those of the European Union, the European Commission, or SERI. Neither the European Union nor the European Commission nor SERI can be held responsible for them. This work was also supported by the R&D Program of "KSTAR Experimental Collaboration and Fusion Plasma Research" (EN2301-14) through the Korea Institute of Fusion Energy (KFE) funded by Korea Ministry of Science and ICT (MSIT). Finally, collection of DIII-D data was supported by the U.S. Department of Energy, Office of Science, Office of Fusion Energy Sciences, using the DIII-D National Fusion Facility, a DOE Office of Science user facility under Award(s) DE-FG02-07ER54917, DE-FC02-04ER54698. **Disclaimer:** This report was prepared as an account of work sponsored by an agency of the United States Government. Neither the

References

[1] Pitts R A *et al.* 2005 *Plasma Phys. Control. Fusion* **47** B303–B322

[2] Whyte D G, Lipschultz B L, Stangeby P C, Boedo J, Rudakov D L, Watkins J G and West W P 2005 *Plasma Phys. Control. Fusion* **47** 1579–1607

[3] Lipschultz B *et al.* 2007 *Nucl. Fusion* **47** 1189–1205

[4] Marandet Y *et al.* 2011 *Nucl. Fusion* **51** 083035

[5] Birkenmeier G *et al.* 2015 *Nucl. Fusion* **55** 033018

[6] Meyer H *et al.* 2017 *Nucl. Fusion* **57** 102014

[7] Zweben S J *et al.* 2002 *Phys. Plasmas* **9**

[8] Terry J, Maqueda R, Pitcher C, Zweben S, LaBombard B, Marmar E, Pigarov A and Wurden G 2001 *J. Nucl. Mater.* **290-293** 757–762

[9] Zweben S *et al.* 2004 *Nucl. Fusion* **44** 134–153

[10] Terry J *et al.* 2005 *Nucl. Fusion* **45** 1321–1327

[11] Terry J, Zweben S, Grulke O, Greenwald M and LaBombard B 2005 *J. Nucl. Mater.* **337-339** 322–326

[12] Zweben S J, Boedo J A, Grulke O, Hidalgo C, LaBombard B, Maqueda R J, Scarin P and Terry J L 2007 *Plasma Phys. Control. Fusion* **49** S1–S23

[13] Zweben S J *et al.* 2016 *Plasma Phys. Control. Fusion* **58** 044007

[14] Zweben S J, Terry J L, Stotler D P and Maqueda R J 2017 *Rev. Sci. Instrum.* **88** 041101

[15] Krasheninnikov S 2001 *Phys. Lett. A* **283** 368–370

[16] LaBombard B, Umansky M, Boivin R, Goetz J, Hughes J, Lipschultz B, Mossessian D, Pitcher C, Terry J and Group A 2000 *Nucl. Fusion* **40** 2041–2060

[17] D'Ippolito D A and Myra J R 2008 *Phys. Plasmas* **15** 082316

[18] D'Ippolito D A, Myra J R and Zweben S J 2011 *Phys. Plasmas* **18** 060501

[19] Stangeby P C 2000 *The plasma boundary of magnetic fusion devices* Plasma physics series (Bristol ; Philadelphia: Institute of Physics Pub)

[20] Pigarov A Y, Krasheninnikov S I, Rognlien T D, Schaffer M J and West W P 2002 *Phys. Plasmas* **9** 1287–1299

[21] Boedo J A *et al.* 2001 *Phys. Plasmas* **8** 4826–4833

[22] LaBombard B, Boivin R L, Greenwald M, Hughes J, Lipschultz B, Mossessian D, Pitcher C S, Terry J L, Zweben S J and Alcator Group 2001 *Phys. Plasmas* **8** 2107–2117

[23] Rudakov D L *et al.* 2002 *Plasma Phys. Control. Fusion* **44** 717–731

[24] Lipschultz B, LaBombard B, Pitcher C S and Boivin R 2002 *Plasma Phys. Control. Fusion* **44** 733–748

[25] Lipschultz B, Whyte D and LaBombard B 2005 *Plasma Phys. Control. Fusion* **47** 1559–1578

[26] Rudakov D *et al.* 2005 *Nucl. Fusion* **45** 1589–1599

[27] Rudakov D *et al.* 2005 *J. Nucl. Mater.* **337-339** 717–721

[28] Garcia O E, Pitts R A, Horacek J, Madsen J, Naulin V, Nielsen A H and Rasmussen J J 2007 *Plasma Phys. Control. Fusion* **49** B47–B57

[29] Garcia O, Horacek J, Pitts R, Nielsen A, Fundamenski W, Naulin V and Rasmussen J J 2007 *Nucl. Fusion* **47** 667–676

[30] Silva C, Gonçalves B, Hidalgo C, Pedrosa M, Fundamenski W, Stamp M and Pitts R 2009 *J. Nucl. Mater.* **390-391** 355–358

[31] Carralero D *et al.* 2015 *J. Nucl. Mater.* **463** 123–127

[32] Militello F, Garzotti L, Harrison J, Omotani J, Scannell R, Allan S, Kirk A, Lupelli I and Thornton A 2016 *Nucl. Fusion* **56** 016006

[33] Garcia O, Kube R, Theodorsen A, Bak J G, Hong S H, Kim H S, Team t K P and Pitts R 2017 *Nucl. Mater. Energy* **12** 36–43

[34] Walkden N R, Wynn A, Militello F, Lipschultz B, Matthews G, Guillemaut C, Harrison J, Moulton D and JET Contributors 2017 *Plasma Phys. Control. Fusion* **59** 085009

[35] Kube R, Garcia O E, Theodorsen A, Brunner D, Kuang A Q, LaBombard B and Terry J L 2018 *Plasma Phys. Control. Fusion* **60** 065002

[36] Wynn A *et al.* 2018 *Nucl. Fusion* **58** 056001

[37] Kuang A, LaBombard B, Brunner D, Garcia O, Kube R and Theodorsen A 2019 *Nucl. Mater. Energy* **19** 295–299

[38] Vianello N *et al.* 2020 *Nucl. Fusion* **60** 016001

[39] Stagni A *et al.* 2022 *Nucl. Fusion* **62** 096031

[40] Greenwald M 2002 *Plasma Phys. Control. Fusion* **44** R27–R53

[41] Sun H *et al.* 2023 *Nucl. Fusion* **63** 016021

[42] Antar G Y, Krasheninnikov S I, Devynck P, Doerner R P, Hollmann E M, Boedo J A, Luckhardt S C and Conn R W 2001 *Phys. Rev. Lett.* **87** 065001

[43] Antar G Y, Counsell G, Yu Y, Labombard B and Devynck P 2003 *Phys. Plasmas* **10**

[44] Boedo J *et al.* 2003 *J. Nucl. Mater.* **313-316** 813–819

[45] Sattin F, Vianello N and Valisa M 2004 *Phys. Plasmas* **11** 5032–5037

[46] Kirnev G, Budaev V, Grashin S, Khimchenko L and Sarytchev D 2005 *Nucl. Fusion* **45** 459–467

[47] LaBombard B, Hughes J, Mossessian D, Greenwald M, Lipschultz B, Terry J and Team t A C M 2005 *Nucl. Fusion* **45** 1658–1675

[48] Garcia O E, Horacek J, Pitts R A, Nielsen A H, Fundamenski W, Graves J P, Naulin V and Rasmussen J J 2006 *Plasma Phys. Control. Fusion* **48** L1–L10

[49] Tanaka H, Ohno N, Asakura N, Tsuji Y, Kawashima H, Takamura S and Uesugi Y 2009 *Nucl. Fusion* **49** 065017

[50] Sattin F, Agostini M, Cavazzana R, Scarin P and Terry J L 2009 *Plasma Phys. Control. Fusion* **51** 095004

[51] Sattin F, Agostini M, Cavazzana R, Serianni G, Scarin P and Vianello N 2009 *Phys. Scr.* **79** 045006

[52] Horacek J, Adamek J, Müller H, Seidl J, Nielsen A, Rohde V, Mehlmann F, Ionita C and Havlíčková E 2010 *Nucl. Fusion* **50** 105001

[53] Garcia O, Cziegler I, Kube R, LaBombard B and Terry J 2013 *J. Nucl. Mater.* **438** S180–S183

[54] Garcia O E, Fritzner S M, Kube R, Cziegler I, LaBombard B and Terry J L 2013 *Phys. Plasmas* **20** 055901

[55] Garcia O, Horacek J and Pitts R 2015 *Nucl. Fusion* **55** 062002

[56] Kube R, Theodorsen A, Garcia O E, LaBombard B and Terry J L 2016 *Plasma Phys. Control. Fusion* **58** 054001

[57] Theodorsen A, Garcia O E, Horacek J, Kube R and Pitts R A 2016 *Plasma Phys. Control. Fusion* **58** 044006

[58] Garcia O E, Kube R, Theodorsen A, LaBombard B and Terry J L 2018 *Phys. Plasmas* **25** 056103

[59] Theodorsen A, Garcia O E, Kube R, LaBombard B and Terry J L 2018 *Phys. Plasmas* **25** 122309

[60] Bencze A, Berta M, Buzás A, Hacek P, Krbec J, Szutyányi M and the COMPASS Team 2019 *Plasma Phys. Control. Fusion* **61** 085014

[61] Kube R, Theodorsen A, Garcia O E, Brunner D, LaBombard B and Terry J L 2020 *J. Plasma Phys.* **86** 905860519

[62] Ahmed S, Garcia O E, Kuang A Q, LaBombard B, Terry J L and Theodorsen A 2023 Submitted to *Plasma. Phys. Control. Fusion*

[63] Kirk A, Lisgo S, Nardon E, Eich T, Herrmann A, Kallenbach A and Loarte A 2009 *J. Nucl. Mater.* **390-391** 727–732

[64] Horacek J *et al.* 2016 *Plasma Phys. Control. Fusion* **58** 074005

[65] Han W, Offeddu N, Golfinopoulos T, Theiler C, Tsui C, Boedo J, Marmar E and The Tcv Team 2021 *Nucl. Fusion* **61** 034003

[66] Han W, Offeddu N, Golfinopoulos T, Theiler C, Terry J, Wüthrich C, Galassi D, Colandrea C and Marmar E 2023 *Nucl. Fusion* **63** 076025

[67] Garcia O E 2012 *Phys. Rev. Lett.* **108** 265001

[68] Militello F and Omotani J 2016 *Nucl. Fusion* **56** 104004

[69] Walkden N, Wynn A, Militello F, Lipschultz B, Matthews G, Guillemaut C, Harrison J and Moulton D 2017 *Nucl. Fusion* **57** 036016

[70] Theodorsen A, Garcia O, Kube R, LaBombard B and Terry J 2017 *Nucl. Fusion* **57** 114004

[71] LaBombard B and Lyons L 2007 *Rev. Sci. Instrum.* **78** 073501

[72] LaBombard B, Golfinopoulos T, Terry J L, Brunner D, Davis E, Greenwald M, Hughes J W and Alcator C-Mod Team 2014 *Phys. Plasmas* **21** 056108

[73] Boedo J A and Rudakov D L 2017 *Rev. Sci. Instrum.* **88** 033505

[74] Ahmed S, Garcia O E and Theodorsen A 2023 *Phys. Rev. E* **107** 054222

[75] Garcia O E and Theodorsen A 2017 *Phys. Plasmas* **24** 032309

[76] Theodorsen A, Garcia O E and Rypdal M 2017 *Phys. Scr.* **92** 054002

[77] Richardson W H 1972 *J. Opt. Soc. Am.* **62** 55

[78] Lucy L B 1974 *Astron. J.* **79** 745

[79] Losada J M, Theodorsen A and Garcia O E 2023 *Phys. Plasmas* **30** 042518

[80] Offeddu N *et al.* 2022 *Nucl. Fusion* **62** 096014

[81] Boedo J A *et al.* 2003 *Phys. Plasmas* **10** 1670–1677

[82] Kube R and Garcia O E 2011 *Phys. Plasmas* **18** 102314

[83] Kube R, Garcia O, Theodorsen A, Kuang A, LaBombard B, Terry J and Brunner D 2019 *Nucl. Mater. Energy* **18** 193–200

[84] Offeddu N *et al.* 2022 *Rev. Sci. Instrum.* **93** 123504

[85] Riva F, Lanti E, Jolliet S and Ricci P 2017 *Plasma Phys. Control. Fusion* **59** 035001

[86] Garcia O, Pitts R, Horacek J, Nielsen A, Fundamenski W, Graves J, Naulin V and Rasmussen J J 2007 *J. Nucl. Mater.* **363-365** 575–580

[87] McCormick K, Kyriakakis G, Neuhauser J, Kakoulidis E, Schweinzer J and Tsois N 1992 *J. Nucl. Mater.* **196-198** 264–270

[88] Banerjee S *et al.* 2012 *Nucl. Fusion* **52** 123016

[89] Maurizio R *et al.* 2019 *Nucl. Mater. Energy* **19** 372–377

[90] Eich T *et al.* 2013 *Nucl. Fusion* **53** 093031

[91] Birkenmeier G *et al.* 2014 *Plasma Phys. Control. Fusion* **56** 075019

[92] Carralero D *et al.* 2017 *Nucl. Fusion* **57** 056044

[93] Tsui C K *et al.* 2022 *Phys. Plasmas* **29** 062507

[94] Creely A J *et al.* 2020 *J. Plasma Phys.* **86** 865860502

[95] Artaud J *et al.* 2018 *Nucl. Fusion* **58** 105001